REVIEWS OF MODERN PHYSICS, VOLUME 92, APRIL–JUNE 2020

Strong-field nano-optics

Péter Dombi* and Zsuzsanna Pápa
Wigner Research Centre for Physics, H-1121 Budapest, Hungary
and ELI-ALPS Research Institute, H-6728 Szeged, Hungary

Jan Vogelsang
Lunds Universitet, SE-22100 Lund, Sweden

Sergey V. Yalunin
University of Göttingen, D-37073 Göttingen, Germany

Murat Sivis
University of Göttingen, D-37073 Göttingen, Germany and Max Planck Institute
for Biophysical Chemistry, D-37077 Göttingen, Germany

Georg Herink
University of Bayreuth, D-95447 Bayreuth, Germany

Sascha Schäfer and Petra Groß
Institute of Physics, University of Oldenburg, D-26129 Oldenburg, Germany

Claus Ropers
University of Göttingen, D-37073 Göttingen, Germany and Max Planck Institute
for Biophysical Chemistry, D-37077 Göttingen, Germany

Christoph Lienau
Institute of Physics and Center of Interface Science, University of Oldenburg,
D-26129 Oldenburg, Germany

(published 9 June 2020)

The present status and development of strong-field nano-optics, an emerging field of nonlinear optics, is discussed. A nonperturbative regime of light-matter interactions is reached when the amplitude of the external electromagnetic fields that are driving a material approach or exceed the field strengths that bind the electrons inside the medium. In this strong-field regime, light-matter interactions depend on the amplitude and phase of the field, rather than its intensity, as in more conventional perturbative nonlinear optics. Traditionally such strong-field interactions have been intensely investigated in atomic and molecular systems, and this has resulted in the generation of high-harmonic radiation and laid the foundations for contemporary attosecond science. Over the past decade, however, a new field of research has emerged, the study of strong-field interactions in solid-state nanostructures. By using nanostructures, specifically those made out of metals, external electromagnetic fields can be localized on length scales of just a few nanometers, resulting in signficantly enhanced field amplitudes that can exceed those of the external field by orders of magnitude in the vicinity of the nanostructures. This leads not only to dramatic enhancements of perturbative nonlinear optical effects but also to significantly increased photoelectron yields. It resulted in a wealth of new phenomena in laser-solid interactions that have been discovered in recent years. These include the observation of above-threshold photoemission from single nanostructures, effects of the carrier-envelope phase on the photoelectron emission yield from metallic nanostructures, and strong-field acceleration of electrons in optical near fields on subcycle timescales. The current state of the art of this field is reviewed, and several scientific applications that have already emerged from the fundamental discoveries are discussed. These include, among others, the coherent control of localized electromagnetic fields at the surface of solid-state nanostructures and of free-electron wave packets by such optical near fields, resulting in the creation of attosecond electron bunches, the coherent control of photocurrents on nanometer length and femtosecond timescales by the

---

[*] dombi.peter@wigner.mta.hu

0034-6861/2020/92(2)/025003(66)

electric field of a laser pulse, and the development of new types of ultrafast electron microscopes with unprecedented spatial, temporal, and energy resolution. The review concludes by highlighting possible future developments, discussing emerging topics in photoemission and potential strong-field nanophotonic devices, and giving perspectives for coherent ultrafast microscopy techniques. More generally, it is shown that the synergy between ultrafast science, plasmonics, and strong-field physics holds promise for pioneering scientific discoveries in the upcoming years.

DOI: 10.1103/RevModPhys.92.025003

CONTENTS

I. INTRODUCTION

Strong-field nano-optics describes an active and rapidly developing field of research that studies the interaction of solid-state nanostructures with femtosecond electromagnetic fields so intense that their amplitude and phase, rather than the intensity alone, affect the motion of free and bound electrons. This research area developed from two important and established fields of contemporary science in the past decade: nonlinear optics and nano-optics. Strong-field nano-optics exploits the interaction of matter with strong laser fields beyond the conventional realm of nonlinear optics.

It was discovered early in the laser era that nonlinear light-matter interaction processes can be exploited for the wavelength conversion of laser light (Franken *et al.*, 1961). In this interaction regime, the optical nonlinearity provided by an external electromagnetic (laser) field represents a small perturbation to the motion of electrons in their binding potential in various media, including atomic and molecular gases, liquids, and solids (Shen, 1984; Boyd, 2003). In contrast, strong-field phenomena in general involve light-matter interaction processes where external electromagnetic fields, as in intense laser beams, exceed the fields that provide the binding of the electrons inside the medium. This represents a distinctive new class of nonlinearities. In this regime, new phenomena can occur, for example, the laser-induced ionization of atoms or molecules and the quiver motion of the liberated electron in the oscillating strong electromagnetic field (Krause, Schafer, and Kulander, 1992; Corkum, 1993; Schafer *et al.*, 1993). This results in high-order harmonic generation (HHG) from the vacuum ultraviolet to the x-ray regime (Popmintchev *et al.*, 2012). Alternatively, the liberated electron may be diffracted off the ionic core, facilitating the tomography of electronic wave functions of molecules (Itatani *et al.*, 2004). Exploiting such extreme nonlinearities has established attosecond science as a broad research field

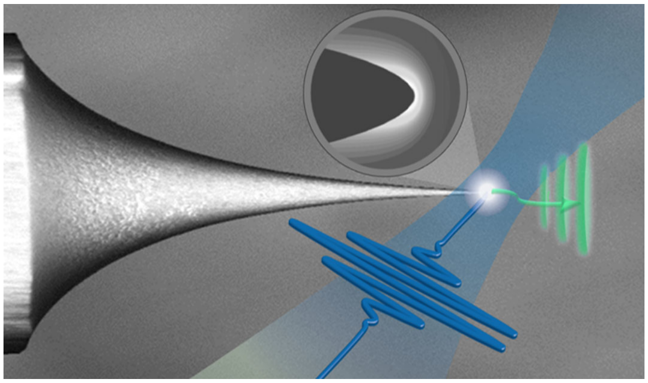

FIG. 1. Illustration of strong-field photoemission at nanostructures. Sharp metallic nanotips localize and enhance the incident optical excitation (blue pulse under the tip) at the apex. Nonlinear photoemission induces ultrafast electron emission (green bunches at the apex), and the trajectories are driven by the optical near field.

(Krausz and Ivanov, 2009) and has yielded fundamental discoveries in the field of atomic and molecular physics over the past two decades (Calegari *et al.*, 2016).

In most circumstances encountered in strong-field atomic and molecular physics, the spatial localization of the driving electromagnetic field is inherently limited by the wavelength of light, which is close to 1 μm in the visible range. In contrast, in strong-field nano-optics electrons interact with strong electromagnetic fields that are, in many cases, spatially confined to a few nanometers only. This is often achieved by exciting tailored nanostructures, the optical modes of which are spatially confined to dimensions given by the size of the nanostructure rather than the wavelength of light (Maier, 2007; Novotny and Hecht, 2012). This field localization can be realized with the help of sharp geometrical features (the optical analogy of the lightning rod effect) or with resonantly excited collective electron oscillations, surface plasmons (Raether, 1988). These excitations entail a pronounced enhancement of the local electric field that can exceed the amplitude of the driving field by orders of magnitude, for example, in the terahertz frequency range, where the optical properties of metals approach that of a perfect, lossless conductor. This pronounced local field enhancement has two important consequences: (i) it lowers the threshold for the onset of strong-field phenomena by orders of magnitude (from 10–100 $\mathrm{TW/cm^2}$ in atomic and molecular systems to $\mathrm{GW/cm^2}$ in tailor-designed plasmonic nanoantennas, and (ii) its spatial confinement results in a class of fundamentally new physical phenomena. To illustrate the latter, we consider photoemission from a sharp metal tip, as illustrated in Fig. 1. Electrons emitted via nonlinear photoemission are accelerated by temporally and spatially varying near fields. At high local field strengths, electrons may experience recollision at the surface, ponderomotive acceleration in the field gradients, or subcycle interactions. For extremely sharp metal tips, or sufficiently long wavelengths, the spatial extent of the localized optical near field is so short that the electron will be accelerated across this near field, into an essentially field-free region, within less than half an oscillation cycle of the light field (Herink *et al.*, 2012).

It is the aim of this review to provide a concise overview of the unique phenomena discovered in the interaction of strong light fields with solid-state nanostructures. We introduce the necessary scientific background and give a summary of the current state of the art, covering several related experimental studies. For certain additional aspects, specifically the theory of attosecond streaking, the strong-field response of atoms in spatially inhomogeneous fields, and strong-field photoemission from dielectric nanoparticles, we refer the interested reader to the review by Ciappina *et al.* (2017) and a book coedited by Hommelhoff and Kling (2015).

To provide relevant background for this review, first we introduce fundamental interaction processes of light with metal nanostructures in Sec. II. We focus on nanostructures that have been most important in strong-field nano-optics applications, namely, plasmonic nanoparticles and metallic nanotips. With the help of these nano-optical building blocks and plasmonic nanofocusing, one can realize more complex architectures. Subsequently we review nonlinearities that can be observed for nanostructured surfaces. Related phenomena such as low-order harmonic generation can be understood in the framework of perturbative nonlinear optics, with the nanostructured surface enhancing the effective nonlinear susceptibility of the medium. Another type of nonlinearity is photoelectron emission from nanostructures, which is also reviewed.

In Sec. III., we move on to specific applications and perspectives of highly nonlinear phenomena at nanostructures. We review how strong-field photoemission provides for a sensitive probe of near fields. Streaking techniques, which are well known in ultrafast science, can also be applied to nanolocalized fields. A particularly interesting aspect of strong-field nano-optics is the potential to drive currents in nanoscale architectures and realize ultrafast switching of optical-frequency signals. Therefore, we also introduce the major steps that have been made so far, leading toward switching currents at petahertz frequencies. Ultrafast nonlinear photoemission from nanotips is a key element in the realization of ultrafast electron imaging and spectroscopy, which is also introduced. Finally, we provide the perspectives of strong-field nano-optics. In Sec. 1.A, we first give a brief overview of historical aspects related to this review.

A. Historical perspective

Perhaps the most important enabling discovery that eventually paved the way to contemporary strong-field physics was photoemission, i.e., the external photoeffect (or photoelectric effect). Its wide range of applications, for example, in the understanding of the electronic structure of materials (Hüfner, 2003) and photodetector technology, illustrates its importance.

Prior to photoemission, field- or heat-induced currents from metals have been known at least since the 18th century, for example, in the form of electric discharges (Winkler, 1744). Measurements of the current as a function of applied static voltage (Millikan and Eyring, 1926; Millikan and Lauritsen, 1928) led to a quantitative theoretical description of field emission by Fowler and Nordheim in the late 1920s (Fowler and Nordheim, 1928; Forbes, 2006). Electron emission from heated cathodes has a long history, from early observations until Richardson's law of thermionic emission (Richardson, 1929; Crowell, 1965).

Photoelectron emission was originally discovered as a by-product of radio wave transmission experiments by Heinrich Hertz and Wilhelm Hallwachs, who initially termed the observation of light-induced currents “light electricity,” called *Lichtelektrizität* in German (Hertz, 1887). Shortly after Thomson’s discovery of the electron (Thomson, 1897), studies of the stopping voltage required to suppress the photocurrent by Lenard (1902) led to the interpretation of this effect by Albert Einstein in 1905 (Einstein, 1905). Marking the birth of the photon concept, Einstein described the phenomenon as the emission of electrons due to the absorption of discrete electromagnetic energy quanta, later termed photons, provided that their energy exceeds the work function of the metal surface. His interpretation was widely accepted only after Millikan (1914) used the effect to measure Planck’s constant. Ultraviolet (UV) photons are applied for electron emission to overcome typical metallic work functions of ∼4 to 5 eV, and extreme-ultraviolet (XUV) illumination is also used for photoemission spectroscopy, depending on the binding energy of the state investigated.

Before the laser era, only linear photoemission processes were experimentally accessible, requiring UV illumination for most metals. Visible light can be used only for certain, mostly alkali-based photoemitters with reduced work functions. With the advent of lasers, nonlinear multiphoton processes such as the two-photon absorption predicted by Goeppert-Mayer (1931) became accessible (Voronov and Delone, 1966; Agostini *et al.*, 1968). The nonlinear photoemission research field has an additional theoretical precursor with the paper of Smith (1962), who also discussed the possibility of the observation of laser-induced field emission. In parallel to multiphoton photoionization studies on atoms, investigations on multiphoton-induced photoemission from solids started (Teich, Schroeer, and Wolga, 1964; Farkas, Náray, and Varga, 1967; Logothetis and Hartman, 1969), and higher-order nonlinearities were demonstrated (Farkas, Horváth, and Kertész, 1972; Bechtel, Smith, and Bloembergen, 1975; Lompre, Thebault, and Farkas, 1975).

In parallel, research on the field emission of electrons involving dc fields also thrived (Plummer and Young, 1970; Gadzuk and Plummer, 1971; Plummer, Gadzuk, and Penn, 1975). These experiments were performed in parallel to photoemission research of that era and field emission results of the 1970s impacted contemporary photoemission studies as well.

As a later development, ultrashort laser pulses provided time-resolved insight into ultrafast charge carrier dynamics in metals, particularly when using time-resolved two-photon photoemission spectroscopy (Haight *et al.*, 1985; Schoenlein *et al.*, 1988; Fann *et al.*, 1992; Schmuttenmaer *et al.*, 1994; Petek and Ogawa, 1997; Echenique *et al.*, 2004; Frischkorn and Wolf, 2006; Bovensiepen, Wolf, and Petek, 2010; Bovensiepen, Petek, and Wolf, 2012; Bauer, Marienfeld, and Aeschlimann, 2015).

Another important step was the discovery of above-threshold photoionization, representing the absorption of more than the minimum number of photons in a bound-free transition (Agostini *et al.*, 1979). At even higher intensities, the atomic or surface potential can be distorted to a degree that the electron tunnels through the barrier (Bunkin and Fedorov, 1965; Keldysh, 1965). Research on related processes culminated in the discovery of high-harmonic generation in the 1980s (Ferray *et al.*, 1988), and subsequently the birth of experimental attosecond science (Papadogiannis *et al.*, 1999; Hentschel *et al.*, 2001; Paul *et al.*, 2001). The term *strong-field interaction* is used for processes that take place at light intensities higher than those required for multiphoton effects, corresponding to the regime of nonperturbative light-matter interaction. Within the field of nonlinear photoemission, there are also recent research efforts that have reshaped our understanding of the mechanisms of above-threshold photoemission phenomena, highlighting the nonsequential nature of this process (Reutzel, Li, and Petek, 2019).

In contrast to strong-field phenomena in isolated atomic systems, collective phenomena cannot be neglected in light-surface interaction experiments, even if the interaction takes place in ultrahigh vacuum and involves completely clean, adsorbate-free single-crystal surfaces. Following initial experiments showing signatures of strong-field photoemission, the field gained significant attraction when the effects of plasmonic excitations and near fields of nanostructures were considered. Only in the last few years have first applications based on nonlinear or strong-field nano-optics emerged.

II. INTERACTION OF LIGHT WITH METAL NANOSTRUCTURES

In this section, we give a brief overview of the fundamental physical processes that are induced when weak or strong electromagnetic fields interact with metals and, in particular, with metallic nanoparticles.

A. Optical properties and field localization in nanoscale media

1. Dielectric functions of metals: Linear optical properties

The optical response of metals is largely governed by the collective response of free electrons. In 1900, Paul Drude laid the foundation for our present understanding of this response by introducing a classical model for the dc electrical conductivity of a metal (Drude, 1900). The electrons are treated as a freely moving gas that can be accelerated during a certain phenomenological relaxation time τ in the direction of an externally applied dc field until random scattering processes randomize the momentum. A sequence of acceleration and scattering steps results in a drift motion of the electrons, and thus a net dc current density. A quantum-mechanical extension of this model was provided by Bethe and Sommerfeld (1967).

When applying a harmonic, time-varying electric field, collective oscillations of the free-electron gas are induced. Their amplitude is given by the equation of motion for a damped harmonic oscillator without restoring force, inducing dipolar charge oscillations and hence a macroscopic polarization of the sample. The frequency-dependent local dielectric function $\varepsilon(\omega)$ of a bulk metal is thus given as

$$\varepsilon(\omega) = 1 - \frac{\omega_p^2}{\omega^2 + i\omega/\tau}, \tag{2.1}$$

where the plasma frequency ω_p denotes a characteristic frequency for the charge-density oscillations (Bohm and Pines, 1953; Pines, 1956). This results in a local dielectric function with a large negative real part and a much smaller positive imaginary part in the infrared and visible spectral range. In the high-frequency limit, ε approaches unity.

In real metals, not only the electron plasma but also single particle excitations respond to the electromagnetic field. The resulting interband dipole transitions are considered by a phenomenological term $\varepsilon_i(\omega)$ as a sum over critical point transitions (Etchegoin, Le Ru, and Meyer, 2006) and by adapting the high-frequency limit ε_∞. Experimental values for the dielectric function of gold and silver (Johnson and Christy, 1972) fit reasonably well to this model when we assume plasma frequencies of 9.1 and 9.2 eV and damping times of 9.3 and 31 fs, respectively. For gold, interband absorption due to *d*- to sp-band excitations already contributes strongly at energies above 2 eV, while for silver such effects are weak up to 3.8 eV. While such a fitting can help in parametrizing the dielectric response of the bulk metal, detailed *ab initio* descriptions of the dynamical response of metals are needed to provide a microscopic understanding of the parameters that enter such phenomenological models and, in particular, of the couplings between collective free-electron and interband excitations (Cazalilla *et al.*, 2000; Stahrenberg *et al.*, 2001; Marini *et al.*, 2002).

Currently such a Drude-like, bulk dielectric function is often used to account for the optical phenomena that are observed in the rapidly growing field of plasmonics (Barnes, Dereux, and Ebbesen, 2003; Zayats, Smolyaninov, and Maradudin, 2005; Maier, 2007; Pitarke *et al.*, 2007). Such a local response function neglects the microscopic spatial distribution of the electron density at a metal surface, i.e., the finite spill out of the electrons and Friedel oscillations in the electron density. It also does not account for the spatially nonlocal electronic response of the metal, i.e., the creation of currents by fields at spatially separated points in the sample (Feibelman, 1982; Pitarke *et al.*, 2007). Both effects are fundamentally important for correctly describing the dynamical screening of electromagnetic fields at metallic surfaces. As such, they govern the spatial variation of electromagnetic fields across metallic surfaces (Feibelman, 1982; Pitarke *et al.*, 2007) as well as the coupling between metallic nanoparticles across subnanometer-sized gaps (Savage *et al.*, 2012; Scholl, Koh, and Dionne, 2012; Scholl *et al.*, 2013). Angle-resolved photoelectron spectra (Reutzel *et al.*, 2019) can provide signatures of nonlocal multipolar interband excitations and their importance for the linear and nonlinear optical response of metals.

2. Surface plasmon polaritons

In 1957, R. H. Ritchie (Ritchie, 1957; Ritchie and Eldridge, 1962) predicted the existence of a resonance in the electron-energy loss spectra of thin metal films at an energy below the bulk plasmon resonance ω_P (Bohm and Pines, 1953). The resonance arises from the excitation of collective charge-density oscillations near the surface of the film. It was observed experimentally in 1959 (Powell and Swan, 1959), and the quanta of this excitation were termed surface plasmons (SPs) soon thereafter (Stern and Ferrell, 1960). In the nonretarded regime of large in-plane SP wave vectors k, the resonance appears at $\omega_{\mathrm{SP}} = \omega_P/\sqrt{2}$, and its electromagnetic mode profile is independent on the finite speed of light. For $k \leq \omega_{\mathrm{SP}}/c$, i.e., in the retarded regime, these surface charge oscillations couple to the electromagnetic field and the dispersion relation of the resulting surface plasmon polaritons (SPPs) lies only slightly outside the light line. In the direction normal to the surface, the net charge-density distribution is confined to an angstrom-thin region near the surface (Bennett, 1970). Its singly peaked monopole character implies that SPs at the interface between two semi-infinite dielectric and metallic media are nonradiative and cannot decay by emitting transversally polarized far-field photons. Concomitantly, far-field light that is incident on such a surface cannot directly excite SPs without an additional source of momentum. For planar interfaces, some of the fundamental SPP properties are readily derived directly from Maxwell's equations (Raether, 1988; Maier, 2007; Pitarke *et al.*, 2007; Muino *et al.*, 2012).

The dispersion relation for SPPs at a planar interface (Raether, 1988; Maier, 2007) between a semi-infinite and nonmagnetic metal with a local dielectric function $\varepsilon_1(\omega)$ and a dielectric function with $\varepsilon_2(\omega)$,

$$k_\parallel = \frac{\omega}{c}\left(\frac{\varepsilon_1\varepsilon_2}{\varepsilon_1+\varepsilon_2}\right)^{1/2}, \tag{2.2}$$

connects the in-plane wave vector k_x of the monochromatic, *p*-polarized SPP wave with its angular frequency ω. In each of the two media, the field amplitude decays exponentially with an inverse decay length

$$\kappa_i = \sqrt{k_\parallel^2 - \varepsilon_i k_0^2}, \qquad i = 1, 2, \tag{2.3}$$

where $k_0 = \omega/c$ denotes the magnitude of the free-space wave vector.

For frequencies above the plasma frequency, $\mathrm{Re}(\varepsilon_1) > 0$ holds. The metal becomes transparent and the curve approaches the light line $\omega = ck_x$, where c is the speed of light in vacuum. Of interest is the region below the classical surface plasmon frequency $\omega_{\mathrm{SP}} = \omega_p/\sqrt{2}$. At sufficiently low frequencies, the SPP dispersion lies only slightly outside of the light line. Here SPPs are lightlike quasiparticles, essentially propagating at the speed of light. The spatial extent of the evanescent SPP field is extremely different on the two sides of the interface. In the metal, it is given by the skin depth, about 25 nm in gold and silver. On the air side, it is much less confined and extends over more than c/ω. In this retarded regime, the interface supports SPP modes, but the fields are only weakly confined to the interface and field localization effects are basically absent.

This situation changes in the nonretarded regime of large in-plane wave vectors $k_x > \omega_{\mathrm{SP}}/c$. In this regime, the propagation speed of the SPPs reduces considerably. Therefore, retardation effects due to the phase variation of the plasmon mode are of minor importance and quasistatic approximations work reasonably well. For a lossless Drude metal, the dispersion relation $\omega(k_x)$ monotonically increases and approaches ω_{SP} asymptotically. The wave vector k_x is much larger than that of a propagating light wave of the same frequency and SPP waves can therefore be localized in volumes much smaller than λ^3, breaking the diffraction limit in conventional far-field optics. In both media, SPP waves are now strongly confined to the interface. The propagation speed of SPPs reduces and quasistatic approximations work reasonably well. Consequently, the magnetic field associated with the SPP mode is weak. For real, i.e., lossy, metals, the finite imaginary part of ε_1 removes the singularity in Eq. (2.2) and limits the in-plane wavelength as well the field confinement to the interface. In particular, the interband contribution to the dielectric function in the case of gold results in dispersion relations deviating significantly from those of a Drude metal.

The penetration of the SPP field into the metal results in damping of SPP waves due to unavoidable Ohmic losses (Kroo *et al.*, 1991; Yi *et al.*, 2017). Typical propagation lengths are 10–100 μm in the visible range, increasing substantially for longer wavelengths. They can be increased to the millimeter range by sandwiching a thin metal film between two dielectric layers, resulting in coupled antisymmetric SPP modes that are only weakly confined to the metal. Geometric patterning of the metal generally reduces the propagation length (Berini, 1999, 2000, 2001; Lamprecht *et al.*, 2001; J. Kim *et al.*, 2003) since the scattering of SPPs by the patterned structure provides the necessary momentum to couple SPPs to far-field photons and to induce a finite amount of radiative SPP damping (J. Kim *et al.*, 2003).

At planar interfaces between semi-infinite dielectric and metallic layers, propagating light fields cannot directly excite SPP modes. Special geometries for coupling far-field light to SPPs exist, such as a total-internal-reflection geometry (Kretschmann and Raether, 1968; Otto, 1968) or a periodic grating structure with a quasi k vector bridging the mismatch between light and SPP dispersion (Teng and Stern, 1967). Alternatively, near-field excitation schemes can also work for light-SPP coupling (Hecht *et al.*, 1996; Zhang *et al.*, 2013). In a total-internal-reflection geometry, the field strength of a thin gold film can be ~10 times higher than that of the incident field. This local enhancement can be significantly increased in nonperfect, grainy films due to plasmon localization (Budai *et al.*, 2018).

3. Metallic nanostructures

Metallic nanostructures of arbitrary shape show a strong optical response at certain resonance frequencies, originating from the collective excitation of the free electrons inside the nanoparticle. The optical properties of these multipolar, localized surface plasmon (LSP) excitations are introduced here since they represent the basis for the strong-field phenomena discussed later. For further discussion, we refer the interested reader to various textbooks and reviews (Hulst, 1981; Bohren and Huffman, 1983; Kreibig and Vollmer, 1995; Maier, 2007; Novotny and Hecht, 2012).

a. Plasmonic nanoparticles

The prototypical model system for the optical response of a metallic nanoparticle is a small nanosphere of dielectric function ε_1 and with a radius a, much smaller than the wavelength of light. In the quasistatic approximation, the isotropic polarizability (α) of such a particle is given as

$$\alpha = 4\pi a^3 \frac{\varepsilon_1 - \varepsilon_2}{\varepsilon_1 + 2\varepsilon_2} \tag{2.4}$$

for an isotropic and nonabsorbing medium surrounding the nanosphere with dielectric constant ε_2 (Le Ru and Etchegoin, 2009).

An incident electromagnetic field $E_0(\omega)$ polarizes the nanoparticle and creates a spatially homogeneous field inside the sphere. In the outside, the field is the sum of the incident field and the field that is reradiated by a fictitious pointlike dipole located in the center of the sphere ($\mathbf{r} = 0$) and with a dipole moment

$$\mathbf{p}(\omega) = \varepsilon_2 \varepsilon_0 \alpha(\omega) \mathbf{E}_0(\omega). \tag{2.5}$$

Its near field is preferentially oriented along the direction of the incident field, whereas the far field vanishes along the dipole axis. The local energy density in the direct vicinity of the particle is orders of magnitude higher than that contained in the far-field term of the dipole field.

Equation (2.4) shows that the polarizability experiences a resonant enhancement if $|\varepsilon_1 + 2\varepsilon_2|$ tends to zero. The quasiparticle associated with this resonance is known as the lowest-order dipolar LSP. For a spherical particle, the condition is met in air at $\omega_0 = \omega_p/\sqrt{3}$. The form of the resonance condition depends on the shape of the particle and for larger particles higher-order multipole resonances also occur (Heilweil and Hochstrasser, 1985).

The scattering cross section of the nanoparticle $C_{\mathrm{sca}}(\omega)$ is obtained as the total power radiated by the dipole divided by the incident intensity:

$$C_{\mathrm{sca}}(\omega) = \frac{k^4}{6\pi} |\alpha(\omega)|^2. \tag{2.6}$$

Similarly, the absorption cross section $C_{\mathrm{abs}}(\omega)$ is

$$C_{\mathrm{abs}} = k \mathrm{Im}[\alpha(\omega)], \tag{2.7}$$

and the extinction cross section is given by the sum $C_{\mathrm{ext}} = C_{\mathrm{sca}} + C_{\mathrm{abs}}$.

The resonant enhancement in these spectra depends critically on ε_2 in the region around $\varepsilon_1 \approx -2\varepsilon_2$, making nanoparticle scattering spectra sensitive to the dielectric function of the environment (Müller *et al.*, 2002). It is seen that the scattering cross section is proportional to $|\alpha|^2$ and hence to the sixth power of the particle radius, while the absorption cross section scales only with a^3. This is why absorption studies are more sensitive for small particles than light scattering, and photothermal imaging techniques have allowed for imaging individual sub-10-nm particles (Boyer *et al.*, 2002). Light scattering from single small particles is challenging to resolve

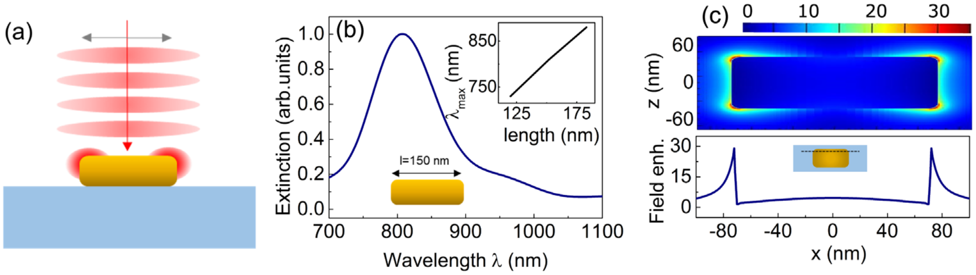

FIG. 2. Localized surface plasmons. (a) LSP generation on a metallic nanorod written onto a glass substrate. (b) Spectral resonance of LSP coupling for a gold nanorod with 150 nm length and (inset) the position of the resonance peak as a function of nanoparticle size. (c) Field amplitude map (in units of the amplitude of the incident field) for a 150-nm-long gold nanorod calculated at the LSP resonance wavelength.

and a variety of near-field-based (Klar *et al.*, 1998) and far-field-based techniques have been developed (Arbouet *et al.*, 2004; Lindfors *et al.*, 2004; van Dijk, Lippitz, and Orrit, 2005; Muskens *et al.*, 2008).

The quasistatic approach neglects the radiative damping of the particle dipole as well as retardation effects due to wave propagation within the particle. Both effects are included in the rigorous electrodynamic model developed by Mie (Meier and Wokaun, 1983; Kuwata *et al.*, 2003). For larger particles, radiation damping is an important contribution to the finite lifetime T_2 of the photoinduced dipole moment p (Heilweil and Hochstrasser, 1985), and hence to a finite homogeneous linewidth $\Gamma = 2\hbar/T_2$ of the linear optical spectrum of a single nanoparticle. The radiative damping rate $1/T_{2,\mathrm{rad}} = \Gamma_{\mathrm{rad}}/2\hbar = \kappa V$ scales with the volume of the particle (Sönnichsen *et al.*, 2002a, 2002b). For gold nanoparticles, the linewidth Γ indeed increases from 200 meV ($T_2 = 6.5$ fs) for 20-nm particles to more than 800 meV ($T_2 = 1.7$ fs) for larger particles of more than 100 nm diameter. κ values of 4×10^{-7} to 6×10^{-7} $\mathrm{fs}^{-1}\,\mathrm{nm}^{-3}$ were deduced (Hu *et al.*, 2008). When reducing the size of the nanoparticle much below 50 nm, nonradiative contributions to the plasmon damping arising from intraband and interband electron-electron scattering, electron-phonon scattering, or impurity scattering dominate. Below 20 nm, the linewidth increases inversely proportionally to the particle radius (Stietz *et al.*, 2000;Baida *et al.*, 2009) due to different microscopic mechanisms, in particular, a reduction of the surface plasmon mean free path due to scattering at the nanoparticle surface (Pustovit and Shahbazyan, 2006). This modifies the decay of the plasmon into electron-hole pairs (Landau damping) and can be understood as enhanced electron scattering resulting from quantum confinement of electronic states (Kawabata and Kubo, 1966; Yannouleas and Broglia, 1992; Thakkar *et al.*, 2018). The inelastic scattering of plasmon excitations at adsorbate or interface states (chemical interface damping) contributes (Hovel *et al.*, 1993; Persson, 1993; Stietz *et al.*, 2000; Kuwata *et al.*, 2003).

To reach maximum LSP field enhancement, the laser frequency should match the peak extinction of the LSP resonance (Rossi *et al.*, 2017), as illustrated in Fig. 2. Because of the small volumes and the 3D localization involved, LSP excitation often gives higher electromagnetic field enhancement than that of SPPs. For complex nanoparticle shapes involving corners and edges with <10 nm radii of curvature, plasmonic hot spots with higher field enhancement emerge (Dombi *et al.*, 2013).

Even more pronounced field enhancement and nanolocalization can occur by exciting strongly coupled plasmons (Halas *et al.*, 2011). For the simplest case, consider two plasmonic metal nanospheres, placed some nanometers apart, as shown in Fig. 3. If resonance conditions are met and their gap distance is small enough, the optical near fields emitted by the driven free electrons are directly coupled across the gap; see Fig. 3(a). Such a system is thus called a plasmonic dimer. A physically intuitive plasmon hybridization model expresses, in a certain analogy to the hybridization of molecular orbitals, the plasmon modes of a complex system in terms of interacting LSP resonances of the elementary components (Nordlander *et al.*, 2004). The enhanced optical fields in the gap increase with decreasing gap distance; see Dhawan *et al.* (2009) and Fig. 3(e). A strong redshifted "bonding mode" peak appears in the spectrum for which the two dipoles oscillate in phase and are coupled strongly to the far field (Halas *et al.*, 2011). The higher-energy "antibonding mode," with antiparallelly aligned dipoles, has zero net dipole moment and cannot couple to the far field.

This intuitive hybridization picture holds only for sufficiently large distances between the coupled particles where electron tunneling between the particles can be neglected. At subnanometer distances, quantum tunneling sets in and exerts a lower limit to the mode confinement (Savage *et al.*, 2012). Gap plasmon phenomena can be exploited for picocavity light localization (Benz *et al.*, 2016) and strong coupling of plasmons to single molecules (Chikkaraddy *et al.*, 2016) or single-molecule spectroscopies (Xu *et al.*, 1999; Zhang *et al.*, 2013, 2015; Richard-Lacroix *et al.*, 2017; Lee *et al.*, 2018, 2019).

b. Metallic nanotips and geometrical field enhancement effects

An alternative option to realize field enhancement and nanolocalization for strong-field applications are nanotips. Nanotips are sharp conical tapers often made of noble metals such as gold and silver. Such conical tapers are the central element of every "apertureless" scanning near-field optical microscope (SNOM) (Inouye and Kawata, 1994; Zenhausern, Martin, and Wickramasinghe, 1995; Knoll and Keilmann, 1999; Hillenbrand and Keilmann, 2000; Hillenbrand, Taubner,

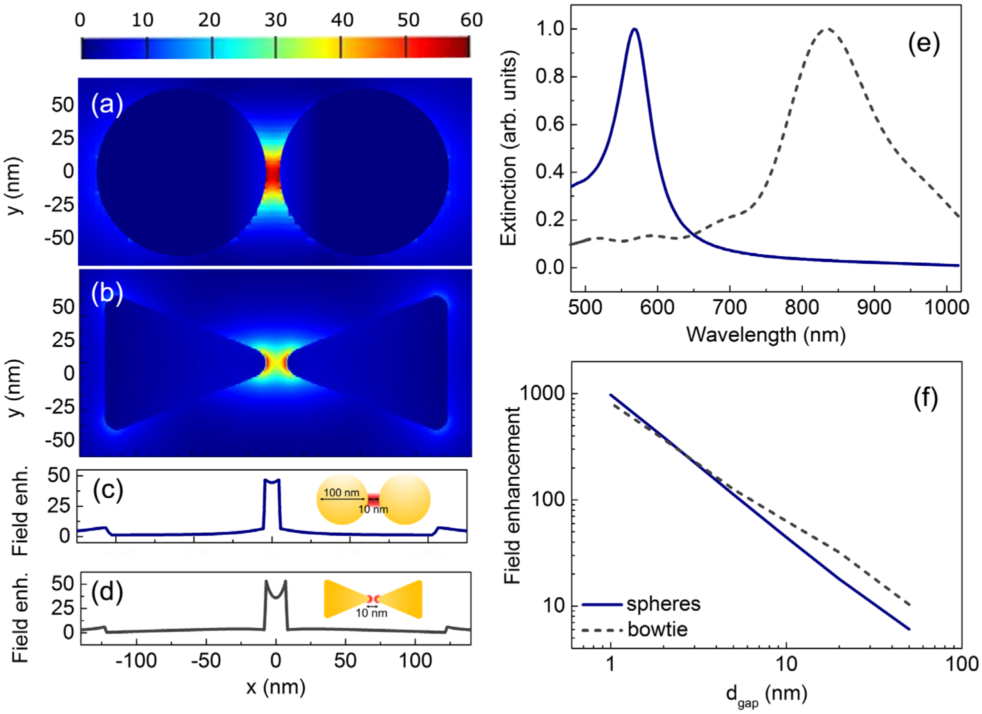

FIG. 3. Properties of plasmonic dimers. (a) 2D field map consisting of two gold nanospheres with 100 nm diameter and 10 nm gap and (b) a bow-tie structure with 10 nm gap. (c),(d) Corresponding field amplitude map in units of the amplitude of the incident field. (e) Extinction spectrum of a plasmonic dimer with two gold spheres ($d = 100$ nm, $d_{\mathrm{gap}} = 10$ nm), and a bow-tie structure with 10 nm gap. (f) Field enhancement in the gap region as a function of gap distance at the resonant wavelength. Data are plotted on a double-logarithmic scale.

and Keilmann, 2002; Neacsu *et al.*, 2006; Qazilbash *et al.*, 2007; Chen *et al.*, 2012; Fei *et al.*, 2012; Esmann *et al.*, 2019) or tip-enhanced Raman microscope (Hayazawa *et al.*, 2000; Hartschuh *et al.*, 2003; Pettinger *et al.*, 2004; Bailo and Deckert, 2008; Deckert-Gaudig *et al.*, 2017). Their linear (Novotny, Bian, and Xie, 1997; Raschke and Lienau, 2003; Roth *et al.*, 2006; Behr and Raschke, 2008) and nonlinear (Sanchez, Novotny, and Xie, 1999; Neacsu, Reider, and Raschke, 2005; Schmidt *et al.*, 2012) light-scattering properties have been studied in some detail. Conical metal tapers can now be fabricated with reasonably high quality and reproducibility using various chemical etching techniques (Klein and Schwitzgebel, 1997); Raschke and Lienau, 2003; Ren, Picardi, and Pettinger, 2004; Mehtani *et al.*, 2006; Bonaccorso *et al.*, 2007; Schmidt *et al.*, 2012; Lindquist *et al.*, 2013; Blum *et al.*, 2014).

A scanning electron microscopy (SEM) image of a sharp tip etched from a single-crystal gold wire is shown in Fig. 4(a). To first order, such a tip illuminated with linearly polarized light along the tip's pointing direction acts as a nanoscale lightning rod. In the quasistatic approximation, reasonably well justified near the apex, this results in electric-field lines that point normal to the surface. Their amplitude scales inversely proportionally to the radius of curvature, resulting in a large local electric-field enhancement (Sanchez, Novotny, and Xie, 1999; Novotny and Stranick, 2006).

Results of a more rigorous finite-difference time-domain (FDTD) simulation of optical near fields of a three-dimensional conical gold taper modeled as a hyperboloid are shown in Figs. 4(b)–4(d). The taper was excited by a linearly polarized, spatially homogeneous 5-fs laser pulse, centered at 800 nm, with the electric-field vector pointing along the taper axis. The different vector components show that the spatial field distribution is essentially that of a small point dipole, polarized along the taper axis and located in the center of a small sphere with a radius given by the apex radius.

The resulting spatial field distribution is rather insensitive to the studied tip material, as illustrated in Fig. 4(e) for different tip materials, ranging from gold to glass. The field distributions are rather insensitive to the frequency of the light field that is exciting the tip, at least for frequencies that are sufficiently below the onset of interband absorption. This is indeed confirmed by electron-energy-loss spectroscopy (EELS) and energy-filtered transmission electron microscopy (EFTEM) measurements (Schröder *et al.*, 2015; Talebi *et al.*, 2015; Guo *et al.*, 2016) and EFTEM studies (Guo *et al.*, 2015; Schröder *et al.*, 2015; Gross *et al.*, 2016).

It is also instructive to interpret EFTEM images by analyzing the eigenmodes of such conical tapers (Babadjanyan, Margaryan, and Nerkararyan, 2000; Stockman, 2004). In a local, classical electromagnetic model, such tapers support a single bound, nonradiative surface plasmon polariton mode even for vanishingly small wire radius, the lowest-order $m = 0$ radially polarized monopole mode of the taper. All higher-order angular momentum modes of the taper can exist as bound modes only for local taper radii exceeding a certain cutoff radius. Hence, they cannot be confined to the taper apex and will not contribute to the local field enhancement. EFTEM measurements thus mainly probe the $m = 0$ mode. Such an eigenmode interpretation can also account for spectral

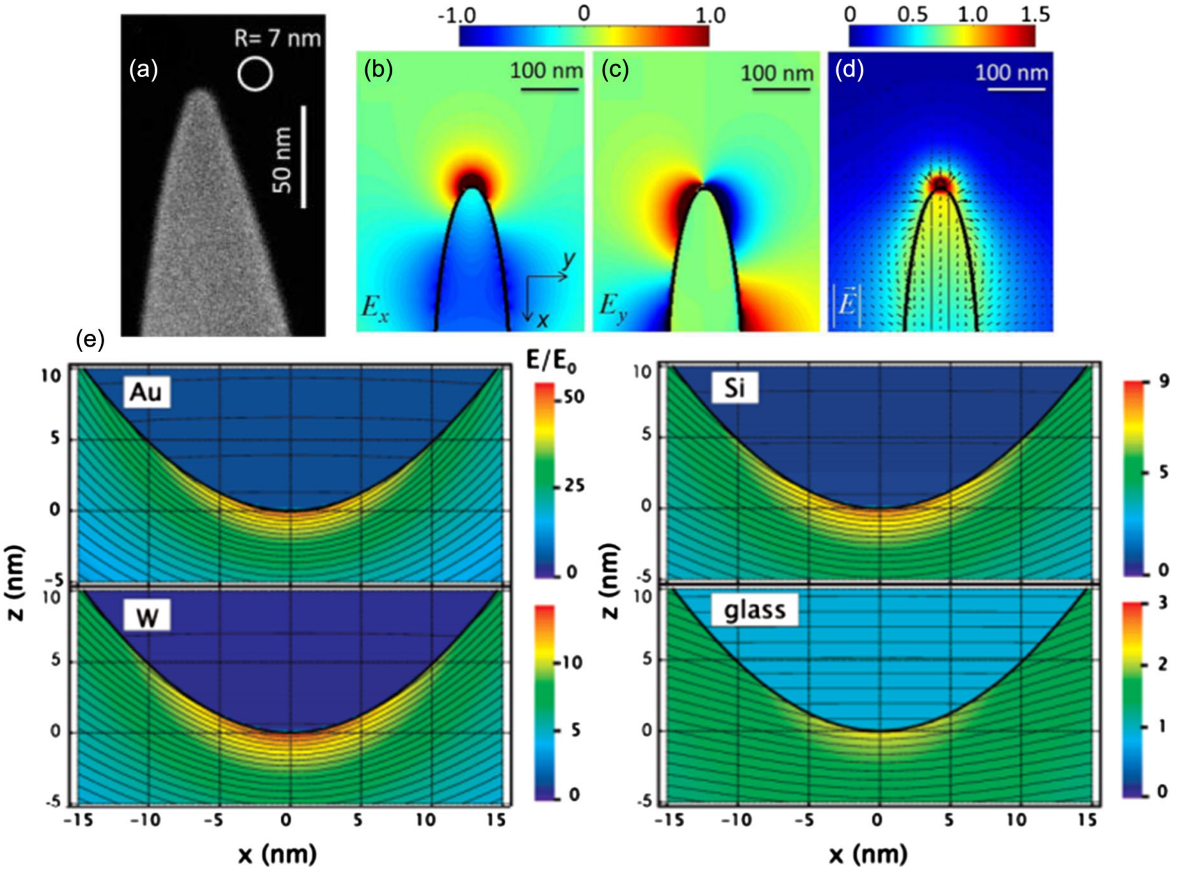

FIG. 4. Properties of nanotips. (a) SEM image of a sharp, chemically etched, single-crystal gold taper with an apex radius of $\sim$7 nm. From Schmidt *et al.*, 2012. (b)–(d) FDTD simulation of the vectorial field around a gold nanotaper. This displays the electric-field component (b) E_z (along the taper axis), and (c) E_x (perpendicular). (d) The absolute value of the electric-field with the vector orientation indicated by arrows (Groß *et al.*, 2016). (e) Dependence of field enhancement E/E_0 on tip material for freestanding tips with apex radius $R = 10$ nm, cone semiangle of $\theta = 20°$, and wavelength $\lambda = 630$ nm. The solid lines represent contours of constant potential. From Behr and Raschke, 2008.

interferences seen in EELS spectra at the shaft of such tapers (Guo *et al.*, 2015; Schröder *et al.*, 2015; Talebi *et al.*, 2015; Yalunin, Schröder, and Ropers, 2016).

These quasistatic calculations predict dramatic field enhancements of up to 50 for noble metal tips. In photoemission experiments, field enhancement factors of up to 10 have been reported for sharp gold tips (Ropers, Solli *et al.*, 2007; Piglosiewicz *et al.*, 2014), while those for tungsten tips range from 4 to 6 (Hommelhoff, Kealhofer, and Kasevich, 2006; Schenk, Krüger, and Hommelhoff, 2010; Krüger, Schenk, and Hommelhoff, 2011; Thomas *et al.*, 2013). These differences between experimental values and numerical predictions have led to rather extensive FDTD simulations (Thomas *et al.*, 2015). For gold tips with 10 nm radius, field enhancement factors of $\sim$10 are predicted at 800 nm wavelength and for taper opening angles of 15°–40°. The predicted values for tungsten in this wavelength range are indeed a factor of 2 to 3 smaller, giving reasonable agreement with experiment (Piglosiewicz *et al.*, 2014). Such field enhancements depend rather sensitively on taper geometry and excitation wavelength, making a quantitative comparison to experiment rather challenging. First promising attempts in this direction emerged recently (Thomas *et al.*, 2013; Rácz *et al.*, 2017).

c. Nanofocusing of light

A unique and intriguing property of metallic nanostructures is their ability to support both SPP and LSP modes. This offers possibilities for realizing "superlens" concepts that rely on the launching of SPPs and their conversion into a LSP mode (Stockman, 2004, 2011; Pile and Gramotnev, 2006; Ropers, Neacsu *et al.*, 2007; Verhagen, Polman, and Kuipers, 2008; De Angelis *et al.*, 2010, 2011; Gramotnev and Bozhevolnyi, 2010, 2014; Lindquist *et al.*, 2010; Berweger *et al.*, 2012).

A particularly interesting geometry for nanofocusing of plasmon modes is a conical taper (Babadjanyan, Margaryan, and Nerkararyan, 2000; Ropers, Neacsu *et al.*, 2007), as illustrated in Fig. 4(a). SPP waves are launched on the shaft of the taper by coupling far-field light to, for example, a grating coupler, positioned at a distance of a few tens of microns from the apex. These SPP waves propagate toward the apex. Upon propagation, the plasmonic wave packet shrinks. The local field enhancement thus results in bright and spatially isolated coherent light sources with dimensions far below the diffraction limit.

To understand this plasmonic nanofocusing, it is instructive to consider a homogeneous circular metal cylinder of radius R

and infinite length (Ashley and Emerson, 1974; Pfeiffer, Economou, and Ngai, 1974; Verhagen, Kuipers, and Polman, 2007). The dielectric function of the metal is $\varepsilon_1(\omega)$ and that of the surrounding homogeneous dielectric medium is $\varepsilon_2(\omega)$. Owing to the rotational symmetry, the electric and magnetic fields inside and outside of the wire can be derived for each nonradiative plasmon eigenmode from scalar functions (Schroter and Dereux, 2001). Here m is an integer denoting the angular momentum quantum and k_z is the wave vector component of the mode along the wire axis. An eigenvalue solution gives

$$k_j^2 = \varepsilon_j(\omega/c)^2 - k_z^2 \tag{2.8}$$

in medium $j = 1, 2$ and provides the wave vector component k_z at a given frequency ω (Stratton, 1941; Groß *et al.*, 2016).

Most interesting are the properties of the lowest order $m = 0$ radially polarized monopole mode. It has electric-field components in the radial direction, pointing perpendicular to the metal surface and parallel to the taper axis (taken as the z direction) (Schroter and Dereux, 2001). It exists as a bound, nonradiative SPP mode even for vanishingly small wire radii. k_z exceeds the free-space wave vector k_0 and the effective refractive index $n_{\mathrm{eff}} = k_z/k_0$ seen by the propagating modes diverges with decreasing radius as $k_z/k_0 \propto 1/R$. Hence, the decay length of the evanescent field in the embedding dielectric decreases substantially for small wire radii and the local field intensity is enhanced near the surface. This is different for the dipolar $m = \pm 1$ modes. Here n_{eff} is slightly larger than unity for radii larger than a certain cutoff radius. For smaller radii, no nonradiative solutions exist. Hence, the $m = \pm 1$ modes do not show the field confinement, and they exist as bound, nonradiative modes only for wire radii exceeding a certain cutoff radius. The same holds true for all higher angular momentum modes whose cutoff radius increases sharply with increasing angular momentum modes.

SPP propagation along conical tapers was first studied theoretically by Babadjanyan, Margaryan, and Nerkararyan (2000). They analyzed the lowest-order $m = 0$ mode and highlighted the divergence of n_{eff} and concomitant decrease in plasmon wavelength when approaching the taper apex. It was suggested that this gives the possibility for spatial field confinement of SPP fields. Later, Stockman (2004) suggested using such conical tapers to transform propagating SPP modes into plasmonic-nanofocusing LSPs. He showed that for a sufficiently small cone opening the energy that is stored in the propagating SPP field is essentially completely localized at the apex, at least if Ohmic losses during propagation are weak and internal reflections of SPPs can be neglected. These criteria are fulfilled if the eikonal or adiabaticity parameter, defined as

$$\delta = |(dR/dz)d(k_0 n_{\mathrm{eff}})/dR|, \tag{2.9}$$

is sufficiently small, i.e., $\delta \ll 1$.

At sufficiently large distances from the apex, the SPP dispersion relation approaches that of a planar interface between a metal with dielectric function ε_1 and a dielectric with ε_2. When approaching the taper apex, the radius of curvature of the taper decreases and the dispersion relation deviates more and more from the light line. This increases n_{eff} much beyond unity for local radii of less than 40 nm. The fraction of the SPP mode that is propagating in the dielectric becomes more strongly bound to the surface of the taper leading to a decrease in group velocity and thus a substantial slowing down of the SPP mode for local taper radii below 50 nm (Bovensiepen, Petek, and Wolf, 2012). Concomitantly, the group velocity decreases and the SPP mode slows down. Conical tapers are almost ideal "plasmonic superlenses," provided that the opening angle of the taper is sufficiently small to prevent SPP back reflections (Jang and Atwater, 2011).

Different alternative nanofocusing geometries, including wedges (Durach *et al.*, 2007; Kurihara *et al.*, 2008), cones (Issa and Guckenberger, 2007; Gramotnev, Vogel, and Stockman, 2008; Baida and Belkhir, 2009), and nanogrooves (Gramotnev, 2005), have been proposed. Experimentally, the effect was studied for the first time in two-dimensional tapered waveguides (Verhagen, Kuipers, and Polman, 2007; Verhagen *et al.*, 2009). Work on conical tapers started in 2007 (Ropers, Neacsu *et al.*, 2007). By equipping a chemically etched gold taper with a line grating [Fig. 5(a)], launching of broadband SPP waves on the taper shaft and focusing into the apex region could be demonstrated (Ropers, Neacsu *et al.*, 2007). Using such tapers, resonant light-scattering spectroscopy with high spatial resolution could be demonstrated (Neacsu *et al.*, 2010; Berweger *et al.*, 2011; Lee *et al.*, 2011; Sadiq *et al.*, 2011). Tip-enhanced Raman spectroscopy with high spatial resolution was demonstrated by De Angelis *et al.* (2010) and Berweger *et al.* (2010). The quality of plasmonic-nanofocusing light sources can be greatly improved by using annealed, single-crystal gold wires for chemical etching (Schmidt *et al.*, 2012). This results in particularly smooth, slightly faceted surfaces [Fig. 5(b)] being ideal for plasmon propagation. The high efficiency of plasmonic nanofocusing can be visualized by imaging far-field light scattering from such conical tapers. As seen in Fig. 5(c), light scattering from the line grating illuminated by a focused laser beam is distinguished from scattering from the apex region, which is solely illuminated by the nanofocusing of SPP waves propagating along the taper shaft.

To illustrate the exceptional properties of this nanolocalized light source, we show in Fig. 6 spectrally resolved light-scattering images of a single gold nanorod 40 nm long and 10 nm in diameter (Esmann *et al.*, 2019). Light from the taper apex is collected in reflection geometry as the taper is raster scanned at a distance of 2 nm across the sample surface. A light-scattering spectrum is recorded at every pixel within an integration time of 20 ms. Near the longitudinal LSP resonance of the nanorod, the images display a pronounced decrease in light-scattering intensity, spatially resolved at better than 5 nm. This demonstrates that plasmonic nanofocusing forms an almost background free, spatially isolated light spot of less than 10 nm. To first order, the images map the local density of optical states (LDOS) of the nanorod. A detailed analysis shows how the experiment probes the coherent near-field coupling between tip and sample. This reveals Purcell effects introduced by the tip and optical Stark

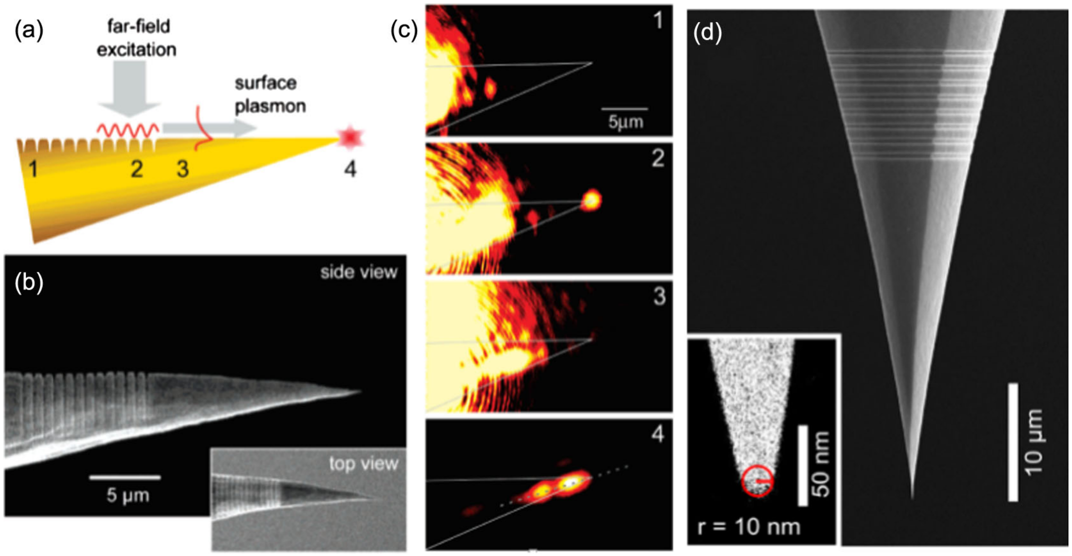

FIG. 5. Working principle of plasmonic nanofocusing. The incident laser light is focused to a ∼5 μm spot size onto a line grating (a). The launched SPP wave packet propagates as an evanescent wave toward the apex, where it is spatially confined and partially scattered into the far field. (b) Representative single-crystal, sharply etched gold taper. The taper opening angle is around 20°, and the apex radius is roughly 10 nm; see the inset of (d). A grating is ion-beam milled onto the shaft at a distance of about 30 μm from the apex. (c) Wide-field image of light scattered from the taper. Light scattering from the grating is spatially well separated from the apex emission, revealing efficient plasmonic nanofocusing toward the apex. (a)–(c) From Ropers, Neacsu *et al.*, 2007. (d) Scanning electron microscope image of a monocrystalline and sharp gold taper equipped with a grating coupler. From Becker *et al.*, 2016.

shifts due to the fact that the nanorod and the off-resonant transverse polarizability of the nanotip are coupled.

The grating coupler can be designed to support broadband light with bandwidths exceeding 200 nm, supporting plasmon wave packets with pulse durations of less than 10 fs (Berweger *et al.*, 2011; Schmidt *et al.*, 2012, 2013; Kravtsov *et al.*, 2016). Chirp effects during propagation can be almost entirely neglected and sub-10-fs time resolution of the nanofocused light spot is readily reached (Schmidt *et al.*, 2012; Kravtsov, Atkin, and Raschke, 2013; Kravtsov *et al.*, 2016). This can also be used to create a few-nanometer-sized electron source with ultrahigh time resolution, as discussed in Sec. III.C.1.c (Schröder *et al.*, 2015; Vogelsang *et al.*, 2015; Müller *et al.*, 2016). Recent tip-enhanced Raman scattering images give clear atomic-scale spatial resolution (Zhang *et al.*, 2013; Lee *et al.*, 2019). This suggests that similar spatial resolution may

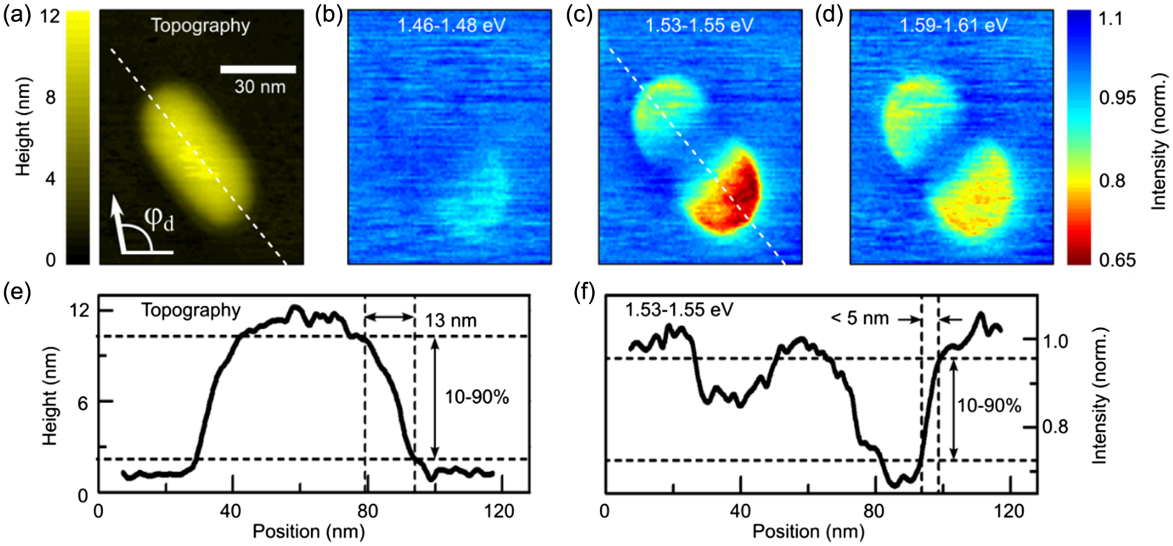

FIG. 6. High-spatial-resolution plasmonic-nanofocusing (PNS) spectra of a single nanorod. (a) Topography of a $40 \times 10\ \mathrm{nm}^2$ gold nanorod. (b)–(d) PNS spectra were recorded at each pixel during the scan. PNS intensity scans in select energy ranges, mapping the optical mode profile of the nanorod with 5 nm resolution. (e),(f) Cross sections extracted along the white dashed lines in (a) and (c), respectively. From Esmann *et al.*, 2019.

also be reached using linear and/or time-resolved tip-enhanced light-scattering spectroscopies.

B. Nonlinear processes driven by enhanced near fields

Field enhancement achieved with the help of nano-optical methods has the advantage that nonlinear phenomena can be induced with significantly lower focused laser intensity than in the case of "conventional" nonlinear optics. In this section, we review nonlinear processes taking place in nano-optical near fields including nonlinear frequency conversion (both low- and high-order harmonics) and nonlinear photoelectron emission. For a general review on nonlinear plasmonics, we refer the interested reader to Kauranen and Zayats (2012). Here we focus mainly on phenomena that are relevant for the applications detailed in Sec. III. We also highlight those features of the photoemission process that are specific to photoemission induced by near fields, namely, subcycle acceleration and carrier-envelope phase phenomena at nanostructures.

1. Nonlinear frequency conversion enhanced by nanostructures

Over the past 20 years, a number of different nonlinear light conversion phenomena in confined optical fields have been studied by using a variety of plasmonic nanostructures. Generally, we can distinguish low- from high-order nonlinear light conversion processes by considering the intensities of the driving fields, the nonlinear polarizabilities involved, and the binding energy of electrons in a material. In the absence of ionization and at moderate local intensities, low-order effects such as second- or third-harmonic generation have been observed in a wide range of examples. For stronger fields capable of inducing multiphoton or tunnel ionization, higher-order effects such as high-harmonic generation have been observed in the nonperturbative intensity regime. The following sections summarize some of the studies treating nonlinear light conversion in localized enhanced fields.

a. Low-order harmonic generation

Second-harmonic fields reflected from a metal surface were first demonstrated by Brown, Parks, and Sleeper (1965), shortly after the first observation of second-harmonic generation (SHG) in quartz crystals by Franken *et al.* (1961). More detailed studies of SHG from media with inversion symmetry were reported by Bloembergen *et al.* (1968), and time-resolved SHG studies at surfaces were performed as well (Tom, Aumiller, and Brito-Cruz, 1988). Inversion symmetry requires that the second-order optical nonlinearity vanishes in the presence of a spatially homogeneous driving electric field (Rudnick and Stern, 1971). Coherent polarizations at the second-harmonic frequency are induced only close to the surface of the material. Three different source terms for these polarizations exist, a bulk polarization $P^{2\omega}_{\mathrm{bulk}}$ extending about a skin depth into that metal and two surface current densities, one being polarized normal to the surface $P^{2\omega}_{\mathrm{surf},\perp}$ and one polarized tangential to the surface $P^{2\omega}_{\mathrm{surf},\parallel}$. Both surface contributions are confined to an angstrom-thin region at the metal surface. The thickness of this region is defined by the Thomas-Fermi screening length of the normal component of the incident electric field inside the metal. Second-harmonic emission thus essentially stems from a sheet of dipoles at the surface (Sipe *et al.*, 1980). Explicit expressions for the second-order polarizations have been derived from hydrodynamic models for the optical response of metals (Sipe *et al.*, 1980; Ciraci, Pendry, and Smith, 2013)

$$P^{2\omega}_{\mathrm{surf},\perp} = \varepsilon_0 \chi_{\perp\perp\perp} \mathbf{E}^{\omega}_{\perp} \mathbf{E}^{\omega}_{\perp}, \tag{2.10}$$

$$P^{2\omega}_{\mathrm{surf},\parallel} = \varepsilon_0 \chi_{\parallel\parallel\perp} \mathbf{E}^{\omega}_{\parallel} \mathbf{E}^{\omega}_{\perp}, \tag{2.11}$$

$$P^{2\omega}_{\mathrm{bulk}} = \varepsilon_0 \gamma \nabla(\mathbf{E}^{\omega} \cdot \mathbf{E}^{\omega}) + \varepsilon_0 \delta' (\mathbf{E}^{\omega} \cdot \nabla) \mathbf{E}^{\omega}. \tag{2.12}$$

The different components of the nonlinear susceptibility tensor, specifically, the surface normal contribution $\chi_{\perp\perp\perp}$, the surface tangential contribution $\chi_{\perp\perp\parallel}$, and the bulk parameters γ' and δ' can be related analytically to the isotropic linear susceptibility of the material (Rudnick and Stern, 1971; Sipe *et al.*, 1980; Ciraci *et al.*, 2012). Here $\mathbf{E}^{\omega}$ is the local field inside the metal at the laser fundamental, and $\mathbf{E}^{\omega}_{\parallel,\perp}$ are its components parallel and perpendicular to the surface, respectively. Often it is assumed that the surface normal susceptibility, reflecting coherent oscillations of the electron gas at the second-harmonic frequency in a direction normal to the surface that are driven by the normal component of the incident field, is the dominant one. Other components are often neglected in the analysis of experimental data (Bouhelier *et al.*, 2003; Wang *et al.*, 2009). For well-defined nanoparticle geometries, the different contributions to the nonlinear emission can, however, be readily distinguished (Feth *et al.*, 2008; Zeng *et al.*, 2009; Yoo *et al.*, 2019). The model introduced earlier can account for the strong sensitivity of SHG to the polarization direction of the incident field and the orientation of the crystal axes (Bloembergen *et al.*, 1968; Sipe, Moss, and Vandriel, 1987), and it explains the high sensitivity of SHG to the presence of molecular adsorbate layers (Heinz *et al.*, 1982). It can also account for the significant enhancement of SHG that is observed when exciting propagating or localized surface plasmons on the surface of the metal (Simon, Mitchell, and Watson, 1974; Bouhelier *et al.*, 2003; Butet, Brevet, and Martin, 2015).

Second-harmonic generation from metallic surfaces raised significant interest when discovering the strong localization of surface plasmon polariton fields in randomly disordered, percolated metallic films (Li, Urbach, and Dai, 1994; Shalaev and Sarychev, 1998; Gresillon *et al.*, 1999; Shalaev, 2000, 2002). In such films, multiple coherent scattering of surface plasmon polaritons results in constructive wave interference in certain nanometer-sized, localized hot spots (Zhang *et al.*, 1998; Gresillon *et al.*, 1999; Markel *et al.*, 1999). This phenomenon, which is analogous to the Anderson localization of waves in random media (Anderson, 1958; John, 1987; Wiersma *et al.*, 1997), gives rise to pronounced enhancements of the local electromagnetic field in these hot spots.

This field localization can induce large enhancements of the emitted second-harmonic intensity from these hot spots, scaling with the fourth power of the incident field, and thus it results in pronounced local fluctuations of the nonlinear optical response of such random media (Breit *et al.*, 2001; Bozhevolnyi, Beermann, and Coello, 2003). Initially, the phenomenon was studied, in particular, to gain a better understanding of surface-enhanced Raman scattering processes (Kneipp *et al.*, 1997; Nie and Emery, 1997; Moskovits, 2005). Stockman later pointed out its potential for coherent spatiotemporal control of electromagnetic fields in randomly disordered nanostructures (Stockman, Faleev, and Bergman, 2002; Stockman *et al.*, 2004; Durach *et al.*, 2007).

Since then, the research in this field has largely focused on analyzing the nonlinear optical response of single metallic nanoparticles and nanoantennas. Third-harmonic generation from small colloidal gold particles with diameters between 40 and 100 nm was first studied by Lippitz, van Dijk, and Orrit (2005). For sufficiently small spherical particles, second-harmonic generation is forbidden by symmetry, whereas third-harmonic emission, stemming mainly from the bulk of the metal, is allowed even for centrosymmetric materials (Hentschel *et al.*, 2012). For larger particles, second-harmonic emission can be observed even when embedding them in a homogeneous medium (Bachelier *et al.*, 2010; Butet *et al.*, 2010).

Second-harmonic generation was also studied for metallic nanotips (Bouhelier *et al.*, 2003; Neacsu, Reider, and Raschke, 2005), and this laid the foundation for nonlinear nanospectroscopy (Neacsu *et al.*, 2009) and for time-domain measurements of the lifetimes of localized plasmonic modes at the apex of sharp metal tips (Anderson *et al.*, 2010; Schmidt *et al.*, 2012). This also triggered studies of photoemission from sharp metal tips (Hommelhoff *et al.*, 2006; Hommelhoff, Kealhofer, and Kasevich, 2006; Ropers, Solli *et al.*, 2007), discussed later.

The generation of the second harmonic from artificial metamaterials and, in particular, from split-ring resonators received much attention (Klein *et al.*, 2006; Feth *et al.*, 2008), and the effect of the Lorentz force exerted on the metal electrons for their nonlinear response has been discussed (Zeng *et al.*, 2009). An important breakthrough was reported in 2005 upon the observation of strong white-light generation from resonant optical nanoantennas (Muhlschlegel *et al.*, 2005). This work has triggered substantial efforts in studying the nonlinear optical response of such antennas (Hanke *et al.*, 2009; Ko *et al.*, 2011; Hentschel *et al.*, 2012; Sivis *et al.*, 2013), allowing for the study of their near-field distributions, resonances, and coupling efficiencies in nanostructures. Since the locally generated nonlinear signals are of immediate interest for applications in spectroscopy and sensing, the microscopic origin of these signals has been studied in some

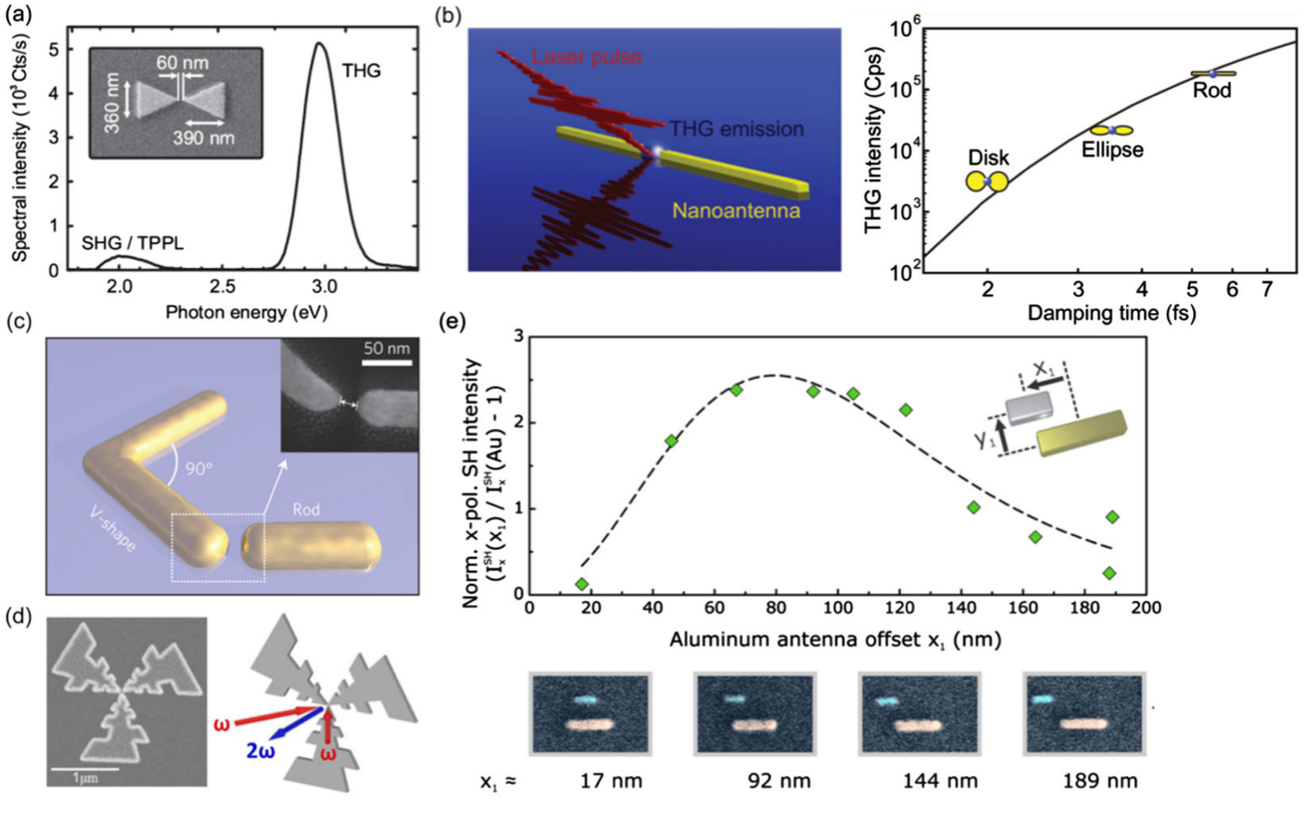

FIG. 7. Harmonic generation from nanostructures. (a) Third-harmonic light generation from a resonant bow-tie nanostructure; see the SEM image in the inset. From Hanke *et al.*, 2009. (b) Schematic illustration (left panel) and efficiency of THG for different nanostructure geometries exhibiting different damping times. From Hanke *et al.*, 2012. (c) Schematic illustration and SEM image (inset) of a multiresonant nanoantenna pair for mode-matched SHG. From Celebrano *et al.*, 2015. (d) SEM image (left panel) and illustration of broadband optical antenna for tunable SHG. From Aouani *et al.*, 2012. (e). Second-harmonic yield as a function of coupling distance of two neighboring nanoantennas (schematically depicted in the graph) for near-field sensing. The different arrangements of the nanoantennas are shown in the insets underneath. From Metzger, Hentschel, and Giessen, 2017.

detail (Ciraci, Pendry, and Smith, 2013) and, in particular, the different origins of second and third-harmonic emission have been emphasized (Metzger *et al.*, 2014). Some examples of tailored nanostructures for enhanced nonlinear harmonic light conversion are presented in Fig. 7.

Hanke *et al.* (2009) demonstrated third-harmonic generation in resonant bow-tie antennas, which exhibit enhanced fields localized in the gap region of the pair antenna as shown in Fig. 7(a). Figure 7(b) depicts a scheme of the generation principle (left panel) and a systematic evaluation of third-harmonic generation efficiencies for different nanoantenna geometries exhibiting different damping times (Hanke *et al.*, 2012). Understanding the spatiotemporal response and the excitation mechanisms in tailored nanoantennas has been the subject of many studies (Neacsu, Reider, and Raschke, 2005; Ko *et al.*, 2011; Hanke *et al.*, 2012; Hentschel *et al.*, 2012; Nieder *et al.*, 2014; Krauth, Giessen, and Hentschel, 2018), and it is also crucial for other localized and enhanced nonlinear effects such as photoelectron emission. The outcome of these efforts resulted in the development of mode-matched, multiresonant nanostructures for efficient second-harmonic generation (Aouani *et al.*, 2012; Celebrano *et al.*, 2015). Figures 7(c) and 7(d) show two examples for such antennas.

Whereas absolute nonlinear signal conversion efficiencies in such nanostructure approaches can typically not compete with phase-matched harmonic generation in thick crystals, the strong localization of the generation volume enables new possibilities for quantitative spectroscopy (Sivis *et al.*, 2013; Krauth, Giessen, and Hentschel, 2018) and sensing (Mesch *et al.*, 2016). Furthermore, near-field distributions and strengths can be mapped with near-field probing techniques (Schaller *et al.*, 2002; Bouhelier *et al.*, 2003; Metzger, Hentschel, and Giessen, 2017) or spectroscopic means (Aouani *et al.*, 2010; Sivis *et al.*, 2013). As an example, Fig. 7(e) shows a measurement of the second-harmonic yield from two mode-coupled antennas as a function of relative position of the two individual nanostructures (Metzger, Hentschel, and Giessen, 2017).

A promising future perspective is the emergence of new types of materials (Reshef *et al.*, 2017, 2019; Fischer *et al.*, 2018) and their possible combination with metamaterials for nonlinear light conversion (Y. Zhang *et al.*, 2011; Husu *et al.*, 2012; Thyagarajan, Butet, and Martin, 2013; Segal *et al.*, 2015; Wolf *et al.*, 2017).

b. High-harmonic generation and nonlinear gas excitation

For sufficiently high local field amplitudes exceeding 0.1 V/nm typically, higher-order nonlinear effects can also be excited in crystals or gases by making use of field enhancements in tailored nanostructures. High-order harmonic generation (Li *et al.*, 1989; Corkum, 1993; Popmintchev *et al.*, 2010) is a prime example for nonlinear coherent light conversion, which has recently been demonstrated in crystalline targets using locally enhanced fields in plasmonic nanostructures (Sivis *et al.*, 2013; Han *et al.*, 2016; Vampa *et al.*, 2017; Imasaka *et al.*, 2018). Another example is the enhancement of nonlinear gas excitation, which led to new insights into incoherent XUV light generation and plasma formation at the nanoscale (S. Kim *et al.*, 2008; Sivis *et al.*, 2012, 2013; Sivis and Ropers, 2013; Iwaszczuk *et al.*, 2015).

Before reviewing these examples, it is worth considering early efforts on plasmonic enhancement of HHG in the gas phase, which turned out to be unfeasible. The first report on this topic (S. Kim *et al.*, 2008) received enormous attention by indicating the possibility to greatly simplify the generation scheme for HHG in gas targets using orders-of-magnitude intensity enhancements in resonant bow-tie antennas. The same group later reported similar results using a hollow waveguide structure (Park *et al.*, 2011). Figure 8(a) schematically depicts the working principle of plasmon-enhanced gas excitation in bow-tie antennas such as those shown in Fig. 8(b). Gas atoms are excited in the bow-tie antenna gaps by the enhanced field of few-cycle, nanojoule-level pulses centered at 800 nm wavelength from a Ti:sapphire laser oscillator. Figure 8(c) shows the spectrum from Ar atoms presented by S. Kim *et al.* (2008), exhibiting several peaks in the extreme ultraviolet that were attributed to high-harmonic generation up to the 17th order of the driving fundamental frequency. These initial reports (Kim *et al.*, 2008; Park *et al.*, 2011) were soon challenged by a series of publications (Sivis *et al.*, 2012, 2013; Sivis and Ropers, 2013) arguing that the localization of the generation volume to subwavelength-sized hot spots leads to predominant generation of incoherent fluorescent emission under the given experimental conditions and using typical gas densities; see spectrum in Fig. 8(d). More specifically, the small number of excited gas atoms in the localized fields poses a significant restriction to the high-harmonic generation conversion efficiency (Sivis *et al.*, 2012, 2013; Raschke, 2013; Sivis and Ropers, 2013) compared to state-of-the-art methods using large gas volumes and amplified laser pulses (Li *et al.*, 1989; Popmintchev *et al.*, 2010) or enhancement cavities (Gohle *et al.*, 2005; Chiang *et al.*, 2012; Cingöz *et al.*, 2012). In fact, one of the reports showing the predominance of incoherent over coherent emission in bow-tie nanostructures (Han *et al.*, 2016) was a subsequent work from the initial reports on plasmon-enhanced HHG (S. Kim *et al.*, 2008; Park *et al.*, 2011). In a repeat measurement of their initial experiment, Han *et al.* (2016) observed only incoherent fluorescent emission [see spectrum in Fig. 8(e)] at a backing gas pressure of 15 bars, which is 30 times higher than in previous experiments. Along with this result, Han *et al.* (2016) acknowledged “that the HHG interpretation of ref. 18 [see J. S. Kim *et al.*, 2008] made with the neglect of fluorescent emission was not fully correct as refuted [i.e., shown] later by similar bow-tie nanostructure experiments”; see Sivis *et al.* (2012, 2013).

Despite the fact that plasmon-enhanced HHG in gaseous media is too inefficient to be of practical use, the studies conducted indicate that light intensities sufficient for highly nonlinear excitation can be reached in such scenarios. Multiphoton and strong-field excitation and ionization of gas atoms accompanied with incoherent XUV light emission (Sivis *et al.*, 2012, 2013;Pfullmann *et al.*, 2013; Sivis and Ropers, 2013; Han *et al.*, 2016) and plasma formation (Iwaszczuk *et al.*, 2015) are two examples of new phenomena, which are observable in enhanced, nanoscale-confined light fields. Figure 9(a) schematically illustrates an experiment conducted by Iwaszczuk *et al.* (2015) in which UV plasma

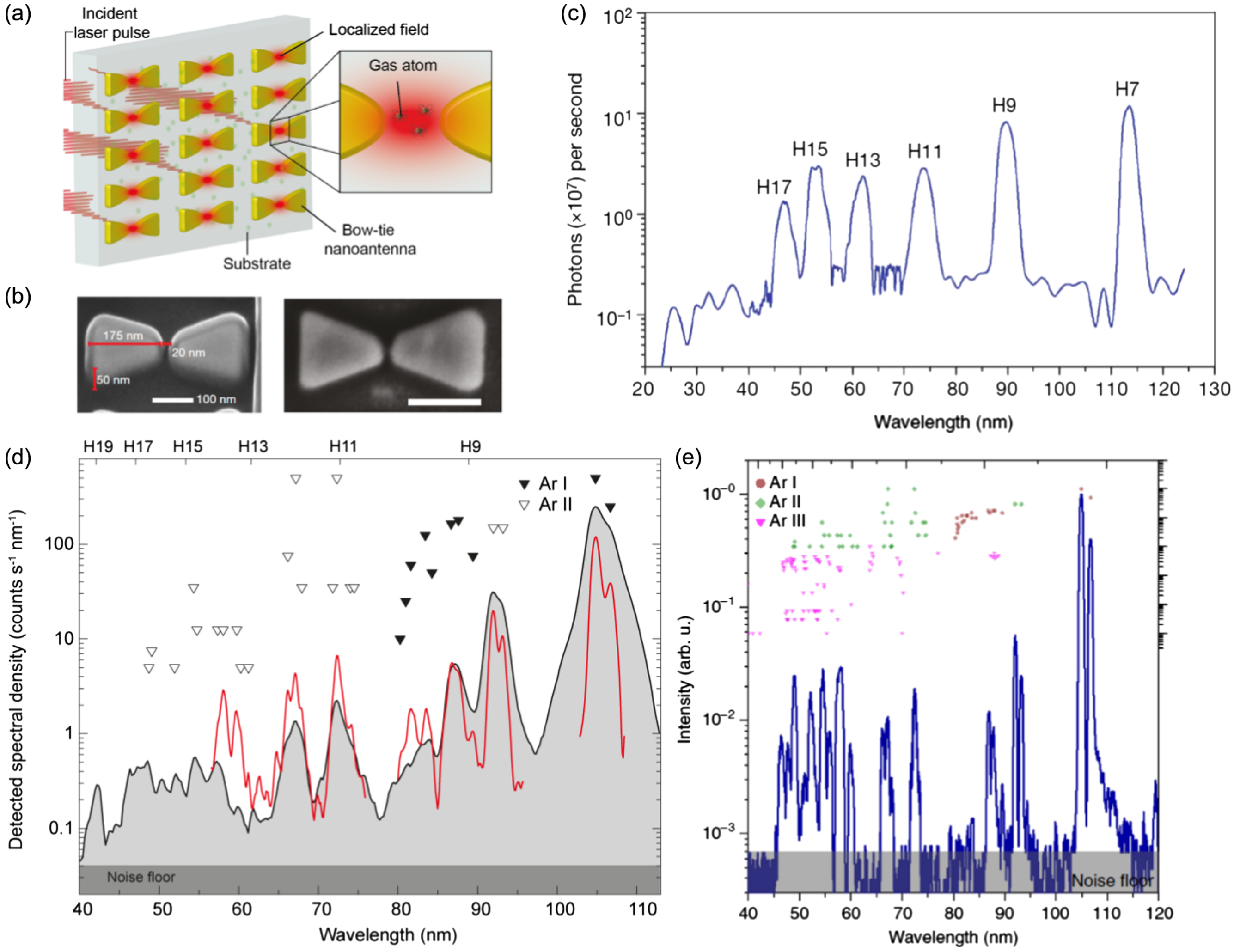

FIG. 8. Attempts for plasmon-enhanced HHG in gaseous media. (a) Schematic illustration of the gas excitation in plasmon-enhanced fields using bow-tie nanoantennas. (Inset) The enhanced near field in which the gas atoms are excited. (b) Scanning electron micrographs of bow-tie antennas used by (left image) S. Kim *et al.* (2008) and (right image) Sivis *et al.* (2012). (c) Extreme-ultraviolet spectrum from argon atoms excited in a plasmon-enhanced field in bow-tie antennas as shown in (b), left image. From S. Kim *et al.*, 2008. (d) XUV spectrum showing exclusively incoherent fluorescence from neutral and singly ionized argon. From Sivis *et al.*, 2012. (e) Reproduction of the results shown initially by S. Kim *et al.* (2008), with consideration of the possibility that the emission can stem from incoherent processes. From Han *et al.*, 2016.

formation of nitrogen molecules was triggered by terahertz-strong-field-emitted and terahertz-strong-field-accelerated photoelectrons near a metallic antenna structure. Figure 9(b) shows an intensity hysteresis of extreme-ultraviolet fluorescence from argon gas excited with femtosecond laser pulses in a tapered hollow waveguide, as depicted in the inset. The hysteresis is caused by an optical bistability in the excitation and ionization of the noble gas atoms.

In contrast to the gas-phase experiments, efficient coherent high-harmonic generation in nanometer-localized fields is possible in solids, facilitated by the orders-of-magnitude higher atomic density compared to the gas phase. The general feasibility of high-harmonic generation in solids was demonstrated by Ghimire *et al.* (2011) using a zinc oxide (ZnO) crystal excited with amplified mid-IR femtosecond laser pulses. This discovery has triggered numerous research efforts making high-harmonic gas-phase attosecond-spectroscopy techniques available in condensed matter systems (Schubert *et al.*, 2014; Luu *et al.*, 2015; Vampa *et al.*, 2015). The first indication for plasmon-enhanced higher-order harmonics from solids was reported by Sivis *et al.* (2013), who observed fifth-harmonic generation from 800-nm femtosecond laser pulses (corresponding to a wavelength of 160 nm) in gold bow-tie nanoantennas on a sapphire crystal. Subsequently, Han *et al.* (2016) demonstrated up to the 13th harmonic of 800 nm driving wavelength using gold-coated sapphire cones, and Vampa *et al.* (2017) and Imasaka *et al.* (2018) demonstrated up to the ninth harmonics of a 2 μm source using gold monopole nanoantennas on silicon and zinc oxide, respectively. Figures 10(a) and 10(b) show the high-harmonic spectra reported by Han *et al.* (2016) and Vampa *et al.* (2017), respectively. All of these approaches utilize plasmonic field localization which is accompanied with orders-of-magnitude intensity enhancements in nanometric hot spots near the nanostructures. Thus, by using only moderate incident laser intensities, highly localized HHG is possible without the need

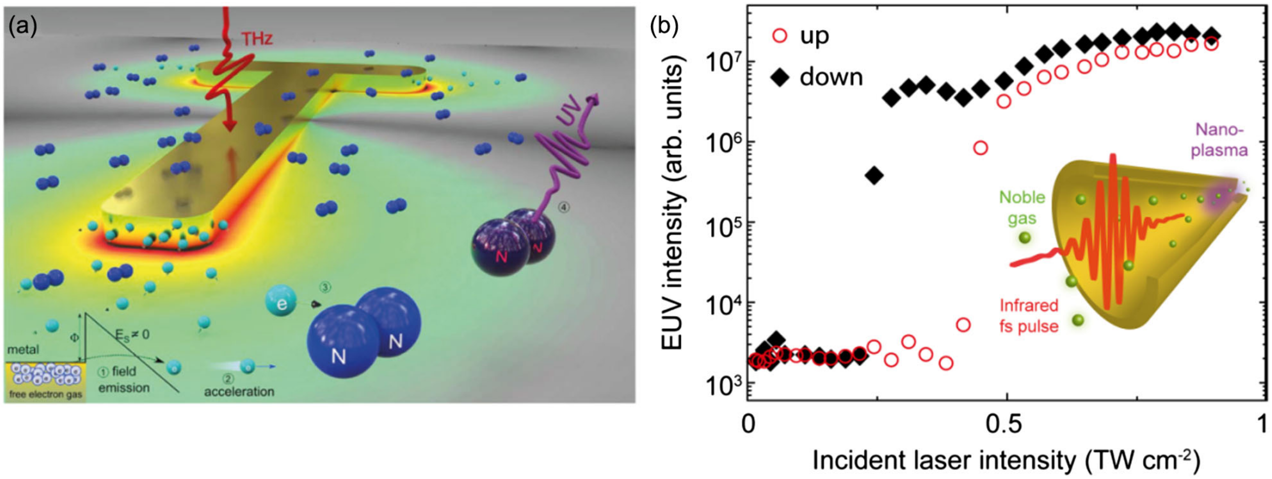

FIG. 9. Nonlinear plasma excitation of gas atoms in tailored nanostructures. (a) Schematic illustration of four-step dissociation of nitrogen molecules in the vicinity of a terahertz-driven metallic antenna. From Iwaszczuk *et al.*, 2015. (b) XUV gas excitation in a hollow waveguide. (Inset) The excitation scheme, where low-energy, femtosecond laser pulses are enhanced at the end of the waveguide and excite injected noble gas atoms. The XUV-intensity hysteresis as a function of incident laser intensity indicates the bistable character of the underlying excitation mechanism. Adapted from Sivis and Ropers, 2013.

for amplified laser pulses. This also enables the use of megahertz repetition rate laser systems (Sivis *et al.*, 2013; Han *et al.*, 2016), rendering this kind of approach possible for efficient HHG spectroscopy. Apart from the general demonstration of plasmon-enhanced HHG, the use of resonant nanostructures emphasizes new means for attosecond physics in inhomogeneous fields. Solid-state HHG in confined fields directly connects to theoretical studies (Husakou, Im, and Herrmann, 2011; Stebbings *et al.*, 2011; Ciappina *et al.*, 2012; Yavuz *et al.*, 2012; Fetić and Milošević, 2013; Pérez-Hernández *et al.*, 2013; Shaaran *et al.*, 2017) that predict the influence of inhomogeneous field distributions on the high-harmonic generation process with the possibility of creating attosecond pulses, as reviewed by Ciappina *et al.* (2017). To date most theoretical studies on this subject have been motivated and conducted in the framework of gas-phase HHG but could be extended to solid-state HHG. However, the differences in the HHG process in solids compared with the atomic case make it necessary to transfer the theoretical models from the single atom picture to the band structure picture of a solid. Whereas the semiclassical atomic three-step model (Corkum, 1993) takes nonperturbative excitations of bound electron states in an atomic potential into account, HHG in solids can be explained by dynamical Bloch

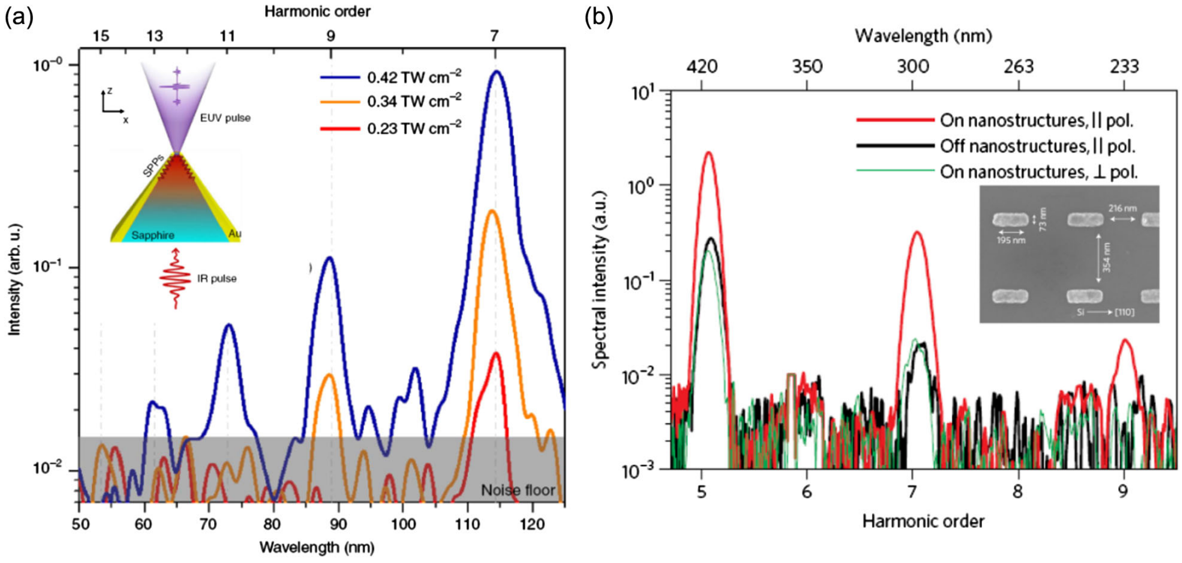

FIG. 10. High-harmonic generation from solids in plasmon-enhanced fields. (a) XUV high-harmonic spectrum from a sapphire target excited with plasmon-enhanced low-energy femtosecond pulses at 800 nm from a megahertz laser oscillator. (Inset) The structure used consisting of sapphire cones with gold coating. Adapted from Han *et al.*, 2016 (b) UV high-harmonic spectrum from silicon using plasmonic enhancement of 2 μm fs laser pulses in rod-type gold nanoantennas (see the SEM image in the inset). Adapted from Vampa *et al.*, 2017.

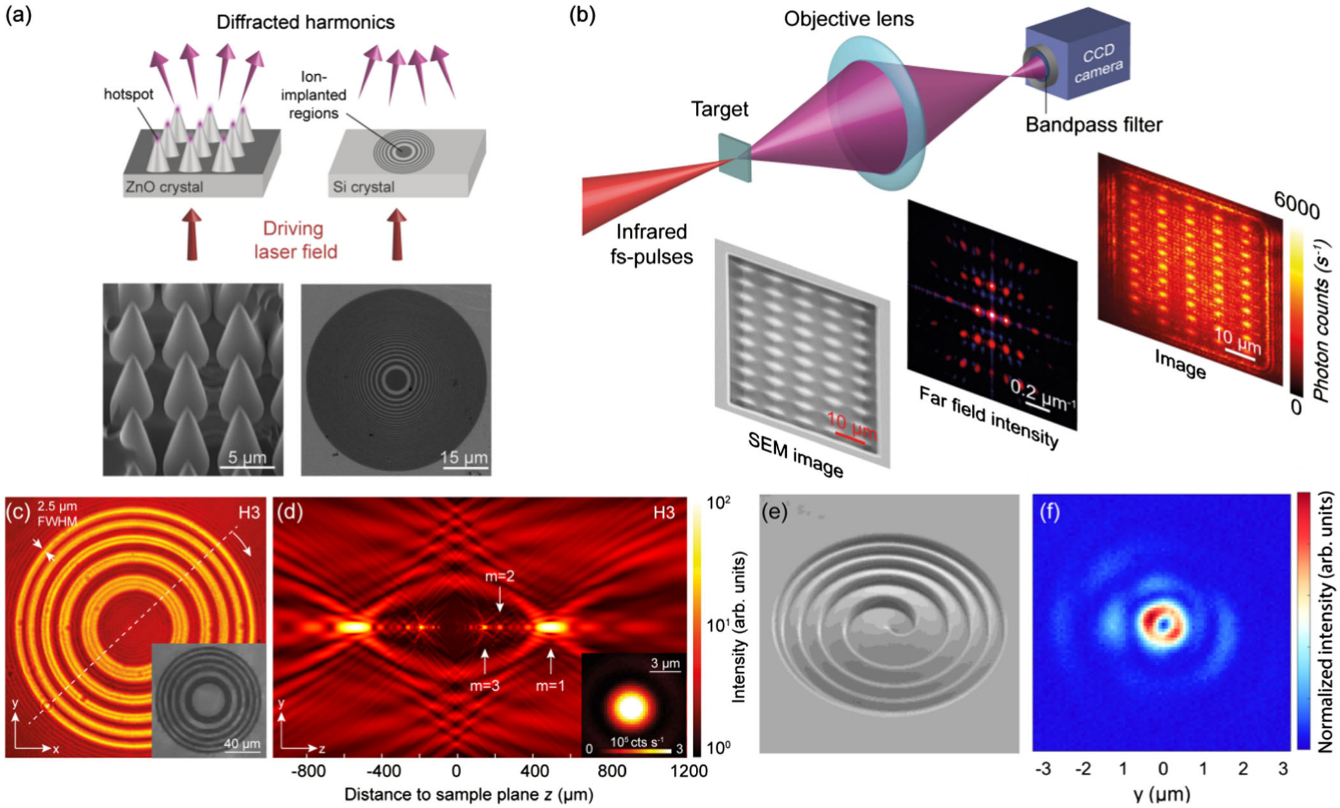

FIG. 11. High-harmonic generation from tailored solids. (a) Principle of high-harmonic generation in structured solids. (Left panels) Cones on a ZnO surface. (Right panels) Gallium-implanted regions in a silicon wafer. (b) HHG from ZnO cones (SEM image, left inset). The incident laser field is localized to the apices of the cones, which leads to enhanced HHG in subwavelength hot spots. The far-field intensity (middle inset) shows a distinct diffraction pattern of the third (red) and fifth (blue) harmonics of 2 μm fundamental laser pulses. The distribution of the fifth harmonic is shown in the right inset. (c) Third-harmonic emission from a gallium-ion-implanted Fresnel-zone-plate silicon target, as shown in the inset. (d) Focusing along the optical axis of the generated radiation to diffraction-limited spot size (see the mode profile of the main diffraction focus in the inset). (a)–(d) Adapted from Sivis *et al.*, 2017. (e) SEM image of a spiral zone plate in ZnO with a gradual depth profile. (f) Donut-shaped focus profile of the fifth harmonic generated in the spiral zone plate from a 2.1 μm fundamental driver. (e),(f) Adapted from Gauthier *et al.*, 2019.

oscillations (Schubert *et al.*, 2014; Luu *et al.*, 2015) of electrons and holes in the conduction and valence bands, respectively, or by considering the semiclassical three-step process with electrons and holes in the band structure of a solid crystal (Vampa *et al.*, 2015).

More generally, high-harmonic generation in solids offers unprecedented means to investigate strong-field phenomena at nanoscales, also involving direct modifications of the target's structure and chemical composition (Sivis *et al.*, 2017; Liu *et al.*, 2018). In turn, control of structure and chemical composition allows for tailored high-harmonic wave fields (Sivis *et al.*, 2017). Figure 11(a) illustrates the principle of high-harmonic generation from structured targets. Surface structure such as cones milled into the surface of a ZnO crystal enables confined and locally enhanced HHG, as shown in Fig. 11(b). Here the conical structures serve as waveguides for the incident infrared laser pulses, which focus down to subwavelength-sized hot spots at the cones tips leading to a more than tenfold increase in local intensities compared to the incident intensity. High harmonics up to the ninth harmonic order are emitted from the two-dimensional array of hot spots that is shown in the SEM image in Fig. 11(b), resulting in a corresponding diffraction pattern in the far field for the third and fifth harmonics; see the middle inset. Imaging with an objective lens confirms the emission pattern for the fifth harmonic order (right inset). In this study, a second structure was demonstrated by using area selective modification of the chemical composition in silicon via gallium-ion implantation without changing the surface morphology. Locally enhanced HHG was found in gallium-implanted regions as shown for a Fresnel-zone-plate target in Fig. 11(c). The inset shows a SEM image of the pattern, where dark regions correspond to gallium-exposed silicon. The gallium bombardment with low doses leads most likely to defect states in the solid that provide midgap energy states allowing for easier generation of free holes and electrons in the bands of the silicon. The local differences in the generation efficiency in the Fresnel zones enable high-harmonic radiation that focuses directly after the silicon target, as shown in the focus scan in Fig. 11(d). Here the azimuthally integrated intensity of the emission pattern [see Fig. 11(c)] is presented for varying distances from the generation plane ($z = 0$). Diffraction-limited foci for different diffraction orders enable local peak intensities in excess of 10^8 W/cm^2 with Gaussian mode profiles; see the inset in Fig. 11(d). These results demonstrate the ability of structured solid sources to facilitate tailored high-harmonic wave fields with controllable intensity, polarization, and emission phase, enabling, for example, vortex beam creation, as demonstrated by Gauthier *et al.* (2019); see also Figs. 11(e) and 11(f).

Apart from new possibilities for device developments, high-harmonic generation in solids opens up novel routes for the investigation of local strong-field phenomena in condensed matter systems, which might become particularly interesting for 2D materials, such as graphene (Cox, Marini, and García de Abajo, 2017; Taucer *et al.*, 2017; Yoshikawa, Tamaya, and Tanaka, 2017; Hafez *et al.*, 2018) and transition-metal dichalcogenides (Langer *et al.*, 2016, 2018; Liu *et al.*, 2017; Tancogne-Dejean and Rubio, 2018; Yoshikawa *et al.*, 2019), as well as for epsilon-near-zero materials (Yang *et al.*, 2019).

2. Nonlinear photoelectron emission from nanostructures

Alongside the previously described parametric frequency conversion, some of the most important nonlinear phenomena involve the photoemission of electrons from surfaces. In this section, we review experimental and theoretical progress in nonlinear and strong-field photoemission from *metallic nanostructures*. Note that a significant and conceptually related body of work was done on strong-field effects in dielectric nanospheres (Zherebtsov *et al.*, 2011, 2012; Süßmann *et al.*, 2015). As these were discussed in detail by Ciappina *et al.* (2017), we place an emphasis on nanotip electron emitters. Over the past 15 years, these structures have repeatedly proven to be effective as controlled model systems for the identification of novel fundamental mechanisms in strong-field photoemission.

a. General considerations and selected experiments

The modern treatment of nonlinear photoemission originated in the 1960s with the seminal work of Keldysh (1965), who introduced a dimensionless parameter useful to distinguish intensity-dependent regimes associated with different photoemission mechanisms. The Keldysh parameter is given by

$$\gamma = \sqrt{\frac{W}{2U_p}} = \frac{\omega\sqrt{2m_e W}}{|eF|}, \tag{2.13}$$

where W is the work function and $U_p = e^2F^2/4m_e\omega^2$ is the ponderomotive energy, defined as the time-averaged kinetic energy of an electron with charge $e = -|e|$ and mass m_e quivering in an oscillating electric field of frequency ω and field strength F. For Keldysh parameters $\gamma \gg 1$, the field strength is not sufficient to significantly distort the binding potential, and the dominant mechanism by which the electron can escape from the metal is the absorption of a minimum threshold number of photons $n = W/\hbar\omega$. Consequently, the photoelectron yield exhibits a power law in the incident laser intensity $N \propto I^n$. In the other limiting case of $\gamma \ll 1$, photoemission approaches quasistatic tunneling, with a yield following the Fowler-Nordheim equation (Fowler and Nordheim, 1928; Forbes, 2006). In solids, experimental investigations of this regime are rather challenging due to optical damage, surface heating, and possible space charge effects. These difficulties can be mitigated in structures with spatially confined emission and absorption, e.g., in nanostructures. Moreover, lower frequencies enhance the ponderomotive energy and thus facilitate access to the high-field regime. Multiphoton photoemission and strong-field phenomena assisted by optical near fields were demonstrated for tungsten and gold tips (Hommelhoff *et al.*, 2006; Ropers, Solli *et al.*, 2007; Bormann *et al.*, 2010; Schenk, Krüger, and Hommelhoff, 2010; Park *et al.*, 2012), tailored plasmonic nanostructures (Dombi *et al.*, 2013; Sivis *et al.*, 2018), and thin metal films and surfaces (Tsang, Srinivasan-Rao, and Fischer, 1990, 1991; Chen, Boneberg, and Leiderer, 1993; Aeschlimann *et al.*, 1995; Dombi *et al.*, 2010; Rácz *et al.*, 2011; Teichmann *et al.*, 2015; Reutzel, Li, and Petek, 2019). Moreover, efficient acceleration of the photoelectrons in the plasmonic fields with steep spatial gradients was evidenced by the observation of electrons with kinetic energies far above the photon energy of the driving field (Yu *et al.*, 2000; Kupersztych *et al.*, 2001; Irvine, Dechant, and Elezzabi, 2004; Dombi *et al.*, 2010).

The largest number of experimental studies have indeed been conducted using sharp metallic tips, benefiting from large local field enhancements due to the excitation of localized surface plasmons and the lighting rod effect (Maier, 2007; Thomas *et al.*, 2015), as discussed in Sec. II.A.3. Various emission regimes in nanotip photoemission were observed, including optical-field emission (Hommelhoff *et al.*, 2006; Hommelhoff, Kealhofer, and Kasevich, 2006), multiphoton photoemission (Barwick *et al.*, 2007; Ropers, Elsaesser *et al.*, 2007; Ropers, Solli *et al.*, 2007), and above-threshold (Schenk, Krüger, and Hommelhoff, 2010; Krüger, Schenk, and Hommelhoff, 2011) and strong-field photoemission (Bormann *et al.*, 2010), as well as photo-assisted tunneling (Yanagisawa *et al.*, 2011; Borz *et al.*, 2019). Rescattering plateaus and carrier-envelope effects were studied by Krüger, Schenk, and Hommelhoff (2011), Wachter *et al.* (2012), Piglosiewicz *et al.* (2014), and Ahn *et al.* (2017). Ponderomotive and subcycle electron acceleration was observed at near-infrared and midinfrared frequencies by Herink *et al.* (2012), Park *et al.* (2012), Echternkamp, Herink *et al.* (2016), and Schötz *et al.* (2018). Control of nanotip photoemission was demonstrated in terahertz-streaking experiments (Herink, Wimmer, and Ropers, 2014; Wimmer *et al.*, 2014; Wimmer, Karnbach *et al.*, 2017), and also with two-color excitation (Förster *et al.*, 2016; Huang *et al.*, 2017; Seiffert *et al.*, 2018). An extensive review was given by Krüger *et al.* (2018).

Figure 12 displays selected experimental results of photoelectron emission from metallic nanotips. Specifically, multiphoton photoemission [Fig. 12(a)] from a gold nanotip was demonstrated using 7-fs laser pulses [see Fig. 12(d) and Ropers, Solli *et al.* (2007)], showing a characteristic scaling with laser power $N \propto P^n$, with $n = 4$ evidencing a four-photon process. Similar results were obtained by Barwick *et al.* (2007). Yanagisawa *et al.* (2011) observed the resulting emission processes in the step-shaped kinetic energy distribution of electrons emitted from a strongly biased tungsten tip; see Fig. 12(e). Hommelhoff *et al.* (2006) showed that the bias-dependent photoemission yield can also be described

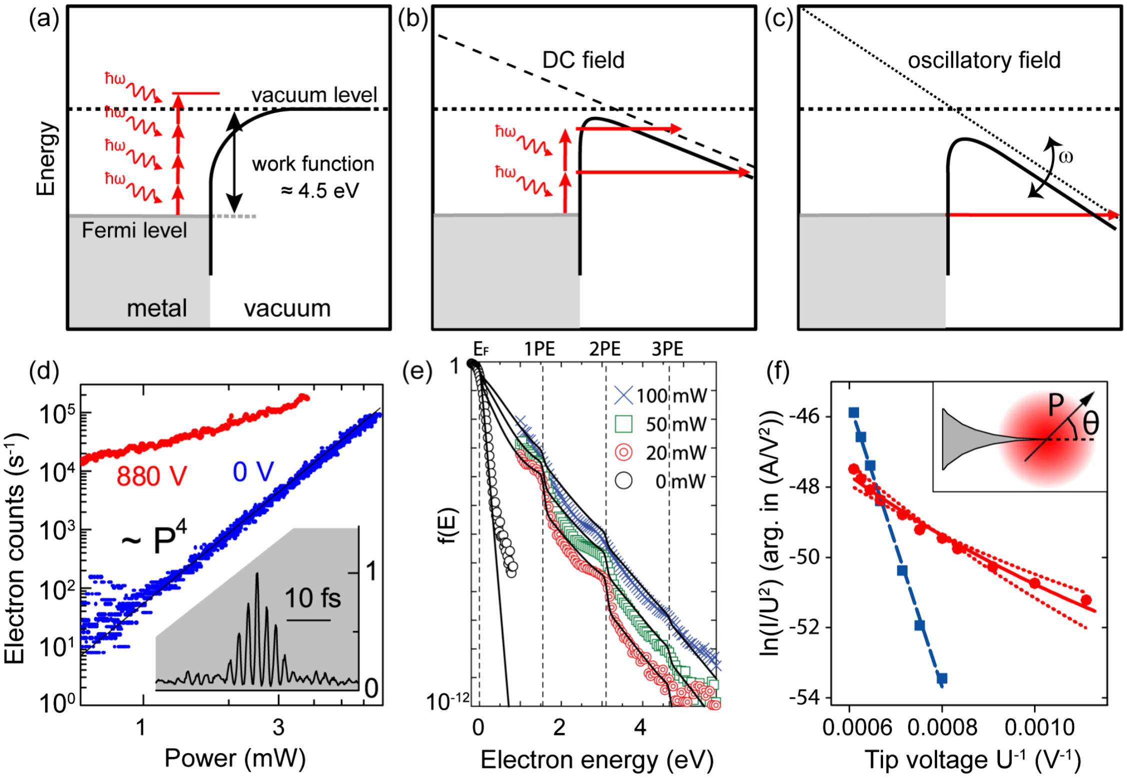

FIG. 12. Photoemission mechanisms and corresponding experimental results. (a) Multiphoton photoemission. (b) Tunnel-assisted below-threshold photoemission. (c) Optically induced tunneling. (d) Log-scale intensity plot of photoelectron yield with (red, upper curve) and without (blue, lower curve) static bias voltage on the tip, showing a reduction of the effective nonlinearity. (Inset) Interferometric autocorrelation of the excitation pulses recorded using photoelectron signal. Adapted from Ropers, Solli *et al.*, 2007. (e) Photoelectron spectra from a negatively biased tungsten tip, evidencing a step-shaped structure from one- and two-photon processes and subsequent tunneling emission. Adapted from Yanagisawa *et al.*, 2011. (f) Fowler-Nordheim plots of dc tunnel emission (blue squares) and photo-field emission (red circles). Adapted from Hommelhoff *et al.*, 2006.

using a Fowler-Nordheim-type scaling $N \propto F^2 e^{-A/F}$, where F includes both the laser and static fields; see Fig. 12(c).

These few results already indicate the richness of mechanisms to consider given the large and widely tunable parameter space spanned by the light intensity, frequency, pulse duration, etc. Rather than giving a survey of all individual observations and corresponding interpretations, we provide a general introduction to the theoretical approaches used to describe nonlinear photoemission at increased field strengths and link the theoretical results to key experimental observations.

b. Theoretical approaches for nonlinear photoemission

The most essential features of the strong-field photoemission from nanotips can be understood within the single-active electron approximation and the time-dependent Schrödinger equation (TDSE), where the many-particle interaction between the conduction electrons is neglected, and the whole system is treated as a free-electron gas. Photoexcitations from the conduction band to the states above the vacuum level are induced by a p-polarized laser field focused on the tip apex. Before specifying a particular model, we first consider the relevant length scales. First, the tip apex radius in the experiments is about 3–10 nm, and the laser wavelength is of the order of $1\,\mu$m, much larger than the de Broglie wavelength $\lambda_e = \hbar/p_F \sim 1$ nm of the electron at the Fermi level. Consequently, the metal surface can be regarded as nearly flat. Second, because of the considerable field enhancement at the tip apex, the field is essentially normal to the surface (in nanotips, the local field can be about 5–10 times higher than the corresponding field at a flat surface). Inside the tip, the near-infrared laser field is strongly screened, with the screening length about $\lambda_{\mathrm{TF}} \sim 0.2$ nm (Liebsch, 1997; Kazansky and Echenique, 2009). Outside the tip, the interaction with the laser and static fields may be described with the dipole approximation $H_I(z,t) = -e[F(t) + F_{\mathrm{st}}]z$, where z is the normal coordinate, with the origin at the surface and positive outside; for alternative formulations, see Petek (2012). It follows that the tangential components of the electron momentum are conserved near the surface and that the electron motion can be regarded as one dimensional.

We proceed with the TDSE in the length gauge with the time-dependent Hamiltonian written as $H(t) = H_0 + H_I(z,t)$, where $H_0 = T + V(z)$ is the unperturbed Hamiltonian, with $T = p^2/2m_e$ the kinetic energy and $V(z)$ the interaction with the semi-infinite lattice:

$$i\hbar \frac{\partial}{\partial t}\Psi(z,t) = [T + V(z) + H_I(z,t)]\Psi(z,t). \qquad (2.14)$$

There are various parametrizations of the lattice potential. The simplest one, proposed by Sommerfeld, describes the interaction with the lattice as a potential step $V(z) = -(E_F + W)\Theta(-z)$, where Θ is the Heaviside function and E_F is the Fermi energy. Another popular choice is the Chulkov parametrization (Chulkov, Silkin, and Echenique, 1999). Alternative models may include corrections due to the presence of a positively charged hole left inside the metal (Kazansky and Echenique, 2009; Siek *et al.*, 2017), the soft jellium potentials (Eguiluz *et al.*, 1984; Jennings, Jones, and Weinert, 1988; Blundell and Guet, 1993), and the screened soft-core Coulomb potentials (Wachter *et al.*, 2012; Yalunin *et al.*, 2013; Liao and Thumm, 2014). At the border of the computational domain, an optical absorbing potential (Muga *et al.*, 2004) or transparent boundary condition (Arnold, Ehrhardt, and Sofronov, 2003; Antoine *et al.*, 2008; Yalunin, Gulde, and Ropers, 2011) is introduced to suppress spurious reflections of the wave function.

The most popular computational methods of solving the TDSE include the split-step propagation algorithm with the fast-Fourier computation of the kinetic energy (Feit, Fleck, and Steiger, 1982; Leforestier *et al.*, 1991), the real-space methods such as the Crank-Nicolson scheme (Press *et al.*, 1994), and its extensions (Watanabe and Tsukada, 2000; Wells and Quiney, 2019). These schemes are unitary and hence unconditionally stable. They also benefit from sparse Hamiltonians and a quasilinear scaling of the computational time. The initial electron states are usually obtained by imaginary time propagation using the aforementioned schemes.

$\ddot{z}(t)$The photoelectron spectrum $N(E)$ can be computed by a usual temporal Fourier transform in the field-free region, far from the surface. This often requires a large and thus computationally demanding domain. Alternatively, the photoelectron spectrum can be computed at a much shorter distance z_0 using the Kramers-Henneberger (KH) frame (Henneberger, 1968; Reed and Burnett, 1991), which removes the quiver motion of photoelectrons and retains only the drift motion (Yalunin *et al.*, 2013):

$$N(E) \propto \sum_n D(E_n)\sqrt{2m_e E} \times \left| \int_{-\infty}^{\infty} \Psi_n(z_0 + z(t), t) e^{iEt/\hbar - iS(t)/\hbar} dt \right|^2. \quad (2.15)$$

Here E is the final (drift) energy and the sum over n extends over the initial electron states, which are described by the projected density $D(E_n)$ onto the surface normal. $z(t)$ is the displacement of the "detector," which is at rest in the KH frame but undergoes a quiver motion in the tip frame according to the Newtonian equation $m_e\ddot{z}(t) = -\partial H_I(z_0, t)/\partial z_0$, with the initial condition that the detector was at rest at $t \to -\infty$. The classical action $S(t)$ is given by

$$S(t) = \int_{-\infty}^{t} \left\{ \frac{m_e \dot{z}^2(\tau)}{2} - H_I(z_0 + z(\tau), \tau) \right\} d\tau \quad (2.16)$$

The physical model previously outlined allows one to estimate the photoelectron yield and spectra in reasonable agreement with experiment. However, being a one-electron treatment, it does not explicitly account for the many-body effects such as inelastic electron-electron and electron-phonon scattering. In metals, these interactions are important for laser-induced absorption in metallic conduction bands (Lugovskoy and Bray, 1999; Rethfeld *et al.*, 2002; Pietanza *et al.*, 2007), inelastic energy relaxation (Chulkov *et al.*, 2006), and attenuation of the one-electron wave functions (Kazansky and Echenique, 2009; Lemell *et al.*, 2009; Rios Rubiano *et al.*, 2012). In addition, the many-body effects may also contribute to the direct photoemission (Banfi *et al.*, 2005; Wu and Ang, 2008) and the rescattering of photoelectrons at surface layers (Yanagisawa *et al.*, 2016).

In nanotips and metal clusters, the collective electronic dynamics was studied numerically using time-dependent density functional theory (TDDFT); see, e.g., Calvayrac *et al.* (2000), Lemell *et al.* (2003), Krüger *et al.* (2012), Wachter, Lemell, and Burgdörfer (2012), and Wachter *et al.* (2012). This method maps the problem of interacting electrons onto an equivalent noninteracting problem (Kohn and Sham, 1965). To this end, the potential $V(z)$ is expressed in terms of the local charge density (local density approximation) as a sum of the electrostatic interaction between the electrons, the interaction between the electrons and ionic cores, and the exchange-correlation potential (Ullrich, 2012):

$$V(z, t) = V_{\mathrm{el}}[n(z, t)] + V_{\mathrm{ion}}[n(z, t)] + V_{\mathrm{xc}}[n(z, t)] \quad (2.17)$$

The local density $n(z, t)$ is then expressed in terms of the Kohn-Sham orbitals

$$n(z, t) = \sum_n f_n |\Psi_n(z, t)|^2, \quad (2.18)$$

with appropriate occupation numbers f_n (Eguiluz *et al.*, 1984). The orbitals are computed from the time-dependent Kohn-Sham equations:

$$i\hbar \frac{\partial}{\partial t} \Psi_n(z, t) = [T + V(z, t) + H_I(z, t)]\Psi_n(z, t). \quad (2.19)$$

The ground-state density is determined from the corresponding stationary Kohn-Sham equations (Liebsch, 1997; Baroni *et al.*, 2001). Just as in static DFT, any application of TDDFT requires a suitable approximation to the exchange-correlation potential $V_{\mathrm{xc}}[n(z, t)]$. For the nanotip photoemission, this point was addressed by Wachter *et al.* (2012). Their numerical results, shown in Fig. 13, demonstrate good agreement with experiment. A useful feature of the TDDFT and TDSE approaches is the visualization of spatiotemporal evolution of wave functions in front of the surface; see Fig. 14. This is especially helpful in providing physical insight into strong-field processes via electron trajectories.

c. Analytic quantum theory of nonlinear photoemission

Even when a numerical solution of the TDSE is carried out, this usually does not easily afford the kind of understanding provided by analytical expressions. In particular, it is instructive to see the experimental phenomenology emerging from the quantum theory. To simplify our description, we begin with the TDSE formalism but leave the exact form of the binding potential unspecified. The only assumption we make

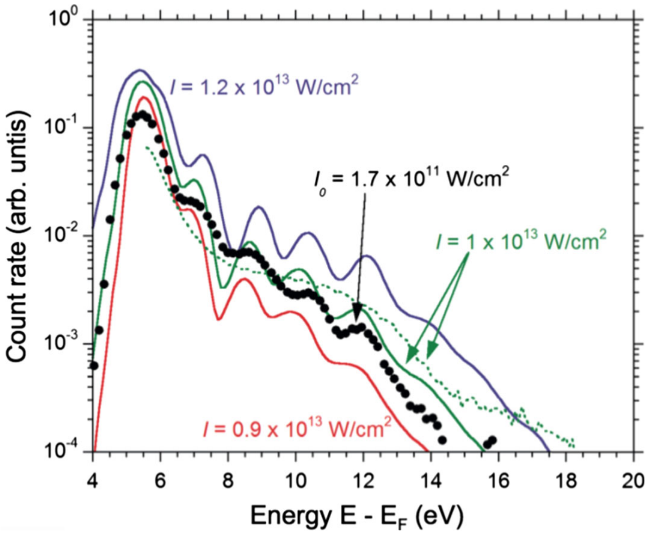

FIG. 13. Experimental photoelectron spectra (dots) in comparison with TDDFT computation (solid lines) for different laser intensities. Adapted from Wachter *et al.*, 2012.

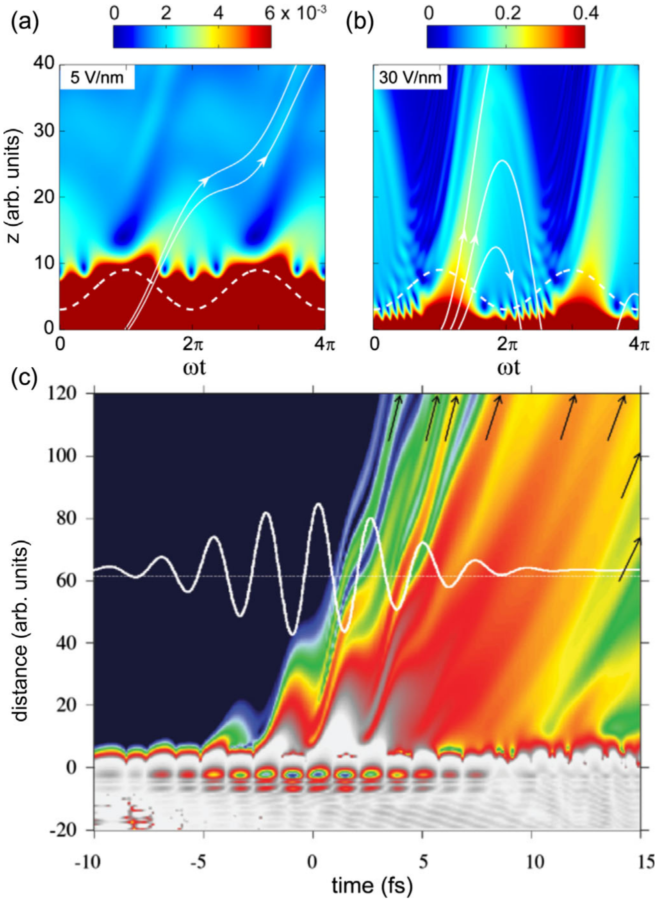

FIG. 14. (a),(b) Magnitude of the electron wave function as a function of distance from the sample and time in the multiphoton and quasistatic tunneling regimes, respectively. Electric force (dashed line) acting on the ejected electrons and their trajectories (solid white lines). Adapted from Yalunin, Gulde, and Ropers, 2011. (c) Local electron density in TDDFT simulation. Adapted from Wachter *et al.*, 2012.

here is that the interaction outside the tip is given by $H_I(z,t) = -eF(t)z$ with $F(t) = -A'(t)$, and the vector potential $A(t)$ vanishes at infinity.

As opposed to surface Shockley states, the Bloch waves within metal tips have a nearly exponential tail outside the surface. Consequently, we assume that the initial state of the electron decays exponentially outside the tip

$$\langle z|\Psi_0\rangle = (2\pi\hbar)^{-1/2} C \exp(-\alpha z/\hbar), \tag{2.20}$$

where α is the decay constant and C depends on the surface barrier. In the Sommerfeld model, the prefactor is given by $C = 2ip_0/(ip_0 - \alpha)$, where p_0 is the Bloch momentum.

The transition from the initial state to a final state with momentum $p > 0$ is described by the transition amplitude (Becker *et al.*, 2002)

$$M_p = -\frac{i}{\hbar}\int_{-\infty}^{\infty} \langle \Psi_p^{(+)}(t)|H_I(t)|\Psi_0(t)\rangle dt, \tag{2.21}$$

where $|\Psi_p^{(+)}(t)\rangle$ is the outgoing final state. A crucial simplification occurs when one introduces the strong-field approximation (SFA) (Keldysh, 1965; Faisal, 1973; Reiss, 1980) that neglects the interaction with the lattice in the outgoing state but retains the interaction with the laser field. Such a wave function was found by Volkov (1935):

$$\langle z|\Psi_p^{(V)}(t)\rangle = (2\pi\hbar)^{-1/2} \exp\left(\frac{i}{\hbar}[p - eA(t)]z - \frac{1}{2m_e\hbar}\int^t [p - eA(\tau)]^2 d\tau\right), \tag{2.22}$$

where p is the electron's drift (canonical) momentum and $p - eA(t)$ is the instantaneous (kinetic) momentum. Substitution of the Volkov state into Eq. (2.21) results in a simple expression for the transition amplitude:

$$M_p^{\mathrm{SFA}} = \frac{C}{4\pi m_e \hbar}\int_{-\infty}^{\infty} [i\alpha + p - eA(t)] e^{iS_p(t)/\hbar} dt, \tag{2.23}$$

where

$$S_p(t) = \frac{1}{2m_e}\int^t [p - eA(\tau)]^2 d\tau - E_0 t$$

and $E_0 = -\alpha^2/2m_e$ is the energy of the Bloch wave. Experiments by Schenk, Krüger, and Hommelhoff (2010), Krüger, Schenk, and Hommelhoff (2011), and Yanagisawa *et al.* (2016) performed at moderate laser intensities suggest that the number of direct electrons emitted according to the SFA is about 10 times larger than that for electrons backscattered from the surface. The accuracy of Eq. (2.23) and its modifications [Fig. 15(a)] were studied by Yalunin, Gulde, and Ropers (2011) and Jouin and Duchateau (2019).

Now consider another useful approximation where the number of photons required for photoemission is large, valid, in particular, for metals with work functions $W \sim 5$ eV exposed to near-infrared light. In this case, the external field varies slowly compared to the period of electron motion.

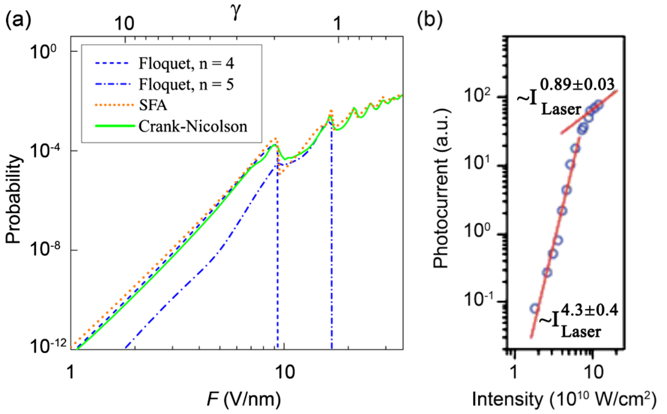

FIG. 15. (a) Photoemission probability within the modified SFA (dotted orange line), TDSE results obtained using Crank–Nicolson approach (solid green line), and Floquet calculations (dashed blue lines) for work function $W = 5.5$ eV and $\hbar\omega = 1.56$ eV. Adapted from Yalunin, Gulde, and Ropers, 2011. (b) Photoelectron yield as a function of intensity. Red lines indicate the decrease of the effective nonlinearity from 4.3 to 0.89 during the transition between photoemission regimes. Adapted from Dombi *et al.*, 2010.

Consequently, the electron responds adiabatically and adjusts its state to the momentary value of the electric field. Mathematically, this leads to a rapidly oscillating exponential in the transition amplitude that allows one to apply the saddle-point method. Accordingly, the integral in Eq. (2.23) is approximated by the integration in the vicinities of saddle points specified by the condition

$$p - eA(t_0) = i\alpha. \tag{2.24}$$

The solutions of this equation are interpreted as the instants when the electron "enters" into the potential barrier (Yudin and Ivanov, 2001). Since this region is classically forbidden, the solutions are complex. According to the general theory of adiabatic transitions (Landau and Lifshitz, 1965), in the case where the final state energy is greater than the initial state energy, the transition amplitude is written as a coherent sum over the saddle points in the upper half-plane of complex t_0. For a cw field, their constructive interference results in $E = p^2/2m_e = n\hbar\omega - (|E_0| + U_p)$, where U_p describes a ponderomotive barrier.

Further, one can construct the probability of direct photoemission. Here we provide only a simple analytical expression valid in the quasistatic tunneling regime ($\gamma \ll 1$), where the tunneling time $\mathrm{Im}(t_0)$ is short compared to the period of field oscillations (Yalunin, Gulde, and Ropers, 2011):

$$w_p^{\mathrm{SFA}} = \frac{p}{p_0}|M_p^{\mathrm{SFA}}|^2 \propto \frac{1}{F(t)} \exp\left(-\frac{2}{3}\frac{\alpha^3}{\hbar m_e e F(t)}\right), \tag{2.25}$$

where $p = eA(t)$ and t is the instant of emission. This expression recovers the signature of the quasistatic tunneling exponential and the F^{-1} scaling of the preexponential factor, and it also links the spectral and temporal characteristics of the released electron wave packets. Other expressions valid up to $\gamma \approx 1$ were given by Perelomov, Popov, and Terent'ev (1966) and Yudin and Ivanov (2001). Perelomov, Popov, and Terent'ev predicted an exponential behavior of photoelectron spectra at moderate laser intensities as a function of energy $p^2/2m_e$. For nanotips, such an exponential shape was observed in the above-threshold photoelectron spectra by Schenk, Krüger, and Hommelhoff (2010) and Förg *et al.* (2016). More recently, the nonsequential, coherent nature of above-threshold photoemission was also revealed for surfaces with two-dimensional photoelectron spectroscopy (Reutzel *et al.*, 2019).

Experimentally accessible quantities like the photoelectron yield are obtained from Eq. (2.25) by integration over all initial states in the metal with energies $|E_0| \geq W$. This results in the Fowler-Nordheim-type scaling of the total yield with the momentary electric field (Bunkin and Fedorov, 1965; Yalunin, Gulde, and Ropers, 2011):

$$N \propto \int_{-\infty}^{\infty} \Theta[eF(t)]F^2(t) \exp\left(-\frac{4}{3}\frac{\sqrt{2m_e}W^{3/2}}{\hbar e F(t)}\right) dt. \tag{2.26}$$

Good agreement with this result was reported by Hommelhoff *et al.* (2006) and Schertz *et al.* (2012).

In the multiphoton regime ($\gamma \gg 1$), the photoemission is determined mainly by the electric-field envelope (Yudin and Ivanov, 2001). Consequently, the total yield is expressed in powers of the cycle-averaged intensity I^n with the corresponding photon order n. Good agreement with the theory in this regime was reported in the experiments with nanotips by Barwick *et al.* (2007), Ropers, Solli *et al.* (2007), and Dombi *et al.* (2010); see Fig. 15(b). The interference of different photon orders in the two-color experiments was reported by Förster *et al.* (2016) and Huang *et al.* (2017).

d. Rescattering mechanisms

Although the SFA produces good agreement with experimental spectra for comparatively low-energy electrons (Schenk, Krüger, and Hommelhoff, 2010), it does not explain the plateau at higher electron energies (Krüger *et al.*, 2012). The latter appears as a horizontal extension of the exponentially decaying energy distribution; see Fig. 16. It can be understood within the three-step model proposed by Corkum (1993), Schafer *et al.* (1993), and Paulus *et al.* (1994). In this model, photoelectrons are separated into direct and rescattered electrons. After emission, the direct electrons are accelerated in the laser field and never return to the metal surface, while the rescattered electrons driven by the field revisit the surface and backscatter, as predicted by Faisal, Kamiński, and Saczuk (2005). During another half period of the laser field, they can reach extra kinetic energy exceeding the energy of direct electrons. It follows that the exact transition amplitude [Eq. (2.21)] can be represented as a sum of two parts $M_p = M_p^{\mathrm{dir}} + M_p^{\mathrm{res}}$, where the direct part coincides with M_p^{SFA}, and the rescattered part is given by

$$M_p^{\mathrm{res}} = \left(-\frac{i}{\hbar}\right)^2 \int_{-\infty}^{\infty} dt \int_{-\infty}^{t} dt' \langle \Psi_p^{(V)}(t)|VU(t,t')H_I(t')|\Psi_0(t')\rangle. \tag{2.27}$$

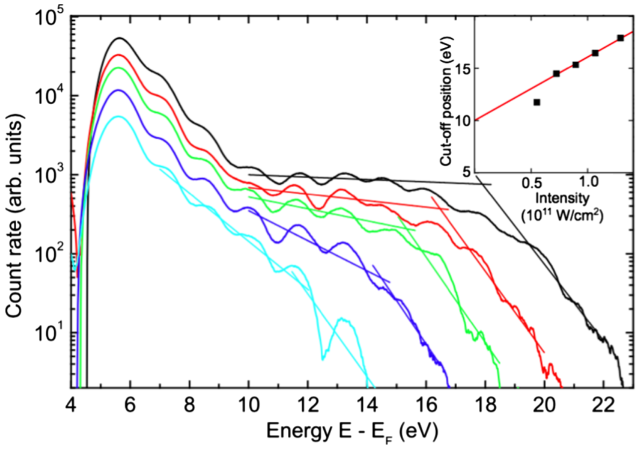

FIG. 16. Rescattering plateau in above-threshold photoemission at laser intensities ranging from 0.55×10^{11} (light blue, lowermost curve) to 1.3×10^{11} W/cm^2 (black, top curve), and $\hbar\omega = 1.56$ eV. (Inset) Cutoff energies as a function of intensity. The plateau region begins at 9 eV and extends up to 20 eV with a soft cutoff. Adapted from Krüger *et al.*, 2012.

As pointed out by Corkum (1993), any electron that scatters in laser field (i.e., abruptly changes its direction) is dephased from its harmonic motion, and therefore can absorb or emit energy from the field. In plasma physics, this mechanism is known as stimulated bremsstrahlung (Agostini *et al.*, 1979). To see this emerging from Eq. (2.27), one may neglect the intermediate interactions with the lattice in the exact evolution operator $U(t, t')$. With this assumption, the integrand becomes proportional to the oscillating exponential $\exp[iS_p(t,t')/\hbar]$ with the phase given by

$$S_p(t,t') = \frac{1}{2m_e}\int^t [p - eA(\tau)]^2 d\tau - \frac{1}{2m_e}\int_{t'}^t [k - eA(\tau)]^2 d\tau - E_0 t', \qquad (2.28)$$

where k is the intermediate electron's momentum. The stationary-phase conditions with respect to t, t' give two relations, one of which defines the instants of emission t_0 and another that corresponds to energy conservation at the time of rescattering:

$$[k - eA(t_0)]^2 = -\alpha^2, \qquad (2.29)$$

$$[k - eA(t)]^2 = [p - eA(t)]^2. \qquad (2.30)$$

A simple classical model of rescattering at surfaces was proposed by Krüger *et al.* (2012). In this model, the direct and rescattered wave packets are released near the metal surface with the same initial momentum distribution $N_d(E) \sim \exp(-p^2/2\sigma_p^2)$, but the rescattered wave packet recollides with the surface and acquires a displacement in momentum space $N_r(E) \sim \exp[-(p - \Delta p)^2/2\sigma_p^2]$, where the displacement follows from Eqs. (2.29) and (2.30): $\Delta p = 2eA(t) - k \approx 2eA(t) - eA(t_0)$. The kinetic energy associated with the displacement reaches a maximum $\Delta p^2/2m_e \sim 10U_p$ at some optimum values of t and t_0 (Paulus *et al.*, 1994).

In nanotips, the photoemission is also sensitive to the applied static field. The effect of the static field is twofold. First, it causes an effective decrease of the work function via the Schottky effect that decreases the effective nonlinearity in the multiphoton regime (Barwick *et al.*, 2007; Ropers, Solli *et al.*, 2007) and facilitates the photo-assisted electron tunneling (Yanagisawa *et al.*, 2011). Second, the static field impacts the dynamics of electron motion in the laser field, modifying electron trajectories, return times, and kinetic energy that electrons can gain in the laser field. Moreover, along with the field inhomogeneity, the static field reduces the number of return electrons released shortly after the peak field (Yalunin *et al.*, 2013). These electrons are the most energetic in the photoemission spectrum, and a reduction of them results in a decrease of the plateau height and the cutoff energy (Krüger *et al.*, 2012).

e. Subcycle interactions and carrier-envelope phase effects at nanostructures

It appears from the previous considerations that the photoemission probability [Eq. (2.25)] decreases exponentially with decreasing field strength. Consequently, the yield, spectral, and temporal characteristics of the photoelectrons become extremely sensitive to the subcycle field variation, and to the differences between the field amplitudes in the subsequent half cycles. The latter can be efficiently controlled by the carrier-envelope phase (CEP) of a few-cycle laser pulse (Lemell *et al.*, 2003; Apolonski *et al.*, 2004; Dombi *et al.*, 2004). Such CEP effects were studied in the photoemission experiments with nanotips (Krüger, Schenk, and Hommelhoff, 2011; Piglosiewicz *et al.*, 2014), as well as with dielectric nanospheres (Zherebtsov *et al.*, 2011; Süßmann *et al.*, 2015).

f. The role of field nanolocalization: Electron quiver motion quenching

Most of the studies dealing with strong-field photoemission were done with the conventional assumption that the field gradients are small and the ponderomotive motion is adiabatic. Considering typical diffraction-limited focusing conditions, this is indeed justified for nonrelativistic electrons. In nanostructures, however, due to high-field localization and enhancement, this assumption is not always valid because the quiver amplitude

$$l_q = \frac{|eF|}{m_e\omega^2} \qquad (2.31)$$

can easily reach or significantly exceed the dimension of the near-field region. This condition is described by the spatial adiabaticity parameter

$$\delta = l_F/l_q = \frac{l_F|eF|}{4U_p}, \qquad (2.32)$$

where l_F is the decay length of the near field.

In the subcycle acceleration regime $\delta \ll 1$, electrons released at the peak field via the quasistatic tunneling mechanism escape from the near field within a small fraction of the optical cycle. Consequently, the quiver motion rapidly quenches [see Fig. 17(e)], and the well-known ponderomotive

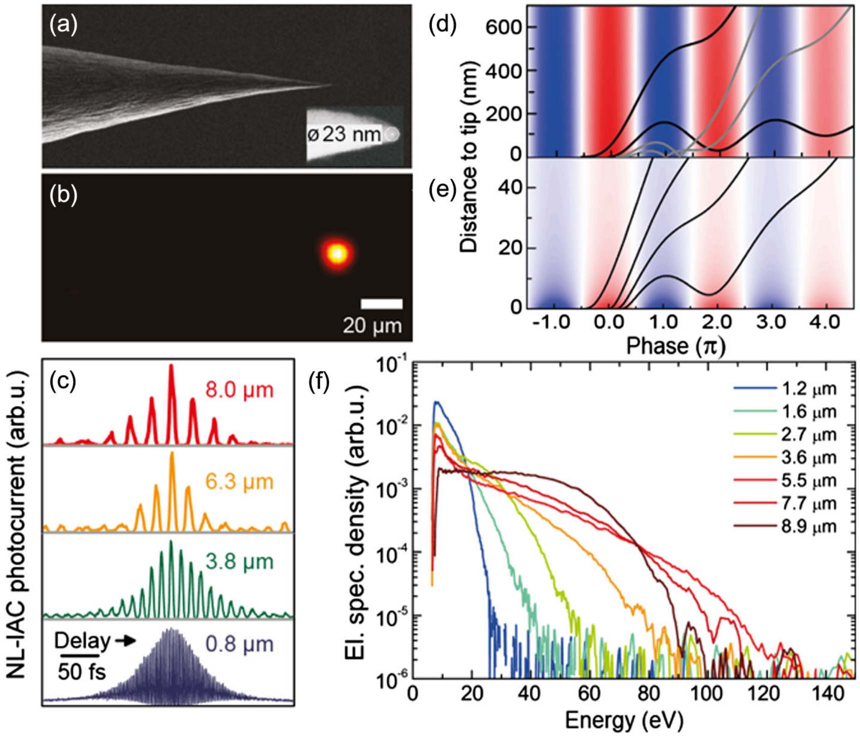

FIG. 17. Subcycle acceleration. (a) Scanning electron micrograph of the gold nanotip with the apex region (inset). (b) Electron emission map obtained by scanning the excitation focus (3.8 μm wavelength) across the structure. (c) Interferometric autocorrelations of the excitation pulses recorded using a photoelectron signal. (d) Electron trajectories (solid lines) calculated in the ponderomotive regime. (e) The same trajectories in the subcycle regime. Adapted from Herink *et al.*, 2012. (f) Photoelectron spectra measured at constant local near field and various excitation wavelengths (1.2–8.9 μm, corresponding to curves moving from left to right). Adapted from Echternkamp, Herink *et al.*, 2016.

scaling of direct photoemission breaks down. For nanotips, the transition from ponderomotive to subcycle acceleration was observed in photoemission experiments employing excitation wavelengths broadly ranging from 800 nm to 8 μm (Herink *et al.*, 2012). With increasing wavelength, the transition was identified via a saturation of the cutoff energies in the photoelectron spectra; see Fig. 17(f).

Photoelectron spectra in the subcycle regime exhibit a plateaulike structure at high electron energies and a pronounced low-energy peak (LEP), which shifts to higher energies as the intensity increases (Schötz *et al.*, 2018). The photoelectron spectra are almost entirely generated by the direct electrons accelerated out of the strong near field (Piglosiewicz *et al.*, 2014; Echternkamp, Herink *et al.*, 2016). In the limiting case, the LEP disappears and the characteristic shape of the photoelectron spectra is inverted. The steep high-energy cutoff shows a linear rather than quadratic scaling with the local field. The limiting case was realized with sharp tungsten tips employing an optimized terahertz excitation (Herink, Wimmer, and Ropers, 2014; Li and Jones, 2016). Similar conditions were also achieved with terahertz micro-antennas (Iwaszczuk *et al.*, 2015). A pronounced field guilding effect in the subcycle regime was reported by Park *et al.* (2012).

Generally, the strong-field photoemission and subcycle regimes are not strictly coupled. The Keldysh parameter distinguishes intensity-dependent dynamics during the emission process, while the adiabaticity parameter δ discerns the postphotoemission dynamics in spatially inhomogeneous fields. Depending on the ponderomotive energy, field decay length, and work function of the material, a set of four limiting cases of strong-field photoemission are identified in Fig. 18.

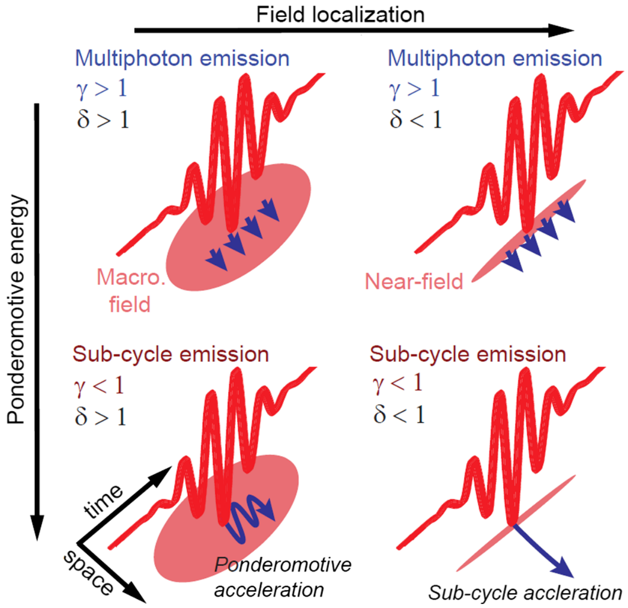

FIG. 18. Limiting cases of instantaneous nonlinear photoemission. For a given material, different regimes of photoemission and acceleration are accessed depending on the field localization and ponderomotive energy.

The well-known multiphoton regime ($\gamma > 1$) occurs at $\delta > 1$. The photoemission yield exhibits a power law with the corresponding photon order. Upon field localization, the emission area is nonlinearly confined without impacting photoelectron spectra. In the quasistatic tunneling regime ($\gamma < 1$), the photoemission is temporally confined to an extremely small fraction of the optical cycle. At $\delta < 1$, photoelectrons undergo a well-known adiabatic quiver motion induced by oscillating fields. In fields with steep gradients ($\delta, \gamma < 1$), the photoemission is accompanied by the entire subcycle acceleration with the previously discussed implications.

III. APPLICATIONS AND PERSPECTIVES OF HIGHLY NONLINEAR PHENOMENA AT NANOSTRUCTURES

The ability of metallic nanostructures to confine electromagnetic fields on nanometer length and femtosecond timescales discussed in Sec. II has triggered enormous research efforts directed toward probing and controlling such electromagnetic fields in real time and space and toward their application for controlling the motion of electrons in strong optical near fields. This section gives an overview of these recent efforts. The section is divided into three subsections. Section III.A focuses on imaging nanoplasmonic fields in space and time and includes a discussion of a series of experimental techniques that have been developed for this purpose, such as time-resolved photoemission electron microscopy (PEEM) or nanoplasmonic streaking methods. Section III.B. summarizes recent attempts to use strong nanoplasmonic near fields to control electron currents in different types of metallic nanoantennas and, in particular, to switch such currents on a subfemtosecond timescale by exploiting the carrier-envelope phase of the driving laser field. Finally, Sec. III.C. presents recent work aimed at creating new types of ultrafast, laser-driven electron microscopes, including ultrafast point-projection and photon-induced near-field electron microscopy. It also provides an overview of strong worldwide efforts in exploiting photoinduced plasmonic near fields to control the motion of free-space electron wave packets. First successful attempts toward the creation of attosecond, low-energy electron pulses have been reported. Some developments that are presented in this section, specifically the use of strong near fields at nanotips to control the motion of free-space electrons, have already been partially discussed ; see Hommelhoff and Kling (2015), Ciappina *et al.* (2017), and Krüger *et al.* (2018). Here we aim at giving a comprehensive overview, from the imaging of nanoplasmonic fields toward their exploitation in novel time-resolved electron microscopy concepts.

A. Probing of optical near fields with photoelectrons and streaking spectroscopy

During the past two decades the optical properties of metallic nanoparticles have been the subject of intense experimental and theoretical investigation, not only because of their interest for strong-field nano-optics but mostly because of a variety of possible applications in diverse fields such as photocatalysis, surface-enhanced Raman scattering, solar energy conversion, and cancer therapy, to name just a few (Pitarke *et al.*, 2007; Myroshnychenko *et al.*, 2008). This has led to a wealth of studies of the linear optical spectra of individual metallic nanoparticles (Klar *et al.*, 1998; Boyer *et al.*, 2002; Sönnichsen *et al.*, 2002b; Arbouet *et al.*, 2004; van Dijk *et al.*, 2006; Husnik *et al.*, 2012) using a range of sensitive spectroscopic methods such as dark field confocal spectroscopy (Sönnichsen *et al.*, 2000, 2002b), photothermal imaging microscopy (Boyer *et al.*, 2002; Berciaud *et al.*, 2004), and spatial modulation spectroscopy (Arbouet *et al.*, 2004; Muskens *et al.*, 2006; Husnik *et al.*, 2012).

More recently, substantial attention has been devoted to imaging the spatial and temporal characteristics of the localized electromagnetic near fields in the vicinity of plasmonic nanoparticles and nanoantennas. This is experimentally rather challenging since these near fields are confined on a spatial scale of few nanometers only and have exceedingly short lifetimes in the range from a few femtoseconds (Hanke *et al.*, 2009; Anderson *et al.*, 2010) to at most a few hundred femtoseconds (Ropers *et al.*, 2005; Aeschlimann *et al.*, 2015). The vectorial properties of such nanolocalized fields are complex (Lee *et al.*, 2007; Schnell *et al.*, 2010; Singh, Calbris, and van Hulst, 2014; Esmann *et al.*, 2019) since the highly curved geometries of the nanoparticles and antennas introduce a high degree of polarization mixing. Consequently, a variety of new and powerful experimental techniques have been developed and optimized to spatially image such nanoplasmonic fields and to track their dynamics. These include, among others, time-resolved near-field scanning optical microscopy [see Novotny and Hecht (2012) and Fig. 19(a)], electron-energy-loss spectroscopy [see de Abajo (2010) and Fig. 19(b)], time-resolved photoemission electron microscopy [see Kubo *et al.* (2005), Aeschlimann *et al.* (2007), and Fig. 19(c)], photon-induced near-field electron microscopy [see Park, Lin, and Zewail (2010) and Fig. 19(d)], and different variants of near-field streaking spectroscopy [see Ciappina *et al.* (2017) and Fig. 19(e)]. This section gives an overview of the application of such methods to the imaging of plasmonic fields in the vicinity of metallic nanoparticles and nanoantennas. It briefly summarizes the working principles of the different techniques and summarizes recent developments.

1. Imaging nanoplasmonic fields

a. Detection of optical near fields

One of the best-established methods to image optical near fields is scanning near-field optical microscopy (Pohl, Denk, and Lanz, 1984; Betzig *et al.*, 1991; Novotny and Hecht, 2012). SNOM aims at imaging the local optical response of a material near the surface with subwavelength spatial resolution (Greffet and Carminati, 1997; Hillenbrand and Keilmann, 2000). It does this by bringing a pointed tip into the sample's near field and by using it to scatter evanescent optical near fields into propagating electromagnetic fields which are then detected in the far field using a distant detector. Ideally, raster scanning this tip across the sample surface provides a map of the local electromagnetic field or, more precisely, the optical LDOS (des Francs *et al.*, 2001; Joulain *et al.*, 2003; Krachmalnicoff *et al.*, 2013) of the sample under

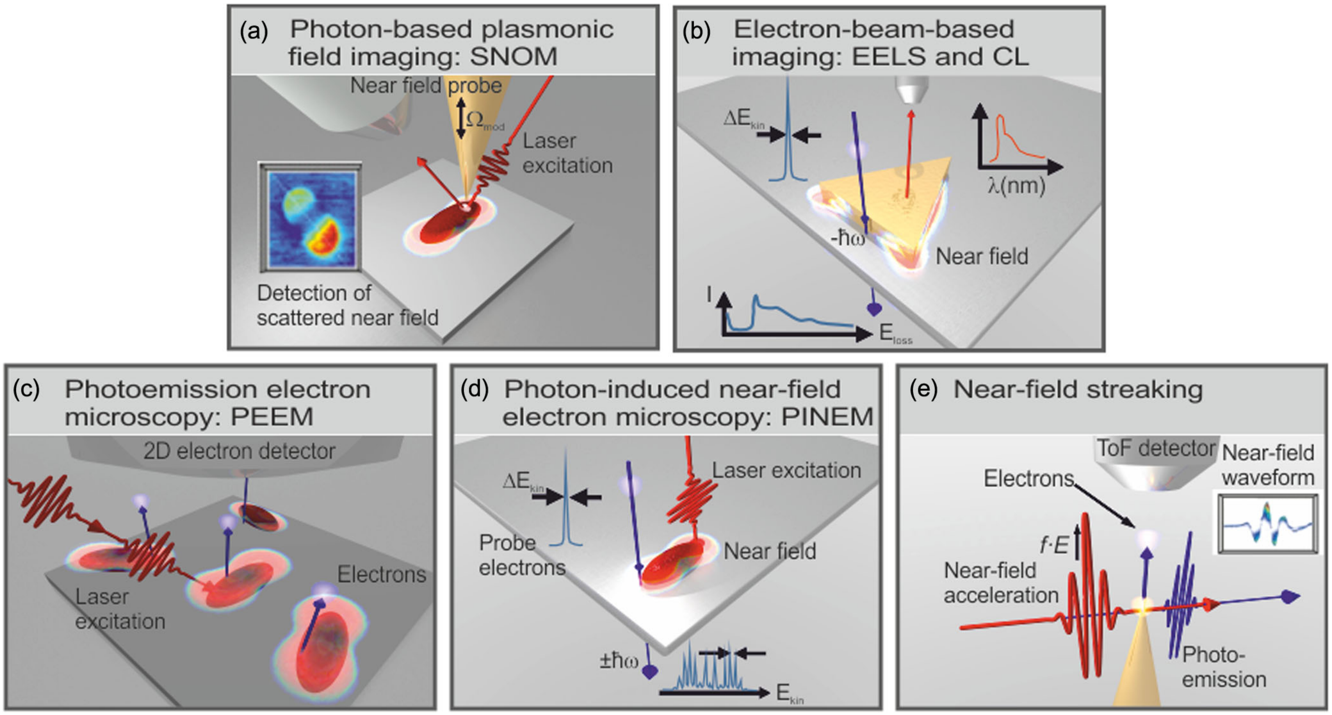

FIG. 19. Experimental techniques for the probing of optical near fields. (a) In scanning near-field optical microscopy, a nanometer-sized probe is brought into close vicinity of a nanostructure, scattering light from the near field to the far field. (b) A beam of swift electrons passing close by or through a nanostructure impulsively excites plasmonic modes. The energy transferred during the process is measured as a loss of the electron kinetic energy, or the light emitted during radiative relaxation is detected as cathodoluminescence (CL). (c) Photoelectrons emitted from the sample surface after far-field illumination are imaged to yield a high-spatial-resolution map of the local field distribution. (d) If a plasmonic nanostructure is excited optically, an electron passing by or through can gain energy, enabling photon-induced near-field electron microscopy. (e) Electrons photoemitted by an ultrashort UV pulse are accelerated in the near field of a nanostructure, driven by a NIR pulse. Measuring the kinetic energy as a function of delay between the UV and the NIR driving field gives access to the temporal near-field structure.

investigation. For media with sufficiently weak losses, the electric-field LDOS at observation point $\mathbf{r}$,

$$\rho_e(\mathbf{r},\omega) = \sum_n \frac{\gamma_n}{2\pi} \frac{|\mathbf{e}_n(\mathbf{r})|^2}{(\omega-\omega_n)^2 + (\gamma_n/2)^2}, \tag{3.1}$$

describes the spectral density of the intensities of the appropriately normalized electric-field distributions $\mathbf{e}_n(\mathbf{r})$ of all optical eigenmodes of the system (Glauber and Lewenstein, 1991). Here ω_n is the energy of mode n, i.e, the energy difference between the ground and excited states of the corresponding optical transition in the medium, and $\gamma_n = 1/T_{2n}$ is the damping rate of the mode or, equivalently, the inverse of the dephasing time T_{2n}. For an overview of the concept of LDOS in plasmonic systems, see Carminati *et al.* (2015). Achieving a true imaging of the LDOS is difficult in practice since this would require not only a homogeneous excitation of all eigenmodes of the sample but also a highly idealized, perfectly isotropic tip scatterer together with an omnidirectional detection of all scattered fields. The polarizability of the tip scatterer should be so weak that multiple scattering between tip and sample can be neglected. In many near-field experiments, this assumption is difficult to fulfill and the presence of the tip scatterer itself affects the measurement result (García-Etxarri *et al.*, 2009; Deutsch, Hillenbrand, and Novotny, 2010; Neuman *et al.*, 2015). Hence, a more realistic modeling of optical near-field images considers the optical properties of both sample and tip scatterer and their coupling. In near-field optics, this is often done by using phenomenological dipole-dipole coupling models (Aravind and Metiu, 1983; Zenhausern, Oboyle, and Wickramasinghe, 1994; Knoll and Keilmann, 2000; Hillenbrand and Keilmann, 2002; Raschke and Lienau, 2003).

Following several studies of evanescent and surface plasmon modes at planar surfaces (Marti *et al.*, 1993; Meixner, Bopp, and Tarrach, 1994; Krenn *et al.*, 1995), the first application of near-field microscopy to the spectroscopy of single metallic nanoparticles was reported by Klar *et al.* (1998). Gold nanoparticles embedded in a dielectric film were illuminated with a tunable laser source transmitted through a small aperture in an Al-coated quartz fiber tip; see Fig. 20(a). A resonant increase of the light intensity that is transmitted through the fiber and detected in the far field is the signature of light scattering by the localized surface plasmon resonance of the particle. The wavelength dependence of the scattering intensity suggests plasmon dephasing times of <10 fs, which agree well with values deduced from the far-field scattering spectra of single particles (Sönnichsen *et al.*, 2002b).

A drawback of such aperture-based probes is that their aperture size is limited to several tens of nanometers. In contrast, sharp metallic, apertureless tips can have an apex

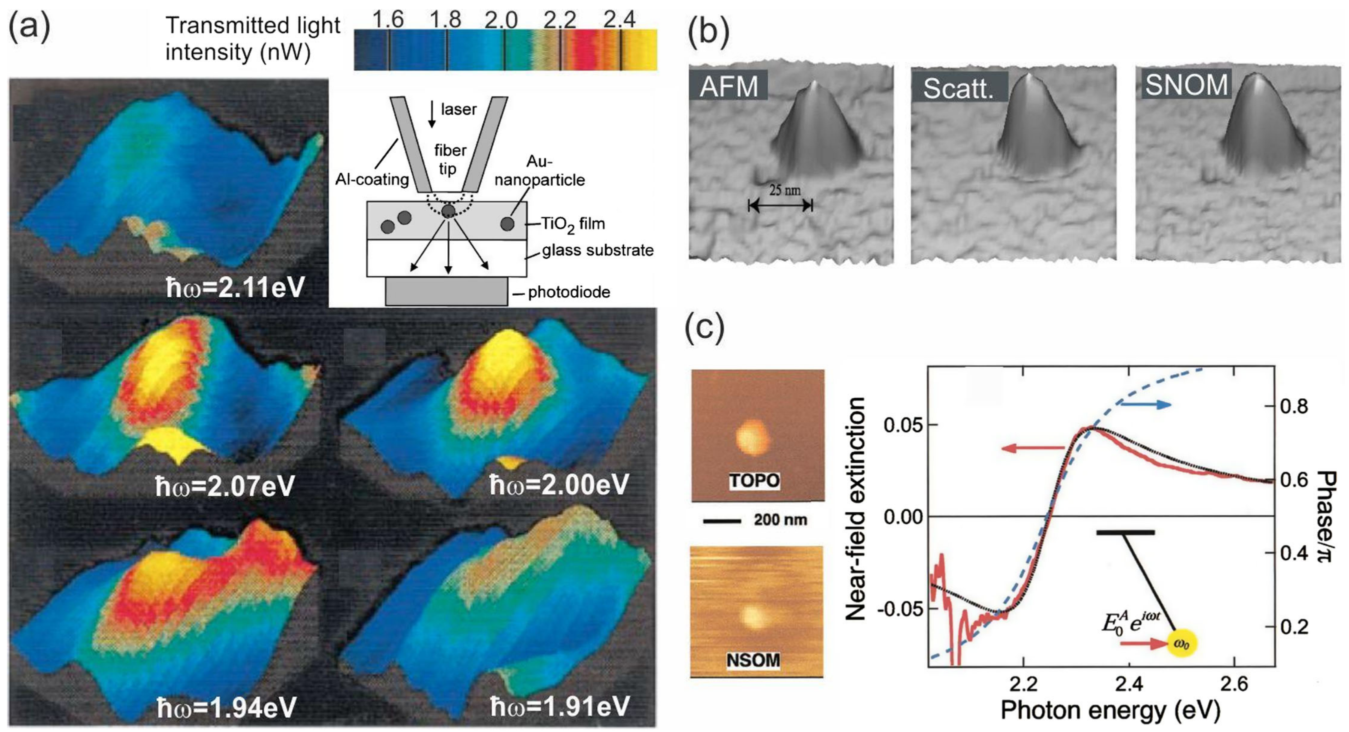

FIG. 20. Scanning near-field optical microscopy of nanoplasmonic fields. (a) SNOM images of individual gold nanoparticles with 40 nm diameter. A local enhancement in light transmission through an aperture-type SNOM probe at certain colors is the signature of resonant light scattering by the nanoparticle. Scans are $750 \times 750\ \mathrm{nm}^2$. From Klar *et al.*, 1998. (b) Scattering-type SNOM imaging of 14-nm Au particles. When an AFM tip is scanned across a particle (left image), a large enhancement in scattered signal intensity is measured (center image). The deduced SNOM signal is shown in the right image. From Hamann, Gallagher, and Nesbitt, 1998. (c) (Top left image) Topography and (top right image) SNOM image of a ∼50-nm gold nanoparticle measured with white-light illumination through a fiber aperture probe. The scattering spectrum of the particle is shown in red together with simulations (solid black and dashed blue curves) based on a forced-oscillator model. From Mikhailovsky *et al.*, 2003.

diameter of down to a few nanometers, more closely approaching the limit of an ideal point-dipole scatterer. They thus offer optical imaging with a spatial resolution that is sufficient to map the nanoplasmonic fields of single nanoparticles (Zenhausern, Martin, and Wickramasinghe, 1995).

The first apertureless SNOM images of a single gold nanoparticle with 14 nm diameter were reported by Hamann, Gallagher, and Nesbitt (1998); see Fig. 20(b). Monochromatic evanescent wave excitation at 550 nm illuminates the particle, and the near field at the particle surface is scattered into the far field using a dielectric AFM tip. The spatial resolution of the measurement is as high as 5 nm. The deduced scattering cross section of 200 nm^2 is much larger than that of an isolated gold particle of the same size, demonstrating the antenna action of the scattering tip.

Gresillon *et al.* (1999) used a similar apertureless SNOM approach to image the eigenmodes of randomly disordered, percolated gold films. In such films, multiple scattering of SPP waves results in complex spatiospectral interference patterns revealing a high density of spatially highly localized hot spots. Because of the comparatively high quality factor of those hot spot modes, the spatial distribution of localized fields varies significantly even for slight changes of the excitation wavelength. Such experiments have triggered efforts in exploiting those hot spots in percolated metals for enhancing optical nonlinearities (Breit *et al.*, 2001). They have also been extended to confined geometries such as submicron-sized gold nanosponges (Zhang *et al.*, 2014; Wang and Schaaf, 2018), perforated with a randomly disordered network of fine nanopores with diameters of only 10 nm (Zhang *et al.*, 2014; Hergert *et al.*, 2017; Zhong *et al.*, 2018). Such particles act as highly efficient nanoantennas (Hergert *et al.*, 2017) since the dipolar LSP mode of the entire particle efficiently couples far-field light into individual localized hot spot modes with diameters down to 10 nm and with quality factors exceeding 40, giving rise to giant Purcell factors (Zhong *et al.*, 2018).

The monochromatic SNOM experiments discussed earlier have been extended to a true spectroscopic imaging of nanoplasmonic modes (Mikhailovsky *et al.*, 2003). The observed spectra can be modeled reasonably well in terms of a coupled dipole model (Mikhailovsky *et al.*, 2004). Related broadband light-scattering near-field techniques have been used to elucidate the optical properties of nanowires, dimers (Kim *et al.*, 2009; Kern *et al.*, 2012), and other types of nanoantenna systems (Koerkamp *et al.*, 2004; Ghenuche *et al.*, 2008; Curto *et al.*, 2010; Huang *et al.*, 2010; Novotny and van Hulst, 2011; Biagioni, Huang, and Hecht, 2012). They have been applied (Novotny and Stranick, 2006) to the study of plasmonic nanogratings (Salomon *et al.*, 2001; Hohng *et al.*, 2002; J. Kim *et al.*, 2003; Ropers *et al.*, 2005; Zayats, Smolyaninov, and Maradudin, 2005) in attempts to clarify the physical mechanisms that are underlying the extraordinary

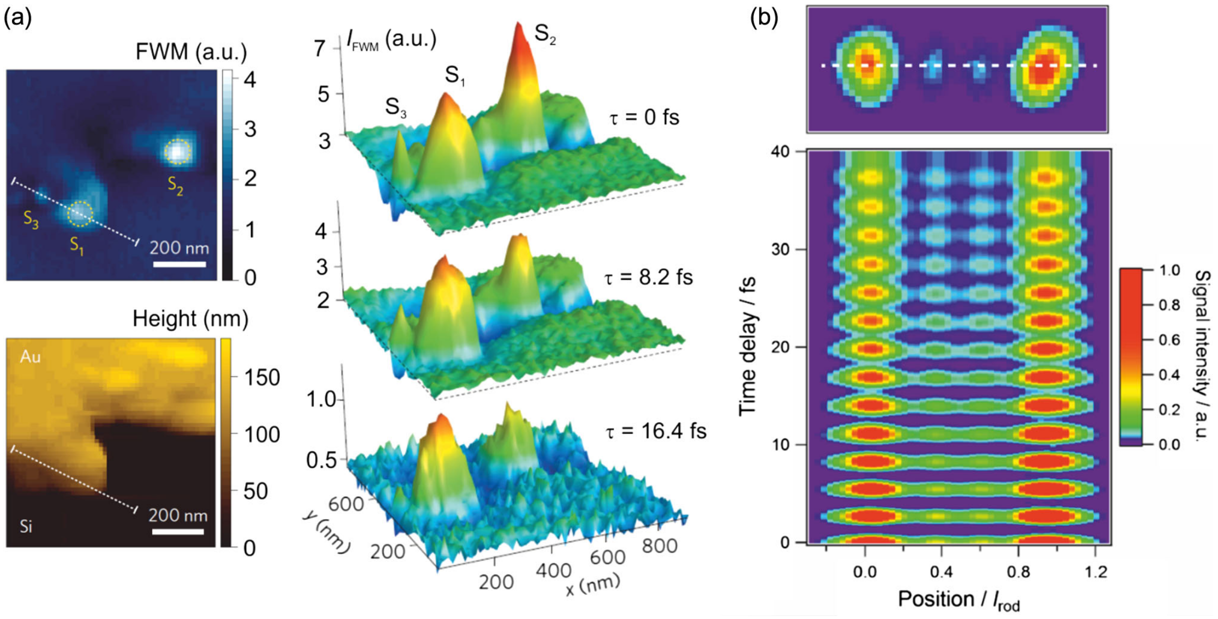

FIG. 21. Time-resolved imaging of nanoplasmonic modes. (a) Plasmonic hot spots on a nanostructured gold film imaged by plasmonic-nanofocusing four-wave mixing (FWM) SNOM. (Left images) FWM signal and topography. Distinctly different dephasing times of the hot spots are found. From Kravtsov *et al.*, 2016. (b) Time-resolved two-photon photoluminescence SNOM imaging of the plasmon dynamics of a gold nanorod with length $l_{\mathrm{rod}} = 615$ nm. (Top panel) SNOM image taken at a fixed time delay of 25.6 fs between two phase-locked excitation pulses. The standing-wave pattern along the horizontal axis, displayed in units of l_{rod}, maps the resonantly excited eigenmode of the rod. A series of images taken as a function of delay times maps the lifetime of the plasmon mode. From Nishiyama, Imura, and Okamoto, 2015.

optical transmission through nanohole arrays discovered by Ebbesen *et al.* (1998). Recent implementations of plasmonic-nanofocusing concepts (Sec. II.A.3.c) to create spatially isolated light spots at the apex of a sharp taper allow one to suppress unwanted background scattering and make it possible to quantitatively study the effects of multiple tip-sample scattering on the linear light-scattering spectra of single nanoantennas (Esmann *et al.*, 2019).

Important progress in nanoplasmonic imaging using near-field methods has been made by implementing interferometric detection schemes, which allow simultaneously imaging of the amplitude and phase of the scattered near field (Zenhausern, Oboyle, and Wickramasinghe, 1994; Hillenbrand and Keilmann, 2000; Bek, Vogelgesang, and Kern, 2006; Ocelic, Huber, and Hillenbrand, 2006). This allows one to retrieve the spatial distribution of one or several components of the electric field of optical modes of plasmonic nanosystems (Hillenbrand and Keilmann, 2001), particularly in differently shaped plasmonic nanostructures like rod antennas (Dorfmüller *et al.*, 2009, 2010), nanoprisms (Rang *et al.*, 2008), and bow ties (Esteban *et al.*, 2008; Rang *et al.*, 2008; Schnell *et al.*, 2009, 2010). A unique advantage of interferometric scattering-type SNOM is that it can be employed in a broad spectral range, from the visible to the mid-IR (Hillenbrand, Taubner, and Keilmann, 2002; Huber *et al.*, 2008; Olmon *et al.*, 2008). As such, it is currently the only available experimental technique that can image electromagnetic fields associated with low-energy plasmonic excitations, e.g., in graphene-based nanostructures (Chen *et al.*, 2012; Woessner *et al.*, 2015).

The strong-field enhancement in the coupling region between the tip and sample greatly enhances nonlinear optical effects. This has been used to improve the plasmon imaging quality by further narrowing the probing volume and by suppressing background scattering (Sanchez, Novotny, and Xie, 1999; Ichimura *et al.*, 2004; Danckwerts and Novotny, 2007; Horneber *et al.*, 2015). It also enables nonlinear spectroscopy on a nanoscale, such as tip-enhanced Raman spectroscopy (Hayazawa *et al.*, 2000; Stöckle *et al.*, 2000; Hartschuh *et al.*, 2003; Neacsu *et al.*, 2006), which now reaches even submolecular chemical specificity (Bailo and Deckert, 2008; Zhang *et al.*, 2013). The exploitation of nonlinear optical effects is also the key to ultrafast, time-resolved near-field optical spectroscopy, first employed for probing charge carrier dynamics in semiconductor nanostructures (Guenther *et al.*, 1999, 2002; Nechay *et al.*, 1999; Emiliani *et al.*, 2000; Unold *et al.*, 2004, 2005) and later also extended to the study of plasmon dynamics (Imura and Okamoto, 2009; Wu *et al.*, 2012; Eisele *et al.*, 2014; Wagner *et al.*, 2014; Nishiyama, Imura, and Okamoto, 2015; Imaeda, Hasegawa, and Imura, 2018). A recent example of such a time-resolved imaging of nanoplasmonic modes is shown in Fig. 21(a). Kravtsov *et al.* (2016) observed hot spots on a structured gold film through four-wave mixing (FWM) at the apex of a sharp plasmonic-nanofocusing tip (Kravtsov *et al.*, 2018). By varying the time delay between a pair of ultrashort excitation pulses, the transport of propagating surface plasmons can be seen in metallic nanostructures in space and time (Rewitz *et al.*, 2012; Blancon *et al.*, 2018; Yao *et al.*, 2018), and the dephasing time of individual hot spots can be measured (Kravtsov, Atkin, and Raschke, 2013).

Similar methods have also been exploited to probe the transport of propagating surface plasmon polariton wave packets in space and time (Rewitz *et al.*, 2012; Kravtsov *et al.*, 2016; Yi *et al.*, 2017). For a specific type of double-strip plasmonic waveguide, a coherent control of the plasmon transport has even been demonstrated (Rewitz *et al.*, 2014). For nanostructures with sizes that are smaller than the SPP propagation length, for example, ∼μm-sized nanowires, the structure acts like a Fabry-Perot cavity and standing-wave plasmon modes appear as eigenmodes of the wire (Dorfmüller *et al.*, 2009; Nishiyama, Imura, and Okamoto, 2015; Nishiyama *et al.*, 2015). When optically exciting such a wire through an aperture-type SNOM fiber, monitoring two-photon luminescence of the wire while scanning the tip across it, the different eigenmodes are clearly seen. When a phase-locked pulse pair is used for excitation as shown in Fig. 21(b) (Nishiyama, Imura, and Okamoto, 2015), the intensity of the spatial standing mode pattern displays a periodic oscillation as a function of interpulse delay with a period given by the energy of the eigenmode. The damping of the pattern for increasing interpulse delays provides a direct measure of the dephasing time of this localized surface plasmon excitation. As such, time-resolved near-field experiments provide important insight into the spatial and temporal transport of plasmonic wave packets in metallic nanostructures.

b. Electron-based imaging of plasmonic fields

Over the past decade, electron-based spectroscopy such as EELS, and also EFTEM and cathodoluminescence (CL), has gained enormous importance for the imaging of nanoplasmonic fields (Yamamoto *et al.*, 2001; de Abajo and Kociak, 2008b; de Abajo, 2010; Losquin and Kociak, 2015). In fact, the energy loss experienced by swift electrons when passing a metal was essential for the first observation and study of plasmons (Ruthemann, 1948; Watanabe, 1956; Ritchie, 1957). A swift electron, accelerated to 100–200 kV and moving at velocities of $0.5c$–$0.7c$, excites a nanostructured sample. Since it takes less than 1 fs for such an electron to pass by or through the sample, it induces to good approximation an impulsive excitation of all optical resonances of the sample from the IR to the UV. In EELS, a tightly focused electron beam is raster scanned across the sample, and the kinetic energy spectrum of the transmitted electrons is recorded. EFTEM is based on the same principle, but instead of raster scanning the sample is imaged in a transmission electron microscope, and the electrons are energy filtered before the detector. In both cases, the kinetic energy of the electron that is lost due to the excitation of optical resonances in the sample is evaluated.

More quantitatively, an electron propagating with velocity $\mathbf{v}$ along a straight line trajectory $\mathbf{r}_\mathbf{e}(t)$ drives optical excitations in the sample and this induces an electric field $\mathbf{E}^{\mathrm{ind}}(\mathbf{r}_\mathbf{e}(t), t)$ that is acting back on the propagating electron. The total energy loss can be obtained by integrating the force $-e\mathbf{E}^{\mathrm{ind}}(\mathbf{r}_\mathbf{e}(t), t)$ exerted on the electron along the trajectory of the electron. The probability that the swift electron loses a quantum of energy at frequency ω can then be written as (de Abajo and Kociak, 2008b; Hohenester, Ditlbacher, and Krenn, 2009; Talebi *et al.*, 2015)

$$\Gamma^{\mathrm{EELS}}(\omega) \propto \left(\frac{-e}{\pi\hbar\omega}\right) R \int_{-\infty}^{\infty} dt \mathbf{v}\mathbf{E}^{\mathrm{ind}}(\mathbf{r}_\mathbf{e}(t), \omega) e^{-i\omega t}. \tag{3.2}$$

Here $\mathbf{E}^{\mathrm{ind}}(\mathbf{r}_\mathbf{e}(t), \omega)$ is the Fourier transform of $\mathbf{E}^{\mathrm{ind}}(\mathbf{r}_\mathbf{e}(t), t)$. Γ^{EELS} is equivalent to the projection of the LDOS along the direction of propagation of the electron (de Abajo and Kociak, 2008b; Hohenester, Ditlbacher, and Krenn, 2009; Boudarham and Kociak, 2012; Losquin and Kociak, 2015).

In CL, the photons emitted from the sample subsequently to the electron-sample interaction are collected, ideally over the complete 4π solid angle. CL records spectra with extremely high spectral resolution, but it detects only excitations that relax radiatively. CL provides the projection along the electron trajectory of the radiative LDOS, which is information complementary to that acquired with EELS (Kuttge *et al.*, 2009; Losquin *et al.*, 2015). EELS and CL provide nanoscopic data related to optical extinction and scattering spectra, respectively (Losquin and Kociak, 2015; Losquin *et al.*, 2015).

Owing to interference of spectrally and spatially overlapping modes in the far field, CL line shapes can be asymmetric and the CL emission pattern can be changed (Kuttge *et al.*, 2009; Losquin and Kociak, 2015). Specifically, as interference of the emission of antisymmetric modes interferes destructively, CL cannot detect dark modes, while these appear in EELS spectra with the same intensity as bright modes (Nelayah *et al.*, 2007; Chu *et al.*, 2009; Duan *et al.*, 2012; Barrow *et al.*, 2014; Losquin and Kociak, 2015).

The loss spectrum of an electron beam that is focused on a flat and thin film carries information about the chemical composition on a subnanometer scale (Bosman *et al.*, 2007). Energy is also transferred to collective electron oscillations, which can be used to resolve symmetric and antisymmetric surface modes on extended thin films (Schmidt *et al.*, 2014). The electron beam impacting on a flat metal surface acts as a broad bandwidth and strongly localized source for propagating SPPs, and CL was used to measure the propagation length of SPPs by placing the electron focus on Ag and Au surfaces at a variable distance from a grating to couple the SPPs to far-field light (Wijngaarden *et al.*, 2006; Bashevoy *et al.*, 2007).

Following these initial demonstrations, both EELS and CL were applied to mapping the spatial distribution of plasmonic fields of diversely shaped nanostructures, such as spheres and dimers, rod antennas, and triangles (Yamamoto, Araya, and García de Abajo, 2001; Yamamoto, Nakano, and Suzuki, 2006; Hofmann *et al.*, 2007; Gómez-Medina *et al.*, 2008; Chaturvedi *et al.*, 2009; Sigle *et al.*, 2009). For EELS imaging of metal nanoparticles, it is relevant that the surrounding dielectric alters the plasmon modes. Hence, EELS probes the eigenmodes of the coupled metal-dielectric system (Li, Cherqui, Bigelow *et al.*, 2015; Li, Cherqui, Wu *et al.*, 2015).

The major challenge in EELS is to extract the faint, low-energy-loss sideband from the strong zero-loss peak of the electron beam. This was first achieved in the seminal work by Nelayah *et al.* (2007), who used EELS to map plasmonic eigenmodes; see Fig. 22(a). They used a scanning transmission electron microscope to scan a 100-kV electron beam, focused down to 1 nm diameter, across an equilateral Ag nanoprism of 78-nm-long sides. EELS spectra measured at the

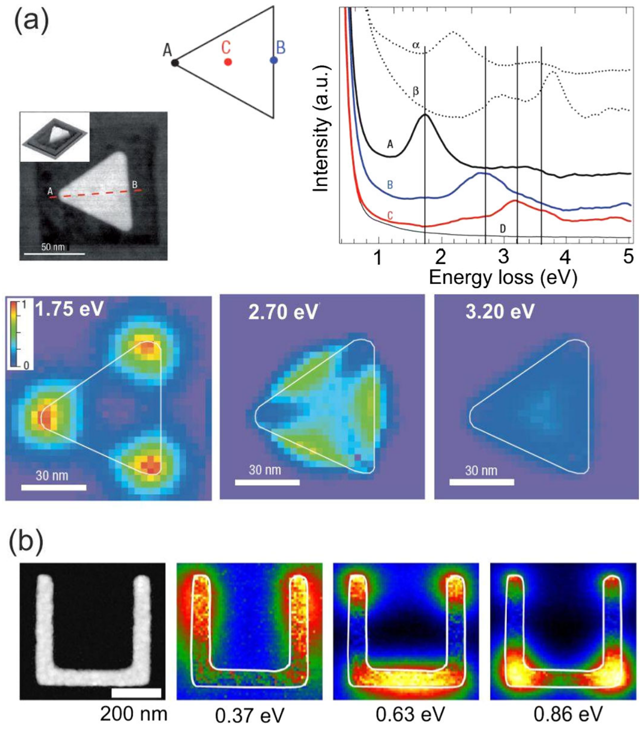

FIG. 22. Electron-beam-based imaging of nanoplasmonic modes. (a) EELS spectra obtained at three different positions on a Ag nanoprism (scanning electron microscopy image on the left): on a corner (A), on the edge (B), and in the center (C). Underneath are EELS images of the nanoprism showing the spatial distribution of the modes centered at 1.75, 2.70, and 3.20 eV. From Nelayah *et al.*, 2007. (b) EELS maps of a split-ring resonator (image on the left) recorded at resonance energies of 0.37, 0.63, and 0.86 eV. From von Cube *et al.*, 2011.

corner, on the edge, and at the center of the nanoprism display distinct peaks corresponding to the resonance energies of three different plasmon modes that are locally excited by the incident electron beam. The three images in the lower part of Fig. 22(a) represent EELS maps that were assembled from the loss intensity at these resonances, and they show the spatial distribution of the plasmonic eigenmodes of the nanoprisms (Shuford, Ratner, and Schatz, 2005; Rang *et al.*, 2008; Chaturvedi *et al.*, 2009; Nelayah *et al.*, 2009; Losquin and Kociak, 2015). The spatial resolution reaches down to $\lambda/40$, with λ being the wavelength of the excited mode, which is about 20 times larger than the beam diameter of the electron probe. One can see that the EELS signal decays quickly outside the nanoprism: a plasmonic mode is excited only for electron beam-particle distances of about 15 nm or less. This partially reflects the finite spatial extent of the optical near field associated with this mode.

The interaction of the swift electron with a delocalized mode of the nanoparticle can be seen in a particularly impressive way when the electron passes a gap, e.g., between a nanoparticle and a substrate (Yamamoto, Ohtani, and de Abajo, 2011), or the gap in a groove etched in gold, like the ones that constitute black gold (Søndergaard *et al.*, 2012). In the latter case, a clear shift of the plasmon resonance energy can be seen as the gap narrows, i.e., as the electron beam passes in a larger depth inside the gap (Raza *et al.*, 2014). This measurement shows that a groove represents a broad bandwidth and ideally nonresonant antenna, analogous to the conical nanotapers discussed by Schröder *et al.* (2015), Talebi *et al.* (2015), and Guo *et al.* (2016) and in Sec. II.A.3.b.

Similarly, the plasmonic eigenmodes of a variety of metallic nanostructures, for example, strip antennas, ridge waveguides, and wire nanoantennas, can be disentangled by their resonance energies and their spatial mode profile mapped both by EELS and by CL (Vesseur *et al.*, 2008; Schaffer *et al.*, 2009; Barnard *et al.*, 2011; Rossouw *et al.*, 2011; Knight *et al.*, 2012). On such flat structures, a large component of the optical near field pointing along the electron propagation direction exists at the antinodes of the charge-density oscillation. Therefore, the EELS map for a certain resonance frequency resembles the local charge-density distribution, which in turn is similar to the spatial profile of a Fabry-Perot resonator mode. For example, EELS maps recorded from silver nanowires of different lengths and shapes show a standing-wave pattern that has its origin in the interference of counterpropagating SPPs and that is independent of the shape of the wire (Rossouw and Botton, 2013).

Such studies are relevant for optimizing the design of metamerials (Boudarham *et al.*, 2010; von Cube *et al.*, 2011). As an example, Fig. 22(b) shows the three lowest-order eigenmodes of a split-ring resonator (depicted on the left), which resemble the Fabry-Perot modes of a straight structure with similar proportions. In measurements on split-ring resonators, first indications of a coupling between the two legs were found (Boudarham *et al.*, 2010). As nanoparticles are in close vicinity to each other, mode hybridization leads to a splitting of resonance energies (Nordlander *et al.*, 2004), which can easily be detected in EELS, EFTEM, and CL (Chu *et al.*, 2009; Koh *et al.*, 2009; N'Gom *et al.*, 2009; Halas *et al.*, 2011; Coenen *et al.*, 2016). Of particular physical interest is the study of such EELS spectra of extremely small nanoparticles, which are of particular relevance for heterogeneous catalysis and sensing applications. For such particles, quantum size effects and the spill out of the electron wave function affect the plasmonic spectra, and these effects can be revealed by EELS (Scholl, Koh, and Dionne, 2012). Care should be taken in relating the results of such studies to findings in the well-established field of cluster physics (Haberland, 2013). The study of couplings and mode hybridization in the regime of quantum plasmonics (Savage *et al.*, 2012), i.e., for nanoparticle separations below 0.5 nm where electron tunneling sets in, has largely benefitted from EELS studies (Scholl *et al.*, 2013). A recent achievement in EELS is the development of in-column monochromators, which make it possible to record spectra with resolutions better than 30 meV from nanometer-sized regions (Krivanek *et al.*, 2014; Lagos *et al.*, 2017). This new technology is likely to find important applications in imaging low-energy phononic and plasmonic excitations in the near future.

Furthermore, we note that tilting the sample and collecting EELS or CL maps for a number of tilting angles allows for tomographic reconstruction and thus for a three-dimensional representation of the LDOS. This is a major advantage over SNOM, as it is a strictly 2D imaging technique. On the other hand, it requires that the sample is transmissive for the electron, which limits the sample thickness to ∼100 nm.

This has been demonstrated theoretically (Hörl, Trügler, and Hohenester, 2013) and experimentally (Nicoletti *et al.*, 2013) for nanocubes, and when using CL for Au nanocrescents (Atre *et al.*, 2015).

In a process complementary to EELS, an electron may also gain energy from a plasmonic mode when passing the optical near field of an optically excited nanostructure. This type of inelastic scattering is the basis for electron-energy-gain spectroscopy, which was proposed as a method combining the high spatial resolution of electron imaging with the spectral resolution of optical spectroscopy (de Abajo and Kociak, 2008a; Barwick, Flannigan, and Zewail, 2009). Further details are provided in Sec. III.C.2.

c. Photoemission electron microscopy

Time-resolved PEEM (TR-PEEM) is a powerful technique for the imaging of the spatiotemporal dynamics of plasmonic near fields with high spatial and temporal resolution (Cinchetti *et al.*, 2005; Kubo *et al.*, 2005; Kubo, Pontius, and Petek, 2007; Spektor *et al.*, 2017). A sample is excited globally by light, typically a sequence of two (and sometimes more than two) phase-locked ultrafast optical pulses, and the photoemitted electrons are detected with a 2D electron detector to create a highly magnified image of the photoelectrons. The spatial resolution is defined by the imaging electron optics and can be better than 10 nm for advanced, aberration-corrected electron columns and especially when using low-energy electrons (Könenkamp *et al.*, 2010; Tromp *et al.*, 2010; Dabrowski, Dai, and Petek, 2017; Huber *et al.*, 2019).

Most TR-PEEM experiments use multiphoton photoelectron emission of the order of n, where the sample work function W exceeds the incident photon energy by roughly a factor of n, $W \approx n\hbar\omega$. The probability for electron emission is then proportional to the local surface polarization to the power of $2n$. Each pixel of the electron detector measures the time-averaged current that is photoemitted from the area around point $\mathbf{r}$ on the sample surface. Since the penetration depth of low-energy electrons is small (typically less than a few nanometers), the measured electron signal $S(\mathbf{r})$ senses the time-integrated local polarization $P_{\text{total}}(\mathbf{r})$ at the sample surface to the power of $2n$ $S(\mathbf{r}) \propto \int_{-\infty}^{\infty} P_{\text{total}}^{2n}(\mathbf{r}, t')dt'$. Here we neglect the vectorial character of the sample polarization, which is treated later. To understand TR-PEEM images, it is often beneficial to distinguish between local P_{light} and propagating P_{SPP} contributions to the sample polarization $P_{\text{total}}(\mathbf{r}, t') = P_{\text{light}}(\mathbf{r}, t') + P_{\text{SPP}}(\mathbf{r}, t')$ (L. Zhang *et al.*, 2011). Here P_{light} is proportional to the linear susceptibility of the sample at point $\mathbf{r}$ that is driven by the space-dependent and time-dependent external light field and that is possibly enhanced by localized SP resonances. Furthermore, if additional momentum is provided to the incident beam, it can generate a SPP excitation at point $\mathbf{r}'$ that can propagate to the emission point $\mathbf{r}$. Both contributions can be isolated by analyzing the spatial and temporal structure of the PEEM images.

The time resolution in PEEM is limited by the duration of the excitation laser pulses, which in principle can be as short as a few femtoseconds or even better. In practice, a combined spatial-temporal resolution in the range of 10 fs and a few tens of nanometers is typically reached (Aeschlimann *et al.*, 2017; Dabrowski, Dai, and Petek, 2017; Spektor *et al.*, 2017; Huber *et al.*, 2019).

In the first application of TR-PEEM to a plasmonic sample by Kubo *et al.* (2005), the nonlinearity intrinsic to two-photon photoemission was already exploited to probe the dynamics of localized surface plasmons. In the investigated rough silver grating, interference of multiply scattering SPP modes results in the formation of localized hot spots (Stockman *et al.*, 2004), which were excited by a phase-locked pair of 10-fs laser pulses at a wavelength of 400 nm, resulting in two-photon photoemission of electrons. An example of PEEM micrographs from that experiment covering an area of $180 \times 120\ \mu\text{m}^2$ is shown in Fig. 23. Compared to single-photon photoemission [Fig. 23(a)], in the case of the two-photon-induced process [Fig. 23(b)] electron emission clearly is concentrated at certain local hot spots.

Kubo *et al.* (2005) recorded PEEM images of the hot spots for varying time delays between the two phase-locked excitation pulses and studied the dynamics of different hot spots in Fig. 23(b). The electron yield from one particular hot spot [Fig. 23(c)] gives a cross-correlation between the LSP field of this hot spot and the laser pulse. For short time delays, it oscillates with the carrier frequency of the pulsed excitation. The LSP is externally driven by the light field, and the oscillation is due to the interference between the pump and probe fields. For delay times longer than the pulse overlap (>20 fs), the interference pattern reflects the free induction decay of the LSP: After the pump pulse ceases, the LSP evolves freely at its own resonance frequency and is probed by the second laser pulse. This can be seen by the shift of the photoemission oscillation [the blue symbols in Fig. 23(c)] with respect to the optical interference of pump and probe pulse (the gray dotted line).

Each hot spot displays an individual beat frequency. The dynamics of four hot spots indicated by the blue box in Fig. 23(b) are shown in Fig. 23(d). Until about 20 fs, the four hot spots oscillate with the same phase, driven by the external field. For later times the phases differ and dephasing of the coherent LSP polarization washes out the interference pattern. There is still long-lived photoemission due to hot electrons, which decreases exponentially. This provides evidence that the plasmonic excitations induced by the two laser pulses can interfere, and that electron emission observed in PEEM stems from the plasmonic fields. This type of interferometric time-resolved PEEM (ITR PEEM) has been used to study the resonance frequencies and lifetimes of individual LSPs in numerous single nanoparticles (Kubo *et al.*, 2005; Bayer *et al.*, 2008; Sun *et al.*, 2013; Lemke *et al.*, 2014; Marsell *et al.*, 2015a; Dabrowski *et al.*, 2016; Sun *et al.*, 2016; Qin *et al.*, 2019). The decay of the interference pattern is a measure for the dephasing time T_2 of the observed LSP mode. Because of the variations in resonance frequency, the observed interference patterns would wash out in ensemble measurements. The measurement of the dephasing time from a single emitter is an important feature of ITR PEEM, and it has been shown that both size and shape of nanoparticles have a strong impact on this dephasing time of LSPs (Bayer *et al.*, 2008; Sun *et al.*, 2016; Ueno *et al.*, 2019).

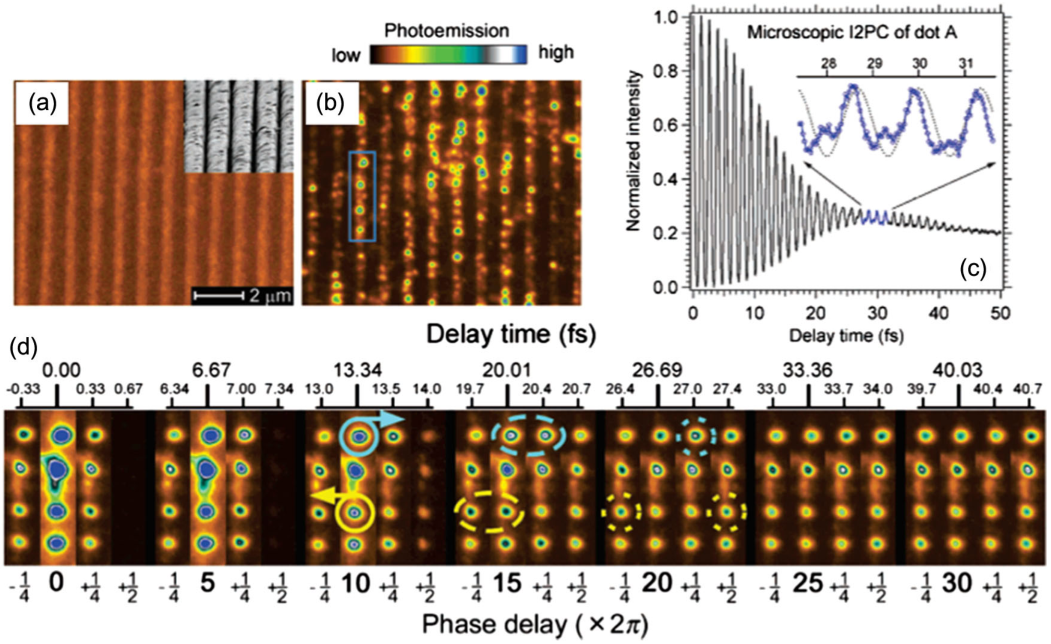

FIG. 23. Photoemission electron microscopy images taken from a silver grating. (a) PEEM image using single-photon photoemission by a Hg lamp. (Inset) SEM image of the grating. (b) Two-photon photoemission image using 400-nm light with p polarization. (c) The electron yield recorded from the topmost of the four hot spots marked in (b) is an interferometric time-resolved cross correlation of the laser pulse with the LSP. The inset magnifies a portion of the scan outside the pulse overlap, showing the shift of the LSP oscillation (blue symbols) with regard to the laser pulse optical interference (gray curve). (d) Details of the marked part in (b) for different time delays between pump and probe pulses. A clear variation of the oscillation phase can be observed after a time delay of approximately 20 fs. From Kubo *et al.*, 2005.

The excitation of such hot spots is highly sensitive to the polarization direction of the incident light. For example, when a structured metal surface that supports hot spots is illuminated by a laser pulse under grazing incidence, a $(\cos\theta)^{2n}$ dependence of the electron yield is detected, where photoemission is near zero ($\theta = 90°$) when the electric-field vector is perpendicular, and photoemission is maximum ($\theta = 0°$) when the electric-field vector is within the plane defined by the incidence and electron detection path (Awada, Barbillon *et al.*, 2012). The polarization state of the incident optical field can therefore be used to control the excitation of plasmonic modes of single or coupled nanoparticles (Awada, Popescu *et al.*, 2012; Marsell *et al.*, 2015a). This has nicely been shown in a study of nanostars, gold nanospheres with five to eight sharp tips pointing outward (Hrelescu *et al.*, 2011): PEEM images showed that the individual tips of the nanostar light up brightly, and changing the polarization of the incident light enabled selective excitation of the plasmonic modes corresponding to the hot spots localized at the tips.

Not only localized SP modes but also propagating SPP modes can be excited by the optical excitation pulses. This was shown for the first time by Kubo, Pontius, and Petek (2007), who reported TR-PEEM measurements on a silver film structured with a single line defect. The PEEM signal on the planar silver film shows a pronounced spatial interference pattern that is continuously evolving in time. The pattern results from the interference between the local polarization P_{light} induced by the two pulses and the propagating plasmon fields P_{SPP} launched by illuminating the line defect with the excitation pulses. For a pulse delay of more than 20 fs exceeding the temporal duration of the excitation pulses, the pattern is dominated by the interference between P_{SPP} created by the first pulse and P_{light} induced by the time-delayed second pulse. Consequently, the spatial period of these fringes $\lambda_{\text{beat}} = 2\pi(k_{\text{SPP}} - k_x)^{-1}$ is given by the difference between the in-plane component $k_x = 2\pi\lambda^{-1}\sin\theta$ of the incident light and the in-plane SPP wave vector k_{SPP}. Analysis of the beat pattern and its dynamics allows for deducing the group velocity and propagation length of the launched SPP wave packet SPP (Kubo, Pontius, and Petek, 2007; Meyer zu Heringdorf *et al.*, 2007; Y. Zhang *et al.*, 2011).

Similar TR-PEEM images have been recorded for different types of extended particles, like nanorods or nanowires (Meyer zu Heringdorf *et al.*, 2007; Marsell *et al.*, 2015b; Dabrowski *et al.*, 2016). An example is shown in Fig. 24(a) (Meyer zu Heringdorf *et al.*, 2007), where a ~12-μm long silver nanowire is illuminated with phase-locked pulse pairs with a center wavelength of 400 nm and with a duration of 20 fs. Close to the lower edge, a time-independent standing-wave pattern emerges due to reflection of the SPP at the wire end. Additionally, the SPP travels up the wire and interferes with the time-delayed probe pulse.

In such TR-PEEM images recorded with oblique sample excitation, the fringe period thus depends not only on the wavelengths of SPP and incident light but also on the angle of incidence. This complication of the image interpretation can be overcome in state-of-the-art normal-incidence PEEM. Here pump and probe pulses propagate along the surface normal and the wave fronts of the incident pulses are therefore parallel to the sample surface. Hence, the fringe spacing measures the

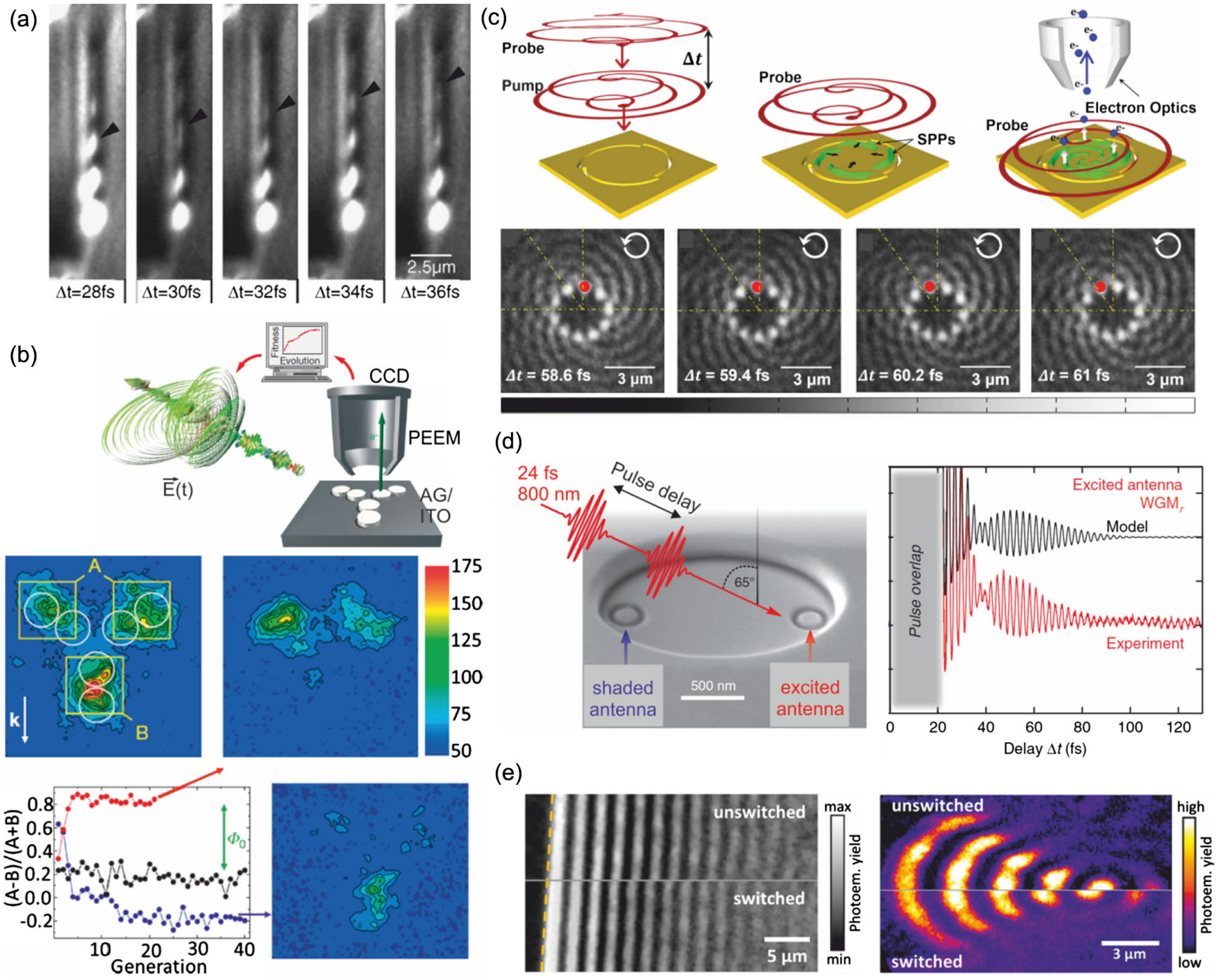

FIG. 24. Nanoplasmonic field imaging with PEEM. (a) PEEM images of a propagating surface plasmon polariton along a silver wire, recorded at time steps of 2 fs. The position of the upper maxima (see the maximum marked with a black arrow) depends on the temporal delay between the pump and the probe pulse, showing that it stems from SPP propagation dynamics on the nanowire. From Meyer zu Heringdorf *et al.*, 2007. (b) PEEM combined with an ultrafast pulse shaper and a learning algorithm (upper sketch) is used to illuminate a nanostructure consisting of three dimers of metal disks (marked with white circles in the first PEEM image). The upper left PEEM image is recorded with p-polarized laser light, the right-hand upper and lower images are recorded after optimization of the pulse shape for emission from regions A and B, respectively (regions A and B are marked with yellow squares). Adaptive optimization of the relative emission strength from regions A and B leads to increased (red, upper curve) and decreased (blue, lower curve) differences of electron yield from the two regions with respect to the unshaped laser pulse (black, curve in the middle). From Aeschlimann *et al.*, 2007. (c) Surface plasmon polaritons with orbital angular momentum are optically excited via a slit in the shape of a spiral on a gold surface. The plasmons travel toward the center of the structure and form a plasmonic vortex. The images are taken at slightly different temporal delays between pump and probe pulse. From Spektor *et al.*, 2017. (d) Two plasmonic antennas are at the focus points of an elliptical cavity, and only one is illuminated by a sequence of ultrashort pulses. The photoemission recorded from the initially illuminated antenna shows coherent energy transfer between the two antennas. From Aeschlimann *et al.*, 2017. (e) The fringe spacing of a LSP image is clearly reduced after illuminating a photochromic molecular switch with UV light, demonstrating control of the plasmon dispersion. This can be used to move the focal point of a plasmonic lens by 500 nm. From Großmann *et al.*, 2015.

effective plasmon wavelength, giving direct access to SPP propagation in different geometries (Kahl *et al.*, 2014; Podbiel, Kahl, and Meyer zu Heringdorf, 2016; Razinskas *et al.*, 2016). Since the incident laser field has no out-of-plane component, the excitation can couple to selected components of the susceptibility tensor of the sample (Podbiel, Kahl, and Meyer zu Heringdorf, 2016).

With these recent developments, TR-PEEM has now become a powerful tool for the characterization and evaluation of plasmonic devices, with the potential use of such devices for future broadband and ultrafast plasmonics in mind (Ozbay, 2006; MacDonald *et al.*, 2009). Of particular interest is the excitation of plasmon fields with well-controlled spatial and temporal properties. This can be achieved by controlling not only the temporal structure but also the polarization properties of the excitation pulses. Such a coherent, spatiotemporal control of electromagnetic fields on the nanoscale was achieved for the first time by Aeschlimann *et al.* (2007).

They used polarization-shaped ultrashort laser pulses to illuminate three nanodimers [Fig. 24(b)] and visualized photoemission by two-photon PEEM. The relative photoemission yield from the upper two dimers (region A) or from the lower dimer (region B) is maximized using an evolutionary learning algorithm. The spectral phase of two transverse polarization components is modulated using spatial light modulators, which results in a controlled intensity, momentary oscillation frequency, and polarization state in the time domain. The two PEEM images after optimization of photoemission from regions A and B are profoundly different. In each case, photoemission stems almost exclusively from the selected region, showing that polarization pulse shaping offers a possibility for controlling selective photoemission from complex nanostructures.

In combination with carefully shaped light fields, PEEM has been employed to unravel exciting properties of SPP, such as their spin and orbital angular momentum (AM). SPPs carrying orbital AM can be created by launching them from an Archimedean spiral cut into a metallic plate and illuminated with circularly polarized light (Gorodetski *et al.*, 2008). The time-resolved PEEM measurements shown in Fig. 24(c) (Spektor *et al.*, 2017) reveal the phase rotation of plasmonic vortex fields toward the center of the spiral, where they form a plasmonic vortex, and directly probe the orbital AM state of the plasmon. Here the SPP wave fronts rotate counterclockwise, corresponding to a positive topological charge m, or an orbital angular momentum parallel to the surface normal (Spektor *et al.*, 2017). For such spirals, SPP wave packets are launched efficiently if the excitation light carries spin AM pointing in the same direction as the orbital AM of the SPP mode. The wavelength of the SPP modes can be substantially shorter than the free-space wavelength, allowing us to carry the AM to dimensions well below the diffraction limit of far-field optics; see Sec. II.A.2. The spin AM of light that is incident on a plasmonic surface has been used to control the directionality of plasmons, e.g., using coupler structures with spin-sensitive geometries (Lee *et al.*, 2012; Lin *et al.*, 2013; Dabrowski, Dai, and Petek, 2017; Dai *et al.*, 2018). This directional coupling can be related to an unusual spin property of evanescent waves, their transverse spin AM, that has been investigated (Bliokh and Nori, 2012; Petersen, Volz, and Rauschenbeutel, 2014; Bliokh *et al.*, 2015). In the plane spanned by the surface normal and propagation direction, the electric field performs a cycloidal motion. This motion is characterized by a transverse spin AM pointing normal to that plane and switching its sign when reversing the propagation direction. The coupling of the spin AM of incident light waves to evanescent waves' transverse spin AM and the resulting spin-direction locking have been studied in a series of experiments (Petersen, Volz, and Rauschenbeutel, 2014; Le Feber, Rotenberg, and Kuipers, 2015; Dabrowski, Dai, and Petek, 2017; Dai *et al.*, 2018). In related TR-PEEM studies, the plasmonic analog of the spin Hall effect has been uncovered. When examining the focusing properties of a plasmonic lens, a sensitivity of the resulting SPP field profile to the helicity of the excitation light has been demonstrated (Dai and Petek, 2019).

TR-PEEM has also been employed to probe energy transfer processes in coupled plasmonic structures (Aeschlimann *et al.*, 2017). Two antennas were placed in the two focal points of an elliptical cavity, and grazing incidence ensured that only one of them was excited by the incident laser pulse; see Fig. 24(d). The recorded photoemission shows the coherent energy transfer between the two antennas over a rather long distance of twice the excitation wavelength. Figure 24(d) shows how the photoemission from the initially excited antenna ceases after ∼40 fs as the energy is transferred to the other antenna, and how it is revived later as the energy is transferred back.

Such well-designed structures for the control of plasmonic fields can even be modified optically (Großmann *et al.*, 2015) using photochromic molecular switches. They can be used to reversibly change the group and phase velocity of SPPs and hence change, for example, the focal length of a plasmonic focusing device. In Fig. 24(e), the focal point of a plasmonic lens is shifted by 500 nm.

The disentanglement of optical excitation and electron detection in PEEM, in combination with sophisticated illumination schemes, enables the adaptation of a multitude of techniques that are established in optical spectroscopy, even in such powerful schemes as 2D spectroscopy (Aeschlimann *et al.*, 2011). Two-dimensional spectroscopy is based on the coherent excitation of a sample using a pulse sequence consisting of four femtosecond pulses whose temporal variation and relative phases are precisely controlled. The electron yield is measured as a function of the delay times and phases and, as PEEM is not limited by diffraction of light, with a spatial resolution far below the wavelength of the exciting light. This can yield detailed information about the dynamics of local material excitations (Aeschlimann *et al.*, 2011) and, in particular, about the coherent and incoherent exchange of energy between these excitations (Brixner *et al.*, 2005; Engel *et al.*, 2007; De Sio *et al.*, 2016; De Sio and Lienau, 2017; Scholes *et al.*, 2017). We anticipate that the implementation of such phase-locked multicolor excitations schemes in PEEM can provide new insight on the photoinduced transfer of charge and energy in isolated nanosystems.

2. Rescattering-based near-field probing

Motivated by the importance of the field enhancement effect, the development of accurate experimental probes for measuring and quantifying electromagnetic fields in nanometric volumes is a basic endeavor in nanoscience for achieving tailored nanostructures for various applications.

Approaches to providing a quantitative description of the local, enhanced field strength include Raman signal enhancement, taking advantage from signal scaling laws in surface enhanced Raman spectroscopy (SERS) (Campion and Kambhampati, 1998; Willets and Van Duyne, 2007). This way, field enhancement factors between 30 and 120 were deduced in an indirect manner for different nanostructured samples dedicated to sensing applications (Fang, Seong, and Dlott, 2008; Rycenga *et al.*, 2011). Quantitative estimates of local field strength can be assessed using a similar indirect measurement concept based on the enhancement of two-photon photoluminescence signal levels (Schuck *et al.*, 2005) and two-photon photoemission yields (Tan, Liu *et al.*, 2017; Tan, Argondizzo *et al.*, 2017). Alternatively, there are also direct methods that rely on irreversible changes induced by a critical value of the electric field. Direct ablation (Harrison and Ben-Yakar, 2010) or typically two-photon photopolymerization of nanopatterned samples (Sundaramurthy *et al.*, 2006; Deeb *et al.*, 2010; Geldhauser *et al.*, 2012) are able to show whether or not a threshold electric-field strength is reached near the investigated nanostructures, but the interactions are irreversible and samples can no longer be used. If the investigated nanostructure consists of two closely spaced parts, tunneling conduction between them leads to optical rectification, producing a dc photocurrent. Based on the measurement of this photocurrent, a particularly high 3-orders-of-magnitude enhancement was deduced experimentally for plasmonic subnanometer gaps (Ward *et al.*, 2010). Determination of the Purcell factor can also provide sound estimates for field enhancement, but only for specific samples (Maier, 2006; Akselrod *et al.*, 2014). Even though all of these methods can be used to determine field enhancement values experimentally, none of them are direct, nondestructive, and generally applicable at the same time.

Photoemission from nanostructures offers a pathway toward overcoming all of these limitations. Plasmonic photoemission exhibits enhanced yield (Tsang, Srinivasan-Rao, and Fischer, 1990; Dombi *et al.*, 2010), and some electrons gain a kinetic energy in the plasmonic near field that significantly exceeds the photon energy (Dombi *et al.*, 2013). These features already show that information about near-field strength is encoded into the plasmonic photoemission spectra.

During the interaction of the photoemitted electron and the oscillating field, the electron experiences quiver motion, the amplitude of which scales with the square of the wavelength; see Sec. II.B.2.f and Eq. (2.31). Quiver amplitudes are in the subnanometer range for the most common short-pulse lasers with ~800 nm central wavelength, indicating that electrons gain kinetic energy from nanometer-scale near fields. For typical 20 V/nm local field strengths less than 0.7 nm electron quiver amplitude can be reached at 800 nm, enabling near-field probing with subnanometer sensitivity. In this regime the electrons that are rescattered at the surface gain the highest kinetic energy [see Busuladzic, Gazibegovic-Busuladzic, and Milosevic (2006) and references therein], as illustrated in Fig. 25(a).

The energy spectra of the electrons emitted from plasmonic systems have been studied extensively (Aeschlimann *et al.*, 1995; Grubisic *et al.*, 2012). Dombi *et al.* (2013) demonstrated that these spectra strongly correlate with plasmonic resonances; see Fig. 25(b). Photoelectron spectra of gold nanorods with different lengths (exhibiting different resonance frequencies) were compared. The most energetic electrons were observed for plasmonically resonant nanoparticles; see Fig. 25(c). These results naturally prompt the question whether one can quantify field enhancement based on plasmonic photoemission.

The energy gain of an electron during ponderomotive acceleration can be deduced by solving the classical equations of motion of an electron in the electromagnetic field of plasmons (Irvine, Dechant, and Elezzabi, 2004). A maximum kinetic energy $Q_{\max}$ up to 10 times the ponderomotive energy U_p (introduced in Sec. II.B.2.a) is reached according to

$$Q_{\max} = 10.007 U_p + 0.538 W, \tag{3.3}$$

a well-known relationship in atomic physics (Paulus *et al.*, 1994). The correction with the work function W can be derived from quantum-mechanical considerations (Busuladzic, Gazibegovic-Busuladzic, and Milosevic, 2006). Equation (3.3) is valid provided that the decay length of the investigated near field is much larger than the quiver amplitude of the free electrons in the enhanced local field (Herink *et al.*, 2012). Since quiver

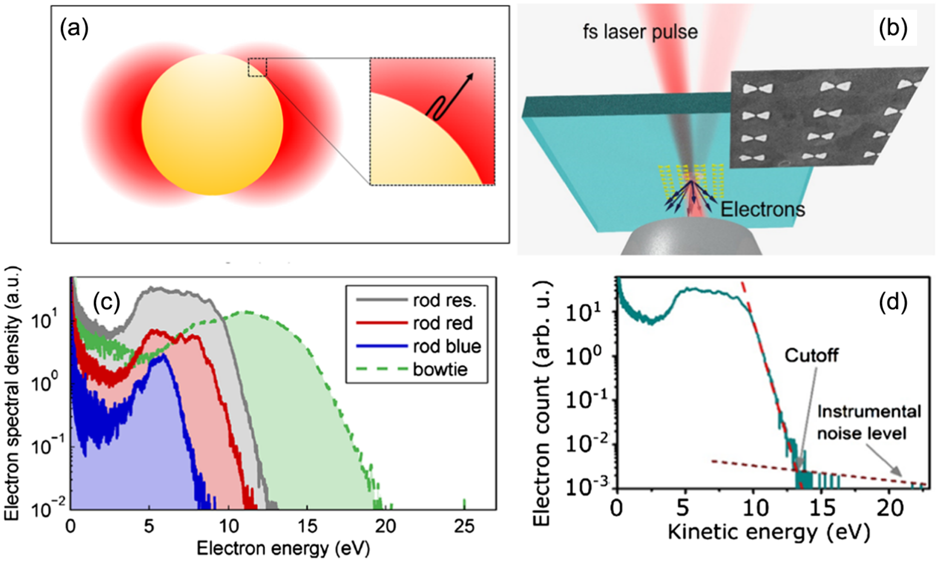

FIG. 25. Principles of rescattering-based near-field probing. (a) Schematic drawing of the electron rescattering in the vicinity of a metal nanosphere. (b) Scheme of the experimental setup for nanoplasmonic near-field measurement with photoelectrons (black arrows). (c) Femtosecond-pulse-induced electron spectra for different nanoparticles (resonant, redshifted, and blueshifted nanorods as well as resonant bow ties) recorded by setting 25 GW/cm^2 focused laser intensity. Spectra are recorded by a time-of-flight spectrometer. (b), (c) From Dombi *et al.*, 2013. (d) Photoelectron spectrum with the spectral cutoff point indicated from which field enhancement is extracted. From Rácz *et al.*, 2017.

amplitudes remain below 1 nm for intensities of around 100 $\mathrm{GW/cm^2}$ and field enhancements of dozens, the requirement condition is commonly fulfilled for near-IR experiments and near-field decay lengths of ∼10 nm for plasmonic nanostructures and hundreds of nanometers for propagating surface plasmons (Budai *et al.*, 2018).

This way maximum hot spot field enhancement can be extracted by (i) measuring spectral cutoffs [Fig. 25(d)], (ii) determining the local near-field intensity using Eq. (3.3), and (iii) determining the focused intensity in an independent measurement. For nanotips, field enhancement values between 3 (50 nm tip radius) and 6 (5 nm radius) were experimentally deduced (Thomas *et al.*, 2013). This study suggested that the geometric effect plays the dominant role since similar enhancements were obtained for plasmonic (gold) and nonplasmonic (tungsten) materials.

Rácz *et al.* (2017) studied various plasmonic nanosystems fabricated in a well-controlled manner; see Fig. 26. Field enhancements of 30–50 were deduced, much higher than the values achievable with nanotips, even for the sharpest possible radii (∼10 nm), providing an opportunity for additional applications and engineering plasmonic nanosystems for specific purposes.

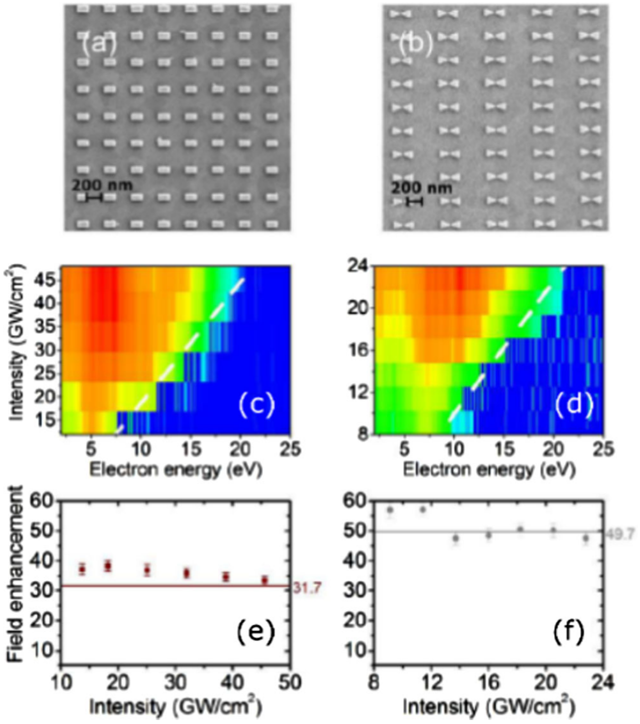

FIG. 26. Measurements of field enhancement factor on different nanostructured samples. (a),(b) SEM images of plasmonic nanoparticle samples. (c),(d) Plasmonic photoemission electron spectra as a function of focused laser intensity for the corresponding samples plotted in logarithmic false color representation. The white dashed lines show the linear dependence of the spectral cutoffs. (e),(f) Maximum plasmonic field enhancement values extracted from the electron spectral cutoffs according to Eq. (3.3) as a function of intensity for the corresponding samples, confirming the robustness of the measurement method. The horizontal lines show the simulated field enhancement values. From Rácz *et al.*, 2017.

3. Near-field streaking for phase-resolved probing

Resolving spatiotemporal dynamics of nanolocalized optical near fields presents a continuing experimental challenge. With the advent of attosecond metrology, however, probing of near-field dynamics on the natural dephasing timescales in solids became within reach via all-optical streaking principles.

Relying on linear photoemission, conventional electro-optical streak cameras translate light intensities into electric charges that are subsequently deflected by rapidly swept electric fields and resolved in the spatial domain. The slope of the streaking electric field, its timing jitter, and the electro-optical imaging performance determine the temporal resolution, allowing subpicoseconds with established streak camera technology and down to ∼100 fs with laser-driven photoswitches (Kassier *et al.*, 2010).

A key step toward ultimate temporal resolution is provided by all-optical schemes based on laser-driven streaking fields. Phase-stable waveforms with absolute carrier-envelope offsets known from shot-to-shot detection or, alternatively, single-shot resolved detection (Wittmann *et al.*, 2009) are prerequisites. Compared to electro-optical streaking, all-optical streaking largely eliminates synchronization jitter between signal and streaking transients, yielding attosecond temporal resolution for the full characterization of optical waveforms and for the detection of XUV-intensity transients in the attosecond domain.

A traditional attosecond streaking experiment performed on atoms, aiming at the reconstruction of the electric field of a few-cycle wave, involves an attosecond XUV pulse generated by high-order harmonic generation and a synchronized laser pulse. The latter often also acts as driving pulse for the HHG, inherently guaranteeing the synchronization of the two pulses. These collinearly propagating pulses are then focused onto a gas target with a controllable delay between them. The attosecond pulse generates photoelectrons that are then accelerated in the laser field (streaking field). During this process, the momentum (velocity) of the photoelectrons changes depending on the vector potential of the field at the moment of release t (Fig. 27) according to

$$\Delta p = -e\int_t^{\infty} E_L(t')dt' = -eA_L(t). \tag{3.4}$$

Recording the photoelectron spectra at each time delay provides direct access to the laser waveform and thus has been applied to the reconstruction of few-cycle laser fields; see Fig. 27(b) and Goulielmakis *et al.* (2004). In turn, attosecond streaking experiments provide information on the XUV pulse profile (Drescher *et al.*, 2001; Itatani *et al.*, 2002; Kitzler *et al.*, 2002; Mairesse and Quéré, 2005; Quéré, Mairesse, and Itatani, 2005). Photoelectron streaking has thus been established as a key technology in attosecond science (Kienberger *et al.*, 2004; Cavalieri *et al.*, 2007; Pfeifer *et al.*, 2008; Frühling *et al.*, 2009; Schütte *et al.*, 2011).

The transfer of all-optical streaking to the study of complex nanostructures and solids offers the prospects of phase-resolved detection of plasmonic near fields and temporal mapping of ultrafast dynamics on the nanoscale.

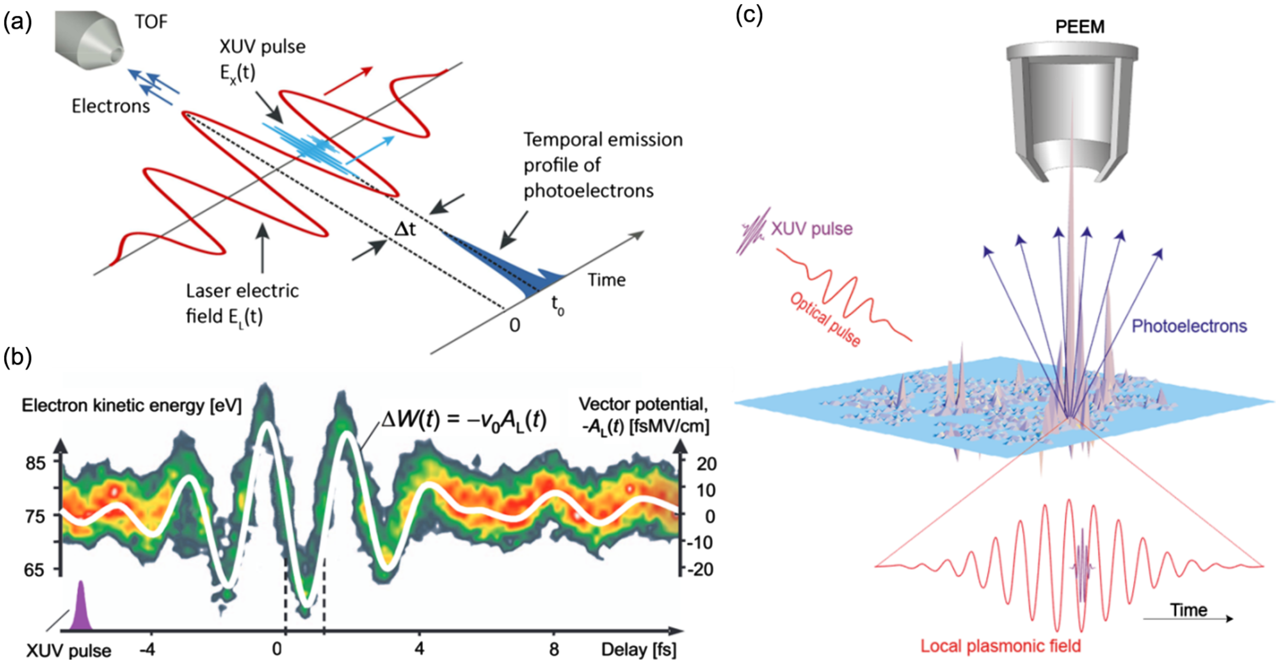

FIG. 27. Attosecond streaking. (a) Concept of an attosecond streaking experiment during which an attosecond XUV pulse interacts with atoms from a gas flow in the presence of a few-cycle laser pulse. The released photoelectrons suffer a change of their initial velocities that is proportional to the vector potential of the field at the instant of release. From Grguraš, 2015. (b) The streaking spectrogram represents a series of kinetic energy spectra of electrons, emitted via attosecond XUV pulses and accelerated via a NIR-streaking field as a function of XUV-NIR delay. The trace represents the vector potential and enables the reconstruction of the streaking field waveform. From Krausz and Ivanov, 2009. (c) Proposed combination of attosecond streaking with photoelectron-microscopy "atto-PEEM" to spatially and temporally resolve local plasmonic fields. From Stockman *et al.*, 2007.

Attosecond streaking spectroscopy at nanostructures was proposed in a combination of all-optical streaking and PEEM (Stockman *et al.*, 2007), a scheme that was implemented by several groups (Mikkelsen *et al.*, 2009; Chew *et al.*, 2012; Hommelhoff and Kling, 2015). In parallel, attosecond streaking has been theoretically investigated and applied to nanoparticle ensembles in the gas phase and isolated individual nanostructures; see Fig. 27(c) and Skopalová *et al.* (2011), Süßmann and Kling (2011), Zherebtsov *et al.* (2011), Borisov, Echenique, and Kazansky (2012), Kelkensberg, Koenderink, and Vrakking (2012), Förg *et al.* (2016), Li, Saydanzad, and Thumm (2017), and Seiffert *et al.* (2017). For spatially localized optical near fields, different regimes of streaking have to be considered.

If the streaking field pulse duration t_p is much shorter than the time it takes the electron to leave the near field t_0 ($t_p \ll t_0$, ponderomotive regime), the electron does not experience the spatial variation of the near field. This corresponds to the conventional streaking in gas targets. In the instantaneous limit ($t_0 \gg T$), the electron leaves the localized field within a fraction of the optical cycle T. This corresponds to quasielectrostatic acceleration, and the streaking field can be described by an electrostatic scalar potential. In contrast to conventional, ponderomotive streaking, the electron streaking curve in the instantaneous regime follows the electric-field evolution. Finally, in the intermediate regime the electron traverses the field within several optical oscillations $t_0 \approx T$, and the streaking trace shows a phase shift, which lies in-between the other two limits. Since the retrieval of the near field in this case requires extensive modeling, the other two regimes are more desirable; see Ciappina *et al.* (2017) and the references therein.

Experimental implementation of attosecond near-field streaking is hindered by several factors. As a linear process, XUV photoemission results in high-energy electrons being emitted from the entire illuminated area that is typically much larger than the nanoscale region of interest. Consequently, the detection scheme averages on the micron scale, making it challenging to characterize near fields since electrons emitted from different regions are streaked by different local fields (Förg *et al.*, 2016).

In the corresponding experiments, collinearly propagating 4.5-fs laser pulses at 720 nm central wavelength (NIR pulse) and isolated 220 as XUV pulses at 95 eV central energy were used to perform streaking measurements on a gold tip (Förg *et al.*, 2016). The XUV probed the near fields of the nanotaper induced by the NIR pulse, the polarization of which was aligned parallel with the nanotaper axis. A gas-phase streaking measurement provided the phase of the incident NIR pulse as a reference. The nanotaper streaking trace is shifted with respect to the gas-phase streaking measurement by 250 ± 50 as in Figs. 28(a) and 28(b). The shift is attributed to the surface electric fields acting on the released electrons, which is related to the collective free-electron polarization response of the gold nanowire. The electric near field retrieved from streaking measurements is shown in Fig. 28(c).

In contrast to single-photon-induced photoemission provided by XUV illumination, the combination of all-optical

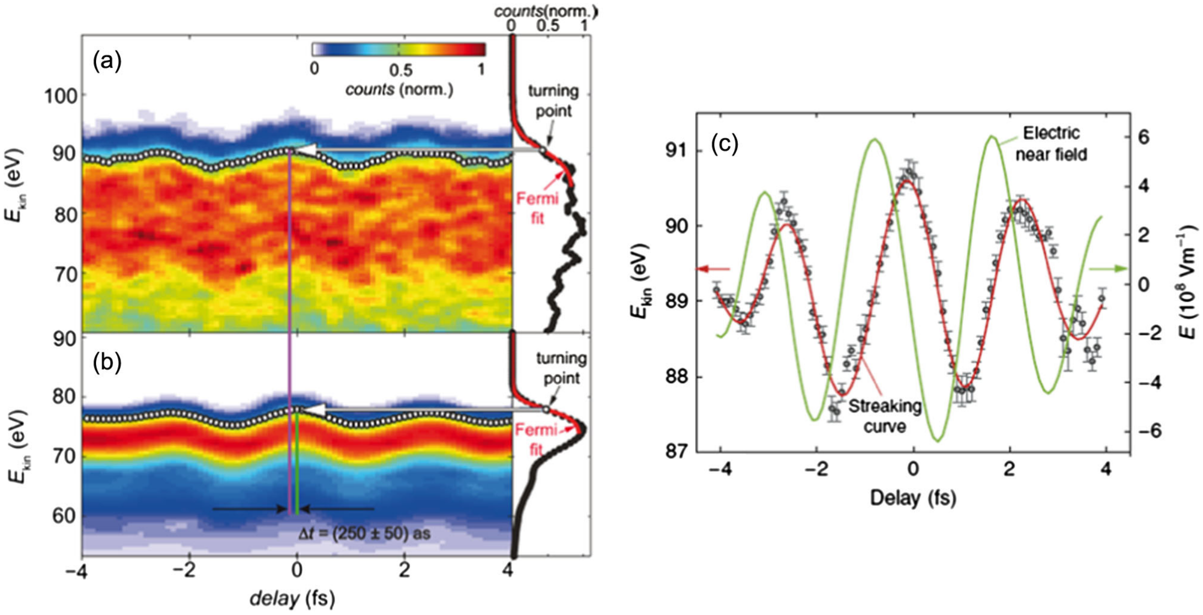

FIG. 28. Streaking measurement from a nanotaper sample. (a) The energy shift of the streaking trace versus the time delay between the XUV and NIR pulses, shown by the white data points, was extracted by fitting a Fermi function (red) to the cutoff. (b) Reference streaking measurement in neon gas. The neon streaking trace is shifted in time by 250 ± 50 as relative to the nanotaper trace. (c) Reconstruction of the local electric near field (green line) and vector potential (red line overlapping with the symbols) at the nanotaper surface from the measured streaking curve (symbols). The error bars indicate 95% confidence intervals of the Fermi fit. From Först *et al.*, 2016.

near-field streaking with *nonlinear photoemission* exploits the intrinsic nanolocalization of the emission process. Nonlinear electron emission confines the signal to sharp features and plasmonic hot spots of nanoresonators, antennas, or nanotip apices. Out-of-plane extensions from bulk substrates, which may dominate in linear vacuum-ultraviolet-emission or XUV-emission streaking experiments, can be effectively suppressed. Based on far-field electron detection and spectroscopy, the spatial selectivity is intrinsically connected to the emission process and the structure of the sample.

Such nonlinear, terahertz near-field streaking is sketched in Fig. 29(a). It is based on multiphoton emission via near-infrared femtosecond pulses and on streaking via collinearly focused single-cycle pulses at 1 THz. The accessible timescales range from a few femtoseconds to hundreds of femtoseconds. Photoelectrons are extracted and spectrally resolved using time-of-flight or retarding field electron spectrometers. In contrast to optical streaking in far-field foci, which imprints the time-integrated vector potential onto the electron kinetic energy, here electrons are accelerated and driven out of the field in a fraction of the optical cycle. This subcycle acceleration process allows us to map the momentary electric near field at the instant τ, $E(\tau)$, and to control electron trajectories on ultrafast timescales. In the subcycle limit, the final kinetic energy Q after escape from the near field of decay length l_F is given by $Q(t) \propto -eE(t)l_F$.

In the following list, we present some recent applications of phase-resolved near-field streaking.

(i) Mapping of near-field waveforms. The high localization and enhancement of incident terahertz fields at the apex of metallic nanotips is utilized in SNOM, ultrafast scanning tunneling microscopy (STM) and

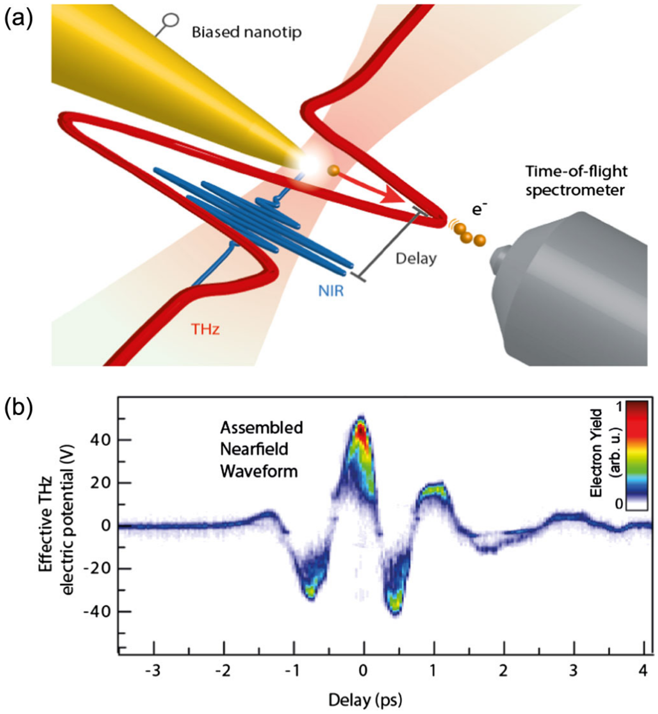

FIG. 29. Terahertz-near-field streaking at nanotips. (a) Realization of terahertz-near-field streaking measurement at nanotips via nonlinear photoemission with near-infrared pulses. (b) The local terahertz-near-field waveform at the apex of a gold nanotip is obtained from streaking spectrograms encoding electron kinetic energies as a function of streaking delay. From Wimmer *et al.*, 2014.

teraherz-driven electron sources (Chen, Kersting, and Cheon Cho, 2003; Cocker *et al.*, 2013; Herink, Wimmer, and Ropers, 2014; Li and Jones, 2016). In a teraherz-streaking implementation, nonlinear photoemission via NIR pulses generates electrons locally at the apex that are accelerated in a temporally delayed near field of a single-cycle terahertz pulse. The energy spectra as a function of delay between NIR and terahertz form streaking spectrograms, which are recorded for opposite absolute terahertz phases. Figure 29(b) displays the local waveform at the apex retrieved from both spectrograms. Compared to the far-field waveform detected via electro-optic sampling at the same position without nanotip, the near-field streaking reveals a phase delay, reshaping and ringing in the near-field waveform. The comparison to the incident far field yields the terhertz response function of the tip and allows us to estimate the local field enhancement.

A spatially resolved mapping of local terahertz waveforms at microstructures was proposed and demonstrated using near-field streaking of ultrashort electron pulses in a projection imaging mode (Fabiańska, Kassier, and Feurer, 2014; Ryabov and Baum, 2016; Zhang *et al.*, 2018; Zhao *et al.*, 2018). Such schemes are realized with remotely generated electron pulses from femtosecond-driven photocathodes, as sketched in Fig. 30(a), and are demonstrated to resolve the teraherz-electric-field evolution at microstructures as shown in Figs. 30(b) and 30(c). The implementation of electron microscopy using high-coherence point sources is expected to provide nanometric resolution (Feist *et al.*, 2017). Besides time-resolved imaging of near fields, the phase-sensitive interaction of ultrashort electron pulses with terahertz near fields allows for the ultrafast control of electron trajectories, i.e., the temporal, angular, and spectral compression (Greig and Elezzabi, 2014; Wimmer *et al.*, 2014; Gliserin *et al.*, 2015; Kealhofer *et al.*, 2016; Wimmer, Karnbach *et al.*, 2017; Ehberger, Kealhofer, and Baum, 2018), with applications in ultrafast electron microscopy and diffraction. The compression of electron bunches and their subsequent streaking was demonstrated in a segmented tereahertz acceleration and manipulation structure, allowing for compact high-field electron bunch manipulation shown in Figs. 30(d) and 30(e).

(ii) Resolving nanoscopic carrier dynamics. Nanoscale materials display intriguing effects with properties significantly different from the bulk. Optical pump-probe schemes resolve ultrafast dynamics, i.e., electronic and vibrational relaxation, via changes in the linear and nonlinear optical properties and reach single nanoparticle sensitivity; see Voisin *et al.* (2001) and Obermeier, Schumacher, and Lippitz (2018) and references therein. A direct access to transient carrier populations is provided via time-resolved two-photon photoemission spectroscopy; see Petek and Ogawa (1997) and references therein. Exploiting instantaneous nonlinear electron emission, the intrinsic localization of near fields can be utilized to confine the emission to the nanoscale region of interest. Applied to the study of carrier relaxation of metallic nanotips, terahertz-induced field emission can be employed to resolve excited electron dynamics exclusively from a nanotip apex. In a study with intense NIR excitation of a tungsten nanotip, a sufficiently high peak terhertz near field liberates hot electrons (excited by the preceding NIR pulse) from the apex which are subsequently accelerated in the enhanced near field (Herink, Wimmer, and Ropers, 2014). The transient terahertz-induced hot electron emission appears to be an additional feature in the streaking spectrograms [see the marked horizontal decay at high electron energies in Fig. 31(b)] and reveals a reduced carrier relaxation time compared to bulk substrates that is related to the nanoscale hot carrier confinement. Future studies with increased temporal and energetic resolution are expected to disentangle the transient nonthermal excitation and the impact of nanolocalization onto carrier thermalization and strong-field effects in different metallic and nonmetallic material systems (Della Valle *et al.*, 2012; Kealhofer *et al.*, 2012; Yanagisawa *et al.*, 2016).

(iii) Clocking surface plasmon propagation and nanofocusing. As discussed in Sec. II.A.3.c, the transformation of propagating SPPs on nanotapers and their nanofocusing into localized surface plasmons at the apex of a nanotip allow for the spatial decoupling of the excitation far field and apex near field for various nanoscopy schemes (Neacsu *et al.*, 2010; Schröder *et al.*, 2015; Vogelsang *et al.*, 2015; Müller *et al.*, 2016), eliminating the far-field scattering background, reducing the thermal load of the nanotip, and enabling exclusively local sample excitation. Incorporating plasmonic propagation into time-resolved instruments necessitates a precise characterization of the plasmon propagation delay and the duration of the confined plasmon (Spektor *et al.*, 2017; Kahl *et al.*, 2018).

Near-field streaking has been demonstrated to enable the clocking of plasmon propagation to a nanotip apex after launching SPPs at a 50-μm distant grating coupler, sketched in Fig. 31(c) (Wimmer, Schröder *et al.*, 2017). Upon nanofocusing, the plasmon-induced nonlinear photoemission is streaked via the terahertz near field. The temporal shift of the spectrogram is compared to the streaking from direct apex excitation [zero delay in the spectrogram, Fig. 31(c)]. The extracted time delay and spectral width encode propagation time and plasmon duration. The results agree with nanofocusing simulations accounting for the actual microscopic evolution of the taper diameter along the structure, and they reveal significant plasmon slowing only in close proximity to

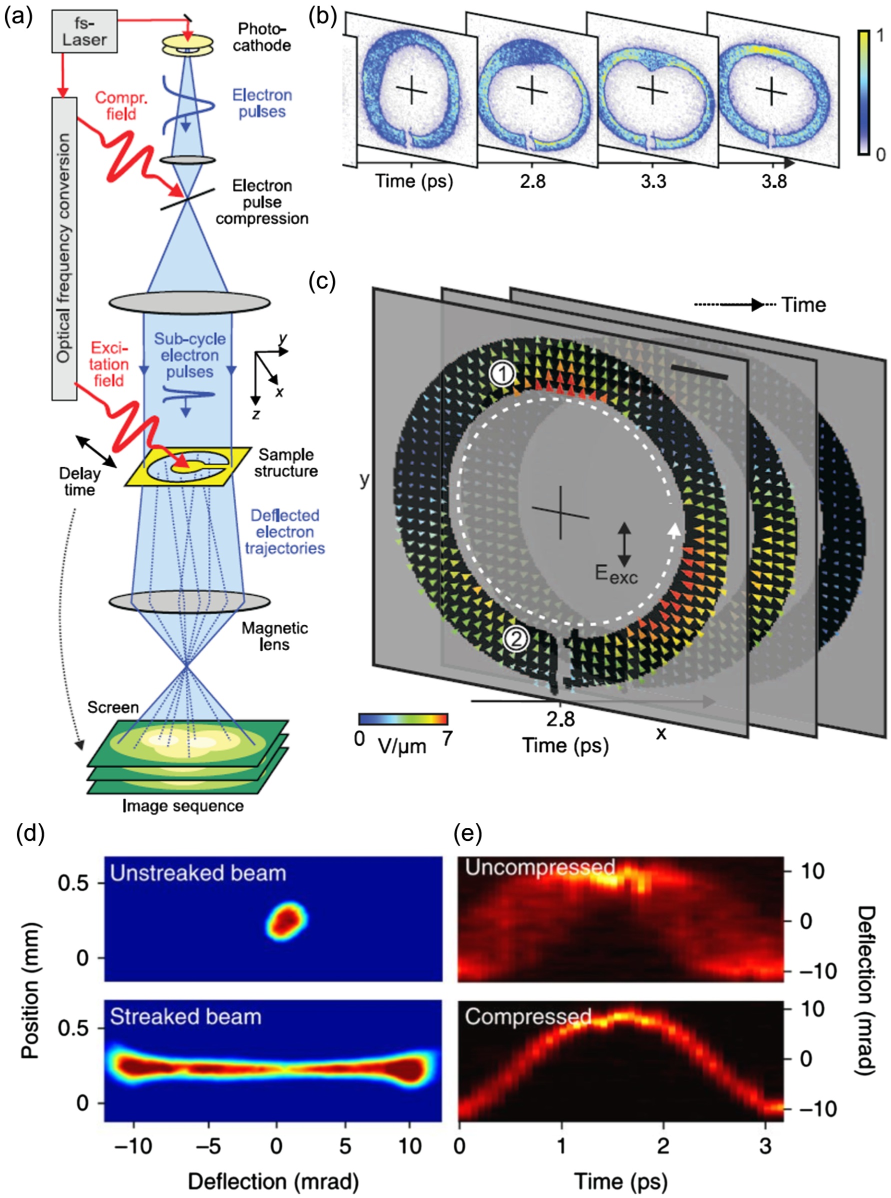

FIG. 30. Near-field imaging with electron microscopy (a) Implementation of near-field imaging via electron microscopy with femtosecond-electron pulses. (b) Sequence of raw images for different terahertz-electron delays. (c) Extracted electric-field vectors at three different delays, scale bar 100 μm. (a)–(c) Adapted from Ryabov and Baum, 2016. (d) Imaged electron beam with and without terahertz-streaking field. (e) Deflection diagrams for different delays, recorded with an uncompressed and terahertz-compressed electron bunch. (d),(e) From Zhang *et al.*, 2018.

the apex. Such plasmon clocking can be applied to various nanotaper geometries and material systems, and the results can directly validate and benchmark plasmon propagation and nanofocusing models in the time domain.

B. Strong-field-driven currents and switching on the nanoscale

The switching and control of currents on ultrafast timescales and on nanometer length scales is a recently emerging application of strong-field phenomena that is triggering hopes to have an impact on future information technology as an enabling technology toward petahertz electronics. Present-day technology relies on the nonlinearity of semiconductors driven by radio-frequency electric fields, with field-effect transistors (FETs) reaching cutoff frequencies in the range of 100 GHz to 1 THz (Schwierz and Liou, 2007; Kim and del Alamo, 2010; Mei *et al.*, 2015). Most devices, however, operate at clock rates of only a few gigahertz. The transport and processing of information in integrated circuits are limited by the time it takes to switch on and off electric currents, i.e., the charging time of the interconnect wires, and ultimately also by the heat deposited in high-speed and densely packed devices (Krausz and Stockman, 2014; Waldrop, 2016). The speed at which electrons can be manipulated by electronic switches is reaching limits that are defined by the finite rest mass of the electron as an information carrier.

Light-wave-driven electronics has been introduced as a potential candidate to advance information technology past

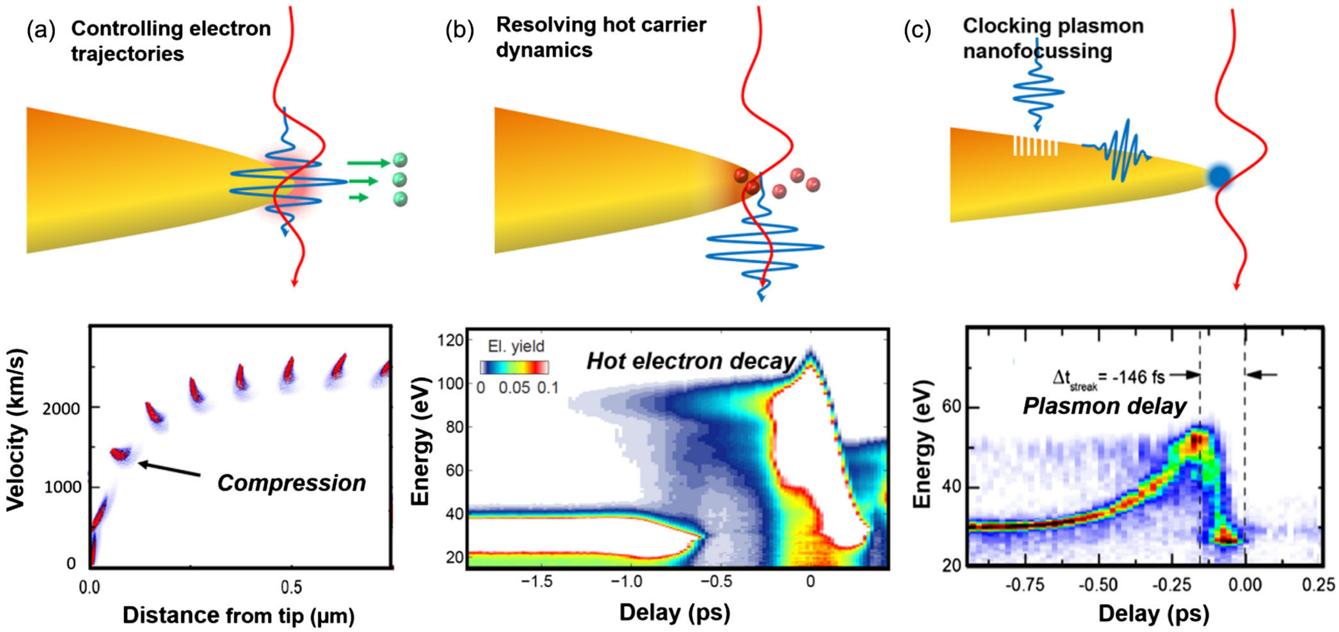

FIG. 31. (a) (Top panel) Nonlinear photoemission into a terahertz near field enables the control of propagation, time structure, and energy of ultrashort electron pulses. (Bottom panel) Simulated energy compression after short propagation of a NIR-emitted electron ensemble via emission into a distinct phase of the terahertz near field, visualized for an equi-temporal set of snapshots. At the desired distance from the tip, the electron pulse reaches minimal velocity spread. Adapted from Wimmer, Karnbach *et al.*, 2017. (b) (Top panel) Intense near-infrared pulses excite carriers in a nanotip. Time-delayed terahertz fields liberate hot electrons via field emission. (Bottom panel) In the streaking spectrograms, hot electron emission appears as the additional feature at 95 eV, tracing the electron relaxation (marked). Adapted from Herink, Wimmer, and Ropers, 2014. (c) (Top panel) Schematic of SPP clocking via terahertz nanostreaking. Propagating surface plasmon polaritons (SPPs) are excited at a grating coupler and emit electrons upon arrival at the apex. The propagation delay is clocked via the instant of emission and streaking by the terahertz near field. (Bottom panel) Experimental streaking spectrogram for grating excitation and terahertz acceleration from the apex. The time delay from $\tau = 0$ encodes the SPP propagation time. From Wimmer, Schröder *et al.*, 2017.

that limit, offering, at least in principle, a bandwidth in the petahertz regime (Miller, 2009; Caulfield and Dolev, 2010; Krausz and Stockman, 2014). Specifically, the switching and driving of coherent, light-induced currents by strong optical fields, i.e., the important optics-to-electronics interface, can benefit from strong-field effects. High electric-field strengths around nanoplasmonic devices tailored to optimize the efficiency of light-matter coupling can help reduce the number of photons that are needed to achieve switching, and thus minimize dissipation.

1. Ultrafast switching in semiconductors and dielectrics

When a semiconductor material is optically excited with strong, ultrafast laser fields with the photon energy well below the band gap, the amplitude can be sufficiently strong to periodically modulate the band structure of the material at the period of the driving field. This band bending can induce electron tunneling from the valence band (VB) to the conduction band (CB) and back, which results in a transient, coherent current in the semiconductor. This current is oscillating at the period of the driving laser and is phase locked to the optical pulse. Mobile charge carriers persist only based on the presence of CB-VB coherence and hence decay with the dephasing time of the interband polarization of the order of a few tens of femtoseconds. This is in stark contrast to photocurrents induced by single-photon or multiphoton excitation of carriers from the VB to the CB at lower field strengths. In the latter case, the charge carriers decay due to electron-hole recombination, limiting switching times to a few picoseconds down to hundreds of femtoseconds.

In the case of strong-field-driven bulk semiconductors, the switching speed is ultimately limited by the band-gap energy of the material. Wide-band-gap semiconductors with band-gap energies in the range of 5–10 eV and, even more so, insulators should enable switching with response times of the order of ~100 as. This possibility has already been verified in proof-of-principle experiments (Gertsvolf *et al.*, 2010; Ghimire *et al.*, 2011; Mitrofanov *et al.*, 2011; Schlaepfer *et al.*, 2018), holding the promise for petahertz electronic signal processing. XUV time-resolved spectroscopy of semiconductors after excitation with NIR pump pulses have shown modulations of the absorbance near the band edge with a periodicity of 860 as in gallium nitride (GaN) (Mashiko *et al.*, 2016), and of 450 as in silicon (Schultze *et al.*, 2014). Both measurements demonstrate a response of the semiconductor electron dynamics above the petahertz barrier. In practice, the large number of photons that is necessary to drive such a transition prohibits practical applications with present-day technology.

In a pioneering study, Paasch-Colberg *et al.* (2016) investigated laser-induced currents in bulk GaN, a semiconductor with a band-gap energy of ~3.4 eV, where they verified that the electric field generates charge carriers as well as driving them in one direction. Charge injection and current driving took place within ∼2 fs (Paasch-Colberg *et al.*, 2016).

Driving large-band-gap materials, i.e. dielectrics, nonresonantly with a strong electric field potentially offers even faster response times. In fused silica, the large 9-eV band gap is in practice further enhanced by a conduction band width of 10 eV. For sufficiently large electric-field strengths, electrons are expected to cross the potential barrier into the entire conduction band by Zener-type transitions (Zener, 1934), which should enable switching well into the petahertz regime. Experiments performed at high field strengths of ∼15 V/nm incident on the silica demonstrated considerable current flows, which could be controlled via the CEP of the driving laser field (Schiffrin *et al.*, 2013; Schultze *et al.*, 2013). Closer investigation allows us to identify carrier injection in the insulator material by the instantaneous field, taking place on timescales of ∼1 fs, as the source for the observed current. The optical-field-induced changes are completely reversible, and the current ceases with the applied field [verified with time-resolved absorption and reflection measurements by Schultze *et al.* (2013)]. At the maximum applicable field strength, an increase in conductivity of 18 orders of magnitude is reached, up to the typical conductivity of a semimetal. Later experiments performed on quartz, sapphire, and calcium fluoride with band gaps of 9.0, 8.8, and 12.2 eV, respectively, also showed field-induced currents at high field strengths with similar behavior (Kwon and Kim, 2016; Kwon *et al.*, 2016). The exact physical mechanisms underlying those observations are currently being intensely discussed. Similar ultrafast switching timescales were predicted by simulations of dielectrics under strong optical fields when taking into account Zener-like band-to-band tunneling and metallization induced by Stark shifts (Durach *et al.*, 2010, 2011; Apalkov and Stockman, 2012). Furthermore, quantum interference due to resonant five-photon versus six-photon absorption (Kruchinin, Korbman, and Yakovlev, 2013) and the excitation of virtual carriers (Khurgin, 2016) have been considered, and it was suggested that the metal-semiconductor interfaces of the nanojunction play an important role in the emergence of a CEP-dependent net current through Stark-shift-induced level alignment (Franco, Shapiro, and Brumer, 2007; Chen *et al.*, 2018).

2. Tunneling currents and photoemission from metals

A second, prototypical geometry for the creation of light-driven currents is the gap between a sharp, highly conductive metal tip and an adjacent sample. With gap distances of a few tenths of a nanometer, this forms a metal-insulator-metal (M-I-M) point contact. The tunneling current depends on the applied voltage and on the gap distance with high nonlinearity, which arises from electrons tunneling through the insulator potential barrier, whose height is modulated by the applied voltage. In STM, this is used to keep the tip-sample distance constant while scanning. This nonlinearity can also be used to convert an oscillating optical field to a dc current, and it can thereby represent a link between electronic and photonic networks. Controlling a current across the potential barrier requires an asymmetry of the tunneling process, which was in the first experiments provided via an applied bias voltage, closely linked to the development of ultrafast STM. Illumination with few-cycle laser pulses with full electric-field control enables us to drive a current in alternate directions, while the design of asymmetric nanostructures reduces this flexibility but may offer a path toward chip-scale solutions. We now review these approaches to the control of ultrafast currents in nanoplasmonic antennas.

Optical-to-electric conversion based on rectification of multicycle oscillating fields was proposed in 1987, originally to measure the tunneling time (Cutler *et al.*, 1987). It has been realized for the rectification of microwave fields coupled to the tip with a microwave strip (Tu, Lee, and Ho, 2006), and also for optical fields directly focused onto the tip-sample region (Nguyen *et al.*, 1989; Völcker, Krieger, and Walther, 1991; Ward *et al.*, 2010). The magnitude and especially the sign of the photoinduced current are then determined by the curvature of the I-V characteristic. This implies that the current direction is determined by the applied bias voltage V_{dc}, which was demonstrated experimentally by measuring the rectified current induced when laser light is focused onto the STM tip (Nguyen *et al.*, 1989; Völcker, Krieger, and Walther, 1991).

A first version of an ultrafast STM was implemented by Weiss *et al.* (1993), who achieved a time resolution of 2 ps. In this experiment, the tunnel current was gated with a photoconductive switch that was integrated into the tip assembly, a technique that was later called photoconductivity gated STM. This gating limits the achievable time resolution to the order of 1 ps (Donati, Rodriguez, and Taylor, 2000), and furthermore the signal arises from a capacitive coupling of tip and sample involving a μm^2-sized sample area (Groeneveld and van Kempen, 1996). A much improved combined spatial and temporal resolution is achieved when utilizing the intrinsic nonlinearity of the I-V characteristic in response to illumination with short laser pulses in junction mixing STM, down to ∼1 nm and tens of picoseconds (Steeves, Elezzabi, and Freeman, 1998; Khusnatdinov, Nagle, and Nunes, 2000).

It has been proven important in such experiments to carefully distinguish a current change due to optical rectification from other changes, caused by thermal expansion of the tip, thermal voltage due to a temperature gradient, surface photovoltaic effects, a rearrangement of the tip material, or even permanent, photoinduced damage (Ward *et al.*, 2010). Specifically, pulsed-laser excitation of the tip causes considerable thermal expansion of the tip that results in a strong change of the tunneling current, due to its exponential dependence on the tunneling gap (Lyubinetsky *et al.*, 1997; Grafström *et al.*, 1998; Gerstner *et al.*, 2000). Focusing a pair of 40-fs pulses on the STM tip, Gerstner *et al.* (2000) saw a 1-nm peak-to-peak variation that closely followed the interference fringes of the two pulses. The interference can be avoided by using two-color, two-photon excitation in combination with a sinusoidal modulation of the pulse delay and lock-in detection [termed the shaken-pulse-pair-excited method; see Takeuchi *et al.* (2004)]. This way, Dolocan *et al.* (2011) entered the regime of subpicosecond STM and demonstrated a photoinduced tunnel current with a duration of 220 fs.

Generally, the duration of the rectified current in such optically driven M-I-M diodes is given by the envelope of a multicycle laser pulse. When the laser pulses become shorter and enter the few-cycle regime, the role of the pulse envelope decreases, and the instantaneous amplitude of the electric field becomes more important as the driving force for electron motion across the tunnel junction. This can be seen in the work by Rybka *et al.* (2016), who fabricated a highly symmetric nanostructure with an 8-nm-wide gap in a contacted bow-tie antenna; see Fig. 32(a). The gap represents a tunnel junction, where the current follows a Fowler-Nordheim curve for both positive and negative stationary bias. In the absence of an applied bias voltage, one may therefore expect a net zero current when illuminating the junction with sufficiently long multicycle laser pulses. Instead, Rybka and colleagues illuminated the gap with a few-cycle NIR laser pulse, with spectral components between 1.0 and 1.8 μm and with a controlled CEP; see Fig. 32(b). They showed that a pulse with a sine-shaped temporal electric field does not generate a net current, whereas such a current does exist for a pulse with cosine-shaped electric field, as shown in Fig. 32(c). The resulting net current, with an amplitude of about $1/50$ of an electron per pulse, is periodically oscillating as a function of CEP phase. Note that, due to the spatial homogeneity of the electric field across the gap, the quiver motion of the electrons in the oscillating driving field has a non-negligible impact and leads to a phase shift of the current with respect to the CEP (Aguirregabiria *et al.*, 2019; Ludwig *et al.*, 2020). During the pulse, electrons are accelerated by the optical near field at the apices of the bow-tie antenna from one arm to the other. Because of the highly nonlinear dependence of the tunneling current on the applied field strength, contributions from the center three half cycles are dominant by far. The symmetry break required for directed electron transport is achieved here via the shape of the applied laser field.

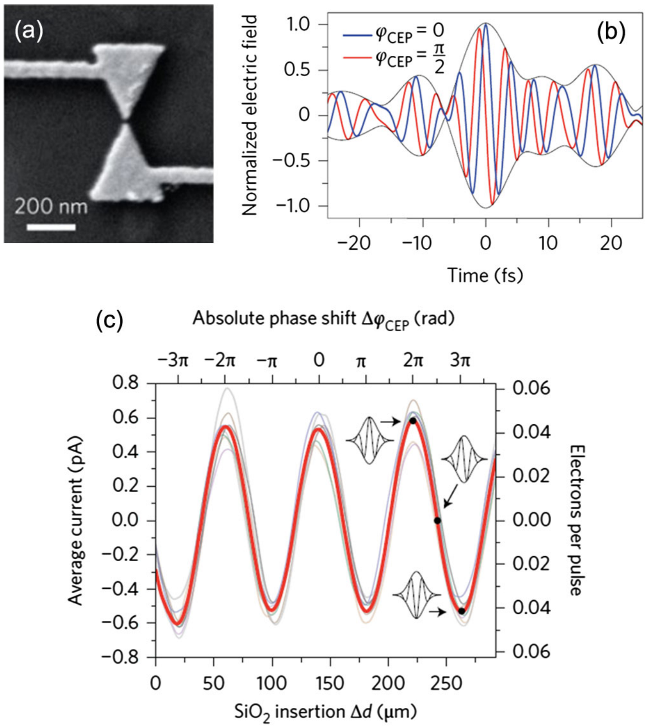

FIG. 32. Field-driven current across a symmetric tunnel junction. (a) Scanning electron microscopy image of the contacted, symmetric bow-tie antenna with an 8-nm-wide gap. (b) Reconstructed electric field of the applied few-cycle laser pulse with the carrier-envelope phase (CEP) set to 0 (blue curve having maximal amplitude at 0 fs) and $\pi/2$ (red curve) by inserting dispersive material in the beam path. (c) Total current over the bow-tie antenna as a function of the CEP variation. Shown are eight individual measurements (thin gray curves) and their average (thick red curve). The black symbols indicate the fundamental symmetry of the electric fields of the applied NIR laser pulses. From Rybka *et al.*, 2016.

In principle, the directionality of the tunnel current can be improved by using more asymmetric laser fields, such as a laser field superimposed with its second harmonic (Schafer and Kulander, 1992), or by further shortening the pulses. In the latter case, the corresponding higher field strength leads to a significantly exponentially increased tunneling probability and an increased impact of the CEP. In recent years, such few-cycle and even single-cycle fields with high field strengths have been generated in the spectral range between roughly 0.1 and 10 THz (Hirori *et al.*, 2011; Kampfrath, Tanaka, and Nelson, 2013). Because of their low photon energy, terahertz fields can enable driving electron tunneling in nanostructures with strongly reduced heating. Yoshioka *et al.* (2016) demonstrated that the intense terahertz field applied to the tunnel junction of a STM can induce electron tunneling either from the tip to the sample or vice versa, depending on the CEP. Terahertz pulses were coupled to a STM tip by Cocker *et al.* (2013) to modulate the tip bias and to enable an ultrafast STM measurement. They observed the carrier capture in single InAs nanodots with a subpicosecond temporal and 2-nm spatial resolution, and in later work they improved terahertz-driven STM even to submolecular resolution (Cocker *et al.*, 2016).

The possibility of STM imaging on the submolecular level implies that the tunneling current must pass through a single molecule or even an atom. Jelic *et al.* (2017) compared images acquired with stationary STM and with terahertz STM, both providing atomic resolution. The images look nearly identical, even though the peak current reached during the maximum of the transient terahertz field is 8×10^6 times greater than the current used for the stationary STM image. These high transient currents become possible due to the terahertz-induced nonequilibrium charging of surface states, and for extremely large negative peak fields band bending accelerates conduction band electrons toward the tunnel junction, where these hot electrons also contribute to the tunneling current.

Finally, the symmetry of the tunneling process can be broken via the geometrical shape of the nanostructure. Sharply etched metal nanotapers similar to those introduced earlier in this review (see, e.g., Sec. II.A.3) may serve as an extreme example. Upon illumination with ultrashort laser pulses, electrons are easily emitted from the enhanced field localized at the apex. Such sharp nanotips with concurrent large field enhancement are a natural choice for a light-driven electron emitter and current source in nanoplasmonic circuitry, while a less strongly curved surface could function as an electron collector. In fact, such a sharp, light-driven metal tip may already be considered a nanostructure-based realization of a classical electronic device: the vacuum-tube diode. Electrons released from a nanotip cathode can be further steered, accelerated or decelerated, and blocked on their path to the anode using electrodes set on deliberate potentials. Here, as in the macroscopic diode, the operation speed of the device is limited by two factors: first by the duration of the laser pulse that initiates photoemission, and second by the propagation time of the electrons from the cathode to the anode. Aspiring a device switching time in the terahertz range or faster thus dictates, besides the use of ultrashort laser pulses to trigger electron emission, that the propagation distance for the photoelectrons within the device should be kept shorter than a micrometer (Higuchi *et al.*, 2015).

Higuchi *et al.* (2015) realized a proof-of-principle nanometric vacuum-tube diode by aligning two tungsten nanotapers along one axis, with a tip-to-tip distance ranging down to 350 nm; see Fig. 33. They chose two tips with different apex radii and showed that, upon illuminating both tips in the focus of ultrashort laser pulses, electrons predominantly traveled from the sharper tip to the blunter one within an estimated 800 fs, while the current in the opposite direction was suppressed by 2 orders of magnitude (Higuchi *et al.*, 2015). As a step toward employing the tip-based diode concept in nanocircuitry, one wants to avoid the free-space positioning of the two opposing tips and, at the same time, reduce the electron transit time. Furthermore, approaches based on a single tip limit the current to typically <1 electron per pulse, i.e., to the femtoampere to picoampere range. In future work, it will therefore be important to develop methods that can scale up the electron emission up, e.g., by using arrays of electron emitters, and that radically increase the photoemission yield to overcome excessive heating problems in these important building blocks of future light-driven nanoplasmonic circuitry.

The first chip-scale solution by Putnam *et al.* (2017) used an array of either nanotriangles or nanorods acting as emitters, separated by a several μm-wide gap from an unstructured electrode acting as collector. Applying a 30-V bias voltage to ensure that the electrons reach the collector resulted in a photocurrent of the order of 100 nA. Recently a different integrated approach to the vacuum-tube diode was realized, where the involved alignment procedure was replaced by an etching process. Rows of pointed electron emitters were fabricated that oppose flat metal surfaces at a distance of ~100 nm (Karnetzky *et al.*, 2018). Several of these alternating rows of tips (cathodes) and flat surfaces (anodes) then covered an area which could be illuminated by a laser focus spot; see Figs. 34(a) and 34(b). Upon illumination with a few-femtosecond laser pulse, bursts of hot electrons are released from the emitters and collected by the flat metal surfaces, creating an intrinsically unidirectional current across the nanodevice. A similar device fabricated by *e*-beam lithography was recently reported by Zimmermann *et al.* (2019). A total of

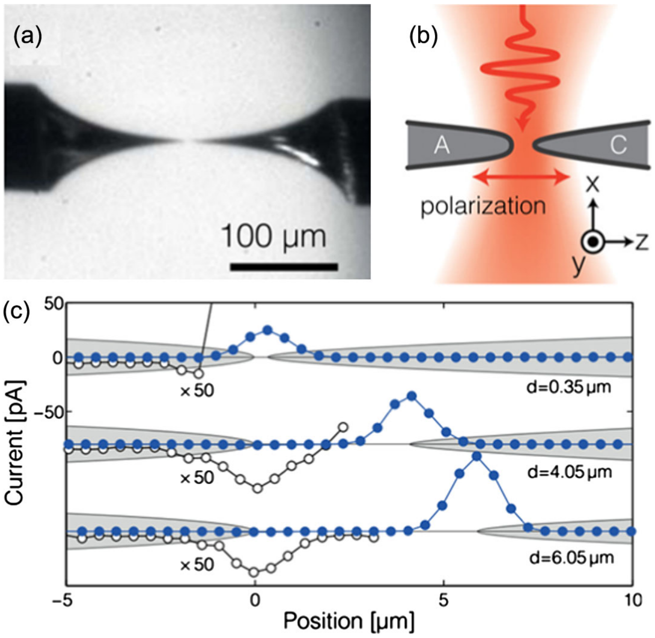

FIG. 33. Nanoplasmonic vacuum-tube diode. (a) Optical microscopic image of the two metal nanotips facing each other. (b) Schematic of the two tips in the focus of a few-cycle laser pulse. The sharper tip functions as the cathode and the blunter as the anode, labeled *C* and *A*, respectively. (c) Laser-induced current between the two tips as a function of the laser focus position for three different tip-tip distances. The curves are offset for clarity. Positive current means the electrons travel from cathode to anode. Negative currents are measured when the blunter tip is illuminated and are shown here magnified by a factor of 50. From Higuchi *et al.*, 2015.

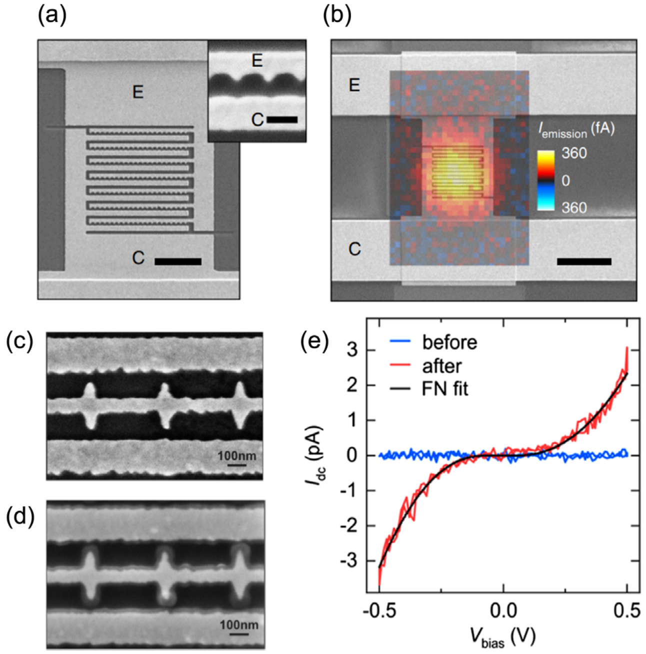

FIG. 34. Chip-scale realizations of plasmonic switches. (a) SEM image of asymmetric nanojunctions with pointed emitters (*E*) opposing flat collectors (*C*). Scale bar, 2 μm. (Inset) Close-up of thee emitter-collector region. Scale bar, 200 nm. (b) The unipolar photocurrent measured as a laser focus is raster scanned across the chip, color coded and overlaid on the SEM. Scale bar, 5 μm. (a),(b) From Karnetzky *et al.*, 2018. SEM image of asymmetric nanojunctions with diamond-shaped emitters (c) before and (d) after laser illumination, showing the structural change and decrease of the gap. (e) Current measured before (blue curve fluctuating around zero) and after (red curve) illumination, as a function of a stationary bias. The red curve can be well fitted with a Fowler-Nordheim curve (black). (c)–(e) From Zimmermann *et al.*, 2019.

42 connected nanodiamonds opposed a flat anode at a distance of ~50 nm, and upon laser illumination without any bias applied a unidirectional photocurrent was measured. Zimmermann *et al.* observed a structural change of the nanodiamonds during laser illumination, most prominently a narrowing of the gap from 50 nm down to ~10 nm; see Figs. 34(c) and 34(d). This results in a transition from multiphoton emission to electrons tunneling across the gap, as can be seen in Fig. 34(e), where the current measured as a function of a stationary bias voltage resembles a Fowler-Nordheim curve.

In the previous examples, the geometry with designated cathodes possessing sharply etched apices opposed to blunter or even flat anodes dictates the directivity of the induced current. Such a combination of antenna and tunnel junction, which is also called a rectifying antenna or *rectenna*, is a highly nonlinear device that has potential applications not only in the generation of directional currents for light-driven electronics but also, e.g., for interconnecting optical and terahertz circuitry (Karnetzky *et al.*, 2018), and potentially as ultra-broad-bandwidth light-to-current converters in solar energy harvesting (Miskovsky *et al.*, 2012). The speed of a rectenna depends on the duration of the driving pulse as well as the gap size. In the limit case in which an electron can cross the gap in a time shorter than the optical half cycle, the electron essentially experiences a static field and can tunnel across the gap before the field reverses. In the opposite limit of a much longer transit time, the electron motion is determined by the field around the nanotip after photoemission. In a rapidly oscillating field, electrons are accelerated back and forth, such that they basically see the static barrier between cathode and anode, which they cross in a slow quiver motion. For longer oscillation periods and stronger localized fields (adiabaticity parameter $\delta < 1$), they experience a strongly directed forward acceleration (Herink *et al.*, 2012; Piglosiewicz *et al.*, 2014). Hence, a decoupling of photoemission and tunneling across the gap enables full control of the electron motion. It may be achieved, for example, by applying a well-controlled terahertz field; see Wimmer *et al.* (2014), Förg *et al.* (2016), and Sec. III.A.3.

In conclusion, both photoemission from metals and charge carrier excitation in semiconductors and dielectrics have the potential for ultrafast, light-induced switching on a timescale of ~1 fs, or even faster. As shown in recent experiments, the emission of photoelectrons from a metal surface or nanostructure is an ultrafast process restricted to negative half cycles of the applied laser field (Ossiander *et al.*, 2018). This results in an extraordinarily pronounced dependence of such currents on the carrier-envelope phase of the driving laser pulse, opening up new degrees of freedom for the coherent control of light-driven ultrafast currents in nanoplasmonic devices. Similar fundamental processes may in the future stimulate new possibilities for ultrafast switching in novel materials, such as graphene, black phosphorus, and transition-metal dichalcogenides (Ni *et al.*, 2016; Sun, Martinez, and Wang, 2016; Huber *et al.*, 2017).

In all of our examples, the directionality of a current is reached by a certain degree of symmetry breaking, such as applying a bias voltage, asymmetric nanostructuring, or asymmetric driving laser fields. In semiconductors and insulators, this symmetry breaking and hence the creation of directional current may also be achieved by exploiting quantum interference between different linear and nonlinear photoexcitation pathways. Such a quantum control of light-driven currents was proposed by Kurizki, Shapiro, and Brumer (1989). Its implementation typically requires phase-stable superposition of a short laser pulse with its second harmonic, and it was shown to lead to fully controlled charge injection in unbiased silicon and in GaAs nanowires (Costa *et al.*, 2007; Ruppert *et al.*, 2010). In fact, quantum-controlled currents may become particularly importat when electronic systems are further downscaled toward single-molecule electronics. It has been proposed that a single molecule, bound to two or three (or more) contacts and illuminated with a shaped control laser pulse, could be used to switch a current between different drains, or that a current through a molecule could be started or stopped (Lehmann *et al.*, 2003; Franco, Shapiro, and Brumer, 2007; Li, Schreiber, and Kleinekathöfer, 2007). Looking from the other side, the measurement and control of electron motion in complex molecules has progressed in theoretical and experimental work in attosecond science (Nisoli *et al.*, 2017). It is fascinating to us to explore such intriguing schemes for a coherent control of individual nanoscale quantum systems.

C. Ultrafast electron imaging and spectroscopy

The interaction of strong optical near fields with bound electrons was discussed in detail earlier, including the photoemission of electrons and their use as sensitive probes for the electric-field strength on sample surfaces. In a further line of research, free-electron pulses in ultrafast electron microscopes are being utilized to probe nano-optical fields. Electron microscopes utilizing continuous electron beams are a cornerstone of today’s nanoscale science, reaching subangstrom spatial resolution due to the short de Broglie wavelength of electrons, even at moderate electron kinetic energies. Stroboscopic variants of transmission electron microscopy were already introduced in 1966 by Spivak *et al.* (1968). At that time, nanosecond electron pulses were generated by chopping a continuous electron beam using electrostatic deflection plates. Employing photocathode sources in electron microscopy allowed for a substantial reduction in electron pulse width down to the picosecond and femtosecond range. Pioneering work in this direction during the 1980s and 1990s was performed in the group of O. Bostanjoglo at the Technical University of Berlin (Domer and Bostanjoglo, 2003), as well as in the 2000s in the group of A. H. Zewail at California Institute of Technology (Zewail, 2010; Flannigan and Zewail, 2012) and at the Lawrence Livermore National Laboratory (S. Kim *et al.*, 2008; LaGrange, Reed, and Masiel, 2015), establishing the field of ultrafast transmission electron microscopy (UTEM).

In UTEM, a laser pulse optically excites dynamics on a sample, which is located inside an electron microscope in a vacuum chamber. A second laser pulse with an adjustable delay compared to the first pulse illuminates an electron source and leads to the emission of an electron wave packet with similar duration as the driving laser pulse. This transfers the high temporal resolution from ultrashort optical pulses to the electron microscope. The short electron pulse then propagates to the previously excited sample and probes the dynamics on the sample at a certain time after the excitation. This process is repeated many times for different delays between excitation and probing to record a movie of sample dynamics.

Besides UTEM, such laser-pump–electron-probe schemes were also implemented using other electron microscopy modalities, such as ultrafast scanning electron microscopy (Merano *et al.*, 2005; Yang, Mohammed, and Zewail, 2010; Sun *et al.*, 2015) and ultrafast point-projection electron microscopy (Quinonez, Handali, and Barwick, 2013; Müller, Paarmann, and Ernstorfer, 2014; Vogelsang *et al.*, 2015; Müller *et al.*, 2016).

For achieving few-nanometer spatial resolution, electron pulses with high spatial coherence are required. Developments in nanoscale tip-shaped photocathodes (Hommelhoff *et al.*, 2006; Barwick *et al.*, 2007; Ropers, Elsaesser *et al.*, 2007; Bormann *et al.*, 2010; Yanagisawa *et al.*, 2010; Ehberger *et al.*, 2015) and their integration in ultrafast electron microscopes (Yang, Mohammed, and Zewail, 2010; Müller, Paarmann, and Ernstorfer, 2014; Vogelsang *et al.*, 2015; Feist *et al.*, 2017; Houdellier *et al.*, 2018) have substantially decreased the spatial resolution limits.

In the past decade, ultrafast transmission electron microscopy was employed in a broad field of investigations, addressing ultrafast nanoscale dynamics in structural, magnetic, and electronic degrees of freedom. In the scope of this review, we focus on investigations of inelastic electron-light scattering in optical near fields.

1. Ultrafast point-projection electron microscopy (UPEM)

The "point projector electron microscope" was introduced by Morton and Ramberg (1939) as a simple alternative to the transmission electron microscope invented a few years before by Ruska and Knoll (Knoll and Ruska, 1932; Ruska, 1987). It comprises a needlelike electron emitter, which illuminates a sample placed in a small distance d. A spatially resolved electron detector is located at a larger distance D. Between the sample and the electron source, a voltage in the range of a few tens of volts to a few hundred volts is applied, leading to a sufficiently high static electric field of several V/nm at the electron source position to induce electrostatic tunneling of electrons (cold-field emitter). The emitted electrons are accelerated toward the sample and form a partially coherent electron wave with an approximately spherical wave front. Because of the low kinetic energy of the electrons of only a few hundred electron volts, the choice of a suitable sample is more limited than in conventional transmission electron microscopy. A clean graphene monolayer already absorbs 27% of the electrons at a kinetic energy of 66 eV (Longchamp *et al.*, 2012), making thin or holey samples necessary. In recent years, graphene turned out to be an ideal "sample holder," leading to a homogeneous field between source and sample and providing the support for small nanostructures or larger molecules (Longchamp, Escher, and Fink, 2013; Longchamp *et al.*, 2014; Latychevskaia *et al.*, 2016; Lorenzo *et al.*, 2018). After partial absorption or scattering in the sample plane, the diverging electron wave propagates to the spatially resolving detector, such as microchannel plates equipped with a phosphor screen or a delay line detector. The latter yields, with adequate triggering, additional information about the electron flight time and hence the kinetic energy of scattered electrons. The magnification M of the recorded image in the sample plane is simply given by the ratio of the distances $M = D/d$. Typical values are $D = 100$ mm and $d = 100$ nm, resulting in a magnification of $M = 10^6$.

An advantage of this microscopy type is the low kinetic energy of the imaging electrons, which yield high contrast even for biological samples, resulting in a lower dose imposed on the sample and hence lower radiation damage. Another unique feature compared to today's conventional electron microscopes is the lack of electron lenses in the system, so lens aberration effects do not occur. This was also a driving force for Dennis Gabor when he invented electron holography in 1948 (Gabor, 1948). His technique for recording in-line holograms of a sample is essentially identical to the point-projection microscope described here. The only difference is the increased transverse coherence of the electron beam due to a smaller emitter size. Gabor realized that part of this coherent electron wave is scattered at edges of a partially transparent sample and interferes on the electron detector with an unperturbed part of the electron wave. At that time, optical methods were used to reconstruct an object's image from a magnified electron hologram; today computers are used due to their better flexibility (Fink, Stocker, and Schmid, 1990; Kreuzer *et al.*, 1992; Kreuzer, 1995; Beyer and Gölzhäuser, 2010; Latychevskaia, Gehri, and Fink, 2010; Jericho and Kreuzer, 2011). In reconstructed images, a spatial resolution of less than a nanometer was reached (Kawasaki *et al.*, 2000; Batelaan and Tonomura, 2009; Longchamp *et al.*, 2017).

a. Laser-driven point-projection electron microscopy

Laser-driven point-projection electron microscopy (PPEM) with a spatial resolution on the 100-nm length scale was demonstrated in 2013 by imaging a holey membrane (Quinonez, Handali, and Barwick, 2013). They recorded classical shadow images of the sample and calculated in detail the expected temporal resolutions for various source-sample distances, as shown in Fig. 35. At reasonable acceleration voltages below 100 V, before the onset of electrostatic tunneling a useful time-of-flight spread on the order of a few tens of femtoseconds can be achieved for tip-sample distances below 10 μm.

Ehberger *et al.* (2015) positioned a single carbon nanotube in front of a sharp tungsten taper and compared its holographic image using two different electron sources: a cold-field emitter and a single-photon laser-driven emitter tip; see Fig. 36. They used the width ξ of the interference fringes observable on the detector as a measure for the transverse coherence length and, consequently, the effective electron source size $r_{\mathrm{eff}} = \lambda_{\mathrm{dB}}(D-d)/\xi\pi$ with λ_{dB} being the de Broglie wavelength of the electrons. By applying an electrostatic field to the emitter, its effective work function was lowered such that a single photon with an energy of 3.1 eV was sufficient to emit electrons from the apex. They found an effective source radius $r_{\mathrm{eff}} = 0.80$ nm for photoemission and

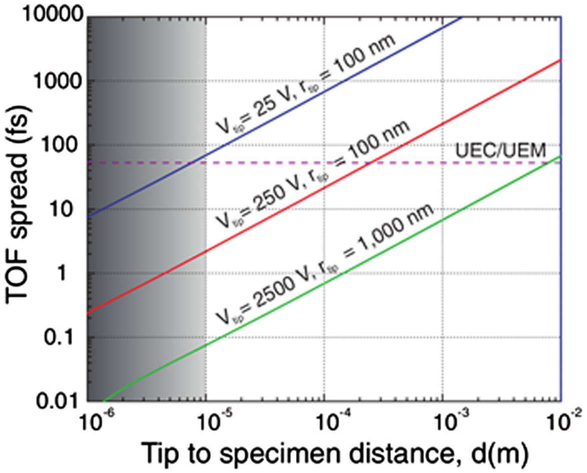

FIG. 35. Achievable temporal resolution in ultrafast point-projection electron microscopy. The time-of-flight spread is shown for various acceleration voltages and tip-sample distances. The region with tip-sample distances below 10 μm is marked in gray to indicate that this region is difficult to reach in a pump-probe setup. From Quinonez, Handali, and Barwick, 2013.

$r_{\mathrm{eff}} = 0.55$ nm for cold-field emission. These results show that electrostatic point-projection electron microscope setups can be extended to laser-driven emission rather directly without losing much of the spatial coherence properties of such sharp metallic tapers.

More laser-driven point-projection experiments were demonstrated shortly thereafter (Vogelsang *et al.*, 2015; Müller *et al.*, 2016). Until recently the high transverse coherence was demonstrated not only for a single-photon photoemission process but also for multiphoton electron emission (Meier *et al.*, 2018; Vogelsang, Talebi *et al.*, 2018). What remains now is to combine this laser-driven electron microscope providing ultrahigh spatial (holographic) resolution with a second, temporally delayed laser pulse triggering dynamics on a sample. In a stroboscopic laser-pump electron-probe experiment, these dynamics can then be imaged with ultrahigh spatiotemporal resolution.

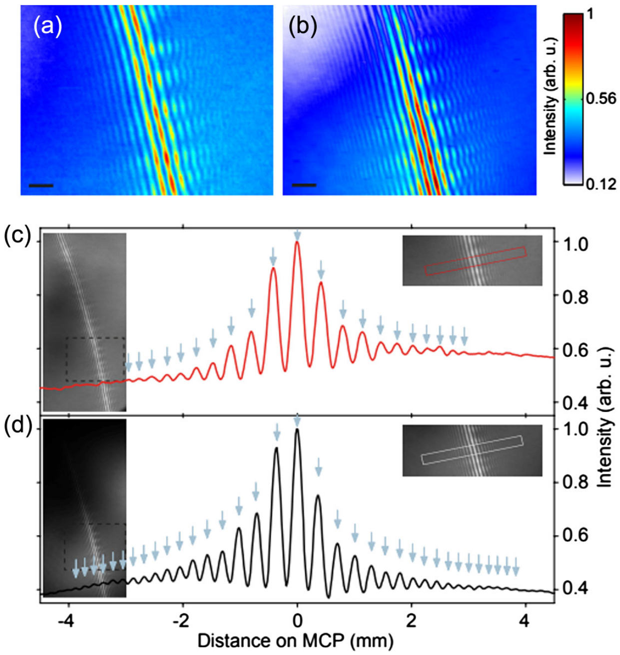

FIG. 36. Point-projection electron microscopy images of a single freestanding carbon nanotube. The interference of electrons being scattered from the nanotube and electrons passing the nanotube unperturbed can be observed. (a) Laser-driven electron emission at 400 nm. (b) Electrostatic electron emission. The corresponding lineouts are shown in (c) for laser-driven emission and (d) for electrostatic tunneling. From Ehberger *et al.*, 2015.

b. Direct UPEM

The first time-resolved UPEM experiments were performed by combining a laser-driven PPEM with a second, pump laser pulse exciting a sample. The temporal delay between optical excitation of the sample and optical photoemission of the probing electron pulse was changed, resulting in a movie of the dynamics on the sample.

Müller, Paarmann, and Ernstorfer (2014) used a sharp tungsten taper as a photoelectron point source and positioned an axially doped InP nanowire in a distance of few tens of micrometers from the source. Local field changes on the sample induced by a pump laser led to a deflection of the probing electrons, resulting in a change of apparent nanowire diameter on the detector. By this, optically excited currents in the nanowire could be tracked with a temporal resolution of ~100 fs and a spatial resolution of less than 100 nm; see Fig. 37.

In a similar setup, Bainbridge, Barlow Myers, and Bryan (2016) probed the emission of a photoelectron cloud from the apex of a second metal taper, optically excited by the pump laser. They reached a spatial resolution of 100 nm and 250 fs temporal resolution, limited by the finite spatial separation between the two tapers that is necessary to avoid spatial overlap of the pump and probe lasers.

c. Nanofocusing-induced photoelectron source

In attempts to further improve this time resolution by reducing the tip-sample separation, several groups (Schröder *et al.*, 2015; Vogelsang *et al.*, 2015; Müller *et al.*, 2016) combined the plasmonic nanofocusing of SPPs on sharp metallic tapers (Sec. II.A.3.c) with multiphoton photoemission from the taper apex. This forms a bright and coherent ultrafast nanolocalized electron source without directly illuminating the electron emission point. Vogelsang *et al.* (2015) illuminated a grating coupler on a gold taper with a tip radius of 12 nm with 16-fs laser pulses at 1600 nm. They observed electron emission exclusively from the taper apex and attributed the absence of emission from the grating coupler to the fifth-order nonlinearity of the photoemission process and the strong-field enhancement at the small taper apex. They showed that the emission of electrons via SPP nanofocusing is 50 times more efficient than direct apex illumination.

Schröder *et al.* (2015) observed electrons coming from both the grating coupler and the apex of a 22-nm sharp gold taper. An extractor-suppressor geometry is used to suppress the unwanted emission from the grating coupler; see Fig. 38. This miniaturized geometry allows one to control the divergence angle of the

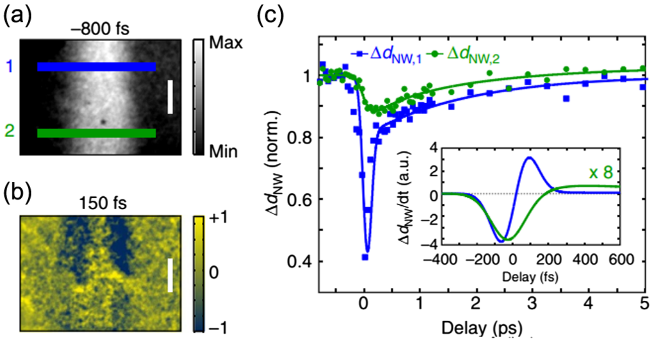

FIG. 37. UPEM of InP nanowires. (a) Image of the nanowire recorded at a negative time delay, i.e., before optical excitation. (b) Normalized difference image recorded at a positive time delay of 150 fs. The different behavior of the p-doped (upper) and n-doped (lower) parts of the nanowire are clearly visible. (c) Apparent width of the nanowire for the two regions and different time delays. (Inset) Extracted current in the nanowire calculated from the width of the wire. From Müller, Paarmann, and Ernstorfer, 2014.

electrons, which is necessary to integrate it into an ultrafast electron diffraction setup (Storeck *et al.*, 2017).

d. Plasmon-driven UPEM

The remotely driven electron source described in Sec. III.C.1.c was first implemented recently in a UPEM setup Vogelsang, Hergert *et al.* (2018). They used a grain boundary 80 μm from the taper apex, illuminated with 15-fs laser pulses at 1.6 μm, for launching SPPs from the apex. Typically one probe electron was emitted from the apex per laser shot. The electrons formed a diverging beam and passed a 30-nm-thick gold film perforated with a plasmonic double nanohole resonator structure (Fig. 39) after a distance of only 2.7 μm. The probe electrons are transmitted through the nanoholes, leading to a magnified shadow image of the structure on the detector screen at a distance of 75 mm with a spatial resolution of 20 nm. Because of the thickness of the sample of 30 nm, electrons scattered from the edge of the nanostructure lose part of their coherence, washing out interference fringes that are visible for thinner samples (Vogelsang, Hergert *et al.*, 2018).

In the second step, an optical pump pulse induces the emission of an electron cloud from the gap region in the double nanohole resonator. The electrons emitted from the taper apex probe the spatial and temporal evolution of this electron cloud with resolutions of 25 fs and 20 nm, respectively. This can be observed by the time-resolved deflection of the probing electrons and consequently a shadow region corresponding approximately to the size of the charge cloud; see Fig. 39.

The spatial resolution in Fig. 39 is limited by the finite thickness of the 30-nm-thick gold film. It can be increased further by at least 1 order of magnitude by making use of the holographic techniques illustrated in Fig. 36. First holograms of bundles of carbon nanotubes have recently been recorded by plasmonic-nanofocusing UPEM (Vogelsang, Talebi *et al.*, 2018). This brings UPEM holography with few-femtosecond temporal resolution well into reach. Such experiments offer a conceptually new approach for imaging and manipulating the spatiotemporal dynamics of optical near fields of single nanostructures with femto-nano resolution.

2. Optically driven inelastic electron scattering in ultrafast transmission electron microscopy

In recent years, nano-focused ultrashort electron pulses in UTEM have emerged as a unique platform for investigating the interaction of electrons with localized light fields.

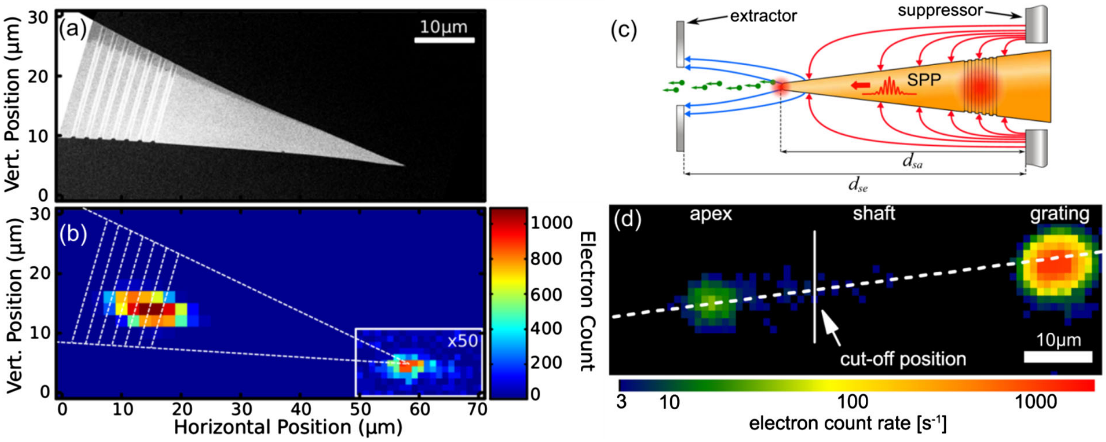

FIG. 38. Two examples of remotely driven electron emission from sharp gold tapers. (a) SEM micrograph of a sharp gold taper with a grating coupler. (b) Number of electrons emitted from the taper apex when raster scanning the taper through a laser focus. Electron emission can be observed only when the grating coupler or the taper apex are illuminated. A 50-fold increase in electron count rate is reached when illuminating the grating coupler compared to the taper apex. This is due to the efficient nanofocusing of surface plasmons at the taper apex after their launching at the grating coupler. (a),(b) From Vogelsang *et al.*, 2015. (c) Drawing of an extractor-suppressor geometry used to suppress unwanted direct electron emission from the grating coupler. For certain voltage settings, only those electrons emitted from the taper apex are extracted. (d) Demonstration of the setup shown in (c). Electrons emitted from the right side of the vertical line are suppressed, proving that grating illumination indeed leads to emission from the apex. (c),(d) From Schröder *et al.*, 2015.

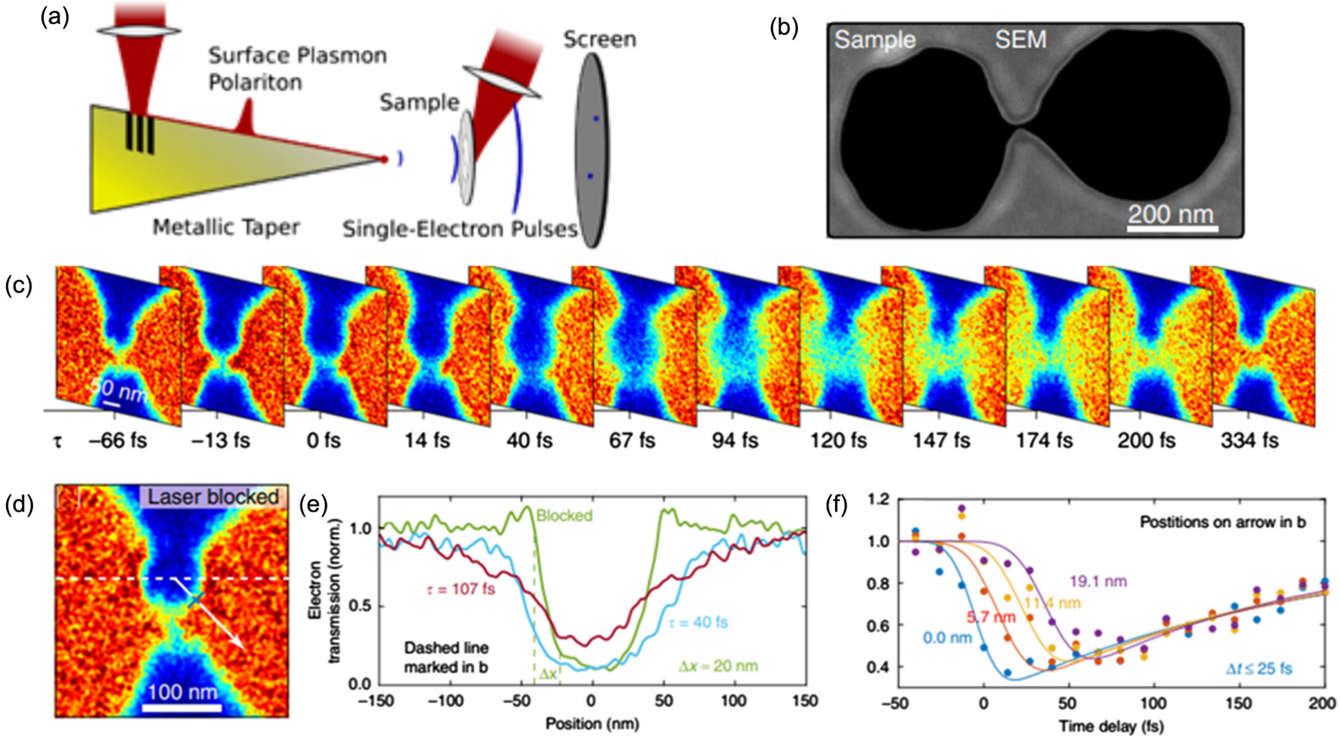

FIG. 39. Ultrafast plasmon-driven point-projection electron microscopy. (a) Schematic of the setup. (b) SEM image of the 30-nm thin gold film sample. A double nanohole structure is milled into it such that it forms a small resonator with a gap region in the middle. (c) Series of shadow images recorded at the central part of the nanostructure shown in (b) for different time delays between the pump laser and the electron-probe pulse. (d) Shadow image without optical excitation of the sample. (e) Lineouts through three images shown in (c) and (d). A spatial resolution of 20 nm is found. (f) Temporal evolution along certain positions on the arrow shown in (d). The expansion of the cloud can be followed with a temporal resolution of less than 25 fs. From Vogelsang, Hergert *et al.*, 2018.

In a seminal work, Barwick, Flannigan, and Zewail (2009) demonstrated the inelastic scattering of electrons in optical near fields; see Fig. 40(a). Electron pulses that traversed the near field of an optically excited nanoparticle acquired or lost energy in multiple photon energy quanta, resulting in electron-energy spectra with photon sidebands on the gain and loss sides; see Figs. 40(b) and 40(c). Since the number of inelastically scattered electrons is related to the strength of the optically driven near field [Figs. 40(d) and 40(e)], it can be utilized as a novel image contrast mechanism in UTEM and was termed photon-induced near-field electron microscopy.

a. Free-electron photon absorption and emission in optical near fields

In a simplified picture, electron-energy gain and loss can be viewed as the absorption or emission of photons from the localized optical field. The process of an electron absorbing or emitting a single photon from a propagating light field is forbidden since the process does not conserve energy and momentum. Specifically, as shown in Fig. 41, starting from the dispersion of a free electron and absorbing the energy and momentum of a photon, one ends outside of the dispersion relation of the electron. The mismatch decreases with increasing electron velocity v_e, and it would vanish as the electron velocity approaches c.

Similarly to the grating-mediated plasmon-light coupling mentioned in Sec. II.A.2, free-electron–light coupling can be facilitated by proper structuring of the light field. In the simplest case, localization of the light field broadens its momentum content [indicated as the horizontal gray area in Fig. 41(b)], such that a partial overlap with the electron dispersion relation is obtained. Stronger localization of the light field yields a broader momentum distribution, so even for slower electrons a sufficient coupling strength is achievable.

The necessary light localization for facilitating energy transfer to a free electron can also be viewed in a spatiotemporal picture, resulting in strong similarities to the physics of strong-field photoemission discussed earlier. For an electron passing a localized light field, the electron-light interaction time is of the order of $t_i = l/v_e$, in which l is the extent of the light field and v_e is the electron velocity. For strongly localized fields and fast electrons, the interaction time can be shorter than the light oscillation period $2\pi/\omega$. In the limiting case $t_i \ll 2\pi/\omega$, the passing electron experiences the momentary light field $E(t)$, resulting in a momentum change $\Delta p(t) = -eE(t)t_i$, largely similar to the case of a strong-field emitted electron from a sharp taper or a nanoparticle; see the δ parameter in Sec. II.B.2.f.

In the opposite limit $t_i \gg 2\pi/\omega$, the electron experiences multiple light cycles. During the passage of the electron through the light field, it is accelerated and decelerated. However, after it has exited the light field it shows a largely unchanged kinetic energy. Such a description is reminiscent of strong-field emitted electrons from atoms or molecules within a micrometer-sized far-field laser focus, in which electrons experience a kinetic energy change governed by the momentary

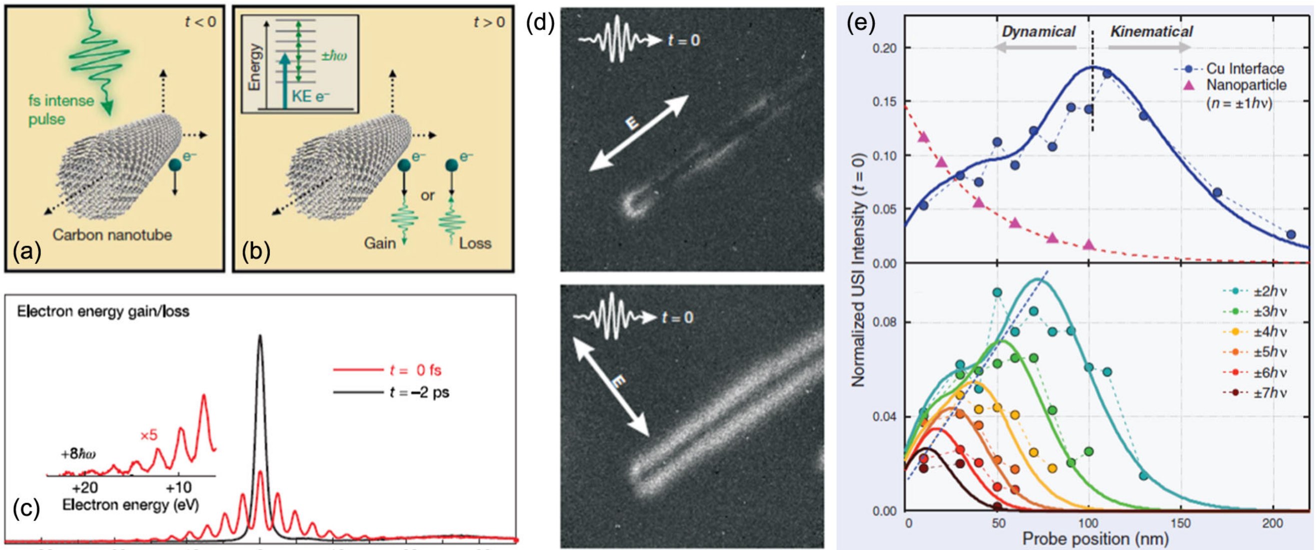

FIG. 40. Inelastic electron-light scattering in optical near fields. (a),(b) Electrons traversing an intense optical near field at a nanostructure gain or lose energies in multiples of the photon energy. (c) The electron-energy spectrum after interaction (red curve, shown also in the inset) consists of multiple photon sidebands. $t = 0$, electron and optical pulse are temporally overlap; $t = -2$ ps, electrons pass the nanostructure before the optical excitation. (d) Energy-filtered electron micrographs collecting electrons that gained between one and four photon energy quanta of an optically excited carbon nanotube (electron–laser pulse delay 0 ps) for two optical polarization directions (indicated as arrows). (a)–(d) From Barwick, Flannigan, and Zewail, 2009. (e) Amplitudes of (upper panel) zero-loss peak and (lower panel) nth-order photon sidebands depending on the distance from the nanoparticle surface. From Yurtsever, van der Veen, and Zewail, 2012.

light vector potential. However, for electrons passing an optical near field, free electrons are not "born" at a certain time within the field, as in the case for photoemitted electrons, but experience an increasing and decreasing light intensity when entering and leaving the localized field, respectively. Consequently, for $t_i \gg 2\pi/\omega$ the overall electron-energy change is $eA(-\infty) = 0$.

Whereas such a classical description can catch the essential scaling behaviors of free-electron–light interactions, it does not reproduce the experimentally observed energy spectrum with multiple photon sidebands. In a quantum-mechanical description, electron wave functions $\psi(r)$ are spatially delocalized. In the longitudinal direction, the minimum temporal width of the wave function is given by $\Delta t_{\min} = \hbar\Delta E/2$ so that for typical electron spectral widths of about 1 eV or below temporal widths of 2 fs are obtained. Thereby, the electron wave function, unlike the classical description, is affected by multiple phases and even several periods of the optical field. Similar to considerations for photon peaks in high-harmonic spectra (Corkum, 1993), the temporal periodic modulation of the electron wave functions (with the optical period $2\pi/\omega$) imprints spectral interference fringes on the electron-energy distribution with a spacing of $\hbar\omega$, i.e., photon sidebands.

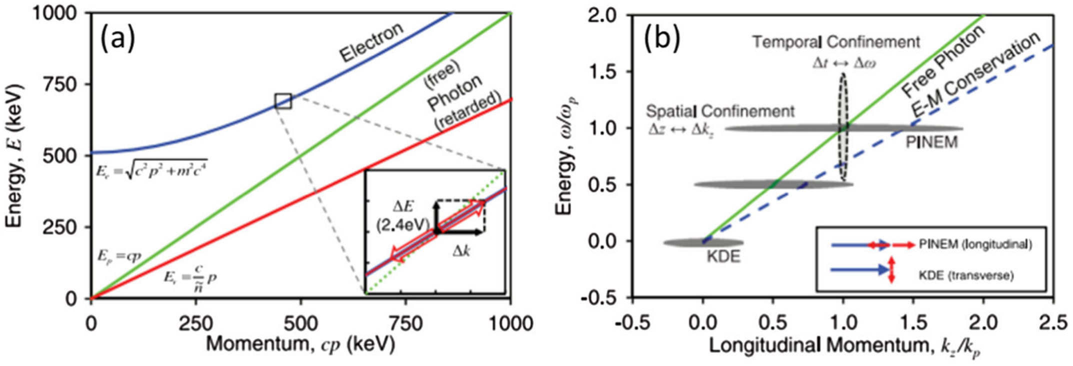

FIG. 41. Energy-momentum matching in inelastic electron-light scattering. (a) Dispersion relation of electrons (blue curve, labeled as "Electron"), free photons (green curve, labeled as "free"), and photons within a dielectric medium (red curve, labeled as "retarded"). From Park, Lin, and Zewail, 2010. (b) Energy-momentum conservation of a free electron and free photon via momentum broadening (horizontal ellipses) due to spatial confinement and energy broadening (vertical ellipse) due to temporal confinement. The solid green line ("Free Photon") represents the dispersion relation of a free photon, and the dotted blue line represents the momentum change of a free electron at the given energy change. From Park, Lin, and Zewail, 2010.

In the low-intensity limit, the probability for photon absorption is given by (de Abajo and Kociak, 2008b)

$$P_{\mathrm{EEGS}}(\omega) = \left(\frac{e}{\hbar\omega}\right)^2 \left| \int dz E_z e^{-i\omega z/v_e} \right|^2, \tag{3.5}$$

where E_z is the optical-field amplitude along the electron beam trajectory. The wave vector ω/v_e is equal to the momentum change required for an electron to increase its energy by $\hbar\omega$. The Fourier transform contained in Eq. (3.5) probes the momentum component of the light field that fulfills energy and momentum conservation in a photon absorption event.

The electron-energy loss and gain at illuminated nanoparticles is tightly linked with conventional plasmon-mediated cathodoluminescence (Asenjo-Garcia and de Abajo, 2013). Focusing on the passing electron beam, cathodoluminescence can be viewed as a spontaneous photon emission during which the electron energy decreases by $\hbar\omega$. Gain and loss at an illuminated nanoparticle corresponds to induced photon emission and absorption. In non-time-resolved transmission electron microscopy, plasmon-mediated cathodoluminescence is typically a low yield process with luminescence probabilities in the range of a few percent (de Abajo, 2010). As optically driven processes, photon absorption and emission probability scale with the light intensity at the nanoparticle, so a strong coupling between electron and light is reachable and directly observable in the multiple photon sidebands observed in the experimental energy spectra (Barwick, Flannigan, and Zewail, 2009).

Whereas strong electron–near-field interactions are more easily achievable with pulsed electron beams, similar experiments were performed with continuous electron beams in a scanning electron microscope employing optically illuminated diffraction gratings as an electron-light coupling element (Breuer and Hommelhoff, 2013). Despite the small duty cycle of the experiment (2.7-MHz laser repetition rate, 110-fs optical pulse duration), inelastically scattered electrons with an electron-energy gain of up to 300 eV are detected. Because of the large acceleration fields compared to the fields used in radio-frequency cavities, such structures were proposed as all-optical electron accelerators at relativistic energies (England *et al.*, 2014).

b. Coherent optical phase modulation of free-electron states.

At high local light fields, inelastic electron-light scattering should show typical strong-field phenomena, such as Rabi cycling or multicolor interference. In early studies, these effects were largely masked due to the incoherent sampling of different interaction strengths. In the experiments, electron pulses with a duration of a few hundred femtoseconds were employed and interacted with a light field of similar temporal duration. Different parts of the electron pulse were scattered off from different light intensities so that intensity-dependent features in the scattering process were averaged out. Similar considerations apply for the transverse direction, for which the electric-field strength in the optical near field exhibits steep gradients, resulting in field averaging unless sharply focused electron probes are employed.

In a first study, focusing on the coherent nature of the inelastic electron-light scattering in an UTEM, Feist *et al.* (2015) utilized light fields much longer than the probing electron pulses, which additionally were focused to nanoscale probing areas. Unlike in earlier studies, they observed pronounced intensity-dependent modulations of the photon-sideband amplitude; see Fig. 42. For example, the zero-loss peak in the spectra exhibits an oscillatory amplitude change, and it even vanishes for certain near-field strengths. Such behavior was predicted theoretically earlier (de Abajo, Asenjo-Garcia, and Kociak, 2010) and corresponds to Rabi oscillations between photon-coupled electron-energy states $|E + n\hbar\omega\rangle$. The population of the nth photon sideband can be analytically expressed as (Park, Lin, and Zewail, 2010)

$$P_n = J_n(2|g|)^2 \quad \text{with } g = \frac{e}{2\hbar\omega} \int_{-\infty}^{\infty} dz E_z e^{-i\omega z/v_e}. \tag{3.6}$$

The low-intensity limit of Eq. (3.6) recovers Eq. (3.5).

In a different setting, Rabi oscillations on an equally spaced energy ladder spectrum with constant coupling strength between the energy states were already investigated in the 1970s by Shore and Eberly (1978) . Unlike Rabi oscillations in a two-level system, in a multilevel spectrum strong-field excitation results in a continuous spread of spectral populations with optical-field strength F, giving a spectral cutoff on the gain-loss side around $\pm 2|g|\hbar\omega$. The spectral spreading can be described by a quantum random walk between states in which the interference between different quantum paths resulting in the same final state governs the spectral shape. Other physical instances in which quantum random walks were observed include, for instance, the mode coupling in an optical cavity (Bouwmeester *et al.*, 1999) and of optically trapped atoms (Karski *et al.*, 2009).

In an equivalent description, the effect of the near field on the electron wave function can be regarded as a sinusoidal modulation of the phase of the incident wave function $\psi_{\mathrm{in}}(z)$,

$$\psi(z) = \exp\left[-2i|g| \sin\left(\frac{\omega z}{v_e} + \arg(g)\right)\right] \psi_{\mathrm{in}}(z), \tag{3.7}$$

forming a phase modulator for electron wave functions at optical frequencies.

With such a picture in mind, advanced phase control schemes for the free-electron wave function are within reach. In a first study, Echternkamp, Feist *et al.* (2016) experimentally realized a sequential interaction of an electron pulse with two phase-locked near fields separated by a 5-μm distance. As schematically shown in Fig. 43(a), the first interaction imprints a phase modulation on the passing electron beam, spectrally corresponding to a comb of photon sidebands. Depending on the relative phase of the near fields, the phase modulation in the second interaction zone either increases the modulation depth constructively or erases the modulation of the first interaction destructively. The corresponding electron-energy spectra, plotted in Fig. 43(b), display either a further spectral broadening or an almost full spectral recompression, respectively. The temporal evolution of a quantum random walk, although the term implies otherwise, is fully deterministic and governed by the Schrödinger equation, so the action of a second near field

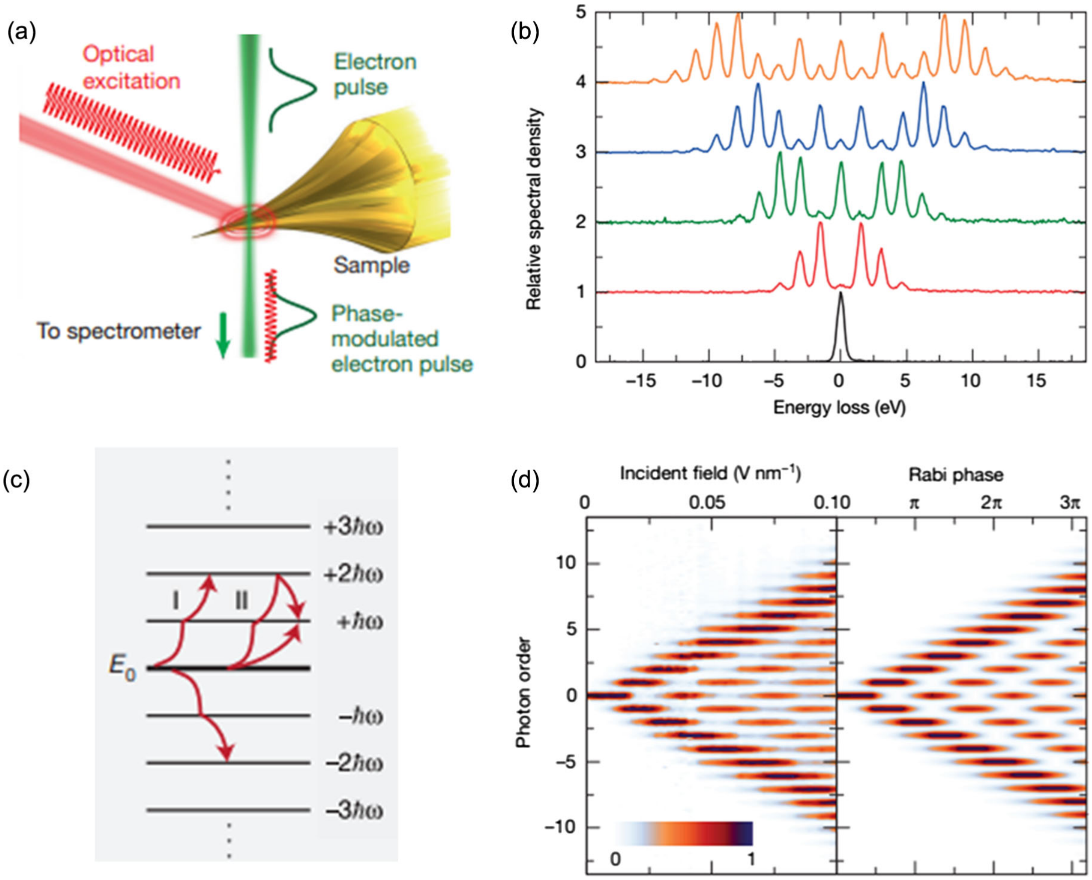

FIG. 42. Coherent optical modulation of a free-electron state. (a) An electron pulse traversing a localized optical near field acquired a sinusoidal phase modulation. (b) Electron-energy spectra at incident optical fields of 0, 0.023, 0.040, 0.053, and 0.068 V/nm (bottom to top). (c) Level diagram of electron energies coupled by the optical near field. Different interfering quantum paths between the levels are indicated by arrows. (d) Experimental electron-energy spectra depending on (left panel) the incident optical-field strength compared to (right panel) a numerical simulation taking. From Feist *et al.*, 2015.

with the correct relative phase can reverse the action of the first field.

For two interaction zones separated by longer distances, electron pulse dispersion results in a substantial reshaping of the electron density distribution. In particular, it was predicted that for specific propagation distances attosecond electron pulse trains are formed with a pulse repetition rate determined by the period of the optical driving field (Feist *et al.*, 2015). In

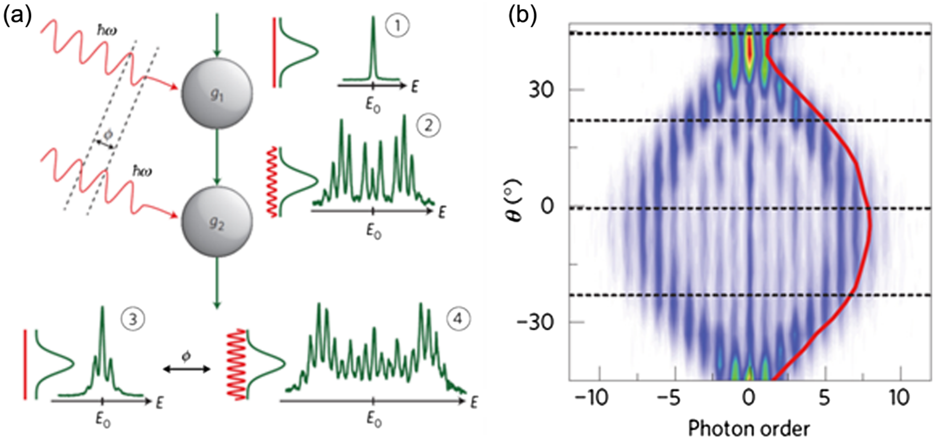

FIG. 43. Ramsey interferometry with free-electron wave functions. (a) Schematic of the Ramsey interferometry approach for free electrons utilizing two phase-locked optical near fields. (b) Electron-energy spectra after the second interaction zone depending on the relative phase of the two near fields. θ denotes the orientation of a $\lambda/2$ plate, used for controlling the relative near-field phase. From Echternkamp, Feist *et al.*, 2016.

a classical picture, electrons gain or lose energy depending on the phase at which they enter the first interaction region. During the subsequent propagation, accelerated electrons can catch up with the slowed-down part of the electron pulse, resulting in a bunching of electron density for specific propagation times. For typical near-field interaction strengths achieved in UTEM experiments and for electron energies of the order of 100 keV, bunching occurs for propagation lengths of the order of few millimeters.

In the first experimental demonstrations of attosecond electron bunching (Kozak *et al.*, 2017; Priebe *et al.*, 2017; Morimoto and Baum, 2018), the structured density was characterized by a second optical near-field interaction phase locked to the first interaction; see Fig. 44. Electron-energy spectra after the second near-field interaction have a qualitatively different shape when one compares bunched and nonbunched electron pulses, as shown in Fig. 44(b). Similar to the case of two nearby interaction zones, the electron-energy spectra depend on the relative phase difference between the two near fields and exhibit a partial spectral refocusing. However, for a larger distance between the interaction zones, the spectra become asymmetric with respect to the gain and loss side since for a train of attosecond electron pulses the density spikes interact with the second near field only within a narrow phase interval, so the corresponding wave function components receive an approximately equal energy shift. Using a phase-retrieval algorithm, it was demonstrated that from the phase-dependent electron-energy spectra, i.e., the spectrogram, the full density matrix of the electron state can be retrieved (Priebe *et al.*, 2017). From the density matrix, the Wigner function can be computed as shown in Fig. 44(c), using the spectrogram in Fig. 44(b) as input. Integration of the Wigner function along the momentum marginal gives the temporal density structure in the pulse, which for the present case exhibits electron spikes with a FWHM of 655 as.

Further complex optical control on the phasing of free-electron wave functions can be exerted by multicolor fields. The first demonstration of an interaction of a free-electron pulse with a two-color $\omega-2\omega$ near field was reported by Priebe *et al.* (2017). In the resulting electron-energy spectra, photon sidebands with a spacing of $\hbar\omega$ and $2\hbar\omega$ occur with amplitudes sensitively depending on the relative phase of both fields.

For a near-field interaction with a single frequency, electron spectra remain symmetric with respect to the initial electron energy, i.e., the nth photon sideband exhibits equal amplitudes on the gain and loss side. For the $\omega-2\omega$ field, spectra are asymmetric on the gain and loss side, although the spectral center of gravity stays constant, so no overall (phase-averaged) electron acceleration or deceleration is observed. The asymmetry in the spectra is understood by considering the phase gradient imprinted on the electron wave. The imprinted phase can be optimized so that a close-to-linear phase ramp is achieved during part of the optical cycle. Electrons interacting with the near field during this time frame acquire a constant energy difference, resulting in a pronounced peak in the envelope of the electron-energy distribution.

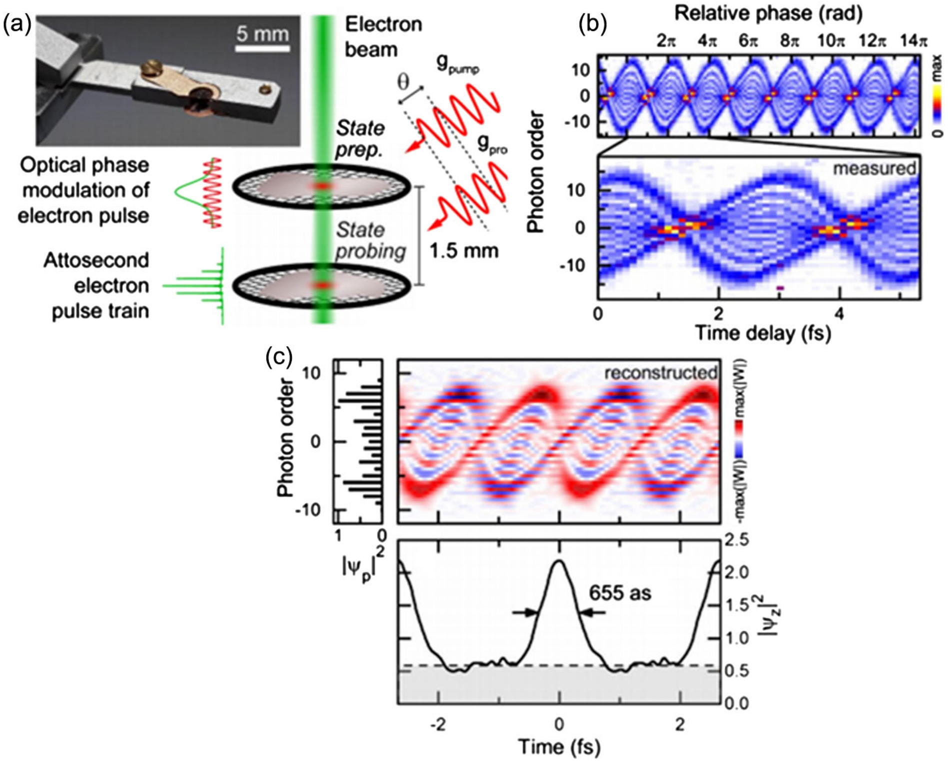

FIG. 44. Formation and characterization of attosecond electron pulse trains. (a) The first optical near field imprints a sinusoidal phase modulation on an ultrashort electron pulse. The second near field probes the temporal structure of the dispersed pulse. (b) Spectrogram showing the dependence of the electron-energy spectra on the relative phase between the two near fields. (c) Reconstructed Wigner function of the propagated electron pulse at the second interaction zone. The time marginal demonstrates the formation of an attosecond electron pulse train with spike widths of 655 as. From Priebe *et al.*, 2017.

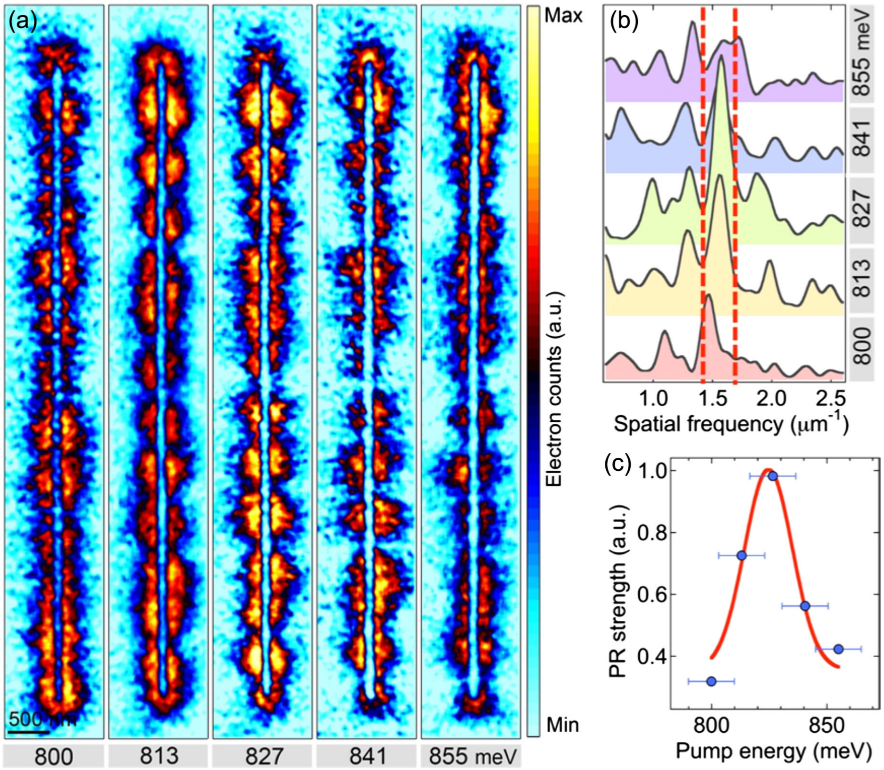

FIG. 45. Mapping plasmonic modes with high-spectral selectivity. (a) Spatial map of inelastic electron scattering probability around a silver nanowire for a range of incident photon energies (given in the bottom line). The scattering probability is characterized by recording energy-filtered electron micrographs at the initial electron energy, thereby quantifying the local electron scattering probability. (b) Spatial Fourier transforms of the photon-energy-dependent scattering probability maps [shown in (a)] evaluated along the wire direction. (c) Fourier amplitude integrated in the spatial frequency range indicated in (b) as a function of the photon energy of the incident light field. From Pomarico *et al.*, 2018.

Pomarico *et al.* (2018) demonstrated the application of optically driven inelastic electron scattering for the spatial mapping of plasmonic modes in a silver nanowire with a spectral selectivity down to 20 meV. For exciting plasmonic modes, they employed a tunable narrow bandwidth optical pulse and recorded the spatially dependent inelastic electron scattering probability as a function of the photon energy; see Fig. 45(a). Optically driven electron scattering is observed over the whole range of photon energies, showing only a moderate scattering efficiency increase at plasmonic resonances (here located at around 825 meV). A clear resonance behavior is observed by considering different spatial frequencies of the scattering efficiency maps, evaluated along the wire direction; see Fig. 45(b). For a narrow band of spatial frequencies around 1.5 $\mu\mathrm{m}^{-1}$ corresponding to the modal structure of the $n = 13$ plasmonic mode of the wire, electron scattering efficiency shows a pronounced peak at about 825 meV. As the energy resolution of such an experiment is governed by the optical spectral bandwidth and not the energy resolution of the employed electron spectrometer, this work opens new avenues for the imaging of material excitations by high-energy electrons at nanoscale spatial and high spectral resolution.

In a further investigation, Vanacore *et al.* (2018) employed sequences of two 60-fs optical pulses and demonstrated delay-dependent changes in the electron-energy spectra, oscillating with the optical period of the light field. Such an approach resembles multidimensional optical spectroscopies, potentially giving access to the homogeneous energy bandwidth of electron states. Vanacore *et al.* (2018) found that delay-dependent oscillations occur for pulses with delays even exceeding 100 fs, although the inhomogeneous coherence time of the electron pulse was of the order of 10 fs. Similar results would have been obtained by considering only optical pulse interference but were ruled out based on their different impact on the high-energy part of the electron spectra.

The interaction with optical near fields also results in an angular deflection of electron beams (Morimoto, Kanya, and Yamanouchi, 2015; Feist *et al.*, 2018; Vanacore *et al.*, 2018). For optical fields with narrow transverse momentum spectra, such as reflected fields from surfaces or grating near fields, electron pulses acquire quantized transverse momenta. Unlike the Kapitza-Dirac effect (Kapitza and Dirac, 1933; Freimund, Aflatooni, and Batelaan, 2001), transverse scattering in a near field is an inelastic process in which the transverse momentum change is correlated with the energy gained or lost within the near field.

Free-electron–near-field interactions, as described in this section, need to be distinguished from approaches employing propagating light fields or free-space standing light waves. In the latter, electron-light interaction times are much longer than the light period, so the net effect on a traversing electron is given by the ponderomotive potential of the light field. In this case, the electron-energy change scales with the intensity of the light field, so typically higher light intensities are required compared to near-field interactions. Theoretical work (Baum and Zewail, 2006, 2007) and recent experiments (Kozak, Schonenberger, and Hommelhoff, 2018; Kozak *et al.*, 2018) have demonstrated the application of copropagating wave fields for electron acceleration and attosecond electron bunching.

IV. CONCLUSIONS AND OUTLOOK

In this review, we have outlined some fundamental aspects of the emerging field of strong-field nano-optics. As a result of largely curiosity-driven research, it has become clear that new degrees of freedom can be accessed by joining concepts of plasmonics and near-field optics with field-driven processes across the electromagnetic spectrum. The phenomena encountered span the entire range of classical versus quantum behavior, with almost purely classical scalings of field-driven photoelectron spectra to pronounced quantum features in the inelastic interaction of near fields with swift electron beams.

An overarching theme in strong-field nano-optics has been the desire to make use of spatially highly localized electromagnetic fields to exert control over the trajectories of electrons on subcycle temporal and nanometer spatial scales. One can expect future developments to continue to expand upon this motif. We expect that an improved microscopic understanding of the optical response of tailored nanostructures and heterostructures, strongly driven by sculpted multicolor and polarization-controlled fields, will play a crucial role, combined with tunable electrostatic and magnetic fields, and possibly with a chemical control of surface properties and work functions. In addition, a further integration of microscopic materials properties and atomic-scale design, e.g., in van der Waals heterostructures, may be envisaged. We anticipate that in the near future not only classical electromagnetic fields will be taken as a control parameter. The vacuum fluctuations of the electromagnetic field, greatly enhanced in spatially confined nano-optical antenna structures, present equally fascinating options for manipulating the motion of charge carriers in nanostructures. This ranges from vacuum-field-driven control of their mobilities over the enhancement of light-driven charge transfer processes to vacuum-field-mediated manipulation of the potential energy surfaces of molecular nanostructures.

To date, strong-field nano-optics has addressed mostly fundamental mechanisms in model geometries, typically employing high-end light sources, in many cases amplified or phase-stabilized mode-locked laser systems. Beyond the fascination about these unique findings, the question is naturally prompted as to whether the observed effects are primarily of an academic nature and if there is a path for more widespread scientific or even technological applications. In the past, we have witnessed astounding scientific developments, resulting in the demonstration of strong-field phenomena with unprecedentedly low pulse energies in the femtojoule to picojoule range.

Anticipating rapid further progress in our microscopic understanding of how strong electromagnetic fields interact with matter on the nanoscale, this brings about the realization of highly efficient, ultrafast plasmonic switching and transistor concepts and more generally places light-wave electronics well in reach. The pronounced spatial field localization in metallic nanostructures, which is a central element of strong-field nano-optics, is of equal importance in merging photonics and electronics. Since plasmonics offers the prospect of localizing electromagnetic fields on the 10-nm length scale that is reached in current electronic transistor structures, strong-field light-matter interactions bridge the seemingly disparate worlds of photonics and electronics and may serve as a noncontact local probe for fields and electronic properties. As an example, the imaging of dynamic field distributions in integrated electronic devices using solid-state high-harmonic generation has been proposed (Vampa *et al.*, 2018). In such nanostructured environments, the propagation and localization of both the driving field and the emitted fields, as well as their interaction with crystal electrons, will have to be considered, touching upon various aspects of the research described earlier. Second, high-speed electronics is likely to approach the terahertz regime in the future, rendering spatiotemporal electron dynamics a key feature in device functionality, either within solids or in new forms of vacuum nanoelectronics. It would therefore be interesting to explore the prospects of petahertz light-field-driven electronics. It is evident that the development of novel, miniaturized, and if possible chip-integrated ultrafast light sources will form a key technological element in such advanced nanophotonic circuitry.

Irrespective of where such developments may lead, a main and recurring lesson from the research discussed here is that an intersection between two complementary fields creates unforeseen opportunities for exciting experimental and theoretical discovery. Further scientific benefits are thus anticipated from incorporating ideas and phenomena from magnetism and spin dynamics, quantum transport, surface science, and various other fields. We are looking forward to learning about and contributing actively to the future developments in this interesting field of research.

ACKNOWLEDGMENTS

We thank all members of our research groups for their invaluable contributions to research related to this review. We acknowledge financial support from the National Research, Development and Innovation Office of Hungary (Projects No. VEKOP-2.3.2-16-2017-00015 and No. 2018-1.2.1-NKP-2018-00012), the Deutsche Forschungsgemeinschaft [Projects No. SPP1391 (Ultrafast Nanooptics), No. SPP1839 (Tailored Disorder), No. SPP1840 (QUTIF), and No. GRK1885], the Korea Foundation for the International Cooperation of Science and Technology (Global Research Laboratory Project No. K20815000003), and the German-Israeli Foundation (Grant No. 1256). J. V. acknowledges a grant from the Studienstiftung des Deutschen Volkes, and he has received funding from the European Union's Horizon 2020 research and innovation program under Marie Skłodowska-Curie Grant Agreement No. 793604 ATTOPIE. P. D. and Z. P. acknowledge funding from the European Union's Horizon 2020 research and innovation programme within the FET Open scheme (PETACom project). S. S. acknowledges support from the Volkswagen Foundation as part of the Lichtenberg grant "Ultrafast nanoscale dynamics probed by time-resolved electron imaging."

REFERENCES

Accanto, N., Nieder, J. B., L. Piatkowski, M. Castro-Lopez, F. Pastorelli, D. Brinks, and N. F. van Hulst, 2014, Light Sci. Appl. **3**, e143.

Aeschlimann, M., M. Bauer, D. Bayer, T. Brixner, F. J. García de Abajo, W. Pfeiffer, M. Rohmer, C. Spindler, and F. Steeb, 2007, Nature (London) **446**, 301–304.

Aeschlimann, M., T. Brixner, A. Fischer, C. Kramer, P. Melchior, W. Pfeiffer, C. Schneider, C. Strüber, P. Tuscherer, and D. V. Voronine, 2011, Science **333**, 1723.

Aeschlimann, M., C. A. Schmuttenmaer, H. E. Elsayed-Ali, R. J. D. Miller, J. Cao, Y. Gao, and D. A. Mantell, 1995, J. Chem. Phys. **102**, 8606.

Aeschlimann, M., *et al.*, 2015, Nat. Photonics **9**, 663.

Aeschlimann, M., *et al.*, 2017, Light Sci. Appl. **6**, e17111.

Agostini, P., G. Barjot, J. Bonnal, G. Mainfray, C. Manus, and J. Morellec, 1968, IEEE J. Quantum Electron. **4**, 667.

Agostini, P., F. Fabre, G. Mainfray, G. Petite, and N. K. Rahman, 1979, Phys. Rev. Lett. **42**, 1127.

Aguirregabiria, G., D.-C. Marinica, M. Ludwig, D. Brida, A. Leitenstorfer, J. Aizpurua, and A. G. Borisov, 2019, Faraday Discuss. **214**, 147.

Ahn, B., *et al.*, 2017, APL Photonics **2**, 036104.

Akselrod, G. M., C. Argyropoulos, T. B. Hoang, C. Ciraci, C. Fang, J. Huang, D. R. Smith, and M. H. Mikkelsen, 2014, Nat. Photonics **8**, 835.

Anderson, A., K. S. Deryckx, X. J. G. Xu, G. Steinmeyer, and M. B. Raschke, 2010, Nano Lett. **10**, 2519.

Anderson, P. W., 1958, Phys. Rev. **109**, 1492.

Antoine, X., A. Arnold, C. Besse, M. Ehrhardt, and A. Schädle, 2008, Commun. Comput. Phys. **4**, 729.

Aouani, H., S. Itzhakov, D. Gachet, E. Devaux, T. W. Ebbesen, H. Rigneault, D. Oron, and J. Wenger, 2010, ACS Nano **4**, 4571.

Aouani, H., M. Navarro-Cia, M. Rahmani, T. P. H. Sidiropoulos, M. Hong, R. F. Oulton, and S. A. Maier, 2012, Nano Lett. **12**, 4997.

Apalkov, M., and M. I. Stockman, 2012, Phys. Rev. B **86**, 165118.

Apolonski, A., *et al.*, 2004, Phys. Rev. Lett. **92**, 073902.

Aravind, P. K., and H. Metiu, 1983, Surf. Sci. **124**, 506.

Arbouet, A., D. Christofilos, N. Del Fatti, F. Vallee, J. R. Huntzinger, L. Arnaud, P. Billaud, and M. Broyer, 2004, Phys. Rev. Lett. **93**, 127401.

Arnold, A., M. Ehrhardt, and I. Sofronov, 2003, Commun. Math. Sci. **1**, 501.

Asenjo-Garcia, A., and F. J. G. de Abajo, 2013, New J. Phys. **15**, 103021.

Ashley, J. C., and L. C. Emerson, 1974, Surf. Sci. **41**, 615.

Atre, A. C., B. J. M. Brenny, T. Coenen, A. García-Etxarri, A. Polman, and J. A. Dionne, 2015, Nat. Nanotechnol. **10**, 429.

Awada, C., G. Barbillon, F. Charra, L. Douillard, and J.-J. Greffet, 2012, Phys. Rev. B **85**, 045438.

Awada, C., T. Popescu, L. Douillard, F. Charra, A. Perron, H. Yockell-Levière, A.-L. Baudrion, P.-M. Adam, and R. Bachelot, 2012, J. Phys. Chem. C **116**, 14591.

Babadjanyan, A. J., N. L. Margaryan, and Kh. V. Nerkararyan, 2000, J. Appl. Phys. **87**, 3785.

Bachelier, G., J. Butet, I. Russier-Antoine, C. Jonin, E. Benichou, and P. F. Brevet, 2010, Phys. Rev. B **82**, 235403.

Baida, F. I., and A. Belkhir, 2009, Plasmonics **4**, 51.

Baida, H., *et al.*, 2009, Nano Lett. **9**, 3463.

Bailo, E., and V. Deckert, 2008, Chem. Soc. Rev. **37**, 921.

Bainbridge, A. R., C. W. Barlow Myers, and W. A. Bryan, 2016, Struct. Dyn. **3**, 023612.

Banfi, F., C. Giannetti, G. Ferrini, G. Galimberti, S. Pagliara, D. Fausti, and F. Parmigiani, 2005, Phys. Rev. Lett. **94**, 037601.

Barnard, E. S., T. Coenen, E. J. R. Vesseur, A. Polman, and M. L. Brongersma, 2011, Nano Lett. **11**, 4265.

Barnes, W. L., A. Dereux, and T. W. Ebbesen, 2003, Nature (London) **424**, 824.

Baroni, S., S. de Gironcoli, A. Dal Corso, and Paolo Giannozzi, 2001, Rev. Mod. Phys. **73**, 515.

Barrow, S. J., D. Rossouw, A. M. Funston, G. A. Botton, and P. Mulvaney, 2014, Nano Lett. **14**, 3799.

Barwick, B., C. Corder, J. Strohaber, N. Chandler-Smith, C. Uiterwaal, and H. Batelaan, 2007, New J. Phys. **9**, 142.

Barwick, B., D. J. Flannigan, and A. H. Zewail, 2009, Nature (London) **462**, 902.

Bashevoy, M. V., F. Jonsson, K. F. MacDonald, Y. Chen, and N. I. Zheludev, 2007, Opt. Express **15**, 11313.

Batelaan, H., and A. Tonomura, 2009, Phys. Today **62**, No. 9, 38.

Bauer, M., A. Marienfeld, and M. Aeschlimann, 2015, Prog. Surf. Sci. **90**, 319.

Baum, P., and A. H. Zewail, 2006, Proc. Natl. Acad. Sci. U.S.A. **103**, 16105.

Baum, P., and A. H. Zewail, 2007, Proc. Natl. Acad. Sci. U.S.A. **104**, 18409.

Bayer, D., C. Wiemann, O. Gaier, M. Bauer, and M. Aeschlimann, 2008, J. Nanomater. **2008**, 249514.

Bechtel, J. H., W. L. Smith, and N. Bloembergen, 1975, Opt. Commun. **13**, 56.

Becker, S. F., M. Esmann, K. W. Yoo, P. Groß, R. Vogelgesang, N. K. Park, and C. Lienau, 2016, ACS Photonics **3**, 223.

Becker, W., F. Grasbon, R. Kopold, D. B. Milošević, G. G. Paulus, and H. Walther, 2002, Adv. At. Mol. Opt. Phys. **48**, 35.

Behr, N., and M. B. Raschke, 2008, J. Phys. Chem. C **112**, 3766.

Bek, A., R. Vogelgesang, and K. Kern, 2006, Rev. Sci. Instrum. **77**, 043703.

Bennett, A. J., 1970, Phys. Rev. B **1**, 203.

Benz, F., *et al.*, 2016, Science **354**, 726.

Berciaud, S., L. Cognet, G. A. Blab, and B. Lounis, 2004, Phys. Rev. Lett. **93**, 257402.

Berini, P., 1999, Opt. Lett. **24**, 1011.

Berini, P., 2000, Phys. Rev. B **61**, 10484.

Berini, P., 2001, Phys. Rev. B **63**, 125417.

Berweger, S., J. M. Atkin, R. L. Olmon, and M. B. Raschke, 2010, J. Phys. Chem. Lett. **1**, 3427.

Berweger, S., J. M. Atkin, R. L. Olmon, and M. B. Raschke, 2012, J. Phys. Chem. Lett. **3**, 945.

Berweger, S., J. M. Atkin, X. G. Xu, R. L. Olmon, and M. B. Raschke, 2011, Nano Lett. **11**, 4309.

Bethe, H. A., and A. Sommerfeld, 1967, *Elektronentheorie der Metalle* (Springer-Verlag, Berlin), 290.

Betzig, E., J. K. Trautman, T. D. Harris, J. S. Weiner, and R. L. Kostelak, 1991, Science **251**, 1468.

Beyer, A., and A. Gölzhäuser, 2010, J. Phys. Condens. Matter **22**, 343001.

Biagioni, P., J. S. Huang, and B. Hecht, 2012, Rep. Prog. Phys. **75**, 024402.

Blancon, J. C., *et al.*, 2018, Nat. Commun. **9**, 2254.

Bliokh, K. Y., and F. Nori, 2012, Phys. Rev. A **85**, 061801(R).

Bliokh, K. Y., F. J. Rodriguez-Fortuno, F. Nori, and A. V. Zayats, 2015, Nat. Photonics **9**, 796.

Bloembergen, N., R. K. Chang, S. S. Jha, and C. H. Lee, 1968, Phys. Rev. **174**, 813.

Blum, C., *et al.*, 2014, J. Raman Spectrosc. **45**, 22.

Blundell, S. A., and C. Guet, 1993 Z. Phys. D **28**, 81.

Bohm, D., and D. Pines, 1953, Phys. Rev. **92**, 609.

Bohren, C. F., and D. R. Huffman, 1983, *Absorption and Scattering of Light by Small Particles* (Wiley, New York), 530.

Bonaccorso, F., G. Calogero, G. Di Marco, O. M. Marago, P. G. Gucciardi, U. Giorgianni, K. Channon, and G. Sabatino, 2007, Rev. Sci. Instrum. **78**, 103702.

Borisov, A. G., P. M. Echenique, and A. K. Kazansky, 2012, New J. Phys. **14**, 023036.

Bormann, R., M. Gulde, A. Weisman, S. V. Yalunin, and C. Ropers, 2010, Phys. Rev. Lett. **105**, 147601.

Borz, M., *et al.*, 2019, Nanoscale **11**, 6852.

Bosman, M., V. J. Keast, J. L. García-Muñoz, A. J. D'Alfonso, S. D. Findlay, and L. J. Allen, 2007, Phys. Rev. Lett. **99**, 086102.

Boudarham, G., N. Feth, V. Myroshnychenko, S. Linden, J. G. de Abajo, M. Wegener, and M. Kociak, 2010, Phys. Rev. Lett. **105**, 255501.

Boudarham, G., and M. Kociak, 2012, Phys. Rev. B **85**, 245447.

Bouhelier, A., M. Beversluis, A. Hartschuh, and L. Novotny, 2003, Phys. Rev. Lett. **90**, 013903.

Bouwmeester, D., I. Marzoli, G. P. Karman, W. Schleich, and J. P. Woerdman, 1999, Phys. Rev. A **61**, 013410.

Bovensiepen, U., H. Petek, and M. Wolf, 2012, *Dynamics at Solid State Surfaces and Interfaces, Volume 2: Fundamentals*, 1st ed. (Wiley-VCH, Weinheim).

Bovensiepen, U., M. Wolf, and H. Petek, 2010, *Dynamics at Solid State Surfaces and Interfaces, Volume 1: Current Developments* (Wiley-VCH, Weinheim).

Boyd, R. W., 2003, *Nonlinear Optics*, 2nd ed. (Academic Press, New York).

Boyer, D., P. Tamarat, A. Maali, B. Lounis, and M. Orrit, 2002, Science **297**, 1160.

Bozhevolnyi, S. I., J. Beermann, and V. Coello, 2003, Phys. Rev. Lett. **90**, 197403.

Breit, M., V. A. Podolskiy, S. Gresillon, G. von Plessen, J. Feldmann, J. C. Rivoal, P. Gadenne, A. K. Sarychev, and V. M. Shalaev, 2001, Phys. Rev. B **64**, 125106.

Breuer, J., and P. Hommelhoff, 2013, Phys. Rev. Lett. **111**, 134803.

Brixner, T., J. Stenger, H. M. Vaswani, M. Cho, R. E. Blankenship, and G. R. Fleming, 2005, Nature (London) **434**, 625.

Brown, F., R. E. Parks, and A. M. Sleeper, 1965, Phys. Rev. Lett. **14**, 1029.

Budai, J., Z. Pápa, I. Márton, P. Wróbel, T. Stefaniuk, Z. Márton, P. Rácz, and P. Dombi, 2018, Nanoscale **10**, 16261.

Bunkin, F. V., and M. V. Fedorov, 1965, Zh. Eksp. Teor. Fiz. **48**, 1341.

Busuladzic, M., A. Gazibegovic-Busuladzic, and D. B. Milosevic, 2006, Laser Phys. **16**, 289.

Butet, J., P. F. Brevet, and O. J. F. Martin, 2015, ACS Nano **9**, 10545.

Butet, J., J. Duboisset, G. Bachelier, I. Russier-Antoine, E. Benichou, C. Jonin, and P.-F. Brevet, 2010, Nano Lett. **10**, 1717.

Calegari, F., A. Trabattoni, A. Palacios, D. Ayuso, M. C. Castrovilli, J. B. Greenwood, P. Decleva, F. Martín, and M. Nisoli, 2016, J. Phys. B **49**, 142001, and references therein.

Calvayrac, F., P.-G. Reinhard, E. Suraud, and C. A. Ullrich, 2000, Phys. Rep. **337**, 493.

Campion, A., and P. Kambhampati, 1998, Chem. Soc. Rev. **27**, 241.

Carminati, R., A. Cazé, D. Cao, F. Peragut, V. Krachmalnicoff, R. Pierrat, and Y. De Wilde, 2015, Surf. Sci. Rep. **70**, 1.

Caulfield, H. J., and S. Dolev, 2010, Nat. Photonics **4**, 261.

Cavalieri, A. L., *et al.*, 2007, Nature (London) **449**, 1029.

Cazalilla, M. A., J. S. Dolado, A. Rubio, and P. M. Echenique, 2000, Phys. Rev. B **61**, 8033.

Celebrano, M., *et al.*, 2015, Nat. Nanotechnol. **10**, 412.

Chaturvedi, P., K. H. Hsu, A. Kumar, K. H. Fung, J. C. Mabon, and N. X. Fang, 2009, ACS Nano **3**, 2965.

Chen, H., J. Boneberg, and P. Leiderer, 1993, Phys. Rev. B **47**, 9956.

Chen, H.-T., R. Kersting, and G. Cheon Cho, 2003, Appl. Phys. Lett. **83**, 3009.

Chen, J., *et al.*, 2012, Nature (London) **487**, 77.

Chen, L., Y. Zhang, G. H. Chen, and I. Franco, 2018, Nat. Commun. **9**, 2070.

Chew, S. H., *et al.*, 2012, Appl. Phys. Lett. **100**, 051904.

Chiang, C. T., A. Blattermann, M. Huth, J. Kirschner, and W. Widdra, 2012, Appl. Phys. Lett. **101**, 071116.

Chikkaraddy, R., B. de Nijs, F. Benz, S. J. Barrow, O. A. Scherman, E. Rosta, A. Demetriadou, P. Fox, O. Hess, and J. J. Baumberg, 2016, Nature (London) **535**, 127.

Chu, M.-W., V. Myroshnychenko, C. H. Chen, J.-P. Deng, C.-Y. Mou, and F. J. G. de Abajo, 2009, Nano Lett. **9**, 399.

Chulkov, E. V., V. M. Silkin, and P. M. Echenique, 1999, Surf. Sci. **437**, 330.

Chulkov, E. V., A. G. Borisov, J. P. Gauyacq, D. Sánchez-Portal, V. M. Silkin, V. P. Zhukov, and P. M. Echenique, 2006, Chem. Rev. **106**, 4160.

Ciappina, M. F., S. S. Aćimović, T. Shaaran, J. Biegert, R. Quidant, and M. Lewenstein, 2012, Opt. Express **20**, 26261.

Ciappina, M. F., *et al.*, 2017, Rep. Prog. Phys. **80**, 054401.

Cinchetti, M., A. Gloskovskii, S. A. Nepjiko, G. Schoenhense, H. Rochholz, and M. Kreiter, 2005, Phys. Rev. Lett. **95**, 047601.

Cingöz, A., D. C. Yost, T. K. Allison, A. Ruehl, M. E. Fermann, I. Hartl, and J. Ye, 2012, Nature (London) **482**, 68.

Ciraci, C., J. B. Pendry, and D. R. Smith, 2013, ChemPhysChem **14**, 1109.

Ciraci, C., E. Poutrina, M. Scalora, and D. R. Smith, 2012, Phys. Rev. B **86**, 115451.

Cocker, T. L., V. Jelic, M. Gupta, S. J. Molesky, J. A. J. Burgess, G. De Los Reyes, L. V. Titova, Y. Y. Tsui, M. R. Freeman, and F. A. Hegmann, 2013, Nat. Photonics **7**, 620.

Cocker, T. L., D. Peller, P. Yu, J. Repp, and R. Huber, 2016, Nature (London) **539**, 263.

Coenen, T., D. T. Schoen, B. J. Brenny, A. Polman, and M. L. Brongersma, 2016, Phys. Rev. B **93**, 195429.

Corkum, P. B., 1993, Phys. Rev. Lett. **71**, 1994.

Costa, L., M. Betz, M. Spasenovic, A. D. Bristow, and H. M. van Driel, 2007, Nat. Phys. **3**, 632.

Cox, J. D., A. Marini, and F. J. García de Abajo, 2017, Nat. Commun. **8**, 14380.

Crowell, C. R., 1965, Solid State Electron. **8**, 395.

Curto, A. G., G. Volpe, T. H. Taminiau, M. P. Kreuzer, R. Quidant, and N. F. van Hulst, 2010, Science **329**, 930.

Cutler, P. H., T. E. Feuchtwang, T. T. Tsong, H. Nguyen, and A. A. Lucas, 1987, Phys. Rev. B **35**, 7774.

Dabrowski, M., Y. Dai, A. Argondizzo, Q. Zou, X. Cui, and H. Petek, 2016, ACS Photonics **3**, 1704.

Dabrowski, M., Y. Dai, and H. Petek, 2017, J. Phys. Chem. Lett. **8**, 4446.

Dai, Y., M. Dabrowski, V. A. Apkarian, and H. Petek, 2018, ACS Nano **12**, 6588.

Dai, Y, and H. Petek, 2019, ACS Photonics **6**, 2005.

Danckwerts, M., and L. Novotny, 2007, Phys. Rev. Lett. **98**, 026104.

de Abajo, F. J. G., 2010, Rev. Mod. Phys. **82**, 209.

de Abajo, F. J. G., A. Asenjo-Garcia, and M. Kociak, 2010, Nano Lett. **10**, 1859.

de Abajo, F. J. G., and M. Kociak, 2008a, Phys. Rev. Lett. **100**, 106804.

de Abajo, F. J. G., and M. Kociak, 2008b, New J. Phys. **10**, 073035.

De Angelis, F., *et al.*, 2010, Nat. Nanotechnol. **5**, 67.
De Angelis, F., *et al.*, 2011, Nat. Photonics **5**, 682.
De Sio, A., and C. Lienau, 2017, Phys. Chem. Chem. Phys. **19**, 18813.
De Sio, A., *et al.*, 2016, Nat. Commun. **7**, 13742.
Deckert-Gaudig, T., A. Taguchi, S. Kawata, and V. Deckert, 2017, Chem. Soc. Rev. **46**, 4077.
Deeb, C. R., *et al.*, 2010, ACS Nano **4**, 4579.
Della Valle, G., M. Conforti, S. Longhi, G. Cerullo, and D. Brida, 2012, Phys. Rev. B **86**, 155139.
des Francs, G. C., C. Girard, J.-C. Weeber, C. Chicane, T. David, A. Dereux, and D. Peyrade, 2001, Phys. Rev. Lett. **86**, 4950.
Deutsch, B., R. Hillenbrand, and L. Novotny, 2010, Nano Lett. **10**, 652.
Dhawan, A., S. J. Norton, M. D. Gerhold, and T. Vo-Dinh, 2009, Opt. Express **17**, 9688.
Dolocan, A., D. P. Acharya, P. Zahl, P. Sutter, and N. Camillone, III, 2011, J. Phys. Chem. C **115**, 10033.
Dombi, P., A. Hörl, P. Rácz, I. Márton, A. Trügler, J. R. Krenn, and U. Hohenester, 2013, Nano Lett. **13**, 674.
Dombi, P., *et al.*, 2004, New J. Phys. **6**, 39.
Dombi, P., *et al.*, 2010, Opt. Express **18**, 24206.
Domer, H., and O. Bostanjoglo, 2003, Rev. Sci. Instrum. **74**, 4369.
Donati, G. P., G. Rodriguez, and A. J. Taylor, 2000, J. Opt. Soc. Am. B **17**, 1077.
Dorfmüller, J., R. Vogelgesang, W. Khunsin, C. Rockstuhl, C. Etrich, and K. Kern, 2010, Nano Lett. **10**, 3596.
Dorfmüller, J., R. Vogelgesang, R. T. Weitz, C. Rockstuhl, C. Etrich, T. Pertsch, F. Lederer, and K. Kern, 2009, Nano Lett. **9**, 2372.
Drescher, M., M. Hentschel, R. Kienberger, G. Tempea, Ch. Spielmann, G. A. Reider, P. B. Corkum, and F. Krausz, 2001, Science **291**, 1923.
Drude, P., 1900, Ann. Phys. (Berlin) **306**, 566.
Duan, H., A. I. Fernández-Domínguez, M. Bosman, S. A. Maier, and J. K. Yang, 2012, Nano Lett. **12**, 1683.
Durach, M., A. Rusina, M. F. Kling, and M. I. Stockman, 2010, Phys. Rev. Lett. **105**, 086803.
Durach, M., A. Rusina, M. F. Kling, and M. I. Stockman, 2011, Phys. Rev. Lett. **107**, 086602.
Durach, M., A. Rusina, M. I. Stockman, and K. Nelson, 2007, Nano Lett. **7**, 3145.
Ebbesen, T. W., H. J. Lezec, H. F. Ghaemi, T. Thio, and P. A. Wolff, 1998, Nature (London) **391**, 667.
Echenique, P. M., R. Berndt, E. V. Chulkov, T. H. Fausterd, A. Goldmann, and U. Hofer, 2004, Surf. Sci. Rep. **52**, 219.
Echternkamp, K. E., A. Feist, S. Schafer, and C. Ropers, 2016, Nat. Phys. **12**, 1000.
Echternkamp, K. E., G. Herink, S. V. Yalunin, K. Rademann, S. Schäfer, and C. Ropers, 2016, Appl. Phys. B **122**, 80.
Eguiluz, A. G., D. A. Campbell, A. A. Maradudin, and R. F. Wallis, 1984, Phys. Rev. B **30**, 5449.
Ehberger, D., J. Hammer, M. Eisele, M. Krüger, J. Noe, A. Högele, and P. Hommelhoff, 2015, Phys. Rev. Lett. **114**, 227601.
Ehberger, D., C. Kealhofer, and P. Baum, 2018, Struct. Dyn. **5**, 044303.
Einstein, A., 1905, Ann. Phys. (Berlin) **322**, 132.
Eisele, M., T. L. Cocker, A. M. Huber, M. Plankl, L. Viti, D. Ercolani, L. Sorba, M. S. Vitiello, and R. Huber, 2014, Nat. Photonics **8**, 841.
Emiliani, V., T. Guenther, C. Lienau, R. Nötzel, and K. H. Ploog, 2000, Phys. Rev. B **61**, R10583.
Engel, G. S., T. R. Calhoun, E. L. Read, T.-K. Ahn, T. Mancal, Y.-C. Cheng, R. E. Blankenship, and G. R. Fleming, 2007, Nature (London) **446**, 782.
England, R. J., *et al.*, 2014, Rev. Mod. Phys. **86**, 1337.
Esmann, M., S. F. Becker, J. Witt, A. Chimeh, A. Korte, J. Zhong, R. Vogelgesang, G. Wittstock, and C. Lienau, 2019, Nat. Nanotechnol. **14**, 698.
Esteban, R., R. Vogelgesang, J. Dorfmüller, A. Dmitriev, C. Rockstuhl, C. Etrich, and K. Kern, 2008, Nano Lett. **8**, 3155.
Etchegoin, P. G., E. C. Le Ru, and M. Meyer, 2006, J. Chem. Phys. **125**, 164705.
Fabiańska, J., G. Kassier, and T. Feurer, 2015, Sci. Rep. **4**, 5645.
Faisal, F. H. M., 1973, J. Phys. B **6**, L89.
Faisal, F. H. M., J. Z. Kamiński, and E. Saczuk, 2005, Phys. Rev. A **72**, 023412.
Fang, Y., N.-H. Seong, and D. D. Dlott, 2008, Science **321**, 388.
Fann, W. S., R. Storz, H. W. K. Tom, and J. Brokor, 1992, Phys. Rev. B **46**, 13592.
Farkas, G., Z. G. Horváth, and I. Kertész, 1972, Phys. Lett. **39A**, 231.
Farkas, G., Z. S. Náray, and P. Varga, 1967, Phys. Lett. **24A**, 134.
Fei, Z., *et al.*, 2012, Nature (London) **487**, 82.
Feibelman, P. J., 1982, Prog. Surf. Sci. **12**, 287.
Feist, A., K. E. Echternkamp, J. Schauss, S. V. Yalunin, S. Schäfer, and C. Ropers, 2015, Nature (London) **521**, 200.
Feist, A., K. E. Priebe, C. Rathje, T. Rittmann, S. V. Yalunin, T. Hohage, S. Schäfer, and C. Ropers, 2018, in *Proceedings of the Conference on Lasers and Electro-Optics (CLEO), Quantum Coherent Transverse and Longitudinal Control for Attosecond Shaping of Free Electron Beams* (Optical Society of America, Washington, DC).
Feist, A., *et al.*, 2017, Ultramicroscopy **176**, 63.
Feit, M. D., J. A. Fleck, and A. Steiger, 1982, J. Comput. Phys. **47**, 412.
Ferray, M., A. L'Huillier, X. F. Li, L. A. Lompre, G. Mainfray, and C. Manus, 1988, J. Phys. B **21**, L31.
Feth, N., *et al.*, 2008, Opt. Lett. **33**, 1975.
Fetić, B., and D. B. Milošević, 2013, J. Mod. Opt. **60**, 1466.
Fink, H.-W., W. Stocker, and H. Schmid, 1990, Phys. Rev. Lett. **65**, 1204.
Fischer, M. P., *et al.*, 2018, Light Sci. Appl. **7**, 106.
Flannigan, D. J., and A. H. Zewail, 2012, Acc. Chem. Res. **45**, 1828.
Forbes, R. G., 2006, Appl. Phys. Lett. **89**, 113122.
Förg, B., *et al.*, 2016, Nat. Commun. **7**, 11717.
Förster, M., T. Paschen, M. Krüger, C. Lemell, G. Wachter, F. Libisch, T. Madlener, J. Burgdörfer, and P. Hommelhoff, 2016, Phys. Rev. Lett. **117**, 217601.
Fowler, R. H., and L. Nordheim, 1928, Proc. R. Soc. A **119**, 173.
Franco, I., M. Shapiro, and P. Brumer, 2007, Phys. Rev. Lett. **99**, 126802.
Franken, P. A., A. E. Hill, C. W. Peters, and G. Weinreich, 1961, Phys. Rev. Lett. **7**, 118.
Freimund, D. L., K. Aflatooni, and H. Batelaan, 2001, Nature (London) **413**, 142.
Frischkorn, C., and M. Wolf, 2006, Chem. Rev. **106**, 4207.
Frühling, U., *et al.*, 2009, Nat. Photonics **3**, 523.
Gabor, D., 1948, Nature (London) **161**, 777.
Gadzuk, J. W., and E. W. Plummer, 1971, Phys. Rev. Lett. **26**, 92.
García-Etxarri, A., I. Romero, F. J. G. de Abajo, R. Hillenbrand, and J. Aizpurua, 2009, Phys. Rev. B **79**, 125439.
Gauthier, D., *et al.*, 2019, Opt. Lett. **44**, 546.
Geldhauser, T., A. Kolloch, N. Murazawa, K. Ueno, J. Boneberg, P. Leiderer, E. Scheer, and H. Misawa, 2012, Langmuir **28**, 9041.
Gerstner, V., A. Knoll, W. Pfeiffer, A. Thon, and G. Gerber, 2000, J. Appl. Phys. **88**, 4851.

Gertsvolf, M., M. Spanner, D. M. Rayner, and P. B. Corkum, 2010, J. Phys. B **43**, 131002.

Ghenuche, P., S. Cherukulappurath, T. H. Taminiau, N. F. van Hulst, and R. Quidant, 2008, Phys. Rev. Lett. **101**, 116805.

Ghimire, S., A. D. DiChiara, E. Sistrunk, P. Agostini, L. F. DiMauro, and D. A. Reis, 2011, Nat. Phys. **7**, 138.

Glauber, R. J., and M. Lewenstein, 1991, Phys. Rev. A **43**, 467.

Gliserin, A., M. Walbran, F. Krausz, and P. Baum, 2015, Nat. Commun. **6**, 8723.

Goeppert-Mayer, M., 1931, Ann. Phys. (Berlin) **401**, 273.

Gohle, C., M. Herrmann, J. Rauschenberger, R. Holzwarth, H. A. Schuessler, F. Krausz, and T. W. Hänsch, 2005, Nature (London) **436**, 234.

Gómez-Medina, R., N. Yamamoto, M. Nakano, and F. J. G. de Abajo, 2008, New J. Phys. **10**, 105009.

Gorodetski, Y., A. Niv, V. Kleiner, and E. Hasman, 2008, Phys. Rev. Lett. **101**, 043903.

Goulielmakis, E., *et al.*, 2004, Science **305**, 1267.

Grafström, S., P. Schuller, J. Kowalski, and R. Neumann, 1998, J. Appl. Phys. **83**, 3453.

Gramotnev, D. K., 2005, J. Appl. Phys. **98**, 104302.

Gramotnev, D. K., and S. I. Bozhevolnyi, 2010, Nat. Photonics **4**, 83.

Gramotnev, D. K., and S. I. Bozhevolnyi, 2014, Nat. Photonics **8**, 13.

Gramotnev, D. K., M. W. Vogel, and M. I. Stockman, 2008, J. Appl. Phys. **104**, 034311.

Greffet, J. J., and R. Carminati, 1997, Prog. Surf. Sci. **56**, 133.

Greig, S. R., and A. Y. Elezzabi, 2014, Appl. Phys. Lett. **105**, 041115.

Gresillon, S., L. Aigouy, A. C. Boccara, J. C. Rivoal, X. Quelin, C. Desmarest, P. Gadenne, V. A. Shubin, A. K. Sarychev, and V. M. Shalaev, 1999, Phys. Rev. Lett. **82**, 4520.

Grguraš, I., 2015, Ph.D. thesis (Universität Hamburg).

Groeneveld, R. H. M., and H. van Kempen, 1996, Appl. Phys. Lett. **69**, 2294.

Groß, P., M. Esmann, S. F. Becker, J. Vogelsang, N. Talebi, and C. Lienau, 2016, Adv. Phys. X **1**, 297.

Großmann, M., *et al.*, 2015, ACS Photonics **2**, 1327–1332.

Grubisic, A., E. Ringe, C. M. Cobley, Y. Xia, L. D. Marks, R. P. Van Duyne, and D. J. Nesbitt, 2012, Nano Lett. **12**, 4823.

Guenther, T., V. Emiliani, F. Intonti, C. Lienau, and T. Elsaesser, 1999, Appl. Phys. Lett. **75**, 3500.

Guenther, T., C. Lienau, T. Elsaesser, M. Glanemann, V. M. Axt, and T. Kuhn, 2002, Phys. Rev. Lett. **89**, 057401.

Guo, S., N. Talebi, W. Sigle, M. Esmann, S. F. Becker, R. Vogelgesang, C. Lienau, and P. A. van Aken, 2015, *Proceedings of the European Conference on Lasers and Electro-Optics* (Optical Society of America, Washington, DC).

Guo, S., N. Talebi, W. Sigle, R. Vogelgesang, G. Richter, M. Esmann, S. F. Becker, C. Lienau, and P. A. van Aken, 2016, Nano Lett. **16**, 6137.

Haberland, H., 2013, Nature (London) **494**, E1.

Hafez, H. A., *et al.*, 2018, Nature (London) **561**, 507.

Haight, R., J. Bokor, J. Stark, R. H. Storz, R. R. Freeman, and P. H. Bucksbaum, 1985, Phys. Rev. Lett. **54**, 1302.

Halas, N. J., S. Lal, W.-S. Chang, S. Link, and P. Nordlander, 2011, Chem. Rev. **111**, 3913.

Hamann, H. F., A. Gallagher, and D. J. Nesbitt, 1998, Appl. Phys. Lett. **73**, 1469.

Han, S., H. Kim, Y. W. Kim, Y.-J. Kim, S. Kim, I.-Y. Park, and S.-W. Kim, 2016, Nat. Commun. **7**, 13105.

Hanke, T, G. Krauss, D. Träutlein, B. Wild, R. Bratschitsch, and A. Leitenstorfer, 2009, Phys. Rev. Lett. **103**, 257404.

Hanke, T., J. Cesar, V. Knittel, A. Trügler, U. Hohenester, A. Leitenstorfer, and R. Bratschitsch, 2012, Nano Lett. **12**, 992.

Harrison, R. K., and A. Ben-Yakar, 2010, Opt. Express **18**, 22556.

Hartschuh, A., E. J. Sanchez, X. S. Xie, and L. Novotny, 2003, Phys. Rev. Lett. **90**, 095503.

Hayazawa, N., Y. Inouye, Z. Sekkat, and S. Kawata, 2000, Opt. Commun. **183**, 333.

Hecht, B., H. Bielefeldt, L. Novotny, Y. Inouye, and D. W. Pohl, 1996, Phys. Rev. Lett. **77**, 1889.

Heilweil, E. J., and R. M. Hochstrasser, 1985, J. Chem. Phys. **82**, 4762.

Heinz, T. F., C. K. Chen, D. Ricard, and Y. R. Shen, 1982, Phys. Rev. Lett. **48**, 478.

Henneberger, W. C., 1968, Phys. Rev. Lett. **21**, 838.

Hentschel, M., R. Kienberger, C. Spielmann, G. A. Reider, N. Milosevic, T. Brabec, P. B. Corkum, U. Heinzmann, M. Drescher, and F. Krausz, 2001, Nature (London) **414**, 509.

Hentschel, M., T. Utikal, H. Giessen, and M. Lippitz, 2012, Nano Lett. **12**, 3778.

Hergert, G., J. Vogelsang, F. Schwarz, D. Wang, H. Kollmann, P. Groß, C. Lienau, E. Runge, and P. Schaaf, 2017, Light Sci. Appl. **6**, e17075.

Herink, G., D. R. Solli, M. Gulde, and C. Ropers, 2012, Nature (London) **483**, 190.

Herink, G., L. Wimmer, and C. Ropers, 2014, New J. Phys. **16**, 123005.

Hertz, H., 1887, Ann. Phys. (Berlin) **267**, 983.

Higuchi, T., L. Maisenbacher, A. Liehl, P. Dombi, and P. Hommelhoff, 2015, Appl. Phys. Lett. **106**, 051109.

Hillenbrand, R., and F. Keilmann, 2000, Phys. Rev. Lett. **85**, 3029.

Hillenbrand, R., and F. Keilmann, 2001, Appl. Phys. B **73**, 239.

Hillenbrand, R., and F. Keilmann, 2002, Appl. Phys. Lett. **80**, 25.

Hillenbrand, R., T. Taubner, and F. Keilmann, 2002, Nature (London) **418**, 159.

Hirori, H., A. Doi, F. Blanchard, and K. Tanaka, 2011, Appl. Phys. Lett. **98**, 091106.

Hofmann, C. E., E. J. R. Vesseur, L. A. Sweatlock, H. J. Lezec, F. J. G. de Abajo, A. Polman, and H. A. Atwater, 2007, Nano Lett. **7**, 3612.

Hohenester, U., H. Ditlbacher, and J. R. Krenn, 2009, Phys. Rev. Lett. **103**, 106801.

Hohng, S. C., *et al.*, 2002, Appl. Phys. Lett. **81**, 3239.

Hommelhoff, P., C. Kealhofer, and M. A. Kasevich, 2006, Phys. Rev. Lett. **97**, 247402.

Hommelhoff, P., and M. Kling, 2015, Eds., *Attosecond Nanophysics: From Basic Science to Applications* (John Wiley & Sons, New York).

Hommelhoff, P., Y. Sortais, A. Aghajani-Talesh, and M. A. Kasevich, 2006, Phys. Rev. Lett. **96**, 077401.

Hörl, A., A. Trügler, U. Hohenester, 2013, Phys. Rev. Lett. **111**, 076801.

Horneber, A., K. Braun, J. Rogalski, P. Leiderer, A. J. Meixnera, and D. Zhang, 2015, Phys. Chem. Chem. Phys. **17**, 21288.

Houdellier, F., G. M. Caruso, S. Weber, M. Kociak, and A. Arbouet, 2018, Ultramicroscopy **186**, 128.

Hovel, H., S. Fritz, A. Hilger, U. Kreibig, and M. Vollmer, 1993, Phys. Rev. B **48**, 18178.

Hrelescu, C., T. K. Sau, A. L. Rogach, F. Jäckel, G. Laurent, L. Douillard, and F. Charra, 2011, Nano Lett. **11**, 402.

Hu, M., C. Novo, A. Funston, H. N. Wang, H. Staleva, S. L. Zou, P. Mulvaney, Y. N. Xia, and G. V. Hartland, 2008, J. Mater. Chem. **18**, 1949.

Huang, J. S., *et al.*, 2010, Nat. Commun. **1**, 8.

Huang, W. C.-W., M. Becker, J. Beck, and H. Batelaan, 2017, New J. Phys. **19**, 023011.

Huber, A. J., F. Keilmann, J. Wittborn, J. Aizpurua, and R. Hillenbrand, 2008, Nano Lett. **8**, 3766.

Huber, B., *et al.*, 2019, Rev. Sci. Instrum. **90**, 113103.

Huber, M. A., *et al.*, 2017, Nat. Nanotechnol. **12**, 207.

Hüfner, S., 2003, *Photoelectron Spectroscopy* (Springer-Verlag, Berlin).

Hulst, H. C., 1981, *Light Scattering by Small Particles* (Dover Publications, New York), p. 470.

Husakou, A., S.-J. Im, and J. Herrmann, 2011, Phys. Rev. A **83**, 043839.

Husnik, M., S. Linden, R. Diehl, J. Niegemann, K. Busch, and M. Wegener, 2012, Phys. Rev. Lett. **109**, 233902.

Husu, H., R. Siikanen, J. Mäkitalo, J. Lehtolahti, J. Laukkanen, M. Kuittinen, and M. Kauranen, 2012, Nano Lett. **12**, 673.

Ichimura, T., N. Hayazawa, M. Hashimoto, Y. Inouye, and S. Kawata, 2004, Phys. Rev. Lett. **92**, 220801.

Imaeda, K., S. Hasegawa, and K. Imura, 2018, J. Phys. Chem. Lett. **9**, 4075.

Imasaka, K., T. Kaji, T. Shimura, and S. Ashihara, 2018, Opt. Express **26**, 21364.

Imura, K., and H. Okamoto, 2009, J. Phys. Chem. C **113**, 11756.

Inouye, Y., and S. Kawata, 1994, Opt. Lett. **19**, 159.

Irvine, S. E., A. Dechant, and A. Y. Elezzabi, 2004, Phys. Rev. Lett. **93**, 184801.

Issa, N., and R. Guckenberger, 2007, Plasmonics **2**, 31.

Itatani, J., J. Levesque, D. Zeidler, H. Niikura, H. Pepin, J. C. Kieffer, P. B. Corkum, and D. M. Villeneuve, 2004, Nature (London) **432**, 867.

Itatani, J., F. Quéré, G. L. Yudin, M. Yu. Ivanov, F. Krausz, and P. B. Corkum, 2002, Phys. Rev. Lett. **88**, 173903.

Iwaszczuk, K., M. Zalkovskij, A. C. Strikwerda, and P. U. Jepsen, 2015, Optica **2**, 116.

Jang, M. S., and H. Atwater, 2011, Phys. Rev. Lett. **107**, 207401.

Jelic, V., K. Iwaszczuk, P. H. Nguyen, C. Rathje, G. J. Hornig, H. M. Sharum, J. R. Hoffman, M. R. Freeman, and F. A. Hegmann, 2017, Nat. Phys. **13**, 591.

Jennings, P. J., R. O. Jones, and M. Weinert, 1988, Phys. Rev. B **37**, 6113.

Jericho, M. H., and H. J. Kreuzer, 2011, in *Coherent Light Microscopy*, edited by P. Ferraro, A. Wax, and Z. Zalevsky (Springer, Berlin), 46, p. 3.

John, S., 1987, Phys. Rev. Lett. **58**, 2486.

Johnson, P. B., and R. W. Christy, 1972, Phys. Rev. B **6**, 4370.

Jouin, H., and G. Duchateau, 2019, Phys. Rev. A **99**, 013433.

Joulain, K., R. Carminati, J. P. Mulet, and J. J. Greffet, 2003, Phys. Rev. B **68**, 245405.

Kahl, P., D. Podbiel, C. Schneider, A. Makris, S. Sindermann, C. Witt, D. Kilbane, M. Horn-von Hoegen, M. Aeschlimann, and F. Meyer zu Heringdorf, 2018, Plasmonics **13**, 239.

Kahl, P., S. Wall, C. Witt, C. Schneider, D. Bayer, A. Fischer, P. Melchior, M. Horn-von Hoegen, M. Aeschlimann, and F.-J. Meyer zu Heringdorf, 2014, Plasmonics **9**, 1401.

Kampfrath, F., K. Tanaka, and K. A. Nelson, 2013, Nat. Photonics **7**, 680.

Kapitza, P. L., and P. A. M. Dirac, 1933, Proc. Cambridge Philos. Soc. **29**, 297.

Karnetzky, C., P. Zimmermann, C. Trummer, C. Duque Sierra, M. Wörle, R. Kienberger, and A. Holleitner, 2018, Nat. Commun. **9**, 2471.

Karski, M., L. Forster, J. M. Choi, A. Steffen, W. Alt, D. Meschede, and A. Widera, 2009 Science **325**, 174.

Kassier, G. H., K. Haupt, N. Erasmus, E. G. Rohwer, H. M. von Bergmann, H. Schwoerer, S. M. M. Coelho, and F. D. Auret, 2010, Rev. Sci. Instrum. **81**, 105103.

Kauranen, M., and A. Zayats, 2012, Nat. Photonics **6**, 737.

Kawabata, A., and R. Kubo, 1966, J. Phys. Soc. Jpn. **21**, 1765.

Kawasaki, T., T. Yoshida, T. Matsuda, N. Osakabe, and A. Tonomura, 2000, Appl. Phys. Lett. **76**, 1342.

Kazansky, A. K., and P. M. Echenique, 2009, Phys. Rev. Lett. **102**, 177401.

Kealhofer, C., S. M. Foreman, S. Gerlich, and M. A. Kasevich, 2012, Phys. Rev. B **86**, 035405.

Kealhofer, C., W. Schneider, D. Ehberger, A. Ryabov, F. Krausz, and P. Baum, 2016, Science **352**, 429.

Keldysh, L. V., 1965, Sov. Phys. JETP **20**, 1307, http://www.jetp.ac.ru/cgi-bin/dn/e_020_05_1307.pdf.

Kelkensberg, F., A. F. Koenderink, and M. J. J. Vrakking, 2012, New J. Phys. **14**, 093034.

Kern, J., S. Großmann, N. V. Tarakina, T. Häckel, M. Emmerling, M. Kamp, J.-S. Huang, P. Biagioni, J. C. Prangsma, and B. Hecht, 2012, Nano Lett. **12**, 5504.

Khurgin, J. B., 2016, J. Opt. Soc. Am. B **33**, C1.

Khusnatdinov, N. N., T. J. Nagle, and G. Nunes, 2000, Appl. Phys. Lett. **77**, 4434.

Kienberger, R. E., *et al.*, 2004, Nature (London) **427**, 817.

Kim, D.-H., and J. A. del Alamo, 2010, IEEE Electron Device Lett. **31**, 806.

Kim, D.-S., J. Heo, S.-H. Ahn, S. W. Han, W. S. Yun, and Z. H. Kim, 2009, Nano Lett. **9**, 3619.

Kim, J., J. Kim, K. I. Song, S. Q. Lee, E. U. Kim, S. E. Choi, Y. Lee, and K. H. Park, 2003, J. Microsc. **209**, 236.

Kim, J. S., T. LaGrange, B. W. Reed, M. L. Taheri, M. R. Armstrong, W. E. King, N. D. Browning, and G. H. Campbell, 2008, Science **321**, 1472.

Kim, S., J. Jin, Y. J. Kim, I. Y. Park, Y. Kim, and S. W. Kim, 2008, Nature (London) **453**, 757.

Kitzler, M., N. Milosevic, A. Scrinzi, F. Krausz, and T. Brabec, 2002, Phys. Rev. Lett. **88**, 173904.

Klar, T., M. Perner, S. Grosse, G. von Plessen, W. Spirkl, and J. Feldmann, 1998, Phys. Rev. Lett. **80**, 4249.

Klein, M., and G. Schwitzgebel, 1997, Rev. Sci. Instrum. **68**, 3099.

Klein, M. W., C. Enkrich, M. Wegener, and S. Linden, 2006, Science **313**, 502.

Kneipp, K., Y. Wang, H. Kneipp, L. T. Perelman, I. Itzkan, R. Dasari, and M. S. Feld, 1997, Phys. Rev. Lett. **78**, 1667.

Knight, M. W., L. Liu, Y. Wang, L. Brown, S. Mukherjee, N. S. King, H. O. Everitt, P. Nordlander, and N. J. Halas, 2012, Nano Lett. **12**, 6000.

Knoll, B., and F. Keilmann, 1999, Nature (London) **399**, 134.

Knoll, B., and F. Keilmann, 2000, Opt. Commun. **182**, 321.

Knoll, M., and E. Ruska, 1932, Z. Phys. **78**, 318.

Ko, K. D., A. Kumar, K. H. Fung, R. Ambekar, G. L. Liu, N. X. Fang, and K. C. Toussaint, 2011, Nano Lett. **11**, 61.

Koerkamp, K. J. K., S. Enoch, F. B. Segerink, N. F. van Hulst, and L. Kuipers, 2004, Phys. Rev. Lett. **92**, 183901.

Koh, A. L., K. Bao, I. Khan, W. E. Smith, G. Kothleitner, P. Nordlander, S. A. Maier, and D. W. McComb, 2009, ACS Nano **3**, 3015.

Kohn, W., and L. J. Sham, 1965, Phys. Rev. **140**, A1133.

Könenkamp, R., R. C. Word, G. F. Rempfer, T. Dixon, L. Almaraz, and T. Jones, 2010, Ultramicroscopy **110**, 899.

Kozak, M., T. Eckstein, N. Schönenberger, and P. Hommelhoff, 2018, Nat. Phys. **14**, 121.

Kozak, M., J. McNeur, K. J. Leedle, H. Deng, N. Schonenberger, A. Ruehl, I. Hartl, J. S. Harris, R. L. Byer, and P. Hommelhoff, 2017, Nat. Commun. **8**, 14342.

Kozak, M., N. Schonenberger, and P. Hommelhoff, 2018, Phys. Rev. Lett. **120**, 103203.

Krachmalnicoff, V., D. Cao, A. Cazé, E. Castanié, R. Pierrat, N. Bardou, S. Collin, R. Carminati, and Y. De Wilde, 2013, Opt. Express **21**, 11536.

Krause, J. L., K. J. Schafer, and K. C. Kulander, 1992, Phys. Rev. Lett. **68**, 3535.

Krausz, F., and M. Ivanov, 2009, Rev. Mod. Phys. **81**, 163.

Krausz, F., and M. I. Stockman, 2014, Nat. Photonics **8**, 205.

Krauth, J., H. Giessen, and M. Hentschel, 2018, ACS Photonics **5**, 1863.

Kravtsov, V., S. AlMutairi, R. Ulbricht, A. R. Kutayiah, A. Belyanin, and M. B. Raschke, 2018, Phys. Rev. Lett. **120**, 203903.

Kravtsov, V., J. M. Atkin, and M. B. Raschke, 2013, Opt. Lett. **38**, 1322.

Kravtsov, V., R. Ulbricht, J. Atkin, and M. B. Raschke, 2016, Nat. Nanotechnol. **11**, 459.

Kreibig, U., and M. Vollmer, 1995, *Optical Properties of Metal Clusters* (Springer, Berlin), p. 532.

Krenn, J., W. Gotschy, D. Somitsch, A. Leitner, and F. Aussenegg, 1995, Appl. Phys. A **61**, 541.

Kretschmann, E., and H. Raether, 1968, Z. Naturforsch. Teil A **23**, 2135.

Kreuzer, H. J., 1995, Micron **26**, 503.

Kreuzer, H. J., K. Nakamura, A. Wierzbicki, H.-W Fink, and H. Schmid, 1992, "Theory of the Point Source Electron Microscope," Ultramicroscopy **45**, 381–403.

Krivanek, O. L., *et al.*, 2014, Nature (London) **514**, 209.

Kroo, N., J. P. Thost, M. Volcker, W. Krieger, and H. Walther, 1991, Europhys. Lett. **15**, 289.

Kruchinin, S. Y., M. Korbman, and V. S. Yakovlev, 2013, Phys. Rev. B **87**, 115201.

Krüger, M., C. Lemell, G. Wachter, J. Burgdörfer, and P. Hommelhoff, 2018, J. Phys. B **51**, 172001.

Krüger, M., M. Schenk, and P. Hommelhoff, 2011, Nature (London) **475**, 78.

Krüger, M., M. Schenk, P. Hommelhoff, G. Wachter, C. Lemell, and J. Burgdörfer, 2012, New J. Phys. **14**, 085019.

Kubo, A., K. Onda, H. Petek, Z. Sun, Y. S. Jung, and H. K. Kim, 2005, Nano Lett. **5**, 1123.

Kubo, A., N. Pontius, and H. Petek, 2007, Nano Lett. **7**, 470.

Kupersztych, J., P. Monchicourt, and M. Raynaud, 2001, Phys. Rev. Lett. **86**, 5180.

Kurihara, K., K. Yamamoto, J. Takahara, and A. Otomo, 2008, J. Phys. A **41**.

Kurizki, G., M. Shapiro, and P. Brumer, 1989, Phys. Rev. B **39**, 3435.

Kuttge, M., E. J. R. Vesseur, A. F. Koenderink, H. J. Lezec, H. A. Atwater, F. J. G. de Abajo, and A. Polman, 2009, Phys. Rev. B **79**, 113405.

Kuwata, H., H. Tamaru, K. Esumi, and K. Miyano, 2003, Appl. Phys. Lett. **83**, 4625.

Kwon, O., and D. Kim, 2016, Appl. Phys. Lett. **108**, 191112.

Kwon, O., T. Paasch-Colberg, V. Apalkov, B.-K. Kim, J.-J. Kim, M. I. Stockman, and D. Kim, 2016, Sci. Rep. **6**, 21272.

Lagos, M. J., A. Trugler, U. Hohenester, and P. E. Batson, 2017, Nature (London) **543**, 529.

LaGrange, T., B. W. Reed, and D. J. Masiel, 2015, MRS Bull. **40**, 22.

Lamprecht, B., J. R. Krenn, G. Schider, H. Ditlbacher, M. Salerno, N. Felidj, A. Leitner, F. R. Aussenegg, and J. C. Weeber, 2001, Appl. Phys. Lett. **79**, 51.

Landau, L. D., and E. M. Lifshitz, 1965, *Quantum Mechanics: Non-relativistic Theory* (Pergamon, Oxford).

Langer, F., *et al.*, 2016, Nature (London) **533**, 225.

Langer, F., *et al.*, 2018, Nature (London) **557**, 76.

Latychevskaia, T., F. Gehri, and H.-W. Fink, 2010, Opt. Express **18**, 22527.

Latychevskaia, T., F. Wicki, J.-N. Longchamp, C. Escher, and H.-W. Fink, 2016, Nano Lett. **16**, 5469.

Le Feber, B., N. Rotenberg, and L. Kuipers, 2015, Nat. Commun. **6**, 6695.

Le Ru, E. C., and P. G. Etchegoin, 2009, *Principles of Surface-Enhanced Raman Spectroscopy and Related Plasmonic Effects* (Elsevier Science, New York).

Lee, J., K. T. Crampton, N. Tallarida, and V. A. Apkarian, 2019, Nature (London) **568**, 78.

Lee, J., N. Tallarida, X. Chen, L. Jensen, and V. A. Apkarian, 2018, Sci. Adv. **4**, eaat5472.

Lee, J. S., S. Han, J. Shirdel, S. Koo, D. Sadiq, C. Lienau, and N. Park, 2011, Opt. Express **19**, 12342.

Lee, K. G., *et al.*, 2007, Nat. Photonics **1**, 53.

Lee, S.-Y., I.-M. Lee, J. Park, S. Oh, W. Lee, K.-Y. Kim, and B. Lee, 2012, Phys. Rev. Lett. **108**, 213907.

Leforestier, C., *et al.*, 1991, J. Comput. Phys. **94**, 59.

Lehmann, J., S. Camalet, S. Kohler, and P. Hänggi, 2003, Chem. Phys. Lett. **368**, 282.

Lemell, C., B. Solleder, K. Tökéesi, and J. Burgdörfer, 2009, Phys. Rev. A **79**, 062901.

Lemell, C., X.-M. Tong, F. Krausz, and J. Burgdörfer, 2003, Phys. Rev. Lett. **90**, 076403.

Lemke, C., *et al.*, 2014, Nano Lett. **14**, 2431.

Lenard, P., 1902, Ann. Phys. (Berlin) **313**, 149.

Li, C. M., L. E. Urbach, and H. L. Dai, 1994, Phys. Rev. B **49**, 2104.

Li, G., C. Cherqui, N. W. Bigelow, G. Duscher, P. J. Straney, J. E. Millstone, D. J. Masiello, and J. P. Camden, 2015, Nano Lett. **15**, 3465.

Li, G., C. Cherqui, Y. Wu, N. W. Bigelow, P. D. Simmons, P. D. Rack, D. J. Masiello, and J. P. Camden, 2015, J. Phys. Chem. Lett. **6**, 2569.

Li, G.-Q., M. Schreiber, and U. Kleinekathöfer, 2007, Europhys. Lett. **79**, 27006.

Li, J., E. Saydanzad, and U. Thumm, 2017, Phys. Rev. A **95**, 043423.

Li, S., and R. R. Jones, 2016, Nat. Commun. **7**, 13405.

Li, X. F., A. L'Huillier, M. Ferray, L. A. Lompré, and G. Mainfray, 1989, Phys. Rev. A **39**, 5751.

Liao, Q., and U. Thumm, 2014, Phys. Rev. Lett. **112**, 023602.

Liebsch, A., 1997, *Electronic Excitations at Metal Surfaces* (Plenum, New York).

Lin, J., Mueller, J. P. B., Q. Wang, G. Yuan, N. Antoniou, X.-C. Yuan, and F. Capasso, 2013, Science **340**, 332.

Lindfors, K., T. Kalkbrenner, P. Stoller, and V. Sandoghdar, 2004, Phys. Rev. Lett. **93**, 037401.

Lindquist, N. C., J. Jose, S. Cherukulappurath, X. S. Chen, T. W. Johnson, and S. H. Oh, 2013, Laser Photonics Rev. **7**, 453.

Lindquist, N. C., P. Nagpal, A. Lesuffleur, D. J. Norris, and S. H. Oh, 2010, Nano Lett. **10**, 1369.

Lippitz, M., M. A. van Dijk, and M. Orrit, 2005, Nano Lett. **5**, 799.

Liu, H., C. Guo, G. Vampa, J. L. Zhang, T. Sarmiento, M. Xiao, P. H. Bucksbaum, J. Vučković, S. Fan, and D. A. Reis, 2018, Nat. Phys. **14**, 1006.

Liu, H., Y. Li, Y. S. You, S. Ghimire, T. F. Heinz, and D. A. Reis, 2017, Nat. Phys. **13**, 262.

Logothetis, E. M., and P. L. Hartman, 1969, Phys. Rev. **187**, 460.

Lompre, L. A., J. Thebault, and G. Farkas, 1975, Appl. Phys. Lett. **27**, 110.

Longchamp, J.-N., C. Escher, and H.-W. Fink, 2013, J. Vac. Sci. Technol. B **31**, 020605.

Longchamp, J.-N., C. Escher, T. Latychevskaia, and H.-W. Fink, 2014, Ultramicroscopy **145**, 80.

Longchamp, J.-N., T. Latychevskaia, C. Escher, and H.-W. Fink, 2012, Appl. Phys. Lett. **101**, 113117.

Longchamp, J.-N., S. Rauschenbach, S. Abb, C. Escher, T. Latychevskaia, K. Kern, and H.-W. Fink, 2017, Proc. Natl. Acad. Sci. U.S.A. **114**, 1474.

Lorenzo, M., C. Escher, T. Latychevskaia, and H.-W. Fink, 2018, Nano Lett. **18**, 3421.

Losquin, A., and M. Kociak, 2015, ACS Photonics **2**, 1619.

Losquin, A., *et al.*, 2015, Nano Lett. **15**, 1229.

Ludwig, M., G. Aguirregabiria, F. Ritzkowsky, T. Rybka, D. C. Marinica, J. Aizpurua, A. G. Borisov, A. Leitenstorfer, and D. Brida, 2020, Nat. Phys. **16**, 341.

Lugovskoy, A. V., and I. Bray, 1999, Phys. Rev. B **60**, 3279.

Luu, T. T., M. Garg, S. Yu. Kruchinin, A. Moulet, M. Th. Hassan, and E. Goulielmakis, 2015, Nature (London) **521**, 498.

Lyubinetsky, I., Z. Dohnálek, V. A. Ukraintsev, and J. T. Yates, 1997, J. Appl. Phys. **82**, 4115.

MacDonald, K. F., Z. L. Samson, M. I. Stockman, and N. I. Zheludev, 2009, Nat. Photonics **3**, 55.

Maier, S. A., 2006, Opt. Express **14**, 1957.

Maier, S. A., 2007, *Plasmonics: Fundamentals and Applications* (Springer, New York).

Mairesse, Y., and F. Quéré, 2005, Phys. Rev. A **71**, 011401.

Marini, A., R. Del Sole, A. Rubio, and G. Onida, 2002, Phys. Rev. B **66**, 5.

Markel, V. A., V. M. Shalaev, P. Zhang, W. Huynh, L. Tay, T. L. Haslett, and M. Moskovits, 1999, Phys. Rev. B **59**, 10903.

Marsell, E., *et al.*, 2015a, Appl. Phys. Lett. **107**, 201111.

Marsell, E., *et al.*, 2015b, Nano Lett. **15**, 6601.

Marti, O., H. Bielefeldt, B. Hecht, S. Herminghaus, P. Leiderer, and J. Mlynek, 1993, Opt. Commun. **96**, 225.

Mashiko, H., K. Oguri, T. Yamaguchi, A. Suda, and H. Gotoh, 2016, Nat. Phys. **12**, 741.

Mehtani, D., N. Lee, R. D. Hartschuh, A. Kisliuk, M. D. Foster, A. P. Sokolov, F. Caiko, and I. Tsukerman, 2006, J. Opt. A **8**, S183.

Mei, X., *et al.*, 2015, IEEE Electron Device Lett. **36**, 327.

Meier, M., and A. Wokaun, 1983, Opt. Lett. **8**, 581.

Meier, S., T. Higuchi, M. Nutz, A. Högele, and P. Hommelhoff, 2018, Appl. Phys. Lett. **113**, 143101.

Meixner, A. J., M. A. Bopp, and G. Tarrach, 1994, Appl. Opt. **33**, 7995.

Merano, M., *et al.*, 2005, Nature (London) **438**, 479.

Mesch, M., B. Metzger, M. Hentschel, and H. Giessen, 2016, Nano Lett. **16**, 3155.

Metzger, B., M. Hentschel, and H. Giessen, 2017, Nano Lett. **17**, 1931.

Metzger, B., M. Hentschel, T. Schumacher, M. Lippitz, X. C. Ye, C. B. Murray, B. Knabe, K. Buse, and H. Giessen, 2014, Nano Lett. **14**, 2867.

Meyer zu Heringdorf, F.-J., L. I. Chelaru, S. Möllenbeck, D. Thien, and M. Horn-von Hoegen, 2007, Surf. Sci. **601**, 4700.

Mikhailovsky, A. A., M. A. Petruska, K. R. Li, M. I. Stockman, and V. I. Klimov, 2004, Phys. Rev. B **69**, 085401.

Mikhailovsky, A. A., M. A. Petruska, M. I. Stockman, and V. I. Klimov, 2003, Opt. Lett. **28**, 1686.

Mikkelsen, A., *et al.*, 2009, Rev. Sci. Instrum. **80**, 123703.

Miller, D. A. B., 2009, Proc. IEEE **97**, 1166.

Millikan, R. A., 1914, Phys. Rev. **4**, 73.

Millikan, R. A., and C. F. Eyring, 1926, Phys. Rev. **27**, 51.

Millikan, R. A., and C. C. Lauritsen, 1928, Proc. Natl. Acad. Sci. U.S.A. **14**, 45.

Miskovsky, N. M., P. H. Cutler, A. Mayer, B. L. Weiss, B. Willis, T. E. Sullivan, and P. B. Lerner, 2012, J. Nanosci. Nanotechnol. **2012**, 512379.

Mitrofanov, A. V., A. J. Verhoef, E. E. Serebryannikov, J. Lumeau, L. Glebov, A. M. Zheltikov, and A. Baltuska, 2011, Phys. Rev. Lett. **106**, 147401.

Morimoto, Y., and P. Baum, 2018, Nat. Phys. **14**, 252.

Morimoto, Y., R. Kanya, and K. Yamanouchi, 2015, Phys. Rev. Lett. **115**, 123201.

Morton, G. A., and E. G. Ramberg, 1939, Phys. Rev. **56**, 705.

Moskovits, M., 2005, J. Raman Spectrosc. **36**, 485.

Muga, J. G., J. P. Palao, B. Navarro, and I. L. Egusquiza, 2004, Phys. Rep. **395**, 357.

Muhlschlegel, P., H. J. Eisler, O. J. F. Martin, B. Hecht, and D. W. Pohl, 2005, Science **308**, 1607.

Muino, R. D., E. E. Krasovskii, W. Schattke, and C. Lienau, and H. Petek, 2012, in *Dynamics at Solid State Surfaces and Interfaces*, edited by U. Bovensiepen, H. Petek, and M. Wolf (Wiley-VCH, Weinheim), p. 181.

Müller, J., C. Sönnichsen, H. von Poschinger, G. von Plessen, T. A. Klar, and J. Feldmann, 2002, Appl. Phys. Lett. **81**, 171.

Müller, M., V. Kravtsov, A. Paarmann, M. B. Raschke, and R. Ernstorfer, 2016, ACS Photonics **3**, 611.

Müller, M., A. Paarmann, and R. Ernstorfer, 2014, Nat. Commun. **5**, 5292.

Muskens, O. L., P. Billaud, M. Broyer, N. Fatti, and F. Vallee, 2008, Phys. Rev. B **78**, 205410.

Muskens, O. L., N. Del Fatti, F. Vallée, J. R. Huntzinger, P. Billaud, and M. Broyer, 2006, Appl. Phys. Lett. **88**, 063109.

Myroshnychenko, V., J. Rodríguez-Fernández, I. Pastoriza-Santos, A. M. Funston, C. Novo, P. Mulvaney, L. M. Liz-Marzánb, and F. J. G. de Abajo, 2008, Chem. Soc. Rev. **37**, 1792.

Neacsu, C. C., S. Berweger, R. L. Olmon, L. V. Saraf, C. Ropers, and M. B. Raschke, 2010, Nano Lett. **10**, 592.

Neacsu, C. C., J. Dreyer, N. Behr, and M. B. Raschke, 2006, Phys. Rev. B **73**, 193406.

Neacsu, C. C., G. A. Reider, and M. B. Raschke, 2005, Phys. Rev. B **71**, 201402.

Neacsu, C. C., B. B. van Aken, M. Fiebig, and M. B. Raschke, 2009, Phys. Rev. B **79**, 100107.

Nechay, B. A., U. Siegner, M. Achermann, H. Bielefeld, and U. Keller, 1999, Rev. Sci. Instrum. **70**, 2758.

Nelayah, J., L. Gu, W. Sigle, C. T. Koch, I. Pastoriza-Santos, L. M. Liz-Marzán, and P. A. van Aken, 2009, Opt. Lett. **34**, 1003.

Nelayah, J., M. Kociak, O. Stéphan, F. J. García de Abajo, M. Tencé, L. Henrard, D. Taverna, I. Pastoriza-Santos, L. M. Liz-Marzán, and C. Colliex, 2007, Nat. Phys. **3**, 348.

Neuman, T., P. Alonso-González, A. Garcia-Etxarri, M. Schnell, R. Hillenbrand, and J. Aizpurua, 2015, Laser Photonics Rev. **9**, 637.

N'Gom, M., S. Li, G. Schatz, R. Erni, A. Agarwal, N. Kotov, and T. B. Norris, 2009, Phys. Rev. B **80**, 113411.

Nguyen, H. Q., P. H. Cutler, T. E. Feuchtwang, Z.-H. Huang, Y. Kuk, P. J. Silverman, A. A. Lucas, and T. E. Sullivan, 1989, IEEE Trans. Electron Devices **36**, 2671.

Ni, G. X., *et al.*, 2016, Nat. Photonics **10**, 244.

Nicoletti, O., F. de la Peña, R. K. Leary, D. J. Holland, C. Ducati, and P. A. Midgley, 2013, Nature (London) **502**, 80.

Nie, S. M., and S. R. Emery, 1997, Science **275**, 1102.

Nishiyama, Y., K. Imaeda, K. Imura, and H. Okamoto, 2015, J. Phys. Chem. C **119**, 16215.

Nishiyama, Y., K. Imura, and H. Okamoto, 2015, Nano Lett. **15**, 7657.

Nisoli, M., P. Decleva, F. Calegari, A. Palacios, and F. Martin, 2017, Chem. Rev. **117**, 10760.

Nordlander, P., C. Oubre, E. Prodan, K. Li, and M. I. Stockman, 2004, Nano Lett. **4**, 899.

Novotny, L., R. X. Bian, and X. S. Xie, 1997, Phys. Rev. Lett. **79**, 645.

Novotny, L., and B. Hecht, 2012, *Principles of Nano-Optics*, 2nd ed. (Cambridge University Press, Cambridge, England).

Novotny, L., and S. J. Stranick, 2006, Annu. Rev. Phys. Chem. **57**, 303.

Novotny, L., and N. van Hulst, 2011, Nat. Photonics **5**, 83.

Obermeier, J., T. Schumacher, and M. Lippitz, 2018, Adv. Phys. X **3**, 1454341.

Ocelic, N., A. Huber, and R. Hillenbrand, 2006, Appl. Phys. Lett. **89**, 101124.

Olmon, R. L., P. M. Krenz, A. C. Jones, G. D. Boreman, and M. B. Raschke, 2008, Opt. Express **16**, 20295.

Ossiander, M., *et al.*, 2018, Nature (London) **561**, 374.

Otto, A., 1968, Z. Phys. **216**, 398.

Ozbay, E., 2006, Science **311**, 189.

Paasch-Colberg, T., *et al.*, 2016, Optica **3**, 1358.

Papadogiannis, N. A., B. Witzel, C. Kalpouzos, and D. Charalambidis, 1999, Phys. Rev. Lett. **83**, 4289.

Park, D. J., B. Piglosiewicz, S. Schmidt, H. Kollmann, M. Mascheck, and C. Lienau, 2012, Phys. Rev. Lett. **109**, 244803.

Park, I., S. Kim, J. Choi, D.-H. Lee, Y.-J. Kim, M. F. Kling, M. I. Stockman, and S.-W. Kim, 2011, Nat. Photonics **5**, 677.

Park, S. T., M. Lin, and A. H. Zewail, 2010, New J. Phys. **12**, 123028.

Paul, P. M., E. S. Toma, P. Breger, G. Mullot, F. Auge, P. Balcou, H. G. Muller, and P. Agostini, 2001, Science **292**, 1689.

Paulus, G. G., W. Becker, W. Nicklich, and H. Walther, 1994, J. Phys. B **27**, L703.

Perelomov, A. M., V. S. Popov, and M. V. Terent'ev, 1966, Sov. Phys. JETP **23**, 1924.

Pérez-Hernández, J., M. F. Ciappina, M. Lewenstein, L. Roso, and A. Zaïr, 2013, Phys. Rev. Lett. **110**, 053001.

Persson, B. N. J., 1993, Surf. Sci. **281**, 153.

Petek, H., 2012, J. Chem. Phys. **137**, 091704.

Petek, H., and S. Ogawa, 1997, Prog. Surf. Sci. **56**, 239.

Petersen, J., J. Volz, and A. Rauschenbeutel, 2014, Science **346**, 67.

Pettinger, B., B. Ren, G. Picardi, R. Schuster, and G. Ertl, 2004, Phys. Rev. Lett. **92**, 096101.

Pfeifer, T., M. J. Abel, P. M. Nagel, A. Jullien, Z-H. Loh, M. J. Bell, D. M. Neumark, and Stephen R. Leone, 2008, Chem. Phys. Lett. **463**, 11.

Pfeiffer, C. A., E. N. Economou, and K. L. Ngai, 1974, Phys. Rev. B **10**, 3038.

Pfullmann, N., *et al.*, 2013, New J. Phys. **15**, 093027.

Pietanza, L. D., G. Colonna, S. Longo, and M. Capitelli, 2007, Eur. Phys. J. D **45**, 369.

Piglosiewicz, B., S. Schmidt, D. J. Park, J. Vogelsang, P. Groß, C. Manzoni, P. Farinello, G. Cerullo, and C. Lienau, 2014, Nat. Photonics **8**, 37.

Pile, D. F. P., and D. K. Gramotnev, 2006, Appl. Phys. Lett. **89**, 041111.

Pines, D., 1956, Rev. Mod. Phys. **28**, 184.

Pitarke, J. M., V. M. Silkin, E. V. Chulkov, and P. M. Echenique, 2007, Rep. Prog. Phys. **70**, 1.

Plummer, E. W., J. W. Gadzuk, and D. R. Penn, 1975, Phys. Today **28**, No. 4, 63.

Plummer, E. W., and R. D. Young, 1970, Phys. Rev. B **1**, 2088.

Podbiel, D., P. Kahl, and F.-J. Meyer zu Heringdorf, 2016, Appl. Phys. B **122**, 90.

Pohl, D. W., W. Denk, and M. Lanz, 1984 Appl. Phys. Lett. **44**, 651.

Pomarico, E., I. Madan, G. Berruto, G. M. Vanacore, K. Wang, I. Kaminer, F. J. G. de Abajo, and F. Carbone, 2018, ACS Photonics **5**, 759.

Popmintchev, T., M.-C. Chen, P. Arpin, M. M. Murnane, and H. C. Kapteyn, 2010, Nat. Photonics **4**, 822.

Popmintchev, T., *et al.*, 2012, Science **336**, 1287.

Powell, C. J., and J. B. Swan, 1959, Phys. Rev. **115**, 869.

Press, W. H., S. A. Teukolsky, W. T. Vetterling, and B. P. Flannery, 1994, *Numerical Recipes in C* (Cambridge University Press, Cambridge, England).

Priebe, K. E., C. Rathje, S. V. Yalunin, T. Hohage, A. Feist, S. Schaer, and C. Ropers, 2017, Nat. Photonics **11**, 793.

Pustovit, V. N., and T. V. Shahbazyan, 2006, Chem. Phys. Lett. **420**, 469.

Putnam, W. P., R. G. Hobbs, P. D. Keathley, K. K. Berggren, and F. X. Kärtner, 2017, Nat. Phys. **13**, 335.

Qazilbash, M. M., *et al.*, 2007, Science **318**, 1750.

Qin, Y., B. Ji, X. Song, and J. Lin, 2019, Appl. Phys. B **125**, 3.

Quéré, F., Y. Mairesse, and J. Itatani, 2005, J. Mod. Opt. **52**, 339.

Quinonez, E., J. Handali, and B. Barwick, 2013, Rev. Sci. Instrum. **84**, 103710.

Rácz, P., S. E. Irvine, M. Lenner, A. Mitrofanov, A. Baltuška, A. Y. Elezzabi, and P. Dombi, 2011, Appl. Phys. Lett. **98**, 111116.

Rácz, P., Z. Pápa, I. Márton, J. Budai, P. Wróbel, T. Stefaniuk, C. Prietl, J. R. Krenn, and P. Dombi, 2017, Nano Lett. **17**, 1181.

Raether, H., 1988, *Surface Plasmons on Smooth and Rough Surfaces and on Gratings* (Springer, Berlin).

Rang, M., A. C. Jones, F. Zhou, Z.-Y. Li, B. J. Wiley, Y. Xia, and M. B. Raschke, 2008, Nano Lett. **8**, 3357.

Raschke, M. B., 2013, Ann. Phys. (Berlin) **525**, A40.

Raschke, M. B., and C. Lienau, 2003, Appl. Phys. Lett. **83**, 5089.

Raza, S., N. Stenger, A. Pors, T. Holmgaard, S. Kadkhodazadeh, J. B. Wagner, K. Pedersen, M. Wubs, S. I. Bozhevolnyi, and N. A. Mortensen, 2014, Nat. Commun. **5**, 4125.

Razinskas, G., D. Kilbane, P. Melchior, P. Geisler, E. Krauss, S. Mathias, B. Hecht, and M. Aeschlimann, 2016, Nano Lett. **16**, 6831.

Reed, V. C., and K. Burnett, 1991, Phys. Rev. A **43**, 6217.

Reiss, H. R., 1980, Phys. Rev. A **22**, 1786.

Ren, B., G. Picardi, and B. Pettinger, 2004, Rev. Sci. Instrum. **75**, 837.

Reshef, O., I. De Leon, M. Z. Alam, and R. W. Boyd, 2019, Nat. Rev. Mater. **4**, 535.

Reshef, O., E. Giese, M. Z. Alam, I. De Leon, J. Upham, and R. W. Boyd, 2017, Opt. Lett. **42**, 3225.

Rethfeld, B., A. Kaiser, M. Vicanek, and G. Simon, 2002, Phys. Rev. B **65**, 214303.

Reutzel, M., A. Li, and H. Petek, 2019, Phys. Rev. X **9**, 011044.

Reutzel, M., A. D. Li, B. Gumhalter, and H. Petek, 2019, Phys. Rev. Lett. **123**, 017404.

Rewitz, C., T. Keitzl, P. Tuchscherer, J.-S. Huang, P. Geisler, G. Razinskas, B. Hecht, and T. Brixner, 2012, Nano Lett. **12**, 45.

Rewitz, C., G. Razinskas, P. Geisler, E. Krauss, S. Goetz, M. Pawłowska, B. Hecht, and T. Brixner, 2014, Phys. Rev. Applied **1**, 6.

Richard-Lacroix, M., Y. Zhang, Z. C. Dong, and V. Deckert, 2017, Chem. Soc. Rev. **46**, 3922.

Richardson, O. W., 1929, Nobel Lecture.

Rios Rubiano, C. A., M. S. Gravielle, D. M. Mitnik, and V. M. Silkin, 2012, Phys. Rev. A **85**, 043422.

Ritchie, R. H., 1957, Phys. Rev. **106**, 874.

Ritchie, R. H., and H. B. Eldridge, 1962, Phys. Rev. **126**, 1935.

Ropers, C., T. Elsaesser, G. Cerullo, M. Zavelani-Rossi, and C. Lienau, 2007, New J. Phys. **9**, 397.

Ropers, C., C. C. Neacsu, T. Elsaesser, M. Albrecht, M. B. Raschke, and C. Lienau, 2007, Nano Lett. **7**, 2784.

Ropers, C., D. J. Park, G. Stibenz, G. Steinmeyer, J. Kim, D. S. Kim, and C. Lienau, 2005, Phys. Rev. Lett. **94**, 113901.

Ropers, C., D. R. Solli, C. P. Schulz, C. Lienau, and T. Elsaesser, 2007, Phys. Rev. Lett. **98**, 043907.

Rossi, T. P., M. Kuisma, M. J. Puska, R. M. Nieminen, and P. Erhart, 2017, J. Chem. Theory Comput. **13**, 4779.

Rossouw, D., and G. A. Botton, 2013, Phys. Rev. Lett. **110**, 066801.

Rossouw, D., M. Couillard, J. Vickery, E. Kumacheva, and G. A. Botton, 2011, Nano Lett. **11**, 1499.

Roth, R. M., N. C. Panoiu, M. M. Adams, R. M. Osgood, C. C. Neacsu, and M. B. Raschke, 2006, Opt. Express **14**, 2921.

Rudnick, J., and E. A. Stern, 1971, Phys. Rev. B **4**, 4274.

Ruppert, C., S. Thunich, G. Abstreiter, A. Fontcuberta i Morral, A. W. Holleitner, and M. Betz, 2010, Nano Lett. **10**, 1799.

Ruska, E., 1987, Rev. Mod. Phys. **59**, 627.

Ruthemann, G., 1948, Ann. Phys. (Berlin) **437**, 113.

Ryabov, A., and P. Baum, 2016, Science **353**, 374.

Rybka, T., M. Ludwig, M. F. Schmalz, V. Knittel, D. Brida, and A. Leitenstorfer, 2016, Nat. Photonics **10**, 667.

Rycenga, M., X. Xia, C. H. Moran, F. Zhou, D. Qin, Z.-Y. Li, and Y. Xia, 2011, Angew. Chem., Int. Ed. Engl. **50**, 5473.

Sadiq, D., J. Shirdel, J. S. Lee, E. Selishcheva, N. Park, and C. Lienau, 2011, Nano Lett. **11**, 1609.

Salomon, L., F. Grillot, A. V. Zayats, and F. de Fornel, 2001, Phys. Rev. Lett. **86**, 1110.

Sanchez, E. J., L. Novotny, and X. S. Xie, 1999, Phys. Rev. Lett. **82**, 4014.

Savage, K.J, M. M. Hawkeye, R. Esteban, A. G. Borisov, J. Aizpurua, and J. J. Baumberg, 2012, Nature (London) **491**, 574.

Schafer, K. J., and K. C. Kulander, 1992, Phys. Rev. A **45**, 8026.

Schafer, K. J., B. Yang, L. F. Dimauro, and K. C. Kulander, 1993, Phys. Rev. Lett. **70**, 1599.

Schaffer, B., U. Hohenester, A. Trügler, and F. Hofer, 2009, Phys. Rev. B **79**, 041401.

Schaller, R. D., J. C. Johnson, K. R. Wilson, L. F. Lee, L. H. Haber, and R. J. Saykally, 2002, J. Phys. Chem. B **106**, 5143.

Schenk, M., M. Krüger, and P. Hommelhoff, 2010, Phys. Rev. Lett. **105**, 257601.

Schertz, F., M. Schmelzeisen, M. Kreiter, H. J. Elmers, and G. Schönhense, 2012, Phys. Rev. Lett. **108**, 237602.

Schiffrin, A., *et al.*, 2013, Nature (London) **493**, 70.

Schlaepfer, F., M. Lucchini, S. A. Sato, M. Volkov, L. Kasmi, N. Hartmann, A. Rubio, L. Gallmann, and U. Keller, 2018, Nat. Phys. **14**, 560.

Schmidt, F.-P., H. Ditlbacher, U. Hohenester, A. Hohenau, F. Hofer, and J. R. Krenn, 2014, Nat. Commun. **5**, 3604.

Schmidt, S., P. Engelke, B. Piglosiewicz, M. Esmann, S. F. Becker, K. Yoo, N. Park, C. Lienau, and P. Groß, 2013, Opt. Express **21**, 26564.

Schmidt, S., B. Piglosiewicz, D. Sadiq, J. Shirdel, J. S. Lee, P. Vasa, N. Park, D.-S. Kim, and C. Lienau, 2012, ACS Nano **6**, 6040.

Schmuttenmaer, C. A., M. Aeschlimann, H. E. Elsayed-Ali, R. J. D. Miller, D. A. Mantell, J. Cao, and Y. Gao, 1994, Phys. Rev. B **50**, 8957(R).

Schnell, M., A. Garcia-Etxarri, J. Alkorta, J. Aizpurua, and R. Hillenbrand, 2010, Nano Lett. **10**, 3524.

Schnell, M., A. Garcia-Etxarri, A. J. Huber, K. Crozier, J. Aizpurua, and R. Hillenbrand, 2009, Nat. Photonics **3**, 287.

Schoenlein, R. W., F. G. Fujimoto, G. L. Eesley, and T. W. Capehart, 1988, Phys. Rev. Lett. **61**, 2596.

Scholes, G. D., *et al.*, 2017, Nature (London) **543**, 647.

Scholl, J. A., A. Garcia-Etxarri, A. L. Koh, and J. A. Dionne, 2013, Nano Lett. **13**, 564.

Scholl, J. A., A. L. Koh, and J. A. Dionne, 2012, Nature (London) **483**, 421.

Schötz, J., *et al.*, 2018, Phys. Rev. A **97**, 013413.

Schröder, B., M. Sivis, R. Bormann, S. Schäfer, and C. Ropers, 2015, Appl. Phys. Lett. **107**, 231105.

Schröder, B., *et al.*, 2015, Phys. Rev. B **92**, 085411.

Schroter, U., and A. Dereux, 2001, Phys. Rev. B **64**, 125420.

Schubert, O., *et al.*, 2014, Nat. Photonics **8**, 119.

Schuck, P. J., D. P. Fromm, A. Sundaramurthy, G. S. Kino, and W. E. Moerner, 2005, Phys. Rev. Lett. **94**, 017402.

Schultze, M., *et al.*, 2013, Nature (London) **493**, 75.

Schultze, M., *et al.*, 2014, Science **346**, 1348.

Schütte, B., U. Frühling, M. Wieland, A. Azima, and M. Drescher, 2011, Opt. Express **19**, 18833.

Schwierz, F., and J. J. Liou, 2007, Solid State Electron. **51**, 1079.

Segal, N., S. Keren-Zur, N. Hendler, and T. Ellenbogen, 2015, Nat. Photonics **9**, 180.

Seiffert, L., T. Paschen, P. Hommelhoff, and T. Fennel, 2018, J. Phys. B **51**, 134001.

Seiffert, L., *et al.*, 2017, Nat. Phys. **13**, 766.

Shaaran, T., *et al.*, 2017, Sci. Rep. **7**, 1.

Shalaev, V. M., 2000, *Nonlinear Optics of Random Media*, Vol. 158 (Springer, Berlin).

Shalaev, V. M., 2002, *Optical Properties of Nanostructured Random Media*, Vol. 82 (Springer, Berlin).

Shalaev, V. M., and A. K. Sarychev, 1998, Phys. Rev. B **57**, 13265.

Shen, Y. R., 1984, *The Principles of Nonlinear Optics* (Wiley, New York).

Shore, B. W., and J. H. Eberly, 1978, Opt. Commun. **24**, 83.

Shuford, K. L., M. A. Ratner, and G. C. Schatz, 2005, J. Chem. Phys. **123**, 114713.

Siek, F., *et al.*, 2017, Science **357**, 1274.

Sigle, W., J. Nelayah, C. T. Koch, and P. A. van Aken, 2009, Opt. Lett. **34**, 2150.

Simon, H. J., D. E. Mitchell, and J. G. Watson, 1974, Phys. Rev. Lett. **33**, 1531.

Singh, A., G. Calbris, and N. F. van Hulst, 2014, Nano Lett. **14**, 4715.

Sipe, J. E., D. J. Moss, and H. M. Vandriel, 1987, Phys. Rev. B **35**, 1129.

Sipe, J. E., V. C. Y. So, M. Fukui, and G. I. Stegeman, 1980, Phys. Rev. B **21**, 4389.

Sivis, M., M. Duwe, B. Abel, and C. Ropers, 2012, Nature (London) **485**, E1.

Sivis, M., M. Duwe, B. Abel, and C. Ropers, 2013, Nat. Phys. **9**, 304.

Sivis, M., N. Pazos-Perez, R. Yu, R. Alvarez-Puebla, F. Javier García de Abajo, and C. Ropers, 2018, Commun. Phys. **1**, 13.

Sivis, M., and C. Ropers, 2013, Phys. Rev. Lett. **111**, 085001.

Sivis, M., M. Taucer, G. Vampa, K. Johnston, A. Staudte, A. Yu. Naumov, D. M. Villeneuve, C. Ropers, and P. B. Corkum, 2017, Science **357**, 303.

Skopalová, E., D. Y. Lei, T. Witting, C. Arrell, F. Frank, Y. Sonnefraud, S. A. Maier, J. W. G. Tisch, and J. P. Marangos, 2011, New J. Phys. **13**, 083003.

Smith, R. L., 1962, Phys. Rev. **128**, 2225.

Søndergaard, T., S. M. Novikov, T. Holmgaard, R. L. Eriksen, J. Beermann, Z. Han, K. Pedersen, and S. I. Bozhevolnyi, 2012, Nat. Commun. **3**, 969.

Sönnichsen, C., T. Franzl, T. Wilk, G. von Plessen, and J. Feldmann, 2002a, New J. Phys. **4**, 93.

Sönnichsen, C., T. Franzl, T. Wilk, G. von Plessen, J. Feldmann, O. Wilson, and P. Mulvaney, 2002b, Phys. Rev. Lett. **88**, 077402.

Sönnichsen, C., S. Geier, N. E. Hecker, G. von Plessen, and J. Feldmann, 2000, Appl. Phys. Lett. **77**, 2949.

Spektor, G., *et al.*, 2017, Science **355**, 1187.

Spivak, G. V., E. M. Dubinina, V. G. Dyukov, A. E. Lukyanov, N. N. Sedov, and V. I. Petrov, Pavlyuch. Op, G. V. Saparin, and A. N. Nevzorov, 1968, Izv. Akad. Nauk SSSR, Ser. Fiz. **32**, 1098.

Stahrenberg, K., T. Herrmann, K. Wilmers, N. Esser, W. Richter, and M. J. G. Lee, 2001, Phys. Rev. B **64**, 115111.

Stebbings, S. L., F. Süßmann, Y.-Y. Yang, A. Scrinzi, M. Durach, A. Rusina, M. I. Stockman, and M. F. Kling, 2011, New J. Phys. **13**, 073010.

Steeves, G. M., A. Y. Elezzabi, and M. R. Freeman, 1998, Appl. Phys. Lett. **72**, 504.

Stern, E. A., and R. A. Ferrell, 1960, Phys. Rev. **120**, 130.

Stietz, F., J. Bosbach, T. Wenzel, T. Vartanyan, A. Goldmann, and F. Trager, 2000, Phys. Rev. Lett. **84**, 5644.

Stöckle, R. M., Y. D. Suh, V. Deckert, and R. Zenobi, 2000, Chem. Phys. Lett. **318**, 131.

Stockman, M. I., 2004, Phys. Rev. Lett. **93**, 137404.

Stockman, M. I., 2011, Opt. Express **19**, 22029.

Stockman, M. I., D. J. Bergman, C. Anceau, S. Brasselet, and J. Zyss, 2004, Phys. Rev. Lett. **92**, 057402.

Stockman, M. I., S. V. Faleev, and D. J. Bergman, 2002, Phys. Rev. Lett. **88**, 067402.

Stockman, M. I., M. F. Kling, U. Kleineberg, and F. Krausz, 2007, Nat. Photonics **1**, 539.

Storeck, G., S. Vogelgesang, M. Sivis, S. Schäfer, and C. Ropers, 2017, Struct. Dyn. **4**, 044024.

Stratton, J. A., 1941, *Electromagnetic Theory* (McGraw-Hill, New York).

Sun, J., V. A. Melnikov, J. I. Khan, and O. F. Mohammed, 2015, J. Phys. Chem. Lett. **6**, 3884.

Sun, Q., K. Ueno, H. Yu, A. Kubo, Y. Matsuo, and H. Misawa, 2013, Light Sci. Appl. **2**, e118.

Sun, Q., H. Yu, K. Ueno, A. Kubo, Y. Matsuo, and H. Misawa, 2016, ACS Nano **10**, 3835.

Sun, Z., A. Martinez, and F. Wang, 2016, Nat. Photonics **10**, 227.

Sundaramurthy, A., P. J. Schuck, N. R. Conley, D. P. Fromm, G. S. Kino, and W. E. Moerner, 2006, Nano Lett. **6**, 355.

Süßmann, F., and M. F. Kling, 2011, Phys. Rev. B **84**, 121406(R).

Süßmann, F., *et al.*, 2015, Nat. Commun. **6**, 7944.

Takeuchi, O., R. Morita, R. Oshima, Y. Okada, H. Oigawa, N. Sano, H. Shigekawa, R. Morita, and M. Yamashita, 2004, Appl. Phys. Lett. **85**, 3268.

Talebi, N., Wilfried Sigle, R. Vogelgesang, M. Esmann, S. F. Becker, C. Lienau, and P. A. van Aken, 2015, ACS Nano **9**, 7641.

Tan, S., A. Argondizzo, J. Ren, L. Liu, J. Zhao, and H. Petek, 2017, Nat. Photonics **11**, 806.

Tan, S., L. Liu, Y. Dai, J. Ren, J. Zhao, and H. Petek, 2017, J. Am. Chem. Soc. **139**, 6160.

Tancogne-Dejean, N., and A. Rubio, 2018, Sci. Adv. **4**, eaao5207.

Taucer, M., *et al.*, 2017, Phys. Rev. B **96**, 195420.

Teich, M. C., J. M. Schroeer, and G. J. Wolga, 1964, Phys. Rev. Lett. **13**, 611.

Teichmann, S. M., P. Rácz, M. F. Ciappina, J. A. Pérez-Hernández, A. Thai, J. Fekete, A. Y. Elezzabi, L. Veisz, J. Biegert, and P. Dombi, 2015, Sci. Rep. **5**, 7584.

Teng, Y. Y., and E. A. Stern, 1967, Phys. Rev. Lett. **19**, 511.

Thakkar, N., N. P. Montoni, C. Cherqui, and D. J. Masiello, 2018, Phys. Rev. B **97**, 121403.

Thomas, S., M. Krüger, M. Förster, M. Schenk, and P. Hommelhoff, 2013, Nano Lett. **13**, 4790.

Thomas, S., G. Wachter, C. Lemell, J. Burgdörfer, and P. Hommelhoff, 2015, New J. Phys. **17**, 063010.

Thomson, J. J., 1897, Philos. Mag. (1798–1977) **44**, 293.

Thyagarajan, K., J. Butet, and O. J. F. Martin, 2013, Nano Lett. **13**, 1847.

Tom, H. W. K., G. D. Aumiller, and C. H. Brito-Cruz, 1988, Phys. Rev. Lett. **60**, 1438.

Tromp, R. M., J. B. Hannon, A. W. Ellis, W. Han, A. Berghaus, and O. Schaff, 2010, Ultramicroscopy **110**, 852.

Tsang, T., T. Srinivasan-Rao, and J. Fischer, 1990, Opt. Lett. **15**, 866.

Tsang, T., T. Srinivasan-Rao, and J. Fischer, 1991, Phys. Rev. B **43**, 8870.

Tu, X. W., J. H. Lee, and W. Ho, 2006, J. Chem. Phys. **124**, 021105.

Ueno, K., J. Yang, Q. Sun, D. Aoyo, H. Yu, T. Oshikiri, A. Kubo, Y. Matsuo, Q. Gong, and H. Misawa, 2019, Appl. Mater. Today **14**, 159.

Ullrich, C. A., 2012, *Time-Dependent Density-Functional Theory: Concepts and Applications* (Oxford University Press, New York).

Unold, T., K. Mueller, C. Lienau, T. Elsaesser, and A. D. Wieck, 2004, Phys. Rev. Lett. **92**, 157401.

Unold, T., K. Mueller, C. Lienau, T. Elsaesser, and A. D. Wieck, 2005, Phys. Rev. Lett. **94**, 137404.

Vampa, G., T. J. Hammond, N. Thiré, B. E. Schmidt, F. Légaré, C. R. McDonald, T. Brabec, and P. B. Corkum, 2015, Nature (London) **522**, 462.

Vampa, G., *et al.*, 2017, Nat. Phys. **13**, 659.

Vampa, G., *et al.*, 2018, Nat. Photonics **12**, 465.

van Dijk, M. A., M. Lippitz, and M. Orrit, 2005, Phys. Rev. Lett. **95**, 267406.

van Dijk, M. A., A. L. Tchebotareva, M. Orrit, M. Lippitz, S. Berciaud, D. Lasne, L. Cognet, and B. Lounis, 2006, Phys. Chem. Chem. Phys. **8**, 3486.

Vanacore, G. M., *et al.*, 2018, Nat. Commun. **9**, 2694.

Verhagen, E., L. Kuipers, and A. Polman, 2007, Nano Lett. **7**, 334.

Verhagen, E., A. Polman, and L. Kuipers, 2008, Opt. Express **16**, 45.

Verhagen, E., M. Spasenović, A. Polman, and L. Kuipers, 2009, Phys. Rev. Lett. **102**, 203904.

Vesseur, E. J. R., R. de Waele, H. J. Lezec, H. A. Atwater, F. J. G. de Abajo, and A. Polman, 2008, Appl. Phys. Lett. **92**, 083110.

Vogelsang, J., G. Hergert, D. Wang, P. Groß, and C. Lienau, 2018, Light Sci. Appl. **7**, 55.

Vogelsang, J., J. Robin, B. J. Nagy, P. Dombi, D. Rosenkranz, M. Schiek, P. Groß, and C. Lienau, 2015, Nano Lett. **15**, 4685.

Vogelsang, J., N. Talebi, G. Hergert, A. Wöste, P. Groß, A. Hartschuh, and C. Lienau, 2018, ACS Photonics **5**, 3584.

Voisin, C., N. Del Fatti, D. Christofilos, and F. Vallée, 2001, J. Phys. Chem. B **105**, 2264.

Völcker, M., W. Krieger, and H. Walther, 1991, Phys. Rev. Lett. **66**, 1717.

Volkov, D. M., 1935, Z. Phys. **94**, 250.

von Cube, F., S. Irsen, J. Niegemann, C. Matyssek, W. Hergert, K. Busch, and S. Linden, 2011, Opt. Mater. Express **1**, 1009.

Voronov, J. S., and N. B. Delone, 1966, Sov. Phys. JETP **23**, 54, http://jetp.ac.ru/cgi-bin/dn/e_023_01_0054.pdf.

Wachter, G., C. Lemell, and J. Burgdörfer, 2012, J. Phys. Conf. Ser. **399**, 012010.

Wachter, G., C. Lemell, J. Burgdörfer, M. Schenk, M. Krüger, and P. Hommelhoff, 2012, Phys. Rev. B **86**, 035402.

Wagner, M., *et al.*, 2014, Nano Lett. **14**, 894.

Waldrop, M. M., 2016, Nature (London) **530**, 144.

Wang, D., and P. Schaaf, 2018, Adv. Phys. X **3**, 1456361.

Wang, F. X., F. J. Rodriguez, W. M. Albers, R. Ahorinta, J. E. Sipe, and M. Kauranen, 2009, Phys. Rev. B **80**, 4.

Ward, D. R., F. Hüser, F. Pauly, J. C. Cuevas, and D. Natelson, 2010, Nat. Nanotechnol. **5**, 732.

Watanabe, H., 1956, J. Phys. Soc. Jpn. **11**, 112.

Watanabe, N., and M. Tsukada, 2000, Phys. Rev. E **62**, 2914.

Weiss, S., D. F. Ogletree, D. Botkin, M. Salmeron, and D. S. Chemla, 1993, Appl. Phys. Lett. **63**, 2567.

Wells, D., and H. Quiney, 2019, Sci. Rep. **9**, 782.

Wiersma, D. S., P. Bartolini, A. Lagendijk, and R. Righini, 1997, Nature (London) **390**, 671.

Wijngaarden, J. T., A. Polman, C. E. Ross, H. J. Lezec, and H. A. Atwater, 2006, Appl. Phys. Lett. **88**, 221111.

Willets, K. A,, and R. P. Van Duyne, 2007, Annu. Rev. Phys. Chem. **58**, 267.

Wimmer, L., G. Herink, D. R. Solli, S. V. Yalunin, K. E. Echternkamp, and C. Ropers, 2014, Nat. Phys. **10**, 432.

Wimmer, L., O. Karnbach, G. Herink, and C. Ropers, 2017, Phys. Rev. B **95**, 165416.

Wimmer, L., B. Schröder, M. Sivis, G. Herink, and C. Ropers, 2017, Appl. Phys. Lett. **111**, 131102.

Winkler, J. H., 1744, *Gedanken von den Eigenschaften, Wirkungen und Ursachen der Elektrizität nebst Beschreibung zweiner elektrischer Maschinen* (Breitkopf, Leipzig).

Wittmann, T., B. Horváth, W. Helml, M. G. Schätzel, X. Gu, A. L. Cavalieri, G. G. Paulus, and R. Kienberger, 2009, Nat. Phys. **5**, 357.

Woessner, A., *et al.*, 2015, Nat. Mater. **14**, 421.

Wolf, O., S. Campione, Y. Yang, and I. Brener, 2017, Sci. Rep. **7**, 8101.

Wu, H. J., Y. Nishiyama, T. Narushima, K. Imura, and H. Okamoto, 2012, Appl. Phys. Express **5**, 062002.

Wu, L., and L. K. Ang, 2008, Phys. Rev. B **78**, 224112.

Xu, H., E. J. Bjerneld, M. Käll, and L. Börjesson, 1999, Phys. Rev. Lett. **83**, 4357.

Yalunin, S. V., M. Gulde, and C. Ropers, 2011, Phys. Rev. B **84**, 195426.

Yalunin, S. V., G. Herink, D. R. Solli, M. Krüger, P. Hommelhoff, M. Diehn, A. Munk, and C. Ropers, 2013, Ann. Phys. (Berlin) **525**, L12.

Yalunin, S. V., B. Schröder, and C. Ropers, 2016, Phys. Rev. B **93**, 115408.

Yamamoto, N., K. Araya, and F. J. García de Abajo, 2001, Phys. Rev. B **64**, 205419.

Yamamoto, N., K. Araya, A. Toda, and H. Sugiyama, 2001, Surf. Interface Anal. **31**, 79.

Yamamoto, N., M. Nakano, and T. Suzuki, 2006, Surf. Interface Anal. **38**, 1725.

Yamamoto, N., and S. Ohtani, F. J. G. de Abajo, 2011, Nano Lett. **11**, 91.

Yanagisawa, H., C. Hafner, P. Doná, M. Klöckner, D. Leuenberger, T. Greber, J. Osterwalder, and M. Hengsberger, 2010, Phys. Rev. B **81**, 115429.

Yanagisawa, H., M. Hengsberger, D. Leuenberger, M. Klöckner, C. Hafner, T. Greber, and J. Osterwalder, 2011, Phys. Rev. Lett. **107**, 087601.

Yanagisawa, H., S. Schnepp, C. Hafner, M. Hengsberger, D. Eon Kim, M. F. Kling, A. Landsman, L. Gallmann, and J. Osterwalder, 2016, Sci. Rep. **6**, 35877.

Yang, D.-S., and O. F. Mohammed, and A. H. Zewail, 2010, Proc. Natl. Acad. Sci. U.S.A. **107**, 14993.

Yang, Y., *et al.*, 2019, Nat. Phys. **15**, 1022.

Yannouleas, C., and R. A. Broglia, 1992, Ann. Phys. (N.Y.) **217**, 105.

Yao, J. S., *et al.*, 2018, J. Am. Chem. Soc. **140**, 3626.

Yavuz, I., E. A. Bleda, Z. Altun, and T. Topcu, 2012, Phys. Rev. A **85**, 013416.

Yi, J. M., D. C. Hou, H. Kollmann, V. Smirnov, Z. Papa, P. Dombi, M. Silies, and C. Lienau, 2017, ACS Photonics **4**, 347.

Yoo, K., S. F. Becker, M. Silies, S. Yu, C. Lienau, and N. Park, 2019 (to be published).

Yoshikawa, N., K. Nagai, K. Uchida, Y. Takaguchi, S. Sasaki, Y. Miyata, and K. Tanaka, 2019, Nat. Commun. **10**, 3709.

Yoshikawa, N., T. Tamaya, and K. Tanaka, 2017, Science **356**, 736.

Yoshioka, K., I. Katayama, Y. Minami, M. Kitajima, S. Yoshida, H. Shigekawa, and J. Takeda, 2016, Nat. Photonics **10**, 762.

Yu, W., M. Y. Yu, J. X. Ma, Z. M. Sheng, J. Zhang, H. Daido, S. B. Liu, Z. Z. Xu, and R. X. Li, 2000, Phys. Rev. E **61**, R2220.

Yudin, G. L., and M. Yu. Ivanov, 2001, Phys. Rev. A **64**, 013409.

Yurtsever, A., R. M. van der Veen, and A. H. Zewail, 2012, Science **335**, 59.

Zayats, A. V., I. I. Smolyaninov, and A. A. Maradudin, 2005, Phys. Rep. **408**, 131.

Zener, C., 1934, Proc. R. Soc. A **145**, 523.

Zeng, Y., W. Hoyer, J. J. Liu, S. W. Koch, and J. V. Moloney, 2009, Phys. Rev. B **79**, 9.

Zenhausern, F., Y. Martin, and H. K. Wickramasinghe, 1995, Science **269**, 1083.

Zenhausern, F., M. P. Oboyle, and H. K. Wickramasinghe, 1994, Appl. Phys. Lett. **65**, 1623.

Zewail, A. H., 2010, Science **328**, 187.

Zhang, D., *et al.*, 2018, Nat. Photonics **12**, 336.

Zhang, L., A. Kubo, L. Wang, H. Petek, and T. Seideman, 2011, Phys. Rev. B **84**, 245442.

Zhang, P., T. L. Haslett, C. Douketis, and M. Moskovits, 1998, Phys. Rev. B **57**, 15513.

Zhang, Q. F., N. Large, P. Nordlander, and H. Wang, 2014, J. Phys. Chem. Lett. **5**, 370.

Zhang, R., *et al.*, 2013, Nature (London) **498**, 82.

Zhang, T., N. Gao, S. Li, M. J. Lang, and Q.-H. Xu, 2015, J. Phys. Chem. Lett. **6**, 2043.

Zhang, Y., N. K. Grady, C. Ayala-Orozco, and N. J. Halas, 2011, Nano Lett. **11**, 5519.

Zhao, L., *et al.*, 2018, Phys. Rev. X **8**, 021061.

Zherebtsov, S., *et al.*, 2011, Nat. Phys. **7**, 656.

Zherebtsov, S., *et al.*, 2012, New J. Phys. **14**, 075010.

Zhong, J., A. Chimeh, A. Korte, F. Schwarz, J. Yi, D. Wang, J. Zhan, P. Schaaf, E. Runge, and C. Lienau, 2018, Nano Lett. **18**, 4957.

Zimmermann, P., A. Hötger, N. Fernandez, A. Nolinder, K. Müller, J. J. Finley, and A. W. Holleitner, 2019, Nano Lett. **19**, 1172.